Freie Universität Berlin

From molecules to tissue: Fluorescence spectroscopy and microscopy of nanoparticles and biomolecules involved in inflammation and pain

Von Molekülen zum Gewebe: Fluoreszenzspektroskopie und -mikroskopie von Nanopartikeln und Biomolekülen in Entzündung und Schmerz

im Fachbereich Physik
der Freien Universität Berlin eingereichte Dissertation

vorgelegt von

Alexander Dylan Piers Boreham

Berlin

Juli 2014

Erstgutachterin: Prof. Dr. Ulrike Alexiev

Zweitgutachter: Prof. Dr. Karsten Heyne

Datum der Disputation:: 17 November 2014

Kurzzusammenfassung

Entzündungsprozesse und Schmerz sind eng miteinander verknüpft. Schmerz- und Opioidrezeptoren sind an der Schmerzwahrnehmung beteiligt. Auf der Suche nach neuen therapeutischen Ansätzen ist die Nanomedizin in den Mittelpunkt des Interesses gerückt. Sie steht in enger Verbindung mit der Nanotechnologie und ist darauf ausgerichtet neuartige nanopartikuläre Wirkstoffe und Wirkstofftransportsysteme zu entwickeln, aber auch neue analytische und bildgebende Verfahren zu etablieren und anzuwenden. Letzteres ist der Schwerpunkt dieser Doktorarbeit. Insbesondere wurden Techniken der zeitaufgelösten Fluoreszenz, Fluoreszenzdepolarisation und state-of-the-art Fluoreszenzmikroskopiemethoden, wie Einzelmolekül-Totalreflexionsfluoreszenzmikroskopie und Fluoreszenzlebensdauerimagingmikroskopie (FLIM) angewandt, um Informationen über molekulare Eigenschaften von Nanopartikeln und ihrer Interaktion mit Gewebe im Kontext von Schmerz- und Entzündungsprozessen zu erhalten.

Basierend auf Methoden der Einzelmolekülmikroskopie konnten die Morphologie und die innere Struktur von *nanostructured lipid carriers* (NLC) bestimmt werden. Zur Visualisierung der Morphologie wurde eine Affinitätslabeling-Strategie entwickelt, die mittels stochastischer Bildrekonstruktion Superresolution-Images der NLC-Strukturen unterhalb des Abbe'schen Beugungslimits ermöglichte. Die internen Strukturen von NLCs wurden mittels Einzel-Partikel-Verfolgung von fluoreszierenden Wirkstoff-Mimetika sichtbar gemacht. Es konnte so zum ersten Mal gezeigt werden, dass die untersuchten NLCs einen fluiden Kern in einer festen Lipidschale haben. Die hier etablierte Methodik der Einzelmolekülmikroskopie erlaubt es somit, direkt die NLC Strukturen sichtbar zu machen. Damit ist eine Korrelation der Struktur und der Zusammensetzung der NLC Komponenten möglich, die für ein zielgerichtetes NLC Design unerlässlich ist.

Die Kenntniss der physikochemischen Eigenschaften von Nanopartikeln ist für ihre Anwendung in der Nanomedizin von großer Bedeutung. In dieser Arbeit wurde anhand der Fluoreszenzlebensdauer und der zeitaufgelösten Fluoreszenzanisotropie der Einfluss der Umgebung und der Temperatur auf die Struktur und Dynamik von zwei Polymerpartikeln (dendritisches Polyglycerolsulfat (dPGS) und Core-Multishell (CMS) Nanopartikel) untersucht. Es konnten Änderungen im physiologischen Temperaturbereich festgestellt werden, die entweder Auswirkungen auf die Größe der Partikel oder auf die Verteilung von Wirkstoff-Mimetika im Inneren des Partikel hatten. Beides kann direkt die therapeutische Wirksamkeit beeinflussen.

Bildgebende Verfahren erlauben die Lokalisation von Nanopartikeln im Gewebe. Konfokale Rastermikroskopie in Kombination mit FLIM basiert auf der Messung der Fluoreszenzlebensdauer von angeregten fluoreszierenden Molekülen in jedem Bildpixel. Damit hat FLIM gegenüber der konventionellen Fluoreszenzmikroskopie einen erhöhten Kontrast. Eine Herausforderung für die Datenanalyse ist jedoch das schlechte Signal-Rausch-Verhältnis der pixelbasierten Fluoreszenzlebensdauerkurven, die eine Bestimmung der Fluoreszenzlebensdauern komplizieren, speziell wenn eine spezifische Fluoreszenzlebensdauer-Signatur, z.B. eines fluoreszenzmarkierten Nanopartikels, im autofluoreszierenden Gewebe detektiert werden soll. Mit Hilfe einer ratiometrischen FLIM Analyse, die das spezifische Amplitudenverhältnis der Fluoreszenzlebensdauern nutzt, konnte sowohl die spezifische Bindung eines Opioids an seinen Membranrezeptor als auch die Lokalisation von dPGS im Lebergewebe gezeigt werden. Da aber die ratiometrische Methode bei niedrigen Photonenstatistiken und Fluoreszenzkurven mit mehr als zwei Zerfallskomponenten an ihre Grenze kommt, wurde eine multivariate Analysemethode in der Arbeitsgruppe entwickelt, die beide Probleme umgeht, und in der vorliegenden Doktorarbeit auf die Penetration und Lokalisierung von CMS und Silizium Nanopartikeln als auch von fluoreszenzmarkierten Biomolekülen in der Haut angewendet wurde.

Abstract

Inflammation and pain are intimately connected. Pain receptors and opioid receptors regulate the perception of pain. In the search for new therapeutic agents, nanomedicine has become a focus of attention. In nanomedicine, which is closely related to the field of nanotechnology, novel nanoparticulate drugs and drug delivery vehicles are being developed and new analytical and imaging methods established and applied. The latter is the main focus of this thesis. In particular, time-resolved fluorescence methods, fluorescence anisotropy and state-of-the-art fluorescence microscopy, such as single-molecule microscopy and fluorescence lifetime imaging microscopy (FLIM), were applied to gain new insights into the molecular properties of nanoparticles and their interaction with tissue in the context of inflammation and pain.

Single-molecule microscopy was applied to determine the morphology and the internal structure of nanostructured lipid carriers (NLC). To visualize the morphology an affinity labeling procedure was developed, employing principals of localized stochastic reconstruction microscopy to generate super-resolution images of NLC structures below the Abbe diffraction limit. Visualization of the internal structure of NLCs was achieved by single particle tracking of fluorescent drug mimetics. It could be shown for the first time that the analyzed NLCs consist of a fluid core in a solid lipid shell. Thus, the single-molecule microscopy methodology established here allows the direct visualization of NLC structures, enabling the correlation between NLC composition and the NLC structure required to generate tailor-made NLCs.

Knowledge of the physicochemical properties of nanoparticles is of paramount importance for their nanomedical application. In this work, fluorescence lifetime and time-resolved fluorescence anisotropy were used to investigate the influence of the environment and temperature on the structure and dynamics of two polymer particles (dendritic polyglycerol sulfate (dPGS) and core-multishell (CMS) nanoparticles). Structural changes within the physiological temperature range were detected, which influence either particle size or the internal distribution of drug mimetics, both of which can directly affect therapeutic efficacy.

Imaging techniques allow for the localization of nanoparticles in tissue. Confocal raster scanning microscopy in combination with FLIM measures the fluorescence lifetime decay curve of excited fluorescent molecules in every image pixel. Therefore FLIM has an increased contrast compared to conventional fluorescence microscopy. A major challenge in FLIM data analysis is the poor signal-to-noise ratio of the fluorescence lifetime curves recorded in each pixel which complicate the determination of fluorescence lifetimes, particularly if a specific fluorescence lifetime signature, e.g. of a fluorescently labeled nanoparticle, is to be detected against the autofluorescent background of tissue samples. Ratiometric FLIM analysis, which uses the specific amplitude ratio of the fluorescence lifetimes, enabled the detection of the specific binding of an opioid to its membrane receptor as well as the localization of dPGS in liver tissue. Since the ratiometric method reaches its limits at low photon count rates and when the fluorescence lifetime decay curves contains more than two decay components, a multivariate analysis method was developed in the group of Prof. Alexiev, and applied in this thesis to study the skin penetration and localization of CMS and silica nanoparticles as well as fluorescently labeled biomolecules.

Contents

Nomenclature

ADC	analog-to-digital converter
AHAPS	n-(6-aminohexyl)aminopropyltrimethoxysilane
BSA	bovine serum albumin
CFD	constant fraction discriminator
CMS	core-multishell
DLS	dynamic light scattering
DMPC	1,2-dimyristoyl-sn-glycero-3-phosphocholine
DMSO	dimethyl sulfoxide
dPGS	dendritic polyglycerol sulfate
EM	electron microscopy
EMCCD	electron-multiplying charge coupled device
FLIM	fluorescence lifetime imaging microscopy
Flu	fluorescein
FRET	fluorescence resonance energy transfer
FWHM	full width half maximum
GUV	giant unilamelar vesicle
HA	hyaluronic acid
HEK	human embryonic kidney
ICC	indocarbocyanine
IRF	instrument response function
ITC	isothiocyanate
LCST	low critical phase transition
LD	laser diffractometry
MIA	N-methylisatoic anhydride
MOR	μ-opioid receptor
mPEG	mono methyl ether poly(ethylene glycol)
NLC	nanostructured lipid carrier

NLX	naloxone
NLX-Flu	naloxone-fluorescein
NR	Nile Red
PALM	photoactived localization microscopy
PDI	polydispersity index
PSF	point spread function
RhB	RhodaminB
rmFLIM	ratiometric fluorescence lifetime imaging microscopy
SC	stratum corneum
SiNP	silica nanoparticles
SLD	step length distribution
SLN	solid lipid nanoparticle
SNR	signal-to-noise ratio
STED	stimulated emission depletion
STORM	stochastic optical reconstruction microscopy
TAC	time-to-amplitude converter
TCSPC	time-correlated single photon counting
TEM	transmission electron microscopy
Ti:Sa-Laser	titanium:sapphire laser
TIRF	total internal reflection fluorescence

Chapter 1

Introduction

Inflammation is the response of the innate immune system to harmful stimuli. It is a complex biological process dedicated to react to noxious stimuli, e.g. pathogens or damaged cells. It can be seen as an attempt by the organism to remove the harmful stimuli and initiate the healing process of the respective tissue at the same time.

Inflammatory disorders are commonly accompanied by pain, which is one of many reasons why the search for effective pharmaceutical agents has been an important aspect of medicinal research for a long time. Conventional opioids are very powerful analgesics, i.e. pain killers. However, their usage is restricted due to side effects such as respiratory depression, dizziness, impaired consciousness, addiction and tolerance. These are mainly caused after passing the blood-brain barrier within the central nervous system [Busch-Dienstfertig and Stein, 2010]. Therefore increased efforts are being made to develop opioid-based drugs that can reduce the pain in peripheral tissue, but are unable to cross the blood-brain barrier and thus avoid the side effects caused within the central nervous system [Stein, 2013]. Peripheral drug delivery by topical application to skin is a promising approach [Schäfer-Korting et al., 2007]. However, the skin barrier prevents most substances from entering the peripheral tissue [Schäfer-Korting et al., 2007]. Thus increased efforts are being made to understand how the skin barrier functions and what defines substances being able to penetrate the skin barrier [Cevc and Vierl, 2010].

In the search for new therapeutic agents the use of nanotechnology has come into the focus of attention [Petros and DeSimone, 2010, Cheng et al., 2012, Weissleder et al., 2014]. In addition to the design of nano-sized multifunctional therapeutics and drug delivery systems the use of analytical tools and devices are key elements of nanotechnology applied to nanomedicine to bring a better understanding of the molecular basis of disease, patient predisposition and response to therapy, and to allow imaging at the molecular, cellular and patient levels [European Science Foundation, 2005]. A prominent class of therapeutic agents are nanoparticles, e.g. acting as inhibitors of inflammation or as delivery vehicles for drugs [Khandare et al., 2012]. These nanosystems comprise a multitude of different structural approaches [Khandare et al., 2012]. Currently the design of nanoparticles with responsive elements is under investigation, allowing for functional changes induced by external triggers [Calderón et al., 2010b]. Also, the topical application of nanocarriers to deliver drug molecules and pain killers to the peripheral tissue, promising minimization of systemic side-effects, e.g. for opioids, and for the treatment of inflammatory skin diseases has been studied [Schäfer-Korting et al., 2007, Wolf et al., 2009]. Several nanoparticles meeting these criteria have been recently developed, amongst other lipid-based nanoparticles, such as nanostructured lipid carriers (NLC), and dendritic polyglycerol-based (dPG) nanoparticles. Both of these nanoparticle types were studied in this thesis.

Nanostructured lipid carriers have been shown to be promising transport vehicles for lipophilic drug molecules. Knowledge of their morphology as well as formation and location of

nanocompartments within NLCs is of paramount importance to design tailor-made NLCs for specific applications. However, reports on the NLC morphology by electron microscopy (EM) are contradictory. While cryoEM measurements showed platelets [Bunjes et al., 2001, Jores et al., 2004, Esposito et al., 2008], transmission electron microscopy (TEM) measurements at room temperature identified spherical particles [Araújo et al., 2010, Jia et al., 2010, Luan et al., 2014, Patel et al., 2012, Tsai et al., 2012]. Further, in cryoEM measurements nanostructures attached to the NLC were visible. No such observations were reported for TEM measurements at room temperature. The different findings could be due to the different formulation and production procedure for the investigated NLC or possibly due to different sample treatment prior to cryoEM and TEM. There is a need for alternative visualization techniques for NLC morphology and nanocompartments. A better understanding of the parameters governing these aspects of NLCs is required for tailor-made NLCs.

A different delivery system are core-multishell (CMS) nanocarriers [Türk et al., 2004, Radowski et al., 2007, Küchler et al., 2009b]. They have a core made from dendritic polyglycerol and their surface is functionalized with a hydrophobic and hydrophilic shell layer, into which drug molecules can be loaded. The successful delivery of anti-inflammatory agents and painkillers has been reported [Wolf et al., 2009]. The drug release is an important parameter for the successful delivery of the drug molecules, and can be influenced by the structure of the nanocarrier and the distribution of the drug. These in turn can be affected in response to environmental changes. Therefore a deeper understanding of the drug distribution within the hydrophobic and hydrophilic shell layers of CMS nanocarriers and the sensitivity to the environment is of interest.

Sulfated dendritic polyglycerols show promising anti-inflammatory activity [Dernedde et al., 2010]. A structure-biological activity relationship for sulfated dendritic polyglycerols was reported, showing that the size and molecular flexibility are important parameters for the anti-inflammatory activity [Weinhart et al., 2011b]. A current area of interest is the distribution of these novel agents within the body, their biodistribution within different tissues and their metabolic clearance. For the application in imaging techniques these dendritic polyglycerols can be tagged with fluorescent dyes. New and high resolution imaging techniques are mandatory to detect the localization and interactions of these nanoparticles in cells and tissues.

1.0.1 Aim

The aim of this thesis was to use time-resolved fluorescence spectroscopy and state-of-the-art fluorescence microscopy together with newly developed analysis techniques, to gain new insights, from the molecular up to the tissue level, on biomolecules and nanoparticles directly involved in or with potential application for the treatment of inflammation and pain. This includes the determination and visualization of structure, dynamics, membrane interaction, biodistribution, skin penetration and metabolic clearance of biomolecules and nanoparticles.

Structure of lipid-based nanoparticles A direct visualization of internal nanocompartments within nanostructured lipid carriers (NLC) under near physiological conditions would aid the development of tailor-made NLC without "trial and error" research in the future and would allow for optimized in vivo performance. Due to their size NLCs are not directly visible in light microscopy. The method of super-resolution microscopy [Hell, 2007], however, can resolve structures smaller than the diffraction limit, while single particle tracking (SPT) can visualize the confinement of dye molecules. Here, the aim was to establish a method based on single-molecule fluorescence microscopy to investigate both the inner structure and drug distribution within nanostructured lipid carriers (NLC) as well as their overall morphology.

Molecular dynamics of polyglycerol nanoparticles The molecular basis of nanoparticle interactions with cells and tissue, which is key to the targeted delivery of drugs, can only be understood with precise knowledge of the environmental dependence of the nanoparticle properties. Therefore a thorough investigation of the effect of various environments on nanoparticles is mandatory. Time-resolved fluorescence lifetime and anisotropy have been widely employed in the field of biophysics (see e.g. [Kim et al., 2012, Alexiev and Farrens, 2014]). Similarly these techniques have also been used to characterize polymeric structures and to analyze their thermal response [Chee et al., 2006] and their intramolecular segmental dynamics [Chee et al., 2011]. Here, time-resolved fluorescence lifetime and anisotropy was applied to nanocarriers containing dendritic polyglycerol as a structural unit, dendritic polyglycerol sulfate (dPGS) and core-multishell (CMS) nanocarriers, to gain information on the environmental dependence of their segmental dynamics and size, as well as the drug distribution within CMS nanocarriers.

Localization of nanoparticles and biomolecules in tissue with FLIM Visualizing the skin penetration, biodistribution and metabolic clearance of nanoparticles and biomolecules is of great importance for their application in nanomedicine. Biodistribution and metabolic clearance are both directly related to cytotoxicity and biocompatibility of nanoparticles and biomolecules, while a deeper understanding of the principals governing the transport of substances across the skin barrier is required for the design of new topical drug delivery vehicles. Fluorescence lifetime imaging microscopy (FLIM) can be used to spatially resolve fluorescent molecules based on their fluorescence lifetime, gaining additional contrast compared to conventional fluorescence microscopy. However, the poor signal-to-noise ratios and high fluorescent backgrounds, e.g. common in FLIM imaging of skin and tissue samples, are a challenge for FLIM data analysis, mandating new concepts for the analysis of FLIM data. Here, the aim was to develop and apply new FLIM analysis techniques, dealing with the challenges presented by samples with high fluorescent backgrounds and poor signal-to-noise ratios, to detect specific ligand binding but also the biodistribution, metabolic clearance and skin penetration of fluorescently labeled biomolecules and nanoparticles in tissue samples.

Chapter 2

Fundamentals

2.1 Nanoparticles

A nanoparticle is primarily defined by its size. An exact definition of where one enters the size range of nanoparticles is hard to come by. Some sources define nanoparticles as particles with at least one dimension smaller than 1 µm [Buzea et al., 2007] while other definitions require three dimensions to be 100 nm or less.

Nanoparticles can be classified into three types depending on their origin. Natural events such as sand storms, fires and volcanic eruptions are the main source of naturally occurring nanoparticles, whereas incidental nanoparticles stem from man-made processes, such as food cooking and many industrial processes. In contrast to incidental nanoparticles which are involuntary byproducts, technological advances over the last decades have resulted in a multitude of engineered nanoparticles. Engineered nanoparticles are designed with specific applications in mind. The envisaged applications are manifold, and range from household goods and cosmetics to the use in biomedical imaging and treatment of diseases, e.g. via highly specific gene or drug delivery. These highly beneficial possibilities offered by engineered nanoparticles are however contrasted by the toxicological threat posed, among other things, by their small size. Hence, a thorough investigation of the physicochemical properties of each nanoparticle systems is required to understand possible health risks, and further the study of their uptake and distribution in the organism is mandatory. An overview of synthetic and non synthetic nanoparticles, uptake routes of the body, and their possible effects is given by Buzea [Buzea et al., 2007].

An exclusively size-based definition of nanoparticles has resulted in the present multitude of differently engineered nanoparticles using all sorts of building blocks. Common building blocks include carbons, metals, ceramics, lipids and polymers. Engineered nanoparticles can further be divided into different classifications depending on their function. For example, nanocarriers are nanoparticles with the ability to load, transport and release cargo molecules. Whereas nanocarriers can be used for drug and cargo delivery, such as gene and other biomolecules. Non-transporting nanoparticles can have intrinsic beneficial properties, e.g. they might be designed to be anti-inflammatory like the dendritic polyglycerol sulfate (dPGS) used in my work.

Since the work presented in this thesis focuses on nanoparticles based on lipids, ceramics and polymers, these three types of nanoparticles will be presented in more detail.

2.1.1 Polymeric nanoparticles

All polymeric nanoparticles share a structural motive based on repeating units of monomeric building blocks. These can be either solely linked to each other but can also be bound to other molecules, such as drugs or proteins. Depending on the way the linkage occurs and how the

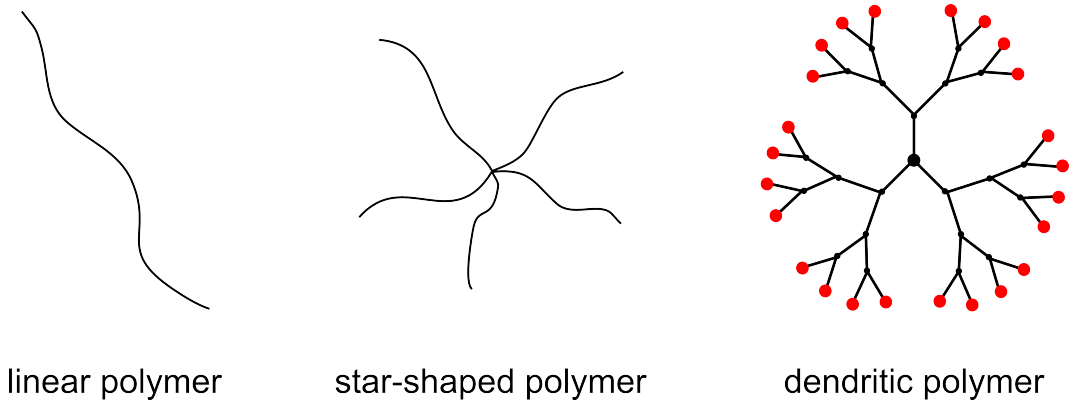

Figure 2.1. Topologies of different polymeric architectures. The complexity increases from linear polymers to star-shaped polymers and dendritic polymers. The functional surface groups of the dendritic architecture are highlighted in red.

synthesis is performed many different architectures can be generated (Figure 2.1), ranging from simple linear polymers to more complex forms, e.g. dendritic polymers.

Compared to linear polymers, dendritic polymers are advantageous for many applications [Lee et al., 2005]. They show good solubility in different solvents, have a well defined structure and a large number of functional groups at the surface. These can be used to apply surface modifications as required, e.g. for specific targeting or reduced toxicity. Further, due the high density of surface groups dendritic nanoparticles can exhibit multivalency, i.e. one dendritic polymer can bind to multiple target molecules. In addition, more complex architectures can be generated using the functional groups of dendritic polymers as starting points. An example are so-called core-multishell nanoparticles, where a dendritic polymer was further modified, creating a structure mimicking liposomes on a unimolecular level [Radowski et al., 2007] and allowing for uptake and transport of other substances.

2.1.2 Lipid-based nanoparticles

The high intrinsic biocompatibility of lipids, as natural components of cells, make lipid-based systems an attractive approach for nanocarrier development. Liposomes are a well known and well characterized transport system based on lipids. However, these have several drawbacks. Among others, high cost of production, leakage of encapsulated substances and limitation to soluble substances reduce the effectiveness and feasibility of liposomes as drug carriers, particularly for lipophilic drugs [Selvamuthukumar and Velmurugan, 2012].

Solid lipid nanoparticles (SLN) were developed in the early 1990s and provided a new system particularly suited to the delivery of hydrophobic drugs. They are formed from an emulsion of a solid lipid, i.e. solid at both room temperature and body temperature, in water. Although SLN combine desirable properties for application, such as safe components and easy technical production in large quantities, particularly of lipophilic actives, they also have several drawbacks. The incorporation of drugs is based on using spaces within the SLN due to defects in the crystalline lipid lattice. As a result, the loading capacity is rather low, and uncontrolled drug release due to rearrangements within the crystal lattice are not uncommon (Figure 2.2) [Müller et al., 2002, Müller et al., 2011].

To overcome these drawbacks nanostructured lipid carriers (NLC) were developed. Instead of consisting of only one solid lipid, these consist of a blend of lipids, where, at room and body temperature, one lipid is solid while the other is liquid (oil). NLCs containing a high percentage of the oil component are thought to have distinct nanocompartments, formed during the cooling process. Using a drug molecule with a high partitioning coefficient for the oil

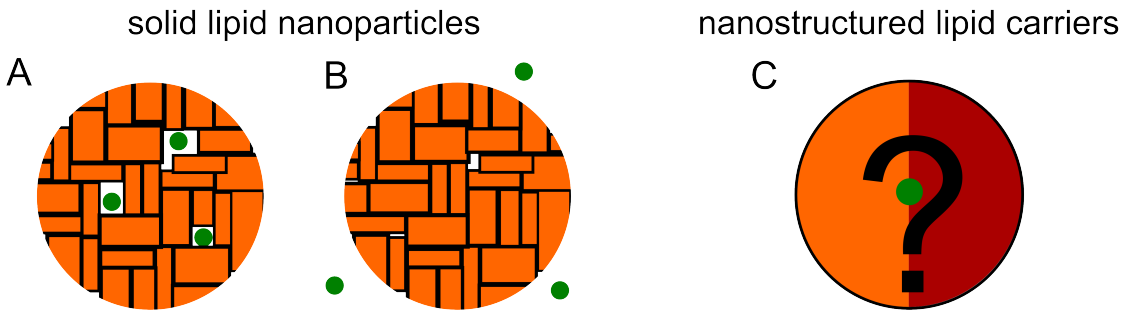

Figure 2.2. Structural models of lipid nanoparticles. The solid lipid nanoparticles consist only of a solid lipid (orange). (A) The drug molecule (green) is localized in defects in the crystal lattice. (B) Drug expulsion can occur spontaneously upon changes within the crystal lattice. (C) Nanostructured lipid carriers contain an additional oil phase (red). It is not clear if and how nanocompartments of the oil phase form within the solid phase.

phase, the drug molecule is thought to be accommodated in these nanocompartments at high concentrations [Müller et al., 2002, Müller et al., 2011].

2.1.3 Ceramic nanoparticles

Ceramic nanoparticles can be fabricated from ceramic materials such as zirconia, silica, titanium dioxide or alumina. High stability, high load capacity, their easy incorporation into hydrophobic and hydrophilic systems and the possibility of further surface functionalization are properties that make ceramic nanoparticles interesting for use in drug delivery and bioimaging. However, there are differing reports on the biocompatibility and toxicity of ceramic nanoparticles in the literature [Moreno-Vega et al., 2012].

Promising ceramic nanoparticles, with few biocompatibility and cytotoxicity issues, are silica-based nanoparticles [Wang et al., 2008]. The potential of silica particles functionalized with AHAPS (n-(6-aminohexyl)aminopropyltrimethoxysilane) has already been shown, for example, in the binding of DNA [Luo and Saltzman, 2006]. Gene transfection with AHAPS silica particles has been studied both in vitro and in vivo [Kneuer et al., 2000, Ravi Kumar et al., 2004].

2.2 Skin as a target for topical nanoparticle application

The skin is the outermost layer of vertebrate organisms. In mammals, it is one of the largest organs. Human skin, for example, covers an area of about $2\,m^2$. As the skin covers such a large area and is, as the outermost layer, the boundary to the environment a number of different requirements need to be meet. Among others, it is responsible for regulating homeostasis and presents a barrier protecting the organism from harmful external agents, e.g. pathogens. Moreover, it also contains sensory neurons, e.g. detecting touch, heat and pain, and numerous cells involved in immune and inflammatory responses. Hence the skin is also both a sensory organ and a protective organ, based on physical, biochemical and immunological barriers. The manifold functions of the skin are reflected in its complex organization.

2.2.1 Skin morphology

At the most basic level, human skin can be divided into two distinct layers, the epidermis and the dermis (Figure 2.3A). The epidermis is the outermost layer conferring the physical and biochemical protective properties. The epidermis itself contains no blood vessels. Therefore the tasks of providing the lower epidermal regions with nutrients is performed by the dermis.

Further important functions of the dermis are to give stability to the whole skin and to host sensory neurons and immune cells. The immune cells, however, are not restricted to the dermis as the epidermis also contains immunocompetent cells. The dermis and epidermis are separated by the *basal membrane* (Figure 2.3A). Below the dermis is the subcutaneous tissue, consisting mainly of fibroblast, adipose cells and macrophages.

The dermis itself can again be subdivided into two characteristic layers (Figure 2.3A). Furthest away from the skin surface lies the so-called *stratum reticulare*, a protein fiber-rich region, mainly collagen (type III) and elastin, of connective tissue responsible for the high stability and elasticity of the skin. The cell types found in this region are mainly fibroblasts, synthesizing the extracellular matrix components, but also a number of immunocompetent cells such as dendritic cells, mast cells and macrophages. It is also the region in which hair follicles and various glands are situated. Above the *stratum reticulare* lies the much thinner *stratum papillare*. It contains characteristic excrescences towards the epidermis, giving the border between the dermis and the epidermis its characteristic rugged appearance (Figure 2.3A). The *stratum papillare* is mainly built up of loose connective tissue but also contains mechanoreceptors, free nerve endings of thermosensory neurons, nociceptors, involved in pain sensation, mast cells and macrophages. Due to its role in supplying the epidermis with nutrients a high number of capillaries are concentrated in this region, generating the large surface area required for an efficient, diffusion driven, nutrient supply of the epidermis. The extent of the epidermis can vary between 75 µm and 600 µm, depending on the site of the body. In contrast to the collagen rich dermis, keratin is the main constituent of the epidermis. It is contained within keratinocytes, the defining cell type of the epidermis. The various differentiation states of the keratinocytes also mark the four different layers of the epidermis (Figure 2.3B). Closest to the dermis, i.e. the layer directly above the *basal membrane*, is the so-called *stratum basale*. It is connected to the *basal membrane* by protein anchors, known as hemidesmosomes. This layer contains the epidermal stem cells and keratinocytes with high mitotic activity. The *stratum basale* is followed by the *stratum spinosum*. High amounts of cell-cell contacts, via desmosomes, and keratin in this region confer a certain stability to the whole epidermis. Above, one finds the *stratum granulosum*, where the most striking differentiation events of the keratinocytes during their transition to non-metabolic cells occur.

Two defining structures are formed within the keratinocytes (Figure 2.3B). Lamellar granules, containing lipids and protein, are secreted from the cells, while membrane devoid keratohyalin granules, filled with keratin fragments and histidine rich profilaggrin, accumulate within the cells themselves. Therefore, the keratinocytes at this stage of their differentiation are also known as granular cells. At the transition between the *stratum granulosum* and the final epidermal layer, the *stratum corneum* (SC), the remaining differentiation steps are initiated. The profilaggrin is converted into the active filaggrin, causing an irreversible linking of the keratin filament via disulfide bridge formation. The content of the lamellar granules is released, mainly lipids such as phospholipids, cholesterol and glycosylceramide which all are essential to the barrier function of the skin. Within this lipid matrix, the remains of the keratinocytes are closely interwoven. The keratinocytes at this stage have fully differentiated into non-metabolic, nucleus devoid corneocytes, providing the vanguard of the skins barrier against external substances together with the lipid matrix (Figure 2.3B). The SC usually has a thickness of 15 µm to 20 µm, although it can also be thicker depending on the site of the body.

2.2.2 Barrier function of the skin

The barrier function of the skin is of great importance for the protection of the organism. There are a number of different mechanisms contributing to the effective barrier of the skin. Most of the protective elements can be found in the epidermal layers. These include physical and

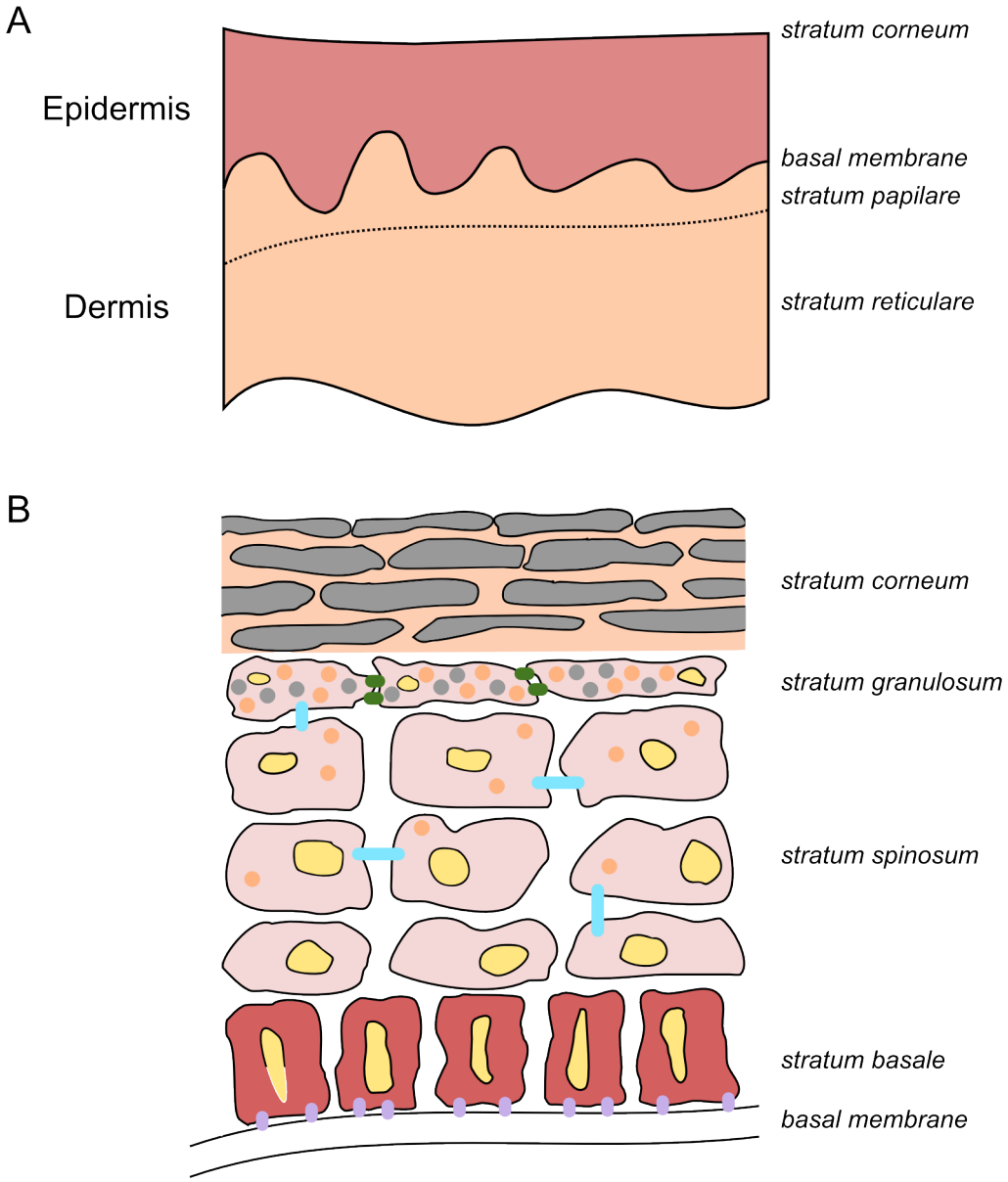

Figure 2.3. Schematic of skin morphology. (A) Basic structure of the skin. (B) Different layers of the epidermis. The *stratum basale* is connected to the basal membrane by hemidesmosomes (violet). The keratinocytes in the *stratum spinosum* are loosely held together by desmosomes (cyan) and lamellar granules (orange) start to form. In the *stratum granulosum* the cells her held in close contact by tight junctions (green) and the cells contain large numbers of lamellar granules and keratohyalin granules (gray). The *stratum corneum* is made up of the corneocytes and the intercellular space is filled mainly by lipids.

biochemical barriers, where the biochemical barrier functions cover a wide range from enzymatic and antimicrobial activities to components of the immune system [Elias, 2007].

Physical barrier

The physical barrier of the skin mainly acts as a permeation barrier, hindering the free diffusion of substances across the skin. Any particle entering the skin, whether pathogen or drug loaded nanocarrier, needs to overcome this barrier. The SC consist of multiple layers of closely interwoven keratinocyte layers, at least 20 but even up to 100 layers, embedded into a lipid matrix, and is specifically designed to hinder foreign molecules from entering the organism.

At is most basic, the structure of the SC can be approximated by the brick and mortar model (Figure 2.4A), where the corneocytes represent the bricks and the lipid matrix is the mortar, filling the gaps between the bricks and thus rendering the whole structure very impermeable [Elias, 1983].

The corneocytes are filled with many keratin fibrils (Figure 2.4B) providing a high amount of mechanical resistance. On the inner side of the corneocyte cell membrane there is a very high density of proteins, mainly filaggrins, involucrins and locrins, forming a very insoluble and penetration resistant barrier, the cornified envelope (Figure 2.4B). Further, specific lipids, mostly ceramides, on the outside of the cell are covalently linked to the cornified envelope generating a very water repelling environment, the lipid envelope (Figure 2.4B). The lipid envelope is also thought to act as a scaffold for the formation of the intercellular lipid bilayer [van Smeden et al., 2014]. Cell-cell contacts between the corneocytes, mediated by specific glycoproteins (corneodesmosomes) are of great importance for the cohesion (or integrity) of the SC and directly effect the permeability of the SC [Elias, 2007] along with the lipid matrix.

The unique mixture of the lipids filling the intercellular space of the SC plays an important roll for the barrier function of the SC [Baroni et al., 2012]. It is composed mainly of ceramides (~50%), cholesterol (~25%) and free fatty acids (~15%) (Figure 2.4C) [Feingold and Elias, 2014]. The lipid matrix however is not entirely hydrophobic. It is built up of a highly ordered mul-

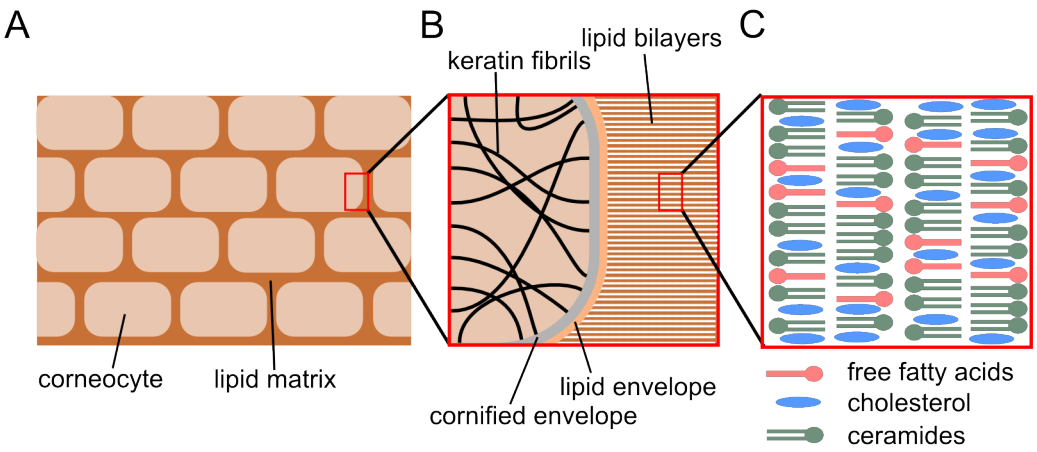

Figure 2.4. Morphology of the *stratum corneum* (A) The brick and Mortar model of the SC. The bricks are a representation of the corneocytes and the lipid matrix is the mortar. (B) Close-up of the bounding region between the corneocyte and the lipid matrix. The corneocyte is filled with keratin fibrils, terminating in the protein rich cornified envelope. The lipid envelope is covalently linked to the cornified envelope and serves as a scaffold for the lipid bilayers filling the intercellular space. (C) Schematic representation of the molecular structure of the SC lipid bilayers. They contain mainly ceramides, but also cholesterol and free fatty acids.

tilamellar system of lipid bilayers (Figure 2.4C). The high degree of order of the intercellular lipids is of importance for the barrier function of the skin. According to Elias [Elias, 2005] it is the combination of the hydrophic character, the absolute quantities, the lipid distribution and the supramolecular organization that is responsible for the physical barrier function of the SC.

The lipid organization can be described both in terms of the lamellar as well as the lateral organization and the structure of both is implicated in the formation of an intact skin barrier (Figure 2.5). The lamellar organization has been shown to follow a so called broad-narrow-broad arrangement of lamellar sheets. Small-angle X-ray diffraction in-vitro experiments on isolated human SC revealed that the extent of the lamellar phases is either 13 nm, known as the long periodicity phase (LPP), or6 nm, the short periodicity phase (SPP) (Figure 2.5) [Bouwstra et al., 1991]. Further, in a study on ruthenium tetroxide fixated excised pig skin, these lamellar phases were shown to occur in 3, 6, 9 or 12 repeats within the intercellular space of the SC suggesting a trilayer arrangement [Swartzendruber et al., 1989, van Smeden et al., 2014].

The lateral organization describes the packing of the lipids within the lamellar phases. Lipid packing depends to a large extent on the geometry of the lipids. Most phospholipids have a bulky head group and are best approximated by a conical shape. The large head group compared to the fatty acid residues leads to a relatively large freedom of movement of the lipid chains and thus to a rather fluid membrane. In the *stratum corneum*, however, phospholipids are basically absent. Instead, there is an abundance of long, straight-chain fatty acids and ceramides, both of which can be approximated by a rod shape. These rod-shaped lipids are better suited to a dense, highly ordered packing, forming much more rigid and impermeable lipid layers than normal cell membranes do [Wertz, 2013].

Three different types of packing can occur: orthorhombic, hexagonal and liquid disorder (Figure 2.5). The orthorhombic packing displays the highest density of lipids and is therefore the most compact. In intact SC, and at normal skin temperatures of 30 °C to 32 °C the orthorhombic is the most prevalent, although a population of lipids packed in the hexagonal organization, and therefore less dense, was also observed. In a study on in vivo and ex vivo human skin samples specially prepared for transmission electron microscopy [Pilgram et al., 1999, Bouwstra et al., 2001] evidence for the existence of a liquid phase was also found , although probably not as a continuous phase throughout the whole SC. Temperatures above the normal skin temperatures can increase the amount of non-orthorhombic packing, as found in a study on isolated human SC and a SC substitute lipid model [Groen et al., 2011].

Currently, the relative importance of the lamellar and lateral organization for the skin barrier is under discussion. In experiments on in vivo human skin, the permeation of water through human SC was found to be dependent on the packing, in particular on the relative amount of lipids in orthorhombically packed [Damien and Boncheva, 2010]. In a different study using benzoic acid, the packing did not seem to influence the benzoic acid penetration through the skin, however, the lamellar organization was found to have a pronounced influence on the permeation through a SC substitute lipid model [Groen et al., 2011]. Generally speaking, both the lamellar and lateral organization of the lipids in SC intercellular space are crucial for the formation of an intact skin barrier. External factors, such as temperature, as well as changes in the lipid composition, as occur in various skin diseases and also implicated to occur in inflammatory skin conditions, can affect the overall lipid organization and thus have an impact on the intactness of the skin barrier [van Smeden et al., 2014].

Further contributions to the skin barrier come from tight junctions, desmosomes and adherens junctions, protein-protein interactions forming connections between cells (desmosomes and tight junctions) and between cells and the cytoskeleton (adherens junctions) [Brandner et al., 2010]. The main tight junction proteins are claudin, occludin and zonal occluding proteins, while desmosomes are formed by cadherins and adherence junctions are formed between

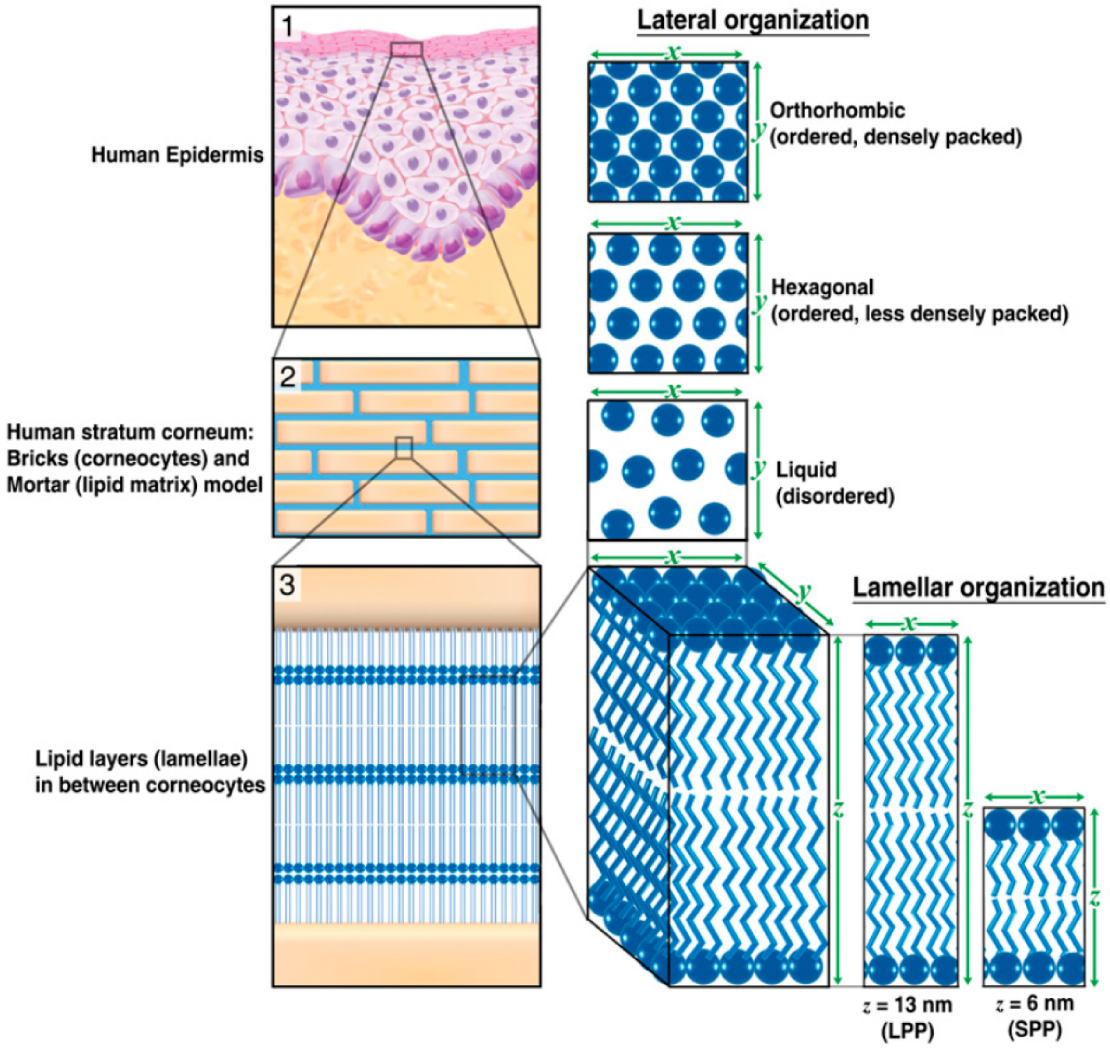

Figure 2.5. Lamellar and lateral organization in human *stratum corneum*. (1) The outermost layer of the epidermis, the SC, consists of dead cells (corneocytes) embedded in a lipid matrix, also referred to as the brick (corneocytes) and mortar (lipids) structure (2). The intercellular lipids are arranged in layers (lamellae) (3), with two coexisting lamellar phases. These lamellar phases have a repeat distance of 6 nm (referred to as the SPP) or 13 nm (referred to as the LPP). The lateral organization is the plane perpendicular to the direction of the lamellar organization. There are three possible arrangements of the lipids: a very dense, ordered orthorhombic organization; a less dense, ordered hexagonal organization; and a disordered liquid organization. Figure and caption taken from [Janssens et al., 2012] (Figure reproduced in compliance with the copyrights permission guidelines for this article, a license was obtained).

cadherin and catenin or nectin and afadin. While the SC contains a special type of desmosome, the corneodesmosome, the other junctions are predominantly found in the epidermis, contributing to an additional barrier below the SC [Brandner et al., 2010]. The tight junctions between cells are particularly abundant in the *stratum granulosum*, further hindering the permeation of substances and thought to be the main factor contributing to the epidermal barrier [Baroni et al., 2012].

Biochemical barrier

The skin not only poses a physical barrier to prevent substances from entering the organism, but there are also manifold biochemical mechanisms that complement the physical barrier function.

The cornified envelope is the source of the strong chemical resistance of the SC. In addition, the SC is relatively acidic compared to normal tissue. It displays a pH gradient, with the most acidic region close to the SC surface. This so-called acid mantle has been revealed to play an important role both for the permeability barrier, the integrity of the skin as well as the antimicrobial barrier [Elias, 2005]. Further, it helps in generating an antimicrobial environment against pathogen growth, while at the same time supporting the growth of the normal skin microflora [Mauro, 2006].

Further contributions to the antimicrobial environment of the SC come from lipids, such as free fatty acids and sphingosine. Beside antimicrobial activity, these also exhibit antifungal and antiviral activity to some extent [Elias, 2007]. Moreover, antimicrobial peptides in the SC extracellular domain also play an important role. Aside from their inherent antimicrobial character, they have also been shown to be important for the homeostasis of the permeability barrier [Elias, 2007] and to help activate the immune response if the skin is breached [Baroni et al., 2012].

In addition to supporting the physical barrier with the right conditions and creating an antimicrobial environment, the skin is also a component of the innate immune response. It comprises both active and passive immune mechanisms and can be seen as a pro-inflammatory tissue. Minimal damages to the skin barrier activate signaling cascades involving pro-inflammatory signaling molecules such as cytokines [Elias, 2005]. These signals reach the epidermal and dermal layers, where a number of immunocompetent cells resides. In the epidermis these are mainly Langerhans cells and T lymphocytes, while the dermis contains many different immune cells, such as dermal dendritic cells, T- and B-cells, natural killer cells, mast cells and macrophages [Di Meglio et al., 2011].

2.2.3 Pathways through the skin

The movement of substances across the SC is mainly driven by diffusion. The properties of the substance will determine how it can cross the SC. The postulated transport routes across the SC include the intercellular space, intracellular trafficking through the corneocytes and also transglandular and transfollicular pathways (Figure 2.6A). The latter have been shown to accommodate particles with sizes between 300 nm and 600 nm, taking advantage of the structures offered by gland ducts and hair follicles [Lademann et al., 2011]. The intracellular pathway, on the other hand, is the most unlikely route for any molecule to take. Substances would have to traverse both polar and apolar regions of the *stratum corneum*, and also overcome the almost impenetrable corneocytes [Nino et al., 2010].

Most substances will traverse the *stratum corneum* using the intercellular route. However, if and how molecules penetrate via the intercellular route will depend on their specific properties, such as size, charge, flexibility and of course their hydrophilicity or lipohilicity. Lipophilic molecules can diffuse within the non-polar regions of the lipidic lamellae, while hydrophilic

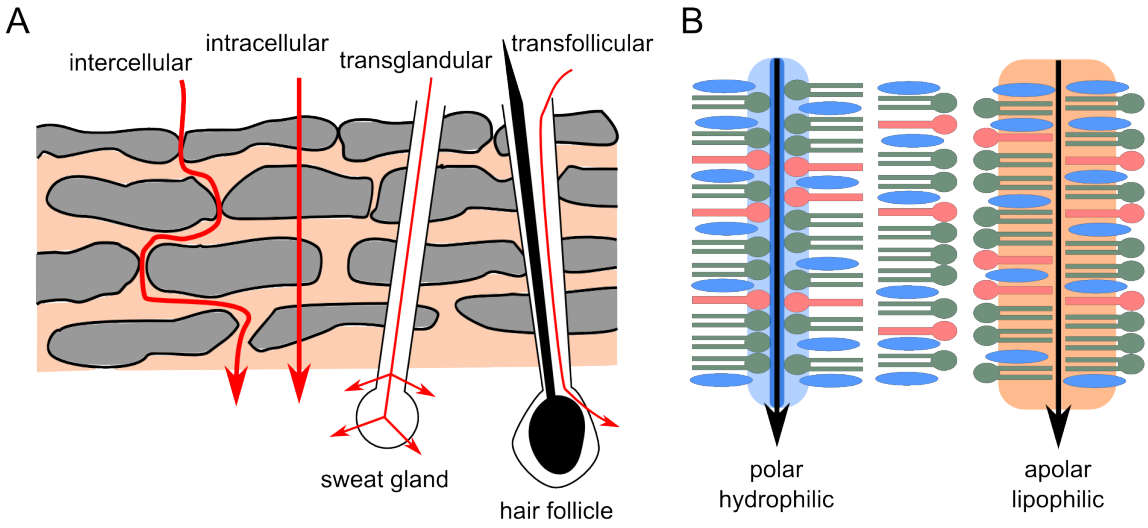

Figure 2.6. Penetration pathways through the *stratum corneum*. (A) Four different possible routes through the SC. (B) Polar and apolar route through the SC bilayer.

molecules can only move along the polar region between the head groups (Figure 2.6B). Studies using neutron scattering on a model lipid matrix revealed a width of 3.8 nm for the lipophilic region, and a width of only 0.5 nm for the hydrophilic space between the head groups [Schröter et al., 2009]. Therefore, under normal conditions, only small polar molecules can overcome the skin barrier.

Lipophilic molecules mainly permeate via the lipid pathway. Here, the permeability coefficients of the lipophilic molecule directly correlate with their partition coefficient [Li and Peck, 2013]. Hence, the barrier to penetration decreases with increasing lipophilicity of a molecule. Skin barrier penetration for lipophilic molecules is mainly limited by the molecular weight, with 500 kDa being the upper limit, unless penetration enhancer are employed [Cevc and Vierl, 2010]. This is due to the dimensions of the lipid matrix. There are hardly any defects within the intercellular lipid matrix large enough to allow lipophilic molecules with a molecular weight above 500 kDa to diffuse across the SC barrier [Cevc and Vierl, 2010].

For hydrophilic molecules, the permeability coefficients did not correlate with partition coefficients as expected from models of the transport across a lipophilic barrier [Li and Peck, 2013]. Peck and coworkers [Peck et al., 1994] compared the passive transport observed in diffusion cells experiments on human skin to mathematical models. They observed that a porous membrane model explained their experimental values better than a solely lipoidal model. Therefore, the existence of an alternative polar pathway was postulated. In vivo experiments on mouse skin revealed that highly deformable vesicles were shown to make use of a narrow aqueous transepidermal pathways, suggesting a mode of passage for polar molecules [Schätzlein and Cevc, 1998]. Hydrophilic molecules should favor passage either in regions where the corneocytes do not fully overlap laterally, gaps between corneocyte clusters, or along the most curved regions of the corneocytes outer membrane, as occurs at lateral cell junctions [Schätzlein and Cevc, 1998,Cevc and Vierl, 2010]. In these areas, hydrophilic regions are created and also the ordering of the lipids is reduced. The narrow aqueous epidermal pathway (or pores) probably do not exceed a diameter of 10 nm in natural skin [Cevc and Vierl, 2010]. Only small skin type dependent differences were found between studies on hairless rat skin [Ruddy and Hadzija, 1992] and porcine skin [Tezel

and Mitragotri, 2003]. These values corresponded well to theoretical predictions [Mitragotri, 2002, Mitragotri, 2003]. However, depending on the skin conditions, hydrophilic pathways as wide as 20 nm to 30 nm can be present [Cevc and Vierl, 2010]. A possible continuous pore pathway was postulated to be formed by lacunar domains within the *stratum corneum*. These are thought to exist at sites of corneodesmosome degradation and can expand and interconnect given the right stimulus, e.g. occlusion, prolonged hydration or iontophoresis, thus forming a continuous pore pathway [Elias et al., 2002].

From the different possible pathways across the skin, it follows that successful penetration of the skin barrier is dependent on more than one single factor. It is a complex interplay between the penetrating molecules size, partition coefficient and surface properties. On the one hand, small lipophilic particles should have a penetration advantage, while nanoparticles have to be small enough to either make use of fluid regions of the lipidic bilayer or potential aqueous pore pathways to be able to traverse the SC [Baroli, 2010]. Despite these insights, the exact interplay between the skin anatomy and the permeability remains unclear and any prediction of the penetration properties of a given molecule has proven very challenging.

2.3 Opioid receptors

Opioid receptors play an important role in the treatment of pain. They belong to the G-protein coupled receptors and three main types have been identified, the μ-, δ- and κ-opioid receptors. Opioid receptors are expressed on peripheral and central neurons as well as neuroendocrine cells, ectodermal cells and cells of the immune system. Opioid receptor activation within the central nervous system, however, has been shown to cause side effects such as respiratory depression, dizziness, impaired consciousness, addiction and tolerance, restricting the use of opioids acting systemically, despite their powerful analgesic effects. Since the activation of opioid receptors outside the central nervous system eliminates most of these side effects [Stein, 2013], peripheral opioid receptors are promising targets for localized pain treatment.

Opioid receptors expression has also been reported for the skin. Opioid receptor activation in the skin is implicated in peripheral regulation of pain and itch, e.g. in chronic dermatitis, and also in the modulation of immune cell types in the skin [Bigliardi et al., 2009]. It has also been suggested that substances acting solely on peripheral opioid receptors could be potent anti-inflammatory drugs [Reich and Szepietowski, 2012]. Further, opioid receptor expression has been shown to be upregulated in inflammed tissue [Philippe et al., 2006, Stein, 2013], providing a natural increase in target molecules. Thus peripheral opioid receptors, beside being a target for analgesics, can also be viewed as a promising target for anti-inflammatory drugs. According to Stein [Stein, 2013] the "future aims in drug development include the design of peripherally restricted opioid agonists, selective targeting of opioids to sites of painful injury and the augmentation of peripheral ligand and receptor synthesis, e.g., by gene therapy"'. Nanocarrier systems have been shown to offer an effective delivery of opioid receptor ligands, while both protecting them from degradation and minimizing systemic toxicity [Wolf et al., 2009, Hua and Wu, 2013, Stein, 2013].

2.4 Diffusion

The driving force for transport of substances across the *stratum corneum* and into the skin is diffusion. Many other biological processes also rely on diffusion, e.g. the spread of signaling molecules at synapses or the movement of proteins within lipid membranes. Fluorescently labeled molecules allow the use fluorescence spectroscopy and microscopy to investigate the diffusion behavior, e.g. with single-molecule microscopy. Further, besides the lateral motion, molecules

can also undergo rotational diffusion.

2.4.1 Brownian Motion

Brownian Motion was first describe in 1827 by Robert Brown and named after him. Brownian Motion is the irregular displacement of particles in a gas or liquid resulting from collisions, induced by thermal agitation, between the particles themselves and the surrounding atoms or molecules. It is a stochastic process, the magnitude of which is proportional to the temperature.

For a quantitative description of Brownian Motion, the particle displacement Δx_i is analyzed in identical time intervals Δt. Due to the stochastic nature of the processes, the average over many displacements ($N \to \infty$, N equals the number of displacements) along one axis will be zero, as displacements in positive directions are as probable as those in negative directions (Figure 2.7),

$$\langle\overline{\Delta x}\rangle = \frac{\sum \Delta x_i}{N} = 0\,. \tag{2.1}$$

However, the mean square displacement (MSD), will differ from zero, as only the length of the steps is averaged,

$$\langle\overline{\Delta x^2}\rangle = \frac{\sum (\Delta x_i^2)}{N} \neq 0\,. \tag{2.2}$$

When extending the MSD to two dimension one obtains

$$\langle\overline{\Delta r^2}\rangle = \frac{\sum (\Delta x_i^2 + \Delta y_i^2)}{N}\,. \tag{2.3}$$

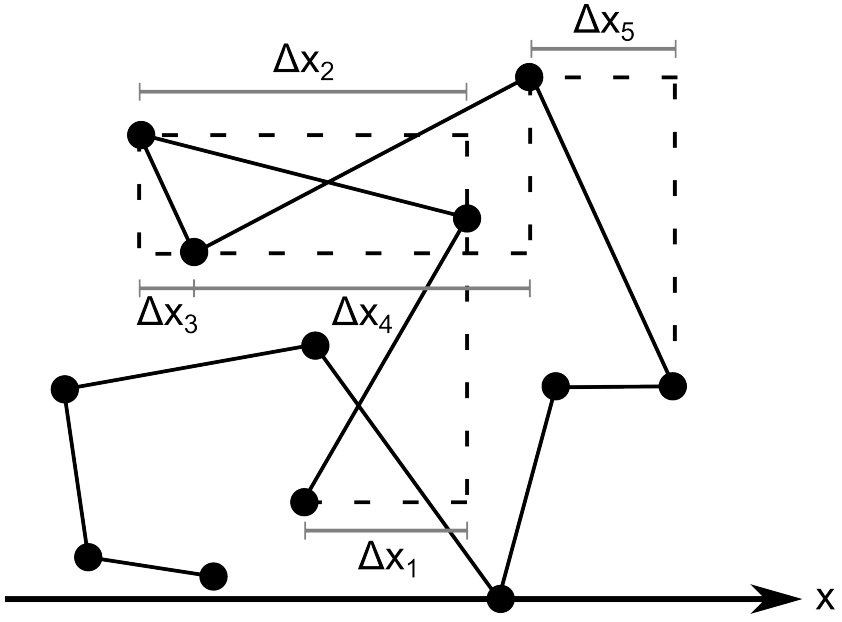

Figure 2.7. Brownian Motion of a particle. The particle trajectory is shown for 10 time points and the displacement along the x-axis is indicated for the first five time points.

2.4.2 Translational Diffusion

The translation diffusion of molecules, which is caused by thermal movement of the particles (the Brownian motion), describes the tendency of particles to distribute themselves stochastically within a given volume. The direction of motion is from high particle concentrations toward low particle concentrations. Diffusion was described mathematically by Adolf Fick.

Assuming an unequal distribution of particle densities n within a defined volume, then the diffusion process will result in a uniform distribution of particle densities n, as long as no particles are generated or removed within the system (e.g. by chemical reactions). The particle density n within a defined volume corresponds to the local concentration $c(\vec{r},t)$. The diffusion process is driven by the gradient of the concentration $\nabla c(\vec{r},t)$. The particle flux $\vec{J}(\vec{r},t)$ is defined as the number of particles moving through a small area in a small time interval. Fick's first law states that the particle flux is proportional to the gradient of the particle concentration.

$$\vec{J}(\vec{r},t) = -D\nabla c(\vec{r},t)\,, \tag{2.4}$$

where D is the diffusion coefficient.

The diffusion coefficient is dependent on parameters describing the system, such as the temperature of the system, the nature of the particles and the viscosity of the diffusion media. Assuming spherical particles with a radius R and Stockes' drag the diffusion constant is given by the Stokes-Einstein equation

$$D = \frac{k_B T}{6\pi\eta R}\,. \tag{2.5}$$

As can be seen the diffusion coefficient increases with temperature, leading to faster diffusion of the particles, whereas larger particles and media with high viscosity decrease the diffusion coefficient, resulting in slower overall diffusion.

Fick's second law can be directly obtained from the continuity equation

$$\frac{\partial c(\vec{r},t)}{\partial t} + \nabla\vec{J}(\vec{r},t) = 0\,, \tag{2.6}$$

stating that the time dependent change in the local concentration $\frac{\partial c(\vec{r},t)}{\partial t}$ is counterbalanced by the spatial change of the particle flux. Inserting 2.4 into 2.6 results in Fick's second law for diffusion coefficients D that are constant

$$\frac{\partial c(\vec{r},t)}{\partial t} = -\nabla\vec{J}(\vec{r},t) = -\nabla(-D\nabla c(\vec{r},t))\,, \tag{2.7}$$

$$\frac{\partial c(\vec{r},t)}{\partial t} = D\Delta c(\vec{r},t))\,. \tag{2.8}$$

For free diffusion the probability density is given by

$$p(\vec{r},t) = \frac{1}{4\pi Dt} exp\left(-\frac{y^2+x^2}{4Dt}\right)\,. \tag{2.9}$$

It is described in terms of a Gaussian distribution with the expected value of 0 and a variance of $4Dt$. Transformation to polar coordinates and subsequent integration gives the expectancy of the mean square deviation as

$$\langle r^2(t)\rangle = 4Dt\,. \tag{2.10}$$

However, this is only true for free diffusion. Other possible types of diffusion include driven diffusion, where a further directed motion is superimposed on the particle diffusion, and confined diffusion, where barriers limit particle diffusion.

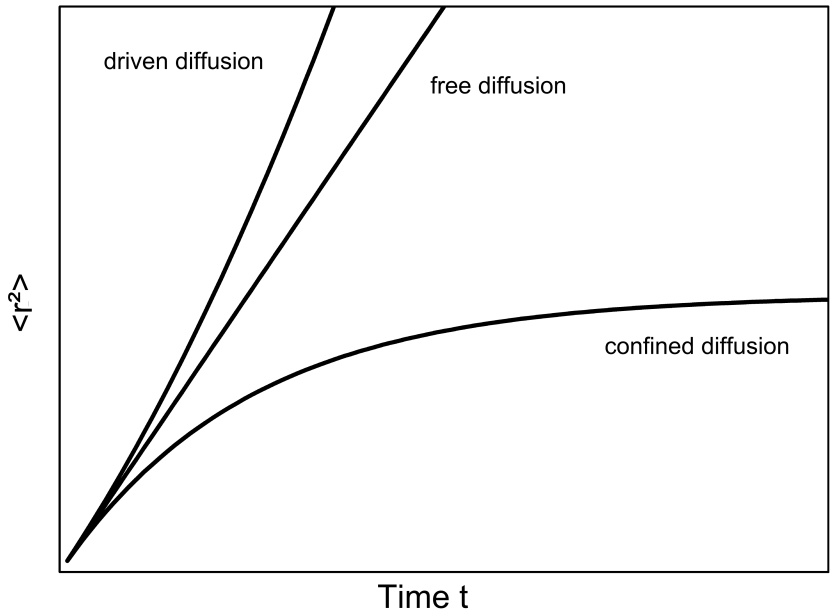

Figure 2.8. Characteristic MSD for different diffusion types.

For driven diffusion, the mean square deviation is obtained by adding a term to equation 2.10 taking the velocity (v) of the particles caused by the directed motion into account

$$\langle r^2(t)\rangle = 4Dt + (vt)^2 \,. \tag{2.11}$$

For confined diffusion the exact description of the mean square displacement depend on the geometry of the barrier. A general description is given by Saxton and Jacobson [Saxton and Jacobson, 1997]

$$\langle r^2(t)\rangle = \langle r_c^2\rangle 1 - A_1 exp\left(-\frac{4A_2 D_0 t}{\langle r_c^2\rangle}\right) . \tag{2.12}$$

The constants A_1 and A_2 are dependent on the barrier geometry and r_c^2 is the confinement length.

When analyzing the mean square displacement of a particle, the type of diffusion can be determined from a plot of the MSD against time. Free diffusion will show a linear behavior, as follows from equation 2.10, while the MSD of driven diffusion will increase with a parabolic component and confined diffusion will approach a constant value (Figure 2.8).

2.4.3 Rotational Diffusion

Particles not only diffuse in space, i.e. change the position of their center of mass, but can also undergo rotational diffusion. Here, as the system strives towards thermal equilibrium, the symmetry axis becomes randomly distributed over time. The respective symmetry axis can be due to intrinsic particle properties, such as geometry or charge distribution (dipole moment), but can also be induced by electromagnetic radiation, utilized in nuclear magnetic resonance and certain fluorescence experiments.

The rotational diffusion can be described similarly to the translation diffusion. Assuming rotational diffusion around a single axis, the orientation density distribution can be defined as

$$\rho(\theta) = \frac{\partial n}{\partial \theta} \,, \tag{2.13}$$

describing the orientation of all molecules $\partial n(\theta)$ oriented with an angle between θ and $\theta + d\theta$ to an arbitrary z-axis at a certain time t. Due to the intrinsic thermal rotational diffusion, the orientation of each molecule can change within a time interval ∂t.

The change can be described in analogy to Fick's First Law (equation 2.4)

$$\frac{\partial n}{\partial t} = -D_r \frac{\partial \rho(\theta)}{\partial \theta}\,, \tag{2.14}$$

with D_r the diffusion coefficient of the rotation. Using the Einstein-Smoluchowski relation

$$D = \mu kT = \frac{kT}{f_R}\,, \tag{2.15}$$

where μ is the mobility and f_R is the fraction factor of the particle, and the friction factor for small spherical particles with the radius R

$$f_R = 8\pi\eta R^3\,, \tag{2.16}$$

the rotational diffusion coefficient can be written as

$$D = \frac{kT}{8\pi\eta R^3} = \frac{kT}{6\eta V}\,. \tag{2.17}$$

2.5 Fluorescence

Fluorescence occurs upon exited state electron relaxation to the ground state by emission of a photon. Molecules with the ability to fluoresce are called fluorophores. Fluorescence spectroscopy and microscopy have become very useful and powerful tools in modern day biophysics. From steady-state to time-resolved fluorescence data, from simple fluorescence emission spectra to state-of-the-art single-molecule methods, the analysis of fluorescence data has been extensively used to study and visualize localization, interactions and dynamics of biomolecules. In the following, I will briefly introduce the main aspects of fluorescence exploited by the different fluorescence methods used in this thesis.

2.5.1 Fluorescence resonance energy transfer

Fluorescence resonance energy transfer (FRET), also known as Förster resonance energy transfer, describes the radiationless energy transfer from the excited state of one molecule (donor) to the ground state of another molecule (acceptor). Through FRET the donor returns to the ground state without emitting a photon, while the acceptor is in the excited state and can relax to the ground state by emitting a photon. The energy transfer in FRET is due to dipole-dipole coupling between the donor and the acceptor. One constraint for FRET is an energetic overlap between the excited states of donor and acceptor. Only then can the donor send out a photon with the energy required to excite the acceptor molecule. The energetic overlap can be determined by comparing the emission spectrum of the donor and the absorption spectrum of the acceptor. FRET can occur if an overlap region exists. Further, as the FRET efficiency E is inversely proportional to the sixth power of the distance r between the molecules

$$E = \frac{R_0^6}{R_0^6 + r^6}\,, \tag{2.18}$$

where R_0 is the donor acceptor pair specific Förster distance. As common Förster distance values are in the low nanometer range, FRET is sensitive to close contacts between the molecules. Due to this distance dependence FRET is sometimes called a 'molecular ruler' and has been used, for example, to study conformational changes with protein structures.

2.5.2 Fluorescence lifetime

The time τ an exited state electron remains in the exited state before relaxing to the ground state by emission of a photon is known as the fluorescence lifetime of the fluorophore. In the simplest case, if the only transition to the ground state is by photon emission, the fluorescence lifetime will only depend on the radiative decay rate k_r

$$\tau = \frac{1}{k_r} \,. \tag{2.19}$$

However, in most systems other non-radiative decay processes also play a role, such as internal conversion, intersystem crossing, excited state reactions and energy transfer, which all influence the observable fluorescence lifetime of a fluorophore. The fluorescence lifetime can then be expressed as

$$\tau = \frac{1}{k_r + k_{nr}} \,, \tag{2.20}$$

with k_{nr} the non-radiative decay rate. The influence of the non-radiative decay rates is also the root of the environmental sensitivity of the fluorescence lifetime. While the intrinsic radiative decay rate remains unchanged, the contribution of the non-radiative decay components is strongly dependent on the environment. For example, polar environments tend to reduce the fluorescence lifetime as the non-radiative decay rate is increased due to a higher efficiency of energy transfer to larger dipole moments of the polar environment. Further, some fluorophores exhibit different fluorescence lifetimes depending on their conformation. Here, environmental constraints favoring a certain conformation, such as steric hindrance, can be deduced from the measured fluorescence lifetime.

2.5.3 Fluorescence anisotropy

The excitation and emission of light by fluorophores is mainly described by their respective absorption and emission dipole moments. In the electronic ground state, the absorption dipole moments are randomly orientated. When exciting such a sample with polarized light, absorption preferentially takes place by fluorophores with an absorption dipole moment parallel to the plane of polarization of the excitation light. Before a photon is emitted, this highly polarized population of excited state dipole moments usually depolarize to a certain extent. One cause is the intrinsic difference in orientation of the absorption and emission dipole moments, as described by the transition dipole moment, but in most cases the main contribution to the depolarization is due to the rotational diffusion of the fluorophore, the rate of which depends on its size and shape and the viscosity of the solvent. Binding of a fluorophore to a target molecule, will alter the rotational diffusion behavior of the fluorophore. The fluorescence depolarization or anisotropy can contain information on the size and the internal flexibility of the target molecule. The fluorescence polarization P is defined as

$$P = \frac{I_{\parallel}(t) - I_{\perp}(t)}{I_{\parallel}(t) + I_{\perp}(t)} \,, \tag{2.21}$$

while the fluorescence anisotropy can be calculated from

$$r(t) = \frac{I_{\parallel}(t) - I_{\perp}(t)}{I_{\parallel}(t) + 2I_{\perp}(t)} \,. \tag{2.22}$$

2.5.4 Microscopy of single fluorophores

The image of a single emitter obtained from an optical imaging system will be a diffraction pattern, known as the airy pattern. It contains the bright airy disk at its center and multiple, less bright, concentric rings around the central airy disk. The radius of the airy disk will depend on the wavelength and the numerical aperture. The airy disk is basically the projection of the three dimensional point spread function onto a two dimensional plane. Kowing the exact form of the PSF allows the particles' position to be calculated with far greater accuracy than the diffraction limited image's resolution.The measured PSF, however, is influenced e.g. by the pixelation and noise. Using image analysis routines, the position of the emitter can still be determined with an accuracy of around 10 nm.

Chapter 3

Materials, sample preparation and experimental procedure

In the following I will give an overview over the fluorophores used in this study, briefly present how the samples were prepared and describe the experimental procedures.

3.1 Fluorescent dyes

For single-molecule experiments the dyes ATTO647, ATTO647N and Oxa12 (all from ATTO-TEC) were chosen. All three dyes have a high photostability, emission intensities and quantum yield but differ in their hydrophobicity and charge (Table 3.1). Further, these dyes can be excited with the 633 nm output wavelength of the helium-neon laser available in the total internal reflection fluorescence (TIRF) microscopy setup (see section 4.1.1). For investigating polyglycerol-based nanoparticles the ICC (indocarbocyanine) dye was used as a covalently attached label while the dye Nile Red (NR) was employed as a hydrophilic drug mimetic. The fluorescently labeled naloxone derivative naloxone-fluorescein was used in experiments on the binding of naloxone (NLX) to the μ-opioid receptor in cell membrane fragments. For experiments with hyaluronic acid (HA) and bovine serum albumin (BSA), HA was labeled with the dye N-methylisatoic anhydride (MIA) and BSA was labeled with the dye RhodaminB-isothiocyanate. To study the distribution of silica particles in mouse skin particles with incorporated fluorescein (Flu) were used. The structures of the dye molecules, in so far as available, are shown in Figure 3.1 together with absorption and emission spectra, and characteristic properties of the dyes are summarized in Table 3.1.

3.1.1 Determination of dye concentration by absorption spectroscopy

Absorption spectroscopy measures the amount of unpolarized monochromatic light absorbed by a sample solution. If monochromatic light with an intensity I_0 passes through a dilute chromophore solution, the light intensity will decline exponentially along the path of the light:

$$I(d) = I_0 \cdot exp^{-\epsilon_\lambda \cdot c \cdot d} \,, \tag{3.1}$$

where ϵ_λ is the wavelength dependent molar extinction coefficient in $M^{-1}\,cm^{-1}$, c is the concentration in M and d is the thickness of the sample in cm. Applying the logarithm converts equation 3.1 into Lambert-Beer's law:

$$lg(\frac{I_0}{I}) = \epsilon_\lambda \cdot c \cdot d \,, \tag{3.2}$$

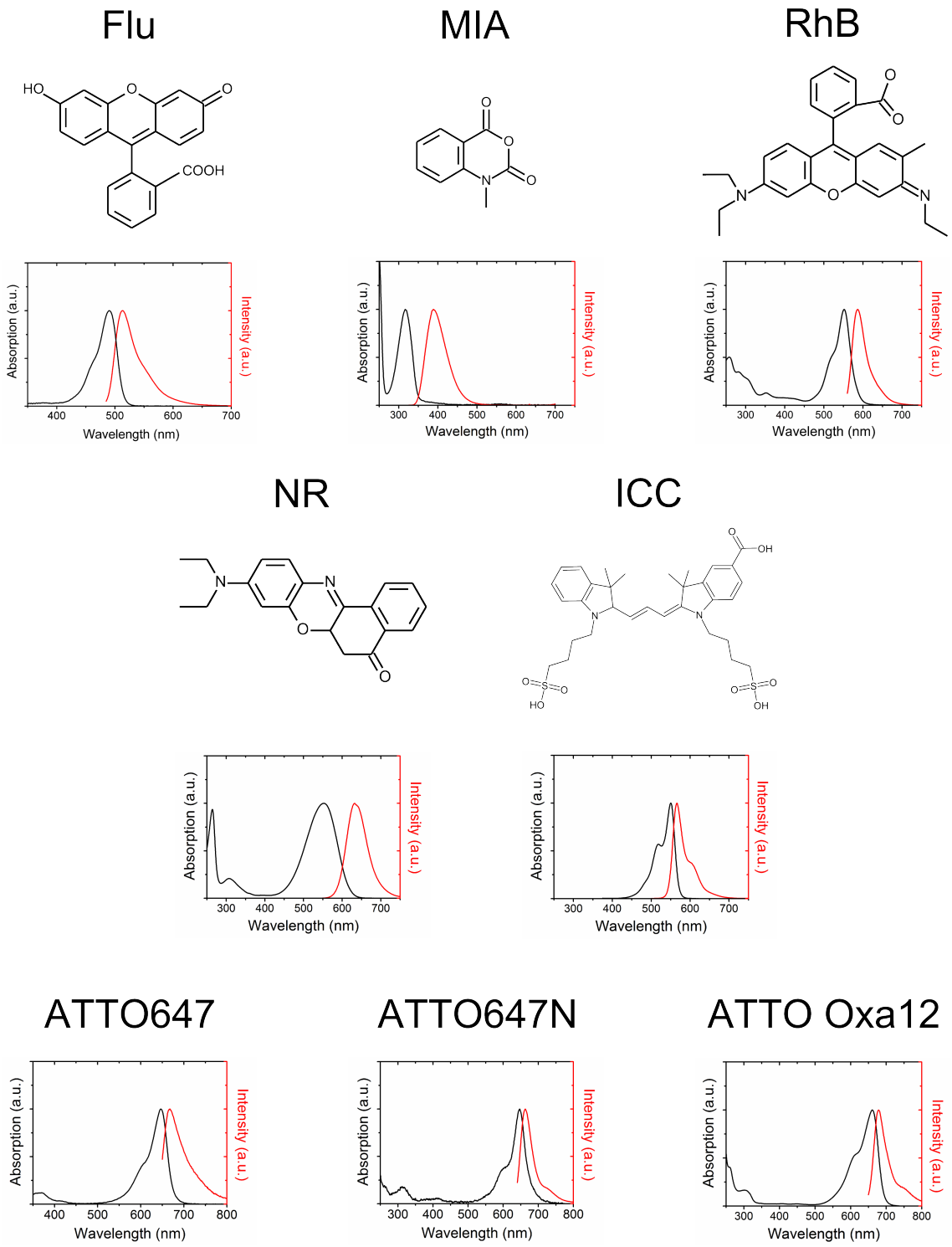

Figure 3.1. Structure and spectra of dyes used in this study. Spectra were recorded in aqueous solution, except for Nile Red, which was recorded in ethanol. The structure of ATTO647, ATTO647N and Oxa12 is not available to date.

Table 3.1. Summary of the properties of the dyes used in this study.

dye	absorption properties		emission properties		chemical properties
	ϵ_λ ($M^{-1}\,cm^{-1}$)	λ_{max}^{abs} (nm)	λ_{max}^{em} (nm)	τ (ns)	
Flu	77000*	492†	515†	4.0†	pH dependent dye
MIA (MeOH)	3450*	316†	388†		small label
Rhodamin B	80000*	554†	584†	1.7‡	
ICC	130000*	550†	566†	0.18†	derived from cyanine dyes, methine linker
NR (in MeOH)	43000*	552†	632†	3.6†	liphophilic, solvent dependent, poorly soluble and quenched in water
Atto647	120000*	645†	669†	2.4*	zwitterionic, zero net charge, high quantum yield and photo-stability*
Atto647N	150000 *	644†	669†	3.5 *	cationic, moderately hydrophilic, high quantum yield and photo-stability*
Oxa12	125000 *	663†	684†	1.8 *	cationic, lipophilic, good quantum yield and excellent photo-stability*

† own data; * data from manufacturer;
‡ http://www.iss.com/resources/pdf/datatables/LifetimeDataFluorophores.pdf

which can also be expressed in terms of the dimensionless quantity A, the absorbance of the sample,

$$A_\lambda = \epsilon_\lambda \cdot c \cdot d \, . \tag{3.3}$$

From equation 3.3 the concentration of the sample can be calculated according to

$$c = \frac{A_\lambda}{\epsilon_\lambda \cdot d} \tag{3.4}$$

if the extinction coefficient and the absorbance at the same specific wavelength are known. The thickness of the sample d is usually determined by the experimental setup used, e.g. the type of cuvette.

3.2 Sample preparation and experimental procedures

3.2.1 Nanostructured lipid carriers (NLC)

NLC production

The nanostructured lipid carriers were produced by D. Peters (Prof. Müller (Institute of Pharmacy, Freie Universität Berlin), Prof. Keck (Institute of Applied Logistic and Polymer Sciences, University of Applied Sciences Kaiserslautern). Briefly, NLCs consisting of Dynasan®118, solid lipid, and Miglyol® 812, medium chain triglycerides, as matrix lipids were produced by hot high pressure homogenization. The dispersion was stabilized by 2 % (w/w) Plantacare® 818 (C8–16 fatty alcohol glycoside, Cognis). I will refer to these as blank NLCs on contrast to dye loaded NLCs. For dye loaded NLCs 0.02 mg of the respective dye was dispersed within 0.4 mg Miglyol® 812 prior to the homogenization procedure to ensure the localization of the dye within the liquid lipid. Hot high pressure homogenization was carried out by applying 3 homogenization cycles at 500 bar and 80 °C. Dynamic light scattering (DLS), laser diffractometry (LD) and zeta potential measurements were done by D. Peters to characterize the particle solutions regarding size averages, size distribution, polydispersity (through the polydispersity index) and charge. The blank sample and the dye loaded samples showed very similar particle characteristics regarding z-average, PDI and size distribution (Table 3.2).

Table 3.2. Summary of the properties of the of NLC samples used in this study.

sample	DLS		LD				Zeta Potential
	z-Average (nm)	PDI	LD50 (nm)	LD90 (nm)	LD95 (nm)	LD99 (nm)	(mV)
blank	166.0	0.173	148	271	323	491	-22
ATTO647	164.1	0.152	163	383	457	536	
ATTO647N	169.5	0.111	157	319	421	512	
Oxa12	167.5	0.163	156	343	431	515	

Single-molecule measurements of NLCs

A requirement for the determination of size and internal structures of the NLCs using single-molecule microscopy is that the dye movement is not superimposed by motion of NLCs. To this end the NLCs needed to be immobilized on the cover glass. A common method in the literature for immobilizing NLCs, e.g. to determine their size by electron microscopy, is to place a drop of solution onto the sample holder and to let the solute evaporate [Araújo et al., 2010, Jia et al., 2010, Luan et al., 2014, Patel et al., 2012]. Here, a 10 µl drop of aqueous NLCs solution was pipetted onto a meticulously cleaned cover slip and the water was left to evaporate. To prevent any contamination of the sample, the cover slip was kept in a cleaned glass container with the lid only slightly open and placed inside a sealable plastic bag. Samples were measured at the earliest three days after application to the cover slip in order to ensure complete evaporation of water. For the measurement the cover slip was assembled together with the measurement chamber and placed on the microscope. For data collection, the microscope setup was operated in TIRF mode (see section 4.1.1). The neutral density filter was adjusted depending on the intensity of the sample. Data acquisition was conducted using the software package Hipic (Hamamatsu).

Affinity labeling experiments were performed with cover slips prepared as described above using an aqueous solution of 0.001 % NLC. An Oxa12 solution with a concentration of 0.1 nM to 20 nM was added to the measurement chamber prior to the measurement. In order to obtain sufficient data to reproduce the NLC particle size, the acquisition of a large number of frames was necessary. The data files analyzed in this thesis contained up to 15000 frames per measurement. Positional stability of the microscopy setup was ensured by test measurements with fluorescent beads. Data analysis was conducted as described in section 4.2.1.

For the measurement of the internal structure cover slips with immobilized NLCs on the surface were prepared using an aqueous solution of 0.1 % NLC and measured at the earliest three days after application to the cover slip.

3.2.2 Nanoparticles containing dendritic polyglycerols

Dendritic polyglycerol sulfate synthesis

Dendritic polyglycerolsulfate (dPGS) labeled with the ICC dye was synthesized in the group of Prof. Haag (Institute of Chemistry and Biochemistry, Freie Universität Berlin). dPGS with a molecular weight of approx. 12 000 g/mol was synthesized via an anionic multi-branching ring-opening polymerization of glycidol and sulfation using sulfurtrioxide-pyridinium complex [Türk et al., 2004]. The detailed procedure of dye labeling is described elsewhere [Licha et al., 2011]. Briefly, the linker 11-azido-1-undecanyl-tosylate was conjugated to polyglycerol at a molar ratio of approximately one linker per polymer. The resulting azido-containing polymer was sulfated [Türk et al., 2004], and then conjugated with a propargyl derivative of ICC [Sisson et al., 2009] by copper-catalyzed 1,3-dipolar cycloaddition (click conjugation) in water/ethanol. The product was purified by chromatography on RP C-18 silica using water as eluent yielding the conjugate as red solid after lyophilization.

Core-multishell nanocarrier synthesis

The core-multishell (CMS) nanocarriers were produced by Dr. E. Fleige in the group of Prof. Haag (Institute of Chemistry and Biochemistry, Freie Universität Berlin). For the CMS nanotransporter with incorporated NR (CMS/NR) the dendritic CMS nanotransporters (PG10000(-NH_2)$_{0.7}$(C_{18}mPEG$_6$)$_{1.0}$) were synthesized and a solution of 5 mg/ml (unless indicated otherwise) was loaded with NR (0.004 %) as described [Radowski et al., 2007, Küchler et al., 2009a].

In the case of the CMS nanotransporter with the covalently attached ICC dye (CMS-ICC) the hyperbranched polyglycerol amine14 (PG-NH_2, M_w = 10 kDa, degree of amination 70 % = 9.45 mmol NH_2/g PG-NH_2, 7 mg = 0.066 mmol NH_2) was dissolved in 10 ml methanol. To the solution 1.8 mg indocarbocyanine dye NHS ester was added and the reaction was stirred at room temperature for 6 h. Finally 49 mg 1-(2,5-dioxopyrrolidin-1-yl)-18-methoxy-poly(ethylene glycol)yl octadecanedioate in methanol was added dropwise and the reaction was stirred for a further 18 h [Radowski et al., 2007]. The methanol was evaporated and the crude residue was dissolved in a small amount of water. After purification via size-exclusion chromatography (Sephadex LH-20, water) followed by freeze-drying of the product fraction 48 mg (95 %) of the ICC labeled CMS nanocarrier was received.

Spectroscopic characterization of dPGS and CMS samples

All fluorescently labeled dendritic polyglycerol-based nanocarriers and the respective fluorescent dyes were characterized by both absorption and emission spectroscopy. For all spectra an aqueous stock solution of the respective sample was diluted to a defined concentration (c) in the respective solvent (Table 3.3). Concentrations refer to the respective dye and were determined by absorption spectroscopy (see section 3.1.1 and below). Absorption spectra were recorded on a UV-PC2450PC double beam spectrophotometer (Shimadzu) at 19 °C in quartz cuvettes with a light path of 3 mm (101.017, Hellma Analytics) or 10 mm, a slit width of 2.0 nm, a step length of 0.5 nm and the scan speed was set to medium. Emission spectra were measured using a HobinYvon Fluoromax fluorospectrometer with an integration time of 0.5 s, a wavelength increment of 1 nm and an excitation and emission slit width of 0.5 mm respectively, equal to a band pass of 2 nm [Jobin Yvon Horiba, 2001]. For excitation-emission scans the excitation wavelength (λ_{ex}) was increased within a predefined range (Table 3.3) in 5 nm steps. At each excitation wavelength an emission spectrum was recorded in a given emission wavelength (λ_{em}) range (Table 3.3).

Time-resolved fluorescence measurements of dPGS and CMS samples

Time-resolved fluorescence lifetime and anisotropy measurements were conducted on a time-correlated single photon setup [Alexiev et al., 2003, Kim et al., 2009a] with a titanium-sapphire laser as excitation light source as described in section 5.1.1. Samples were pipetted into quartz cuvettes with a light path of 3 mm (101.017, Hellma Analytics) and were excited at 485 nm. Emission was collected using a long pass filter OG 515. For lifetime measurements the emission polarizer was set to the magic angle of 54.7°. For temperature dependent anisotropy measurements the emission polarizer was alternated between parallel and perpendicular, with respect to the polarization of the excitation beam. Eleven pairs of parallel and perpendicular polarization were recorded for each temperature. The temperature was increased in 5 °C steps in the temperature range of 5 °C to 55 °C. All measurements were conducted using 1024 channels and a sample dependent time-resolution resulting in a specific channel width (Table 3.3).

3.2.3 NLX-Flu binding to μ-opioid receptor in HEK membrane fragments

Preparation of μ-opioid receptor samples

The μ-opioid receptor expression and membrane fragment preparation was done by Dr. Viola Spahn in the group of Prof. Stein (Clinic for anesthesiology, Charité Berlin) as described [Boreham et al., 2011]. The μ-opioid receptor was expressed in HEK293 cells and membrane fragments were obtained from both transfected and untransfected HEK293 cells. In brief, HEK293 cells were washed carefully with 10 ml 50 mM Tris buffer (pH 7.4, 4 °C). Then 10 ml of 50 mM Tris

Table 3.3. Sample dependent measurement conditions. The table shows the absorption and emission wavelength range of excitation-emission scans and the TCSPC measurement settings.

		excitation-emission scans		TCSPC settings	
sample	c (µM)	λ_{ex} (nm)	λ_{em} (nm)	time-resolution (ns)	channel width (ps)
ICC	1.0	450–600	500–750	5	5.34
dPGS-ICC	0.5	450–600	500–750	10	9.76
CMS-ICC	1.4	450–600	500–750	10	9.76
NR	4.0	425–650	550–750	20	19.7
CMS/NR	1.0	425–650	550–750	20	19.7

buffer was added to all cell culture dishes and the cells were solubilized using a cell scraper. The cell suspension was transferred to a 30 ml tube, disrupted using a rod homogenizer and centrifuged (42 000 g, 4 °C, 20 min). The supernatant was discarded, the pellet resuspended in 10 ml 50 mM Tris buffer and centrifuged. After discarding the supernatant, the pellet was resuspended in 500 µl of 5 mM Tris buffer. The total protein concentration was determined using a Bradford assay (fragments from untransfected cells: 2.6 mg/ml; fragments from transfected cells: 2.8 mg/ml). All steps were performed on ice.

Fluorescence spectroscopy experiments

Samples of membrane fragments with (+MOR membranes) and without (-MOR membranes) expressed µ-opioid receptor (MOR) were used. 10.5 µL of a 1.25 mM naloxone-fluorescein (NLX-Flu) stock were added to 250 µL of the respective membrane fragments in Tris buffer at pH 7.4. Based on an estimate of the µ-opioid receptor in the +MOR membranes from the total protein content, this should roughly be an excess of a factor 10. After 1.5 h incubation at room temperature incubation was stopped by adding 500 µL of 5 mM Tris pH 7.4. The samples were then washed three times, by repeated centrifugation at 16 000 x g and 4 °C for 20 min. The supernatant was collected each time and the pellet was resuspended in 500 µL of 5 mM Tris pH 7.4. After the final washing step, the sample was resuspended in 150 µL 5 mM Tris pH 7.4.

An aliquot was brought to pH 9 by adding highly concentrated Tris buffer at pH 9 and the absorption spectra were recorded on a UV-PC2450PC double beam spectrophotometer (Shimadzu) at 19 °C in quartz cuvettes, with a light path of 3 mm (101.017, Hellma Analytics) a slit width of 2.0 nm, a step length of 0.5 nm and the scan speed was set to medium. An integrating sphere was used, due to the scattering inherent to samples containing membrane fragments. Emission spectra were measured in Tris buffer at pH 9 on a HobinYvon Fluoromax fluorospectrometer with an integration time of 0.5 s, a wavelength increment of 1 nm and an excitation and emission slit width of 0.5 mm respectively, equal to a band pass of 2 nm.

The time-resolved fluorescence lifetime measurements were performed using the TCSPC setup described in section 5.1.1. Samples were pipetted into quartz cuvettes with a light path of 3 mm (101.017, Hellma Analytics) and were excited at 485 nm. Emission was collected using a long pass filter OG 515. The emission polarizer was set to the magic angle of 54.7°. All measurements were conducted using 1024 channels and a time-resolution of 20 ns.

Fluorescence lifetime imaging microscopy experiments

Fluorescence lifetime imaging microscopy (FLIM) experiments were conducted in WillCo-dish glass bottom dishes (GWSt-3512) at 20 °C on the setup described in section 6.1.1. 5 µl of

membrane fragments in 5 mM Tris buffer at pH 7.4 were diluted with 10 µl of 5 mM Tris buffer at pH 7.5 and 150 mM NaCl and pipetted onto the WillCo-dish glass bottom dish. Binding of fluorescein-naloxone (NLX-Flu, Sigma-Aldrich) was initiated by adding 2 µl of a 10 µM NLX-Flu stock in 5 mM Tris at pH 7.5 and 150 mM NaCl resulting in a final concentration of 1.2 µM NLX-Flu. FLIM measurement were performed after at least 15 min of incubation time. Samples were excited at 485 nm. The emission was detected with a band-pass filter (HQ525/50) with a range of 500–550 nm. The data was analyzed with the SPCImage software (Becker&Hickel).

For the analysis of NLX-Flu displacement by NLX HEK293 membrane fragments with NLX-Flu were prepared as described above. A measurement was conducted in the absence of unlabeled naloxone (NLX). The displacement of NLX-Flu was induced by the addition of unlabeled nonfluorescent NLX and a measurement was conducted for every concentration of NLX. Concentrations of NLX were increased by a factor of 10 within the range of 10^{-2} µM and 10^{2} µM. Measurement conditions as for NLX-Flu binding. Data analysis was also performed with the SPCImage software (Becker&Hickel).

3.2.4 dPGS-ICC detection in rat liver tissue

Preparation of rat liver samples with dPGS-ICC

The rat liver sections were produced by Dr. L Mundhenck in the group of Prof. Gruber (Department of Veterinary Medicine, Freie Universität Berlin) as published [Boreham et al., 2011]. The animals were maintained in accordance with the Guide for the Care and Use of Laboratory Animals published by the US National Institute of Health (all experiments were approved by the local animal welfare committee). Prior to injection the rats were immobilized with an inhalation anesthesia with 2–3 % isoflurane (Florene, Abbott) and medical oxygen. The tail base was shaved and disinfected. A 0.2 ml solution of dPGS-ICC (2 mg/kg b.w.) in PBS was then injected intravenously. After three hours, animals received lethal injections in deep anesthesia by intravenous injection of T61 ad us. vet. (Intervet) at a dose of 2 ml per animal. Liver tissue was immediately removed, fixed in 4 % formalin dehydrated, and embedded in paraffin. Tissue sections were cut at 1 µm. The 1 µm liver sections were mounted on 0.17 mm thick cleaned cover glasses (Marienfeld-Superior; Precision cover glasses thickness No. 1.5H for high performance microscopes) for subsequent confocal FLIM analysis.

FLIM measurements of dPGS in rat liver samples

Rat liver sections were placed on 0.17 mm thick cleaned cover slips (Marienfeld-Superior; Precision cover glasses thickness No. 1.5H for high performance microscopes). Fluorescence lifetime imaging microscopy measurements were conducted on the FLIM setup described in 6.1.1 with a 40x objective. Samples were excited at 485 nm. A colored glass filter (OG515) and a high quality band-pass filter (HQ525/50) were used as emission filters. The time range was set to 23 ns for 256 channels resulting in a resolution of 90 ps/ch. The data was analyzed with the SPCImage software (Becker&Hickel).

3.2.5 CMS-ICC detection in human skin

Preparation of human skin samples with CMS-ICC

The human skin samples were produced by N. Alnasif in the group of Prof. Schäfer-Korting (Institute of Pharmacy, Freie Universität Berlin) as described [Alnasif et al., 2014]. Briefly, human skin was thawed and prepared for testing prior to the experiment. Tape stripping (Tesafilm, Beiersdorf, Hamburg, Germany) was performed in order to remove relevant parts of the *stratum corneum* and thus induce barrier impairment. The stripping procedure [Lademann et al., 2006]

was repeated 30 times to ensure sufficient damage. Subsequently, skin discs of 2 cm diameter were punched and mounted onto the Franz cells (diameter 15 mm, volume 12 ml, PermeGear, Bethlehem, PA, USA) with the *stratum corneum* facing the air and the dermis having contact with the receptor fluid phosphate buffered saline pH 7.4 (PBS). After equilibration for 1 h, 20 µl cm^{-1} of CMS-ICC nanotransporters were applied onto the skin surface and remained there for 24 h sealing the donor compartment with Nescofilm®. Then the skin was removed from the Franz cells and surplus CMS nanotransporter formulation was gently removed by carefully washing the surface using PBS. Subsequently, the skin was embedded in tissue freezing medium (Jung, Nussloch, Germany) and stored in Peel-Aways® (Polyscience, Eppelheim, Germany) at −80 °C. Skin discs were cut into vertical slices of 10 µm thickness using a freeze microtome (Frigocut 2800 N, Leica, Bensheim, Germany). Vertical slices of normal and stripped skin were placed on cleaned 0.17 mm thick cover glasses.

FLIM measurements of CMS in human skin samples

Vertical slices of normal and stripped skin were placed on 0.17 mm thick cleaned cover slips (Marienfeld-Superior; Precision cover glasses thickness No. 1.5H for high performance microscopes). Fluorescence lifetime imaging microscopy measurements were conducted on the FLIM setup described in 6.1.1 with a 40x objective. Samples were excited at 498 nm. A colored glass filter (OG515) was used emission filters. The time range was set to 20 ns for 256 channels resulting in a resolution of 78 ps/ch. Cluster-based FLIM analysis routines (see section 6.1.2) were used to analyze the data.

3.2.6 Hyaluronic acid and bovine serum albumin detection in pig skin

Before the labeling of hyaluronic acid could be performed, the degree of labeling per hyaluronic acid (HA) unit in the different HA molecular weight samples had to be considered, as this has implications for the comparability of the fluorescence signal from the different samples.

The number of N-methylisatoic anhydride (MIA) dye molecules bound to a single HA molecule depends on the HA chain length, and hence its molecular weight. With the labeling procedure described above one dye molecule will be bound every 40 to 50 hyaluronic acid units. Therefore higher molecular weight samples will have more dyes bound per HA chain than low molecular weight samples. A 5 kDa HA molecule consist of around 12.5 HA units, as one HA unit has a molecular weight of around 0.4 kDa. The degree of labeling of a 5 kDa HA molecule will thus be 0.25, i.e. only every fourth HA molecule is bound to a dye molecule. A 100 kDa HA molecule, on the other hand, is made up of 250 individual HA units and the degree of labeling will therefore be around 5, i.e. one HA molecule has 5 dye molecules attached.

This, of course, has implications for the fluorescence. One labeled 5 kDa HA molecule will only have a fifth of the fluorescence of a 100 kDa HA molecule under the same conditions. In order to keep the fluorescence of the sample comparable there are two possibilities. The first, comparability on the molecular level, requires that each HA molecule, independent of its molecular weight has the same number of bound dye molecules (e.g. 2 dyes per HA molecule), making substantial adjustments and further development of the labeling technique necessary. The second option is to use HA solutions of the same percentage (weight/volume) for all molecular weights. As at equal weight each sample will contain an equal amount of HA units, and thus also of bound dye molecules, the total fluorescence should be the same for all samples, irrespective of their molecular weight. This approach can be implemented directly without the need for developing new labeling protocols. Here, all samples used contained 5 % HA.

Preparation of HA and BSA samples

The labeling of hyaluronic acid and of BSA and the preparation of skin samples was performed by M. Witting in the group of Prof. Frieß (Institute for pharmaceutical Technology and Biopharmaceutics, Ludwigs-Maximilians-Universität Munich).

HA was labeled with N-methylisatoic anhydride (MIA) [DeAngelis, 2000]. HA and dye solution were mixed at a ratio of 1:10 (dye : HA) protected from light. Successful labeling was confirmed using fluorescence spectroscopy and fluorescence microscopy. Fluorescence labeling of BSA was performed using Rhodamin B isothiocyanate (RhB-ITC). Protein and dye solution were mixed at a ratio of 1:170 (dye:protein) protected from light. Unbound dye was removed by washing procedure and spectroscopically confirmed. A degree of labeling of around 1 was determined. Pig skin samples were cleaned and punched discs were mounted onto static-type Franz cells. 300 µl of the test formulations (10 mg ml^{-1} BSA-RhB, 5 % HA samples) were applied onto the skin and distributed homogeneously and incubated for 6 h. Before freezing of the skin at −80 °C any remaining sample on the skin surface was gently removed. 5 µm thick tissue slices (cross-sections) were prepared for imaging. Tape-stripping was performed by pressing adhesive tape strips with constant pressure onto the skin and repeated 30 times.

Spectroscopic characterization of HA and BSA samples

Absorption spectra were recorded on a UV-PC2450PC double beam spectrophotometer (Shimadzu) at 19 °C in quartz cuvettes, with a light path of 3 mm (101.017, Hellma Analytics), a slit width of 2.0 nm, a step length of 0.5 nm and the scan speed was set to medium. Emission spectra were measured in Tris buffer at pH 9 on a HobinYvon Fluoromax fluorospectrometer with an integration time of 0.5 s, a wavelength increment of 1 nm and an excitation and emission slit width of 0.5 mm respectively, equal to a band pass of 2 nm. To dissolve the lyophilized dye MIA a small amount of the dye (a pipette tip) was dissolved in roughly 5 µl of DMSO and then diluted with H_20 MQ. Emission spectra of samples containing the MIA dye were recorded using the maximum wavelength of absorption as excitation wavelength, i.e. 317 nm for MIA and 353 nm for HA-MANT samples. To dissolve the lyophilized dye RhodaminB (RhB) a small amount of the dye (a pipette tip) was dissolved in roughly 5 µl of DMSO and then diluted with H_20 MQ. BSA-RhB emission spectra were recorded with excitation wavelengths of 405 nm, 488 nm and 552 nm.

FLIM measurements of HA and BSA in pig skin samples

All FLIM measurements were conducted on the setup described in section 6.1.1 with a 20x objective and a time range of 20 ns and 256 channels, equivalent to 78 ps/ch. To evaluate the penetration of BSA-RhB with and without HA-MANT, the samples were excited at 488 nm using the Ti:Sa Laser (frequency doubled 976 nm wavelength). The emission filter pair consisted of a color glass filter OG515LP combined with HQ545LP filter. To analyze the penetration behavior of hyaluronic acid on its own, samples only with HA-MANT were excited using the 405 nm diode laser. HA-MANT emission was detected using a long pass filter HQ435LP combined with band pass filter HQ480/40BP. In order to detect FRET emission of BSA-RhB in samples containing both BSA-RhB and HA-MANT, the samples were excited at 405 nm, for HA-MANT, and the emission filters were chosen to selectively detect BSA-RhB emission, using a HQ545LP combined with a HQ620/60BP emission filter.

The recorded FLIM data was subjected to cluster-based image analysis (see section 6.1.2). Samples not treated with hyaluronic acid or BSA (blank samples) were used to determine autofluorescent background levels. Background levels were determined independently for both normal skin and tape-stripped skin. The determined autofluorescent background levels were then set as

the minimum threshold for the cluster-based FLIM analysis. Hence, only pixels with intensities greater than the autofluorescent background are included in the data analysis. However, it has to be mentioned that this does not mean that the pixels included in the analysis do not have any contribution from the autofluorescent background. On the contrary, the autofluorescent background is still contained in the pixel intensity. What it does mean is that pixels without any additional contribution to the intensity besides inherent background intensity are excluded from the analysis.

BSA-RhB samples without HA-MANT and with the three different HA-MANT molecular weights were analyzed together for normal skin and tape-stripped skin respectively. Normal skin and tape-stripped skin samples were analyzed separately, due to the different background intensity levels observed in the two skin types. To supplement the lifetime analysis, intensity line scans were generated using the cluster FLIM software. For averaged intensity line scans three intensity line scans perpendicular to the skin surface were taken at representative positions within the sample and averaged.

3.2.7 Silica particle detection in mouse skin

Preparation of mouse skin samples with silica nanoparticles

The particle preparation was performed by D. Nordmeyer in the group of Prof. Rühl (Institute of Chemistry and Biochemistry, Freie Universität Berlin). The spherical silica nanoparticles with covalently labeled fluoresceine isothiocyanate (FITC) were prepared, functionalized and transferred from ethanol to sterile ultra pure water (AlleMan Pharma GmbH, Pfullingen, Germany) as previously reported [Graf et al., 2012]. The final particle concentration was 5 g/l and the suspension was stored under argon in the dark at 4 °C until use.

The mouse skin samples were produced by A. Ostrowski in the group of Prof. Gruber (Department of Veterinary Medicine, Freie Universität Berlin) as described [Ostrowski et al., 2014]. Briefly, hairless mice (Male SKH1 mice; Crl:SKH1-Hr hr; Charles River, Germany) received subcutaneous injections with silica nanoparticles (SiNP) functionalized with N-(6-aminohexyl)-aminopropyltrimethoxysilane (AHAPS), yielding AHAPS-SiNP, over five consecutive days, the daily dose of 250 µg AHAPS-SiNP being administered by one single injection, in the right flank. Prior to application the particle suspension was sonicated for 10 minutes. Tissue samples from the right flank, the untreated left flank (contralateral side) and from mice not having received any injections were prepared for histopathologic analysis. The tissue samples were fixed in 4 % neutral buffered formalin for 24 h and then embedded in paraffin. Further, as a reference sample, AHAPS-SiNP were embedded in paraffin at a fixed concentration. To this end, 100 µl Agarose (1.5 %) were mixed with 100 µl of a 5 g/l solution of AHAPS-SiNP in ultra pure water. The resulting solution (2.5 g/l AHAPS-SiNP) was left to harden and then treated in the same way as the tissue samples. All paraffin sections were mounted on 0.17 mm thick cleaned cover slips (Marienfeld-Superior; Precision cover glasses thickness No. 1.5H for high performance microscopes).

FLIM measurements of silica particles in mouse tissue

FLIM measurements were conducted on the setup described in section 6.1.1 with a 40x objective. Samples were excited with 486 nm. A colored glass filter (OG515) and a high quality band-pass filter (HQ525/50) were used as emission filters. The time range was set to 20 ns for 256 channels resulting in a resolution of 78 ps/ch. Data analysis was performed with the cluster-based FLIM analysis routines.

Chapter 4

Size, shape and internal structure of NLCs

A single-molecule microscopy study

In this chapter a novel single-molecule fluorescence method to determine the size, shape and internal structure of nanostructured lipid carriers (NLC) is presented. NLCs and their predecessors, the solid lipid nanocarriers (SLN), are nanoparticles made from lipids and were developed to increase the loading capacity of poorly soluble drugs. Whereas the lipid matrix of SLN consists of only one solid lipid, the matrix of the NLC consists of a blend of a solid and a liquid lipid (solid and liquid referring to the respective state of the lipid at room and body temperature). This leads to the formation of 'nanostructures' within the lipid matrix [Müller et al., 2011]. The nanostructures increase the drug loading capacity and lead to a modification in the distribution and release profile of the drug [Müller et al., 2011]. Hence, the nanostructures play a key role in defining the in vivo performance of NLCs. For optimal formulation development, i.e. tailoring the release profile to a specific application, it is therefore of fundamental importance to gain insights into the nanostructures. This should help to better understand the drug distribution within the particle and also the release of the drug. There are some theories about the nanostructures and the resulting drug distribution within NLCs (Figure 4.1) [Müller et al., 2002, Selvamuthukumar and Velmurugan, 2012]. It is proposed that, depending on the NLC formulation and production conditions, the liquid lipid (oil) can be homogeneously distributed within the particle or localized in nanocompartments. There could either be multiple nanocompartments, a single core or shell, or the nanocompartment could only be associated to or even separated from the particle itself.

In cooperation with Prof. Keck (Institute of Applied Logistic and Polymer Sciences, Univer-

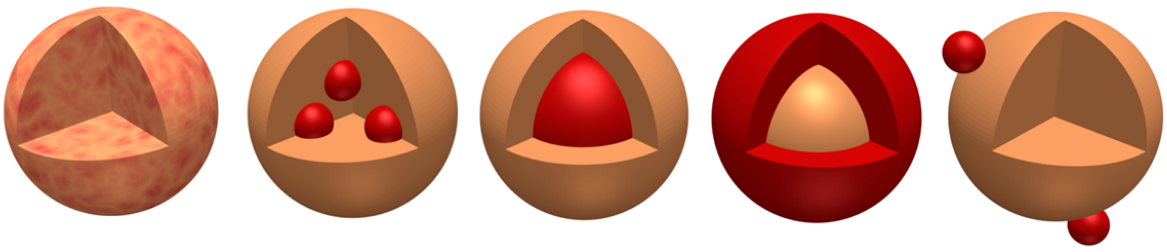

Figure 4.1. Possible arrangements of the solid and liquid lipid in nanostructured lipid carriers. From left to right: homogenous mixture, multiple liquid droplets, one liquid core, one solid core surrounded by liquid lipid, (multiple) external liquid droplet adhesion.

sity of Applied Sciences Kaiserslautern) the size, shape and internal structure of NLCs consisting of Dynasan, Miglyol and the stabilizing agent Plantacare was investigated. A new technique was developed to visualize the size and internal structure of individual NLC particles using total internal reflection fluorescence (TIRF) microscopy combined with experimental approaches from single-molecule microscopy and data analysis techniques used in localization-based microscopy and single particle tracking.

In the following a will give a brief introduction to single-molecule microscopy, the microscopy setup and single-molecule data analysis. Then the results will be presented, before concluding with a discussion.

4.1 Methods

4.1.1 Single-molecule microscopy

Single-molecule microscopy has proven an invaluable asset to analyze the behavior of individual fluorescent particles, as opposed to ensemble averages, and also to analyze structures smaller than the diffraction limit. Conventional wide-field microscopy is limited in terms of resolution by the Abbe law stating that two objects can only be separated if they have a distance greater than $\frac{\lambda}{2NA}$, where λ is the wavelength of the incident light and NA the numerical aperture of the objective. Even using objectives with a high numerical aperture and wavelengths in the low visible region the resolution limit will be on the order of 200 nm. In recent years different methods have been proposed to circumvent Abbes law and increase the resolution down to 1–10 nm. These have been termed super-resolution microscopy (e.g. stimulated emission depletion (STED), photoactived localization microscopy (PALM), stochastic optical reconstruction microscopy (STORM) [Schermelleh et al., 2010]). Abbes law still holds of course. It is the combination of experimental setup and data analysis that allows for this increase in resolution. The general idea is to reduce the concentration of emitting fluorophores so far, that there is only one emitter in a diffraction limited spot. The position of the emitter can then be located with a great increase in precision by analytic methods such as approximating the point spread function (PSF) of the emitter with a 2D-gaussian or calculating its center-of-mass. Thus an increase in resolution is achieved, even though the resolution of the recorded image is still limited by Abbes law [Hell, 2007].

One possible experimental setup for single-molecule microscopy is to operate an inverted microscope in total internal reflection fluorescence (TIRF) microscopy mode. Here, the exciting laser beam is coupled into the microscope objective so that the beam is totally reflected at the interface between two media with different refractive indices, e.g. glass cover slip and sample (Figure 4.2). The total internal reflection of the collimated beam results in an evanescent electrical field that extends beyond the interface and into the sample. As the intensity of the evanescent field decreases exponentially with increasing distance to the interface, penetration of the excitation light of only a few hundred nanometers into the sample is achieved. Consequently, only fluorescent probes within this well defined region can be excited (Figure 4.2), thus eliminating background fluorescence from outside the focal plane, and hence the signal-to-noise ratio (SNR) is increased. TIRF microscopy is therefore well suited to observe samples close to

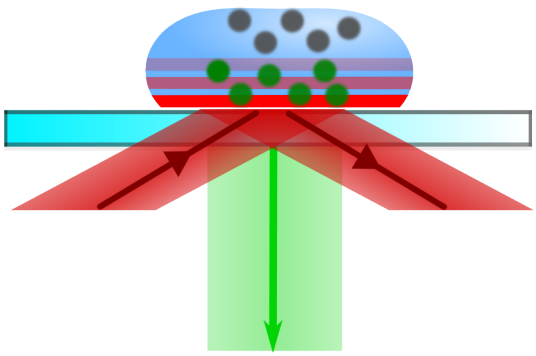

Figure 4.2. Schematic of the principal of TIRF illumination. The incident laser light (red) is total internally reflected at the cover slip interface, generating an evanescent wave, only capable of exciting fluorescent molecules close to the cover slip surface (green circles). Those further from the surface remain in the non-emitting ground state (grey).

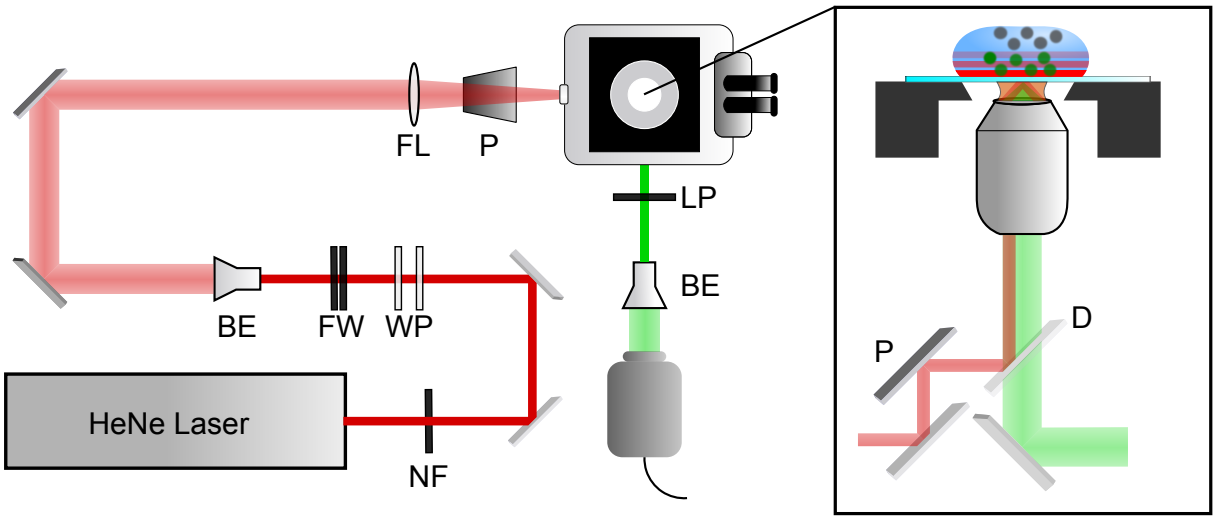

Figure 4.3. Schematic of the TIRF setup employed. Abbreviations: notch filter (NF), wave plate (WP), neutral density filter wheel (FW), beam expander (BE), focusing lens (FL), periscope (P), long pass filter (LP), dichroic mirror (D).

the surface of the cover slip with a high SNR, allowing for its use in single-molecule experiments. An objective with a high numerical aperture is required for TIRF microscopy in order to obtain the critical angle required for total internal reflection.

Total Internal Reflection Microscopy setup

The setup used [Kirchberg et al., 2010] for the TIRF microscopy measurements (Figure 4.3), consisted of a conventional inverted wide-field microscope (Olympus IX-71) equipped with a 60x oil immersion objective (PLAPON60xOTIRFM, Olympus) with a numerical aperture of 1.45. The excitation light stems from a 21 mW 623.8 nm helium-neon laser source [HeNe laser](1145P/JSD Uniphase). The linearly polarized light passed a $\frac{\lambda}{2}$ plate, altering the plane of polarization by 45°, and subsequently turned into circular polarized light by the $\frac{\lambda}{4}$ plate [both wave plates are indicated by WP in Figure 4.3]. The intensity of the excitation light was controlled by combining neutral density filters of two filter wheels [FW] before passing a 10x beam expander [BE]. Using the focusing lens [FL] the beam was focused onto the back focal plane of the microscopy objective. However, to achieve total internal reflection, the focus had to be slightly off-axis, and hence the beam passed through the outer portion of the aperture (Figure 4.3, blow up). A periscope [P] was used to adjust the height of the beam, so that it could be coupled into the rear port of the microscope. Fluorescence emission was collected by the same objective and separated from excitation light, e.g. from scattering, by a dichroic mirror [D] inside the microscope and also a by a long pass cut-off filter [LP] in the emission path to the detector. After passing the cut-off filter a beam expander [BE] mapped the emission onto a cooled electron-multiplying charge coupled device (EMCCD) camera (ImagEM C9100-13, Hamamatsu).

4.1.2 Data acquisition and analysis techniques

All single-molecule microscopy data were obtained on the setup described above. The EMCCD camera and data acquisition was controlled using the HiPic software (Version 1.8.0). The single-molecule data was analyzed with a software package for single particle tracing (SPT) [Kirchberg

et al., 2010] and also with a software package for particle correlation analysis (UPICS), both developed in the group of Prof. Alexiev.

Particle identification and localization

A microscopy image of single fluorescing particle is characterized by its point spread function. Determining the center of the PSF by mathematical means has been proven a useful tool to obtain the particles localization with an accuracy far below the diffraction limit [Kirchberg et al., 2010]. Here, the center of the PSF was detected using the Marr-Hilderth-algorithm, or so-called Mexican-Hat method, implemented within the SPT software package. Briefly, a Gaussian smoothing filter is applied to each frame *f(x,y)* using a two dimensional Gaussian operator of the form $g(x,y) = \frac{1}{2\pi\sigma^2} exp(-\frac{x^2+y^2}{2\sigma^2})$. As a result, information from discontinuous step edges are transformed to smoothed step edges and information from previously smooth step edges is preserved. Discontinuous step edges can occur when the differences between adjacent pixels are very high. Now, the Laplace operator, $\Delta = \frac{\delta^2}{\delta x^2} + \frac{\delta^2}{\delta y^2}$ can be employed on the smoothed data. The zero of the 2-nd order can then be used to determine the center of mass of the edges. Hence, the Mexican-Hat method allows for the detection of places with large changes in intensity within each frame [Marr and Hildreth, 1980]. The adjustable parameters for the picking algorithm are the size of the particle, in pixel, and a minimum intensity threshold value. Once a particle is detected due to the change in intensity, the position is determined as the center of intensity. After the localization of the particles has been identified for each frame of a given movie, the time dependence of a particles position can be analyzed either with particle correlation or single particle tracking.

Single particle tracing

In the single particle analysis the movement of a detected fluorophore is followed over multiple frames. The single particle tracing algorithm uses a nearest neighbor approach in order to identify two picked points in subsequent frames with the same particle. The process of combining the points from subsequent frames is called tracking and the resulting connection between the different points in time is the so-called trace or trajectory. This approach is limited to low particle concentrations, since at high particle concentrations the likelihood that the nearest neighbor is the same particle is greatly reduced. The implementation of the single particle tracking algorithm provides two parameters to optimize the tracking results. On the one hand a minimal trace length can be set, excluding particles that only appear for short times, and, on the other hand, a maximum step length can be defined for the maximum distance two points are still recognized as one particle between two frames.

Visit map-based super-resolution microscopy

In conventional super-resolution microscopy the positions of bound fluorophores are used to visualize subdiffraction sized structures. The idea behind visit maps is visualizing affinity-based interactions to resolve the underlaying structures with sub diffraction resolution. Visit maps, highlighting the places visited by the fluorophores, were calculated using the SPT program [Kim et al., 2012, Alexiev and Farrens, 2014]. The visit maps are generated using Bresenham's Line-Drawing Algorithm from the individual traces [Kirchberg et al., 2010]. Each pixel of the visit map contains the information regarding the number of trajectory segments that were drawn at its position [Kirchberg et al., 2010], i.e. how often this position was visited by the fluorophore molecules. Bright places in the visit map, i.e. places often visited by the fluorophore molecules, will be referred to as 'hot spots'. For the generation of visit maps, the original raw data pixels are further divided into an equal number of pixels in each dimension, thus producing an image

with increased resolution. This is only possible, due to the resolution increase provided by the single-molecule experiments and single-molecule data analysis.

Particle correlation

The particle correlation analysis allows for the determination of the step length distribution (SLD) in a tracking independent fashion. The idea for using this strategy was published by Semrau and Schmidt [Semrau and Schmidt, 2007]. A new version of particle correlation analysis was developed in the group of Prof. Alexiev and was used in this thesis. The universal particle correlation spectroscopy method (UPICS), does not depend on following individual particles from one frame to the next and so can also be used for high particle concentrations. The particle correlation analysis is a statistical method, determining all distances between the picked particles between two pairs of frames for a given time interval $n \cdot t_{lag}$, where t_{lag} is the time interval between two frames in the original movie, and then generates the distribution function. In the process a statistical background function is computed. Subtraction of the background function from the distribution function gives rise to the step length distribution.

4.2 Results

4.2.1 NLC size determination using stochastic localization microscopy

Common methods used to determine the mean size or the size distribution of NLC particles are based on ensemble measurements such as dynamic light scattering (DLS) or laser diffraction (LD). From DLS a mean hydrodynamic diameter and an estimate of the polydispersity of the sample are obtained, whereas LD measurements describe the particle distribution in terms of a median value LD50 (i.e. 50% of particles are smaller than that value) and broadness of the distribution (LD90; LD95; LD99). However, both methods have their drawbacks which can lead to inaccuracies. DLS is inherently biased towards larger particles, so small amounts of aggregates or large contaminants (dust) can lead to false results [Filipe et al., 2010], while LD suffers from a low resolving power, many parameters influencing the accuracy of the measurements and LD results can be heavily influenced by non-homogeneous and non-spherical particles. An approach based on single-molecule microscopy has the advantage that aggregates can be excluded from the analysis and thus a much better estimate of the non-aggregated NLC particle size distribution can be obtained. And in contrast to both DLS and LD, which approximate the NLC size from scattering parameters, the single-molecule microscopy approach has the advantage of directly visualizing the size and shape for each individual NLC particle.

Affinity-based size determination of NLCs

To visualize structures with fluorescence microscopy these are commonly tagged with fluorophores. Here, an affinity-based method was developed to visualize the morphology of NLC particles with subdiffraction size. The method is based on specific interactions of a lipophilic dye molecule, Oxa12, with the lipid particles and is similar in its approach to the method published by Mei, Gao and Hochstrasser [Mei et al., 2006], where the activation of the hydrophobic fluorophore Nile Red upon collision with lipid vesicles was used to determine their sub-diffraction structure. Oxa12 was chosen instead of Nile Red, as Oxa12 is lipophilic and readily excitable with the 633 nm wavelength of the helium-neon laser accessible in the TIRF setup. For single-molecule microscopy an optically resolvable subset of emitting fluorophores per frame is required. In the affinity-based method this is generated by both the physiochemical properties of Oxa12 and NLCs and the unique characteristics of TIRF illumination (Figure 4.4).

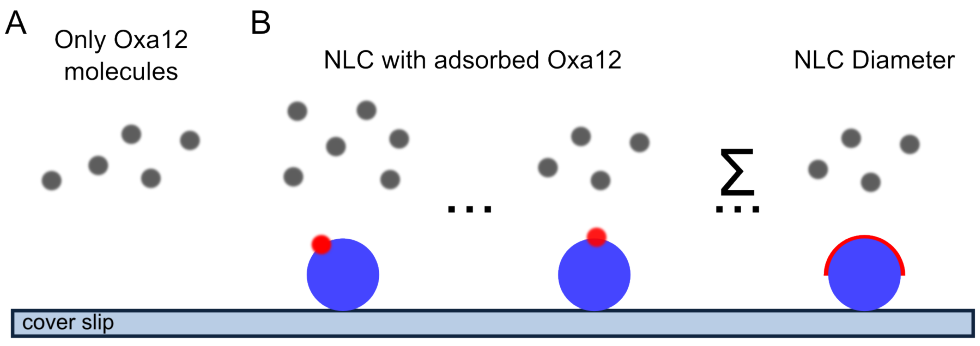

Figure 4.4. Basic concept of the affinity labeling assay. Without NLCs hardly any fluorescence should be visible under TIRF illumination, as Oxa12 is not attracted to the cover slip surface, while Oxa12 can be excited in the presence of NLCs, as the affinity for the lipophilic NLCs surface brings Oxa12 into the TIRF excitation range. Application of super-resolution microscopy analysis techniques allows for the generation of super-resolution visit maps from which the diameter of the NLCs can be determined.

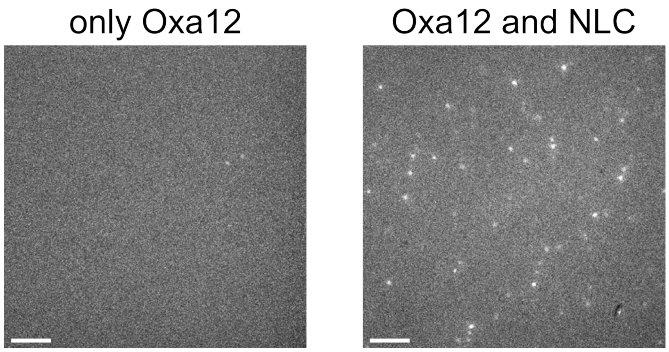

Figure 4.5. Results from the affinity labeling control experiment. The left image shows a representative frame for a clean cover slip covered with buffer solution containing Oxa12. The right image shows a corresponding image using a cover slip with NLCs on the cover slip surface. The experimental conditions in both experiments were otherwise identical. Scale bar: 5 µm.(Buffer solution: 5 mM Tris pH 8; dye concentration: 0.1 nM; T = 20 °C; exposure time: 100 ms; Gain: 5; EMG: 123; ND: 0.0).

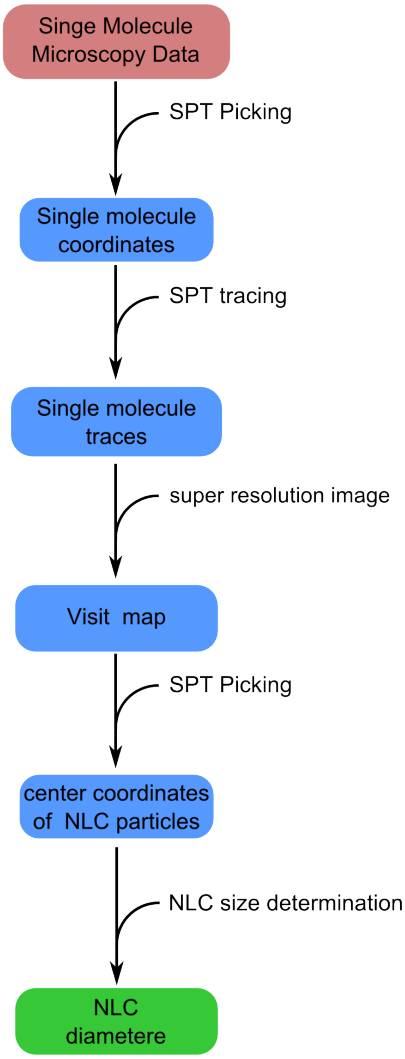

Figure 4.6. Sequence of analysis steps for data from affinity-based experiments. Raw data is underlaid in red, intermediate analysis results in blue and the final analysis result in green.

NLCs have a lipophilic surface and are thus distinctly different from the surface properties of the cover glass, which is highly hydrophilic due to an abundance of -OH groups on the surface. Therefore the lipophilic dye Oxa12 interacts preferentially with NLCs deposited on the glass surface. Under TIRF illumination conditions only those Oxa12 molecules fluoresce that are close enough to the glass surface to be excited by the evanescent wave. When NLCs are deposited on the glass surface, then Oxa12 molecules interacting with the lipophilic NLC surface are excited, while the dyes in the bulk solution remain non-fluorescent (Figure 4.4A,B).

To test whether it is indeed the case that Oxa12 can be used as an affinity label for NLCs molecules the following experiment was performed. An empty cover slip served as a control sample and a cover slip with NLCs immobilized on the surface was prepared as described (see section 3.2.1). Both samples were then measured under identical excitation and detection settings. The control sample (only Oxa12 molecules) did not show any fluorescing molecules in the TIRF experiment. A characteristic frame for the control sample is shown in Figure 4.5. For the sample with NLCs immobilized on the surface (Oxa12 and NLC), on the other hand, multiple fluorescent spots could be detected (Figure 4.5). Hence, Oxa12 preferentially interacts with NLCs and not with the glass surface. In the absence of NLCs on the cover slip surface, Oxa12 molecules remain in the bulk solution, and do not come into the region of TIRF illumination long enough to be detected (at a frame rate of 31 ms). The results of the control experiment showed that Oxa12 can be used as an affinity label for NLC particles in single-molecule microscopy experiments.

To analyze the data the following steps were performed (Figure 4.6). The data files obtained from the affinity labeling experiments were loaded into the SPT software package and particle positions were determined with the SPT picking routine. Subsequently, single particle tracking was performed and from the resulting single-molecule traces visit maps were computed (Figure 4.6), visualizing the individual NLC particles. In the next step, the dimension of these particles was determined. First, the coordinates of the particles were identified and then, with a separate routine (written by T. Schlieter in Python), the diameters could be determined. Since all the hot-spots have a circular shape (Figure 4.7A) a Gaussian was used to approximate the diameter. A line scans (Figure 4.7A) in x-direction and in y-direction through each hot spot was approximated with a Gaussian fitting routine. The respective diameter is defined as the length that includes 98% of the Gaussin area. The mean hot spot diameter is taken to be the average of the x and y dimensions. To reject regions with insufficient counts, two parameters could be set. The minimum value of counts for the peak/maximum value within the defined distance from the center coordinates and the minimum value for the total counts within the hot spot region were defined.

In order to obtain high quality super-resolution images both the concentration of NLCs on the surface (by diluting the original 10% NLC solution to 0.001% NLC before application to the cover slip) and the Oxa12 dye concentration (0.1 nM to 20 nM) was optimized. The results are summarized in Figure 4.7. From the diameters determined for 469 individual hot-spots a size distribution histogram for the blank NLCs was generated (Figure 4.7B). The majority of particles exhibit diameters between 100 nm and 200 nm. The shape of the distribution histogram allowed for a fit with two Gaussians. The two peak values of 173 nm and 115 nm respectively were obtained. For better comparison of the results from the external TIRF analysis with the results from DLS measurements the distribution histogram was also fit with a single Gaussian. The resulting peak value of $155\,\text{nm} \pm 6\,\text{nm}$ is well in accordance with results for the diameter from DLS ($166\,\text{nm} \pm 3\,\text{nm}$) and LD (LD50 = 148 nm) measurements (Figure 4.7C).

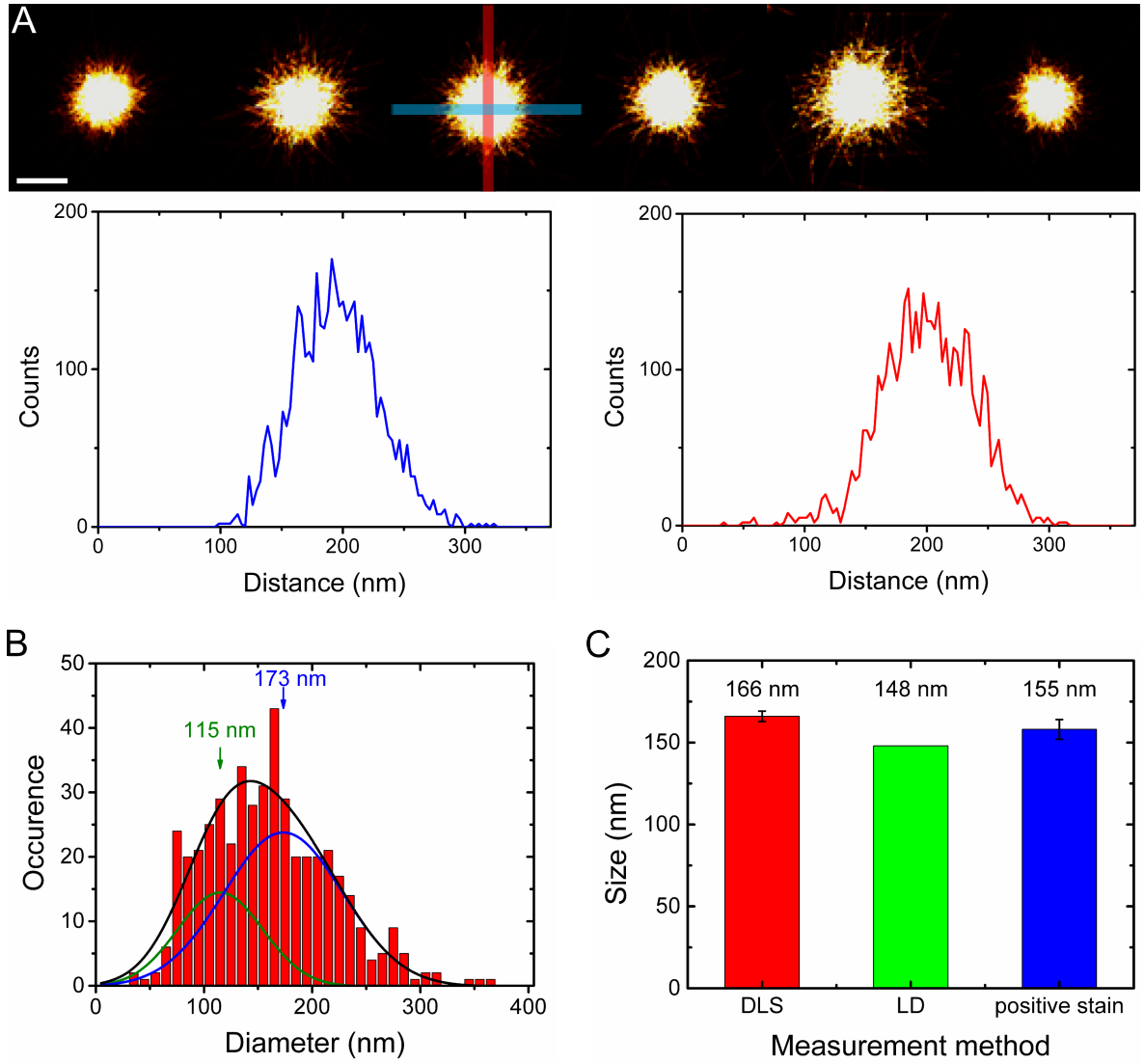

Figure 4.7. Results from the affinity labeling experiments. (A) Visit maps (pixel size = 3.08 nm) of representative individual hot spots as seen by the affinity staining, highlighting their circular shape. Scale bar: 100 nm. Below, line scans through a hot spot as indicated by the cross-hair. (B) Histogram of the size distribution for 469 individual NLC particles (blank = not dye loaded). (C) Comparison with data obtained from DLS and LD.

4.2.2 Internal structure of NLCs

As noted earlier (Figure 4.1) the distribution of the of the oil phase within the NLCs is dependent on production and conditions of measurements. A method based on single-molecule fluorescence microscopy combined with single particle tracking algorithms was applied to directly visualize the internal structures of NLCs. Fluorescent drug mimetics were incorporated into the oil phase and NLCs were then produced together with the solid lipid as described (see section 3.2.1). These were then immobilized on cover slips (see section 3.2.1) and measured on a TIRF microscopy setup (see section 4.1.1). Three dye molecules with different physicochemical properties (Table 4.1) were used to analyze whether the internal structures are influenced by the physiochemical properties of the fluorescent drug mimetic incorporated into the oil phase. ATTO647N was used as a fluorescent reporter group to mimic moderately hydrophilic drugs with a net positive charge, whereas ATTO647 has a stronger hydrophilicity but no net charge. Oxa12, on the other hand, was chosen as a relatively hydrophobic drug mimetic with a net positive charge.

Table 4.1. Overview over fluorescent drug mimetics. Hydrophobicity and charge as stated by the manufacturer ATTO-TEC.

drug mimetic	hydrophobicity	charge
ATTO 647N	hydrophilic	positive
ATTO 647	very hydrophilic	neutral
Oxa12	hydrophobic	positive

SPT analysis of dye loaded NLCs

The diffusion of fluorescent drug mimetics within the oil phase of NLCs was followed by single particle tracking. Since an entrapment, in one way or the other, is assumed the single particle tracking analysis was extended to directly determine the entrapment size, i.e. the confinement of the fluorescent drug mimetics diffusion. Based on the obtained confinement data one can discriminate between different scenarios of the distribution of the oil phase, containing the fluorescent drug mimetic, within the solid lipid, as outlined in Figure 4.8.

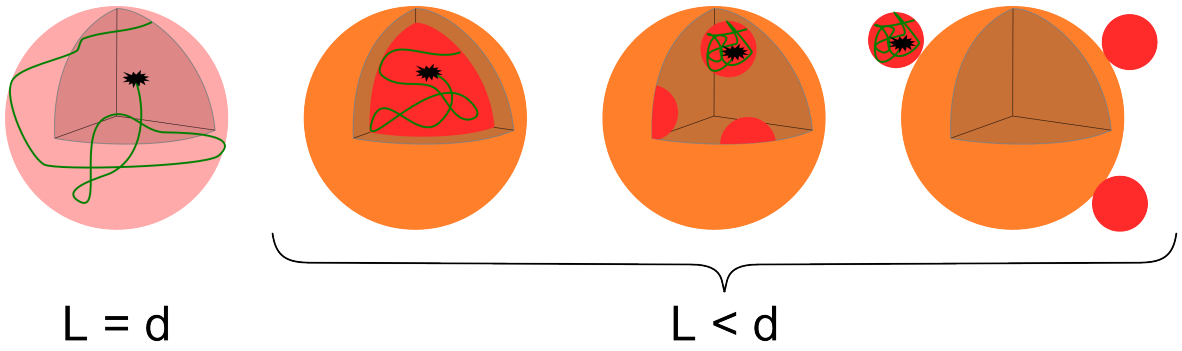

Figure 4.8. Basic concept of the determination of the internal structure of NLCs by confinement length analysis. For a homogeneous distribution a confinement length (L) of the fluorescent drug mimetic (black) on the order of the particle diameter (d) is expected. A single core or multiple oil nanocompartments should give confinement lengths smaller than the particle diameter. External droplets could also give smaller confinement lengths.

The data was analyzed both on the level of individual fluorescent molecules but also for all fluorescing molecules in a global statistical analysis. As outlined in section 4.1.2 single fluorescent molecules were localized and traced. Visit maps were generated, with hot-spots highlighting drug mimetic localizations. These drug mimetic hot-spots are circular in shape for all three mimetics used (Figure 4.9). The size of the drug mimetic confinement was directly determined from the hot-spots based on their intensity profile. Furthermore, hot-spots were analyzed by using the respective traces and statistical analysis of the step length distribution (SLD). Fitting the SLDs with a single disk line picking distribution [Solomon, 1978]

$$P(r) = A\left(\frac{2r}{R^2} - \frac{r^2\sqrt{4R^2 - r^2}}{\pi R^4} - \frac{4r\arcsin(\frac{r}{2R})}{\pi R^2}\right), \tag{4.1}$$

with r the step length and R the radius of a circular disk, the diameter (d=2R) of the circular confinement can be obtained. In the following the results of the three different fluorescent drug mimetics are described in more detail for two representative visit map hot-spots.

ATTO647N It is evident, that both drug mimetic ATTO647N molecules shown in Figure 4.9 (top panel) are confined. The molecule shown to the left (Figure 4.9A,C), however, has a lesser restriction on its freedom of movement/space than the molecule shown to the right (Figure 4.9E,G). The differences between the stronger and less confined molecule can also clearly be seen in the width of the cross section profile through the visits map (Figure 4.9B,F) and the width of the SLD distribution (tlag=1) (Figure 4.9D,H).

For ATTO647N the visit map for the particle with more freedom of movement (Figure 4.9A), i.e. larger confinement length, clearly shows the dyes confinement to an almost perfectly circular region. From a line scan through this hot spot in the visit map (Figure 4.9B) the diameter of the region to which the particle is confined was estimated to be 102 nm. From the individual traces (Figure 4.9C) the SLD (for tlag=1) was computed. A fit of the SLD (Figure 4.9D) according to equation 4.1 for confinement to a circular region, gave rise to a similar value for the diameter of the confinement of 105 nm.

The particle with less freedom of movement (Figure 4.9E-H), i.e. stronger confinement, was also confined to a circular region (Figure 4.9E,G), however with a clearly smaller diameter of confinement. The confinement diameter was estimated to be 57 nm from the line scan (Figure 4.9F), and 50 nm (Figure 4.9H) from the SLD (for tlag=1).

ATTO647 For ATTO647 the individual traces and corresponding visit maps for each particle are shown in the middle panel of Figure 4.9. As for ATTO647N, particles with clearly different confinements could be identified. The difference in the freedom of movement/space an also clearly by seen when comparing the traces and visit maps of the less confined dye molecule (left) with the more confined dye molecule (right). Further, both molecules also display confinement to a circular region (Figure 4.9I,M).

From the line scan through the circular hot spot in the visit map the diameter of the region to which the particle is confined was estimated to be 125 nm for the less confined molecule and 88 nm for the stronger confined molecule (Figure 4.9J,N). The values of 131 nm and 93 nm obtained from the SLD (for tlag=1) (Figure 4.9L,P) of the individual traces (Figure 4.9K,O) compare well to those obtained from the line scan width.

Oxa12 The bottom panel of Figure 4.9, depicts the corresponding data for two individual Oxa12 dye molecules. Again, the individual traces and corresponding visit maps for a more and a less confined dye molecule are shown and the difference in the freedom of movement/space is clearly visible, when comparing the traces and visit maps of the less confined dye molecule

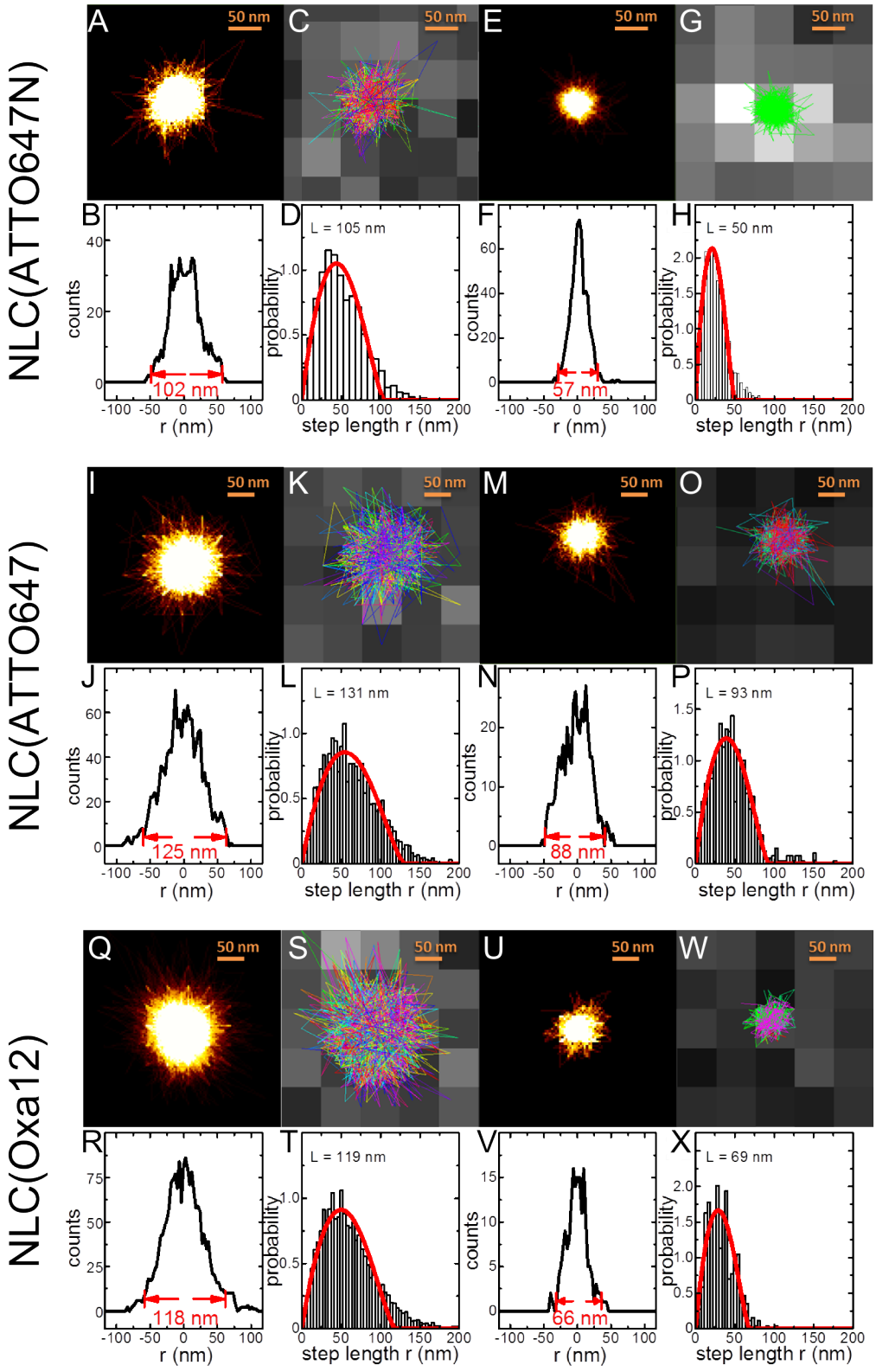

Figure 4.9. Analysis of the confinement of individual dye molecules (either ATTO647N, ATTO647 or Oxa12) dissolved in the liquid phase of NLCs. Characteristic visit maps hot spots (A,E,I,M,Q,U) are shown along with a corresponding line scan through the hot spot (B,F,J,N,R,V). Further, the SPT-traces (C,G,K,O,S,W) and the resulting step length histograms (D,H,L,P,T,X) are depicted.

(Figure 4.9Q,R) with the more confined dye molecule (Figure 4.9U,V). These differences also become apparent in the cross section profile through the visits map and the step length distribution (tlag=1) for each of the representative dye molecules (Figure 4.9S,T,W,X).

From the line scan through the circular hot spot in the visit map the diameter of the region to which the particle is confined was estimated to be 118 nm for the less confined molecule and 66 nm for the stronger confined molecule (Figure 4.9R,V). The values of 119 nm and 69 nm obtained from the SLD (Figure 4.9T,X) of the individual traces (Figure 4.9S,W) the SLD (for tlag=1) are nearly identical to those obtained from the line scan width.

Particle Image correlation analysis of dye loaded NLCs

In a second step, the dye localizations were subjected to a global analysis. The global analysis relies on the correlation between the positions of individual dye molecules in the frames of the movie, and yields SLDs, as shown in Figure 4.10. The fitting of the SLDs and subsequent analysis of the fitting parameters was conducted using routines written in Mathematica by P. Volz and J. Balke in the group of Prof. Alexiev. For the fitting of the SLDs either equation 4.1 for a single population was used or for multiple populations a sum thereof

$$P(r) = \sum_i A_i \left(\frac{2r}{{R_i}^2} - \frac{r^2\sqrt{4R_i^2 - r^2}}{\pi {R_i}^4} - \frac{4r \arcsin(\frac{r}{2R_i})}{\pi {R_i}^2} \right) . \tag{4.2}$$

If the free diffusion of the dye molecule cannot be resolved within the time resolution of the measurement, then the R-values of the confined diffusion correspond to the mean square displacements ($\langle r^2 \rangle$). From the fit of the mean square displacements as a function of different time intervals between individual frames, $n \cdot t_{lag}$, where t_{lag} is the time interval between two frames in the original movie, with

$$\left\langle r^2 \right\rangle = L^2 \left(1 - 8 \sum_i \frac{exp\left(-\frac{t_{lag} D \beta_i^2}{L^2} \right)}{(\beta_i^2 - 1)} \frac{(J_0^2(\beta_i))}{(J_1^2(\beta_i))} \right) , \tag{4.3}$$

where J_n is the Bessel function of order n, the confinement length L for a circular confinement can be obtained [Saxton, 1993]. This equation is only valid in cases where the free diffusion of the molecule is much faster than the time interval t_{lag} and thus is not resolved, as is the case in this study for the diffusion of the dye molecules within the oil phase of NLCs. The sequence of analysis steps is summarized in Figure 4.11.

The first step in the global analysis of the particles was to generate the global SLD from the picking coordinates with the help of the UPICS software (see section 4.1.2). The global SLDs were computed for different time intervals $n \cdot t_{lag}$ ($n = 1, 2, 3, \cdots, 10$). The individual particle analysis had shown that for all three dyes the shape of the confinement was circular. Hence, the global SLDs needed to be fit with the disk line picking distribution equations, either for one (eq. 4.1) or multiple (eq. 4.2) populations. The global SLDs for $n = 1$ and $n = 10$ together with the fits for one, two and three populations, and the respective residues of the fits, are shown in Figure 4.10 for all three drug mimetics. It can be readily seen that a single population is insufficient for all t_{lag} and dyes (Figure 4.10A-C, left panels). A fit with two subpopulations generates a vastly improved overall fit to the SLD for all t_{lag} (Figure 4.10A-C, middle panels). Adding a third subpopulation hardly leads to any further improvements in the fit (Figure 4.10A-C, right panels). It can therefore be concluded that two different populations of fluorophores, regarding the confinement within the oil phase, exist.

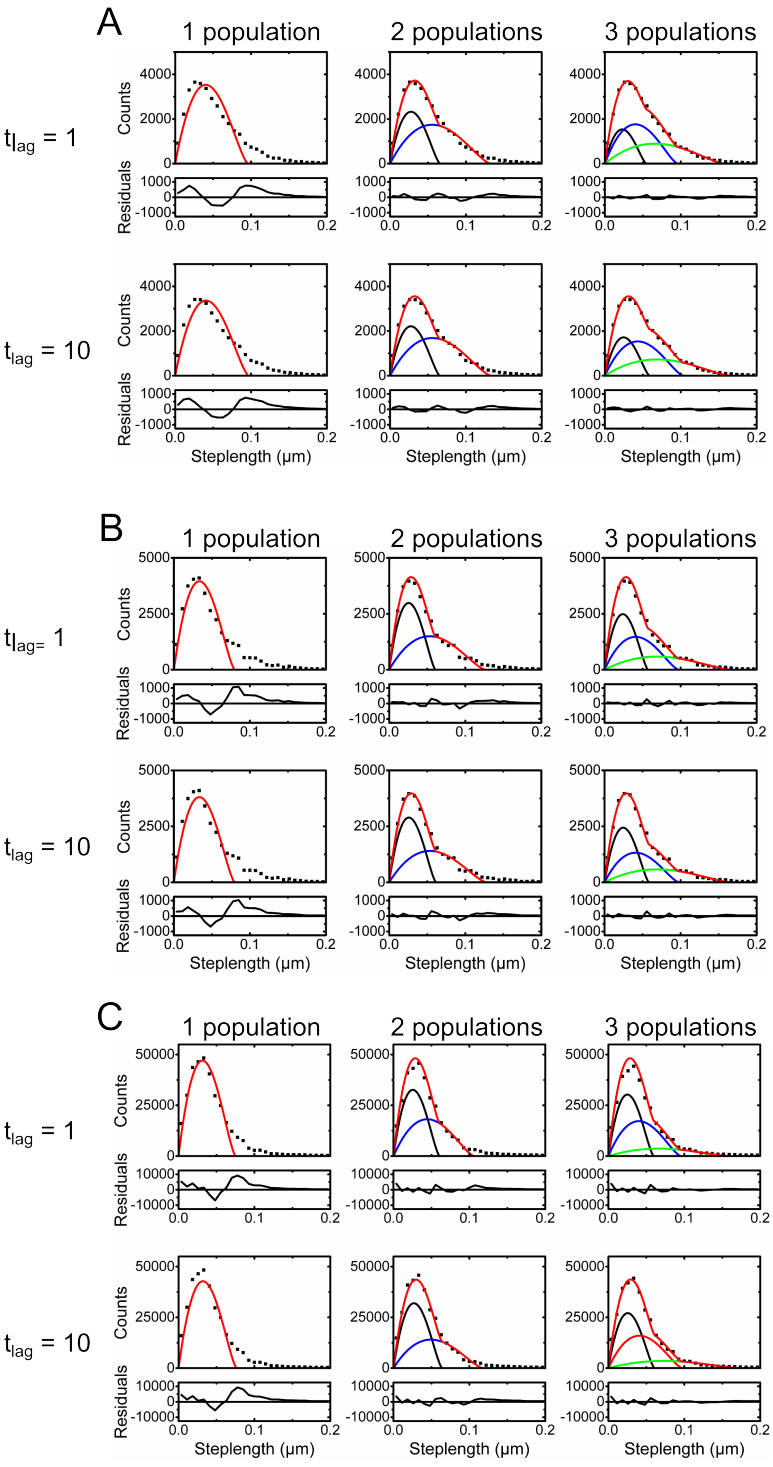

Figure 4.10. Fits of the step length distributions with different numbers of subpopulations. For each subpopulation the fit curves and residuals are shown for two different t_{lag} ($t_{lag} = 1$ and $t_{lag} = 10$). (A) ATTO647N, (B) ATTO647 and (C) Oxa12.

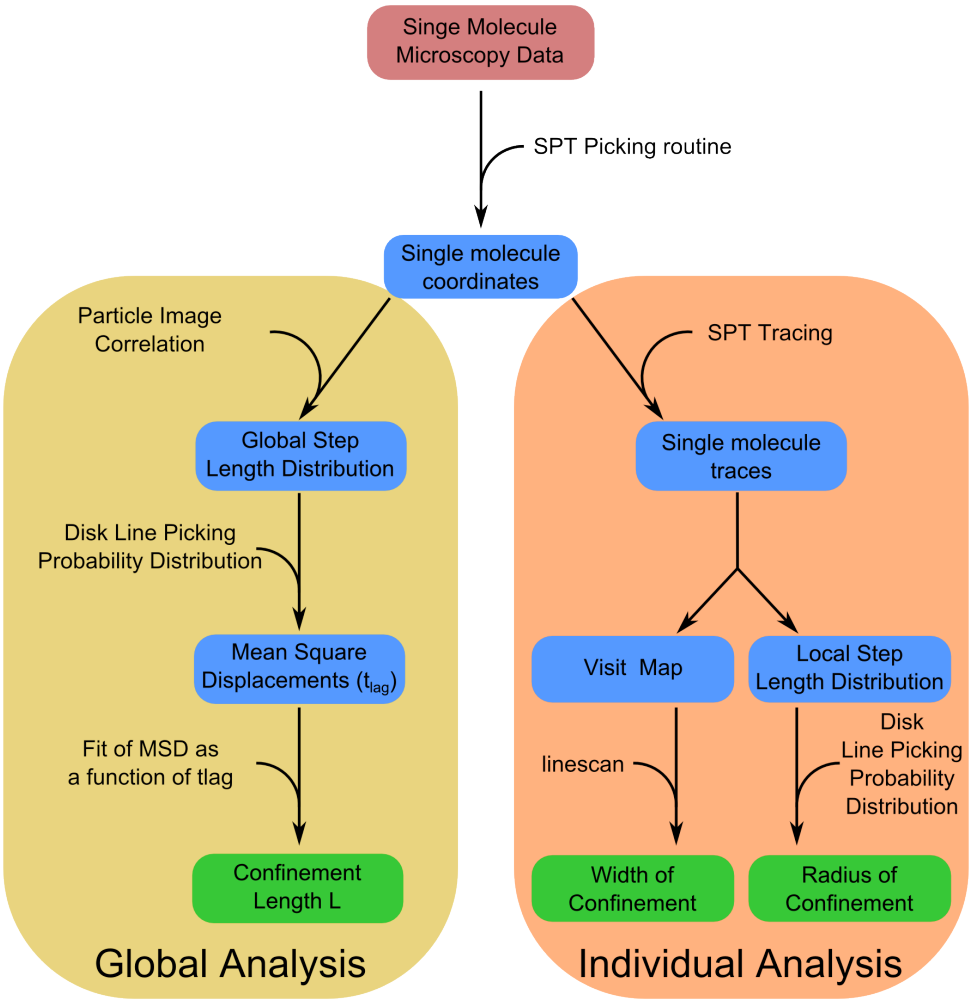

Figure 4.11. Sequence of analysis steps for data from dye loaded NLCs. The sequence of analysis steps is shown both for the individual fluorescent molecules and for the global statistical analysis. Raw data is underlaid in red, intermediate analysis results in blue and the final analysis result in green.

The next step was to determine the confinement lengths. The $\langle r^2 \rangle$ values for each population and dye were plotted against t_{lag} for $t_{lag} = 1, \cdots, 10$. The $\langle r^2 \rangle$ plots (figure 4.12) clearly show a nearly constant $\langle r^2 \rangle$ value over t_{lag}, for all populations and dyes. Therefore, the confinement lengths could be determined by fitting the respective $\langle r^2 \rangle$ data with equation 4.3. A confinement length L_1 of $61.9\,\text{nm} \pm 2.7\,\text{nm}$, of $69.6\,\text{nm} \pm 7.7\,\text{nm}$ and of $68.1\,\text{nm} \pm 5.0\,\text{nm}$ was obtained for the smaller subpopulation of ATTO647N, ATTO647 and Oxa12 respectively. For the larger subpopulation L_2 was determined to be $119.5\,\text{nm} \pm 7.3\,\text{nm}$, $134.4\,\text{nm} \pm 11.3\,\text{nm}$ and $126.2\,\text{nm} \pm 10.7\,\text{nm}$ for ATTO647N, ATTO647 and Oxa12 respectively (Table 4.2). The overall size of the particles as determined from DLS is clearly larger than confinement length value for both the subpopulations, indicating that the dye molecules are confined to nanostructures smaller than the whole particle (Figure 4.12D, Table 4.2).

It can further be seen that the plateau value of the MSD is already reached for $t_{lag} = 1$ and therefore it is not possible to determine the exact diffusion coefficient as this would require the existence of a linear component for small t_{lag}. However, an upper limit could be extracted. The upper limit of the diffusion coefficient was determined to be on the order of $10^{-9}\,\text{cm}^2\,\text{s}^{-1}$ for the frame rate of 31 ms used in the internal analysis measurements. As faster frame rates might

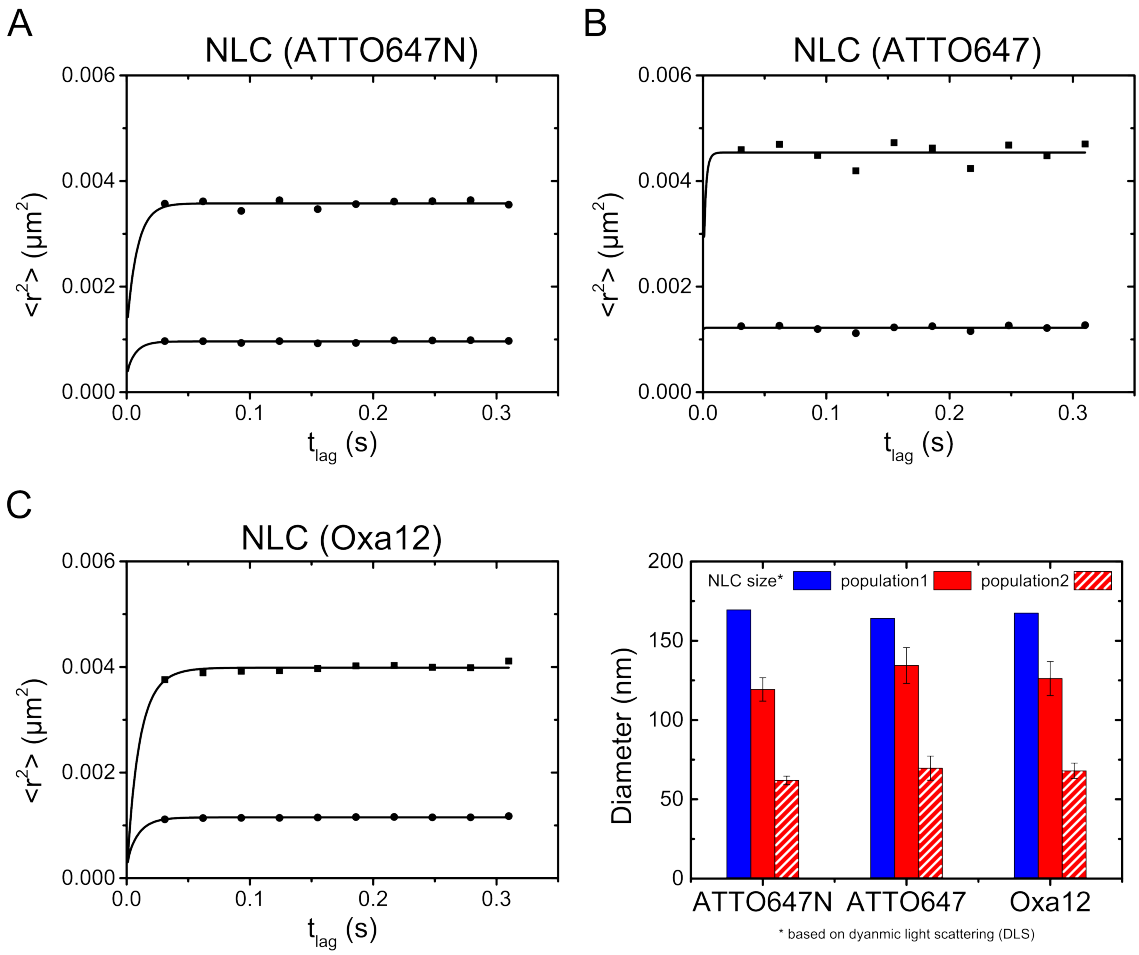

Figure 4.12. Fits of the MSD as a function of t_{lag} for the two identified subpopulations with equation 4.3. (A) ATTO647N, (B) ATTO647 and (C) Oxa12. Data points and the resulting fit curves are shown. (D) Comparison of internal confinement lengths with the results from DLS measurements for total particle size.

Table 4.2. Comparison of the confinement lengths obtained from the global analysis of the TIRF data and the external size as determined from DLS.

	internal analysis (TIRF)		external size (DLS)
sample	L_1 (nm)	L_2 (nm)	d (nm)
ATTO647N	61.9 ± 2.7	119.5 ± 7.3	164.1
ATTO647	69.6 ± 7.7	134.4 ± 11.3	169.5
Oxa12	68.1 ± 5.0	126.2 ± 10.7	167.5

allow to resolve the diffusion coefficient, a further measurement was conducted at the fastest possible frame rate (5 ms) on the TIRF setup used here. However, again only an upper limit of the diffusion coefficient ($0.6 \times 10^{-8}\,\mathrm{cm^2\,s^{-1}}$) could be extracted. The diffusion coefficient of an ATTO dye dissolved in the oil Mygliol was therefore independently determined by fluorescence correlation spectroscopy. The diffusion coefficient was found to be $0.8 \times 10^{-7}\,\mathrm{cm^2\,s^{-1}}$. This explains why the diffusion coefficient could not be resolved, and thus is in agreement with the data from the TIRF experiments.

In conclusion, the internal analysis revealed the restriction of the fluorescent dyes to oil (Miglyol) nanocompartments. Two populations with different confinement lengths could be identified. For all three dyes analyzed the confinement lengths of both populations are smaller than the particle size itself. Therefore, a homogeneous distribution of the dye within the particle and also a drug distribution within a liquid phase surrounding a solid core can be exclude. However, a single or multiple internal liquid cores or liquid phase droplets outside of a solid phase particle cannot be excluded at this stage of the analysis.

4.2.3 Direct comparison of oil droplet and NLC size

In order to answer the remaining question if the liquid phase exists as a single or multiple internal liquid cores or liquid droplets outside of a solid phase particle, an experiment directly comparing the liquid phase size and localization and the NLC size and localization was conducted. Cover slips with NLC particles containing the dye ATTO647 were prepared as previously described (see section 3.2.1) and measured. Next, a solution containing Oxa12 was added to determine the particle size from an affinity labeling experiment. Data was recorded and analyzed as described for affinity labeling experiments (see section 4.2.1). Visit maps were generated and are shown for three representative particles in the top panel of Figure 4.13, both for the internal dye molecules motion (Figure 4.13A) as well as for the affinity labeling with Oxa12 (Figure 4.13B). It can clearly be seen that the internal motion is confined to circular areas much smaller in diameter than the circular NLC particles, in accordance with the results from the separate internal and external analysis. More importantly the analysis here shows, that individual NLC particles only contain one liquid phase droplet. Figure 4.13 also shows the comparisons between line scans through the oil droplet and the NLC particle (Figure 4.13C) on the one hand, and on the other hand it also depicts the comparison of the SLDs (Figure 4.13D), both clearly showing the difference in size as detected by the movement of the dye molecule included in the liquid phase versus the detection of the NLC particle via the affinity labeling experiment.

4.2.4 Drug release upon membrane interaction

Not only the drug incorporation into NLCs is of importance but also how this influences the drug release. In order to analyze the drug release from NLCs with single-molecule techniques a model membrane system (bovine disk membranes) were applied to the cover slip as previously described [Kim et al., 2009b, Kirchberg et al., 2010]. NLCs containing Oxa12 were then added. Measurements were performed directly after addition and after 20 h of incubation. The SLD both directly after addition and after 20 h both required three populations for a good fit to the data. The resulting plot of the $\langle r^2 \rangle$ over t_{lag} (Figure 4.14A) indicating that two of these populations compare well to those found for the internal analysis of dye molecules confined within the NLCs. The $\langle r^2 \rangle$ of the third population clearly exhibits a linear dependence for the first couple of t_{lag} values, before leveling off towards a plateau value. This plateau value is considerably larger than those observed for dye molecules confined within NLCs, and is even larger after 20 h of incubation than directly after addition (Figure 4.14A) and is indicative of highly mobile dye molecules within the membrane and not confined within NLCs.

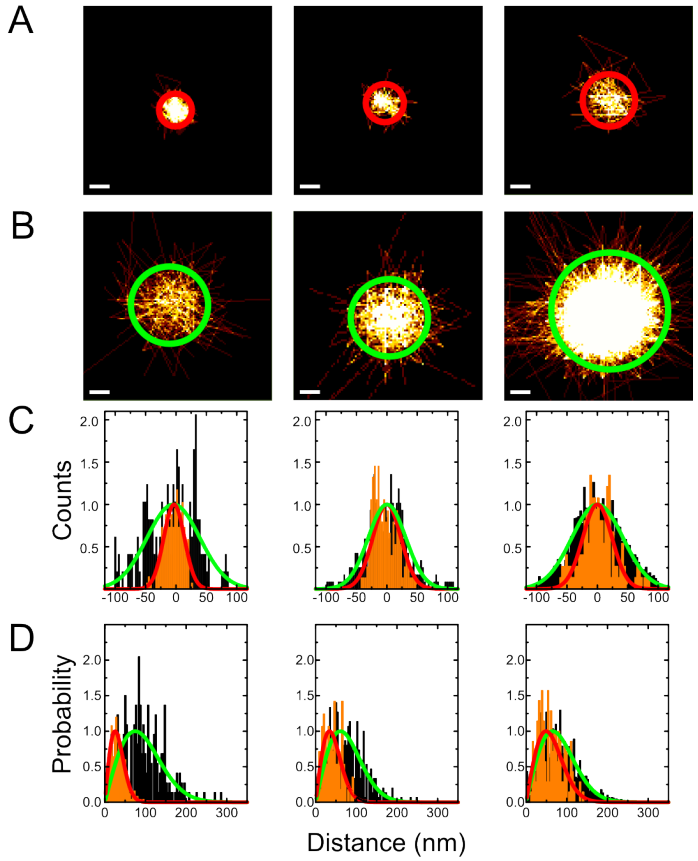

Figure 4.13. Direct comparison of confinement of dye molecules inside NLCs and the external NLC size. (A) Internal confinement of ATTO647 in NLCs. (B) The overall NLC size determined from an affinity labeling experiment at identical sample position as (A). Scale bars: 50 µm (C) Representative line scan through the internal confinement (red) and the affinity label hot spot (green). (D) SLD for the internal confinement (red) and for the affinity labeling experiment(green).

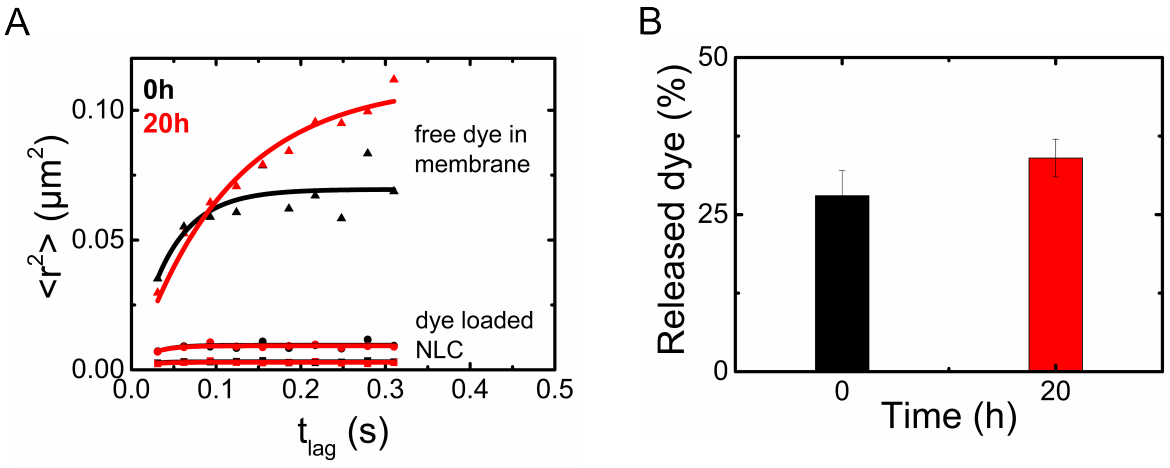

Figure 4.14. Drug release of NLCs upon membrane interaction. (A) $\langle r^2 \rangle$ from fits of the SLD plotted against t_{lag}. Fits of the SLD required three subpopulations. Two are identical to those observed for dye molecules confined within NLCs. The third indicates a highly mobile fraction, the free dye in the membrane. (B) Histogram of the percentage of the released dye as obtained from the amplitudes of the free dye population in the SLD fits.

From the corresponding amplitudes fit of the SLD with three populations, the relative contribution of each population can be deduced. The amplitude of the third population is a measure of the amount of released dye. Directly after addition around 25 % of the total dye were released, while the remaining 75 % were still confined with NLCs (Figure 4.14B). After 20 h of incubation, the amount of released dye had increased, but more than 50 % of the dye still remain within NLCs (Figure 4.14B).

4.3 Discussion

Dynamic light scattering (DLS) and laser diffraction (LD) are routine measurement methods to determine the size of nanostructured lipid carriers (NLCs) although they have low resolving power and the determined sizes are affected by either large aggregates and inhomogeneously formed particles. Further, no information on the internal structure of NLCs can be obtained from DLS and LD. The NLC particle morphology and internal structure has been investigated by different electron microscopy (EM) methods. However, depending on the EM method and measurement conditions different results were obtained. CryoEM measurements identified NLC platelets with nanostructures attached to the NLC surface [Bunjes et al., 2001, Jores et al., 2004, Esposito et al., 2008], while with TEM measurements at room temperature spherical NLC particles were seen but no nanostructures could be detected [Araújo et al., 2010, Jia et al., 2010, Luan et al., 2014, Patel et al., 2012, Tsai et al., 2012]. The different results could be due to different sample treatment prior to cryoEM and TEM or to different formulation and production procedures of the analyzed NLCs. Formulation and production are both thought to influence the arrangement of solid and liquid lipids within the NLCs. In this part of the thesis, a new method to directly visualize NLC morphology and internal structure based on single-molecule fluorescence microscopy techniques was developed and applied to NLC particles produced by hot high pressure homogenization and consisting of Dynasan and Miglyol (Miglyol content: 20 % (w/w)) .

4.3.1 NLC size and shape

To visualize and determine the size and shape of NLCs on the individual particle level using single-molecule microscopy an affinity-based labeling was developed. The experimental concept was an adaptation of other single-molecule methods used to elucidate structures smaller than the diffraction limit with high resolution, such as PALM and STORM (see 4.1.1). In contrast to these methods, where the structures of interest are usually labeled prior to the experiment, the assay developed here used the affinity of a lipophilic dye molecule to the NLCs. This is a similar approach to that reported by Mei, Gao and Hochstrasser [Mei et al., 2006] where the fluorescence emission of the hydrophobic dye molecule upon collision with lipid vesicles was used to determine the sub diffraction vesicle size. Here, Oxa12 was identified as a suitable dye molecule for the affinity labeling of NLCs. Due to its physicochemical properties Oxa12 is not attracted to the cover slip surface but shows a high affinity for the lipophilic NLC surface.

Visit maps generated from the affinity labeling measurement data revealed the presence of hot spots of Oxa12 localizations. Since Oxa12 selectively attaches to NLCs, these hot spots coincide with NLC particles. The shape and size of the hot spots hence reflects the shape and size of the NLC particles. The hot spots were found to be spherical and the diameter of each NLC was determined from two orthogonal intensity profiles through the hot spot using an automated analysis routine based on a Gaussian fitting procedure. The resulting mean diameter of 155 nm ± 6 nm for the whole population corresponded very well with data obtained from DLS (166 nm ± 3 nm) and LD (LD50 = 148 nm) measurements. An advantage of single-molecule-based methods is the direct visualization of the nanoparticle size and thus the detection of subpopulations is possible, which is not feasible with DLS and LD measurements.

Results from DLS and LD are also heavily affected by either large aggregates and contaminations or non-spherical and inhomogeneously shaped particles. NLC particle visualization with the affinity labeling assay has the advantage of determining the mean NLC size from individual particles allowing for a simultaneous determination of particle shape and also detection and exclusion of aggregates. The samples investigated here all showed a very homogeneous spherical particle shape and low occurrence of aggregates.

Another method recently proposed to circumvent problems from DLS and LD is the nanoparticle tracking analysis (NTA). NTA is a single-molecule technique, which tracks the particle movement (Brownian motion) of the nanoparticles from which the particle size can be derived if temperature and solvent viscosity are known. Many of the advantages stated for NTA over DLS [Nanosight Ltd., 2010], e.g. size determination from single particles, no dependency on detection angle or wavelength and not being weighted towards larger particles, also apply to the single-molecule microscopy approach developed here. However, NTA still relies on calculations of the particle size, whereas with the affinity-based labeling developed here, the molecules size and shape can be directly visualized. Further, the external size but also the internal structure could be visualized with single-molecule fluorescence microscopy.

In conclusion, the affinity labeling assay adds a further dimension to commonly used methods for NLC size determination, enabling the visualization of shape and size of individual NLCs molecules, while still being able to determine the size distribution and the mean size of the NLC population. Further, due to the high accuracy achievable by single-molecule microscopy, the existence of subpopulations not discernible by either DLS or LD, both suffering from low resolving power, can be achieved.

4.3.2 NLC internal structure

One of the main aims of the investigation of NLCs was to elucidate the internal structure of NLCs. Three different structural models have been proposed for NLCs, the imperfect crystal type, amorphous NLCs and NLCs containing distinct nanocompartments. The imperfect crystal type is though to form when the oil component is used at low concentrations. The oil phase reduces the crystallinity of the mixture and forms a heterogeneous matrix with the solid lipid, however with increased occurrence of defects in the crystal lattice, thus increasing the dye loading capacity compared to the NLCs predecessor SLN (solid lipid nanoparticles). The imperfect NLCs are prone to the expulsion of active due to rearrangements in the crystal lattice. The other two proposed models should not display the same problem of expulsion of active, as lipids are selected so that no crystallization occurs. Using specific lipids, amorphous NLCs can be generated. These are solid particles with an amorphous lipid matrix instead of a crystalline matrix. Nanostructured NLCs are thought to form when a high percentage of the oil component is used. During the cooling process of the lipid melt an oversaturation with the liquid phase should then occur, which would lead to the formation of nanocompartments. Using an active with a high partitioning coefficient for the oil phase, the active could then be accommodated in these nanocompartments at high concentrations. Further, due to the lack of crystallinity, spontaneous burst expulsion should be prevented.

Here, a single-molecule microscopy method was established to identify and visualize these nanocompartments. A fluorescent drug mimetic was incorporated into the oil phase before producing the NLCs. Single particle tracking of the loaded fluorescent drug mimetics was used to analyze the dimensions of the nanostructures within the particles. Super-resolution microscopy techniques based on dye localizations and traces were employed to determine size and shape of the nanocompartments containing the loaded dye. Since nanocompartments with different sizes were observed, a statistical approach developed in the group (UPICS, see section 4.1.2) was employed to determine the number of subpopulations for the size of the nanocompartments. This approach revealed two subpopulations, indicative of fluorescent drug mimetics confined in nanocompartments with sizes of about 60 nm to 70 nm and 120 nm to 135 nm.

To investigate whether the two different nanocompartment sizes (see Figure 4.12) correlate with the two observed subpopulations in NLC size (Figure 4.7) a direct comparison of the inner and outer structure in one and the same experiment was performed and revealed a single nanocompartment within a single NLC. Figure 4.15 compares the size distribution of the NLC

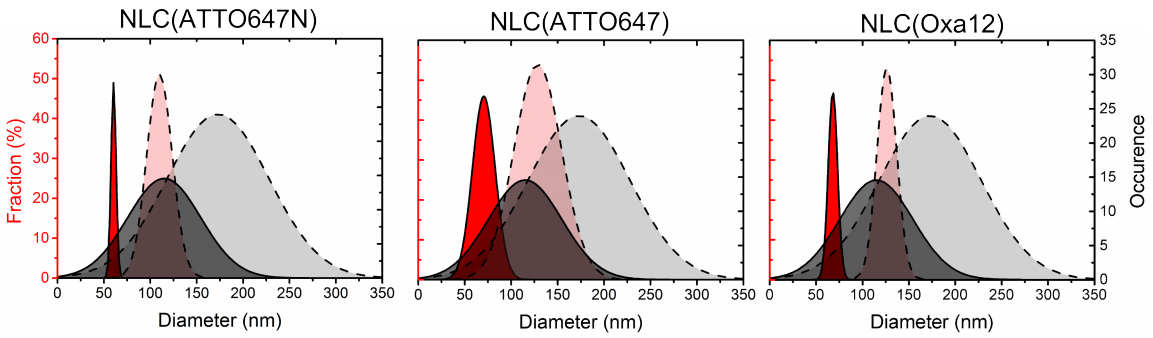

Figure 4.15. Comparison of the size distribution of NLC nanocompartments (red tones) filled with the dyes ATTO647N, ATTO647 and Oxa12 and the NLCs size distribution of the blank NLCs (grey tones).

compartments with the different drug mimetics with the NLC size distribution. Although the width of the nanocompartment size distribution varies for the different drug mimetics, their distribution is much narrower than the distribution of the NLC size. One can conclude that the loaded drug may influence the size distribution of the inner compartments, however, for the given formulation one nanocompartment per NLC seems to be the overall structural motif. The NLCs investigated here, therefore correspond to the liquid core model of the NLC nanostructures (Figure 4.16). The other models, i.e. homogeneous mixture, multiple liquid droplets, one solid core surrounded by liquid lipid and (multiple) external liquid droplet adhesion can be excluded for the NLC nanoparticles investigated here. It can not be excluded that these may exist in NLC particles formed from other solid and liquid lipids or even in other mixtures of the lipids used here. The single-molecule microscopy methods presented here, however, establishes a method to allow these questions to be answered also for other NLC formulations.

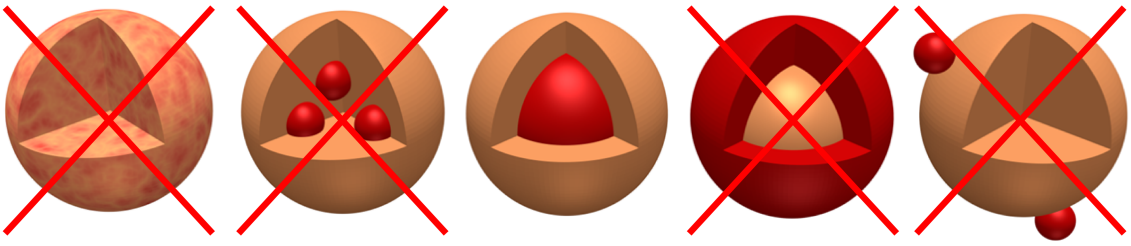

Figure 4.16. NLC nanocompartment organization as determined from single-molecule microscopy. The results obtained here identified NLCs particles containing one liquid core. This excludes a homogeneous mixture, multiple liquid droplets, one solid core surrounded by liquid lipid and (multiple) external liquid droplet adhesion for the NLC particles investigated here.

4.3.3 Drug release upon membrane interaction

Drug release properties are important for all drug delivery systems. Therefore, the drug release properties of NLCs upon membrane interaction were also investigated using single-molecule microscopy. Bovine disk membranes, as model membranes, were deposited at the surface of a glass cover slip and NLCs containing Oxa12 were added. Analysis of the step length distribution of Oxa12 molecules identified a third population of particles. The diffusion analysis showed these to be highly mobile compared to the two populations confined within NLC nanocompartments.

Analysis of the relative amplitudes revealed an initial release of around 25 % followed by a slower release, so that after 20 h still more than 50 % of the dye molecules were contained within the NLCs. Similar release profiles have been observed for other NLC particles loaded with different drugs [Jia et al., 2010,Patel et al., 2012,Luan et al., 2014]. Thus, beside structure determination, the single-molecule microscopy approach can also be used to obtain the drug release profile which is relevant for pharmacological application and tailor-made NLCs.

Chapter 5

Size, molecular flexibility and drug distribution of dendritic polyglycerol-based nanoparticles

A time-resolved fluorescence spectroscopy study

Nanoparticles built from polyglycerols are thought to be able to provide a novel platform for next generation biomaterials [Khandare et al., 2012], mainly due to the high biocompatibility and multifunctionality exhibited by polyglyerols [Kainthan et al., 2006, Kainthan et al., 2007, Kainthan and Brooks, 2007, Imran ul-haq et al., 2012]. In my thesis the physiochemical properties of two polyglycerol-based nanoparticles, dendritic polyglycerol sulfate (dPGS) and core-multishell (CMS) nanocarriers, were investigated.

The free OH-groups on the surface of a dendritic polyglycerol (dPG) were functionalized with negatively charged sulfate groups, yielding dPGS, with a highly ordered, branched architecture and a globular shape (Figure 5.1) [Calderón et al., 2010a, Quadir et al., 2008]. dPGS has been shown to be a bioactive nanoparticle and has been used as a biomarker for disease sores and joints with early signs of inflammation in rheumatoid arthritis [Licha et al., 2011,Khandare et al., 2012] and to monitor lung inflammation in mice with allergic asthma [Biffi et al., 2013]. Additionally, it has been shown to interact with the complement system, part of the innate immune system, and

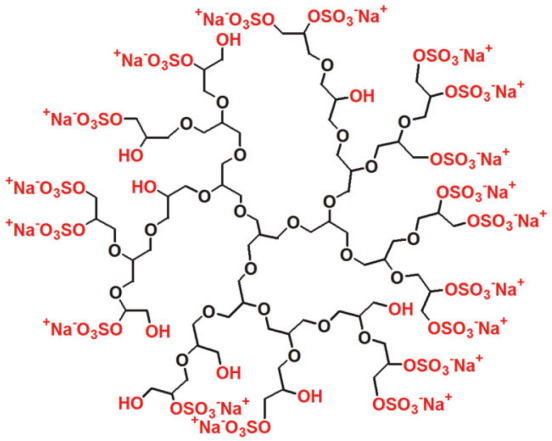

Figure 5.1. Structure of dendritic polyglycerol sulfate. (Reprinted from [Calderón et al., 2010a] Copyright 2010, with permission from Wiley.)

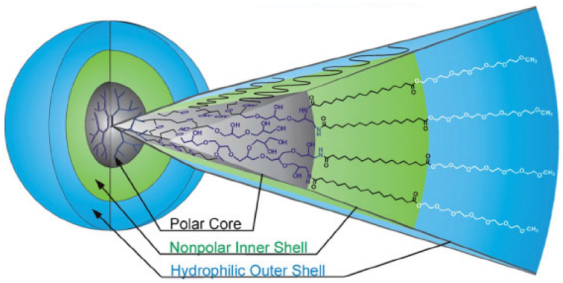

Figure 5.2. Structure of a core-multishell nanocarrier. (Reprinted from [Calderón et al., 2010a] Copyright 2010, with permission from Wiley.)

to have anti-inflammatory properties. It was found to be as effective as glucocorticoids, steroid hormones dampening the immune response and inflammation, in rats with contact dermatitis [Dernedde et al., 2010]. The anti-inflammatory activity has been shown to be mediated by the binding of dPGS to selectins (L- and P-selectin), cell adhesion molecules that normally bind sugar molecules and are involved in inflammatory processes [Dernedde et al., 2010, Papp et al., 2008]. dPGS binding to selectin can efficiently block leukocyte migration [Dernedde et al., 2010], one of the main stages of the inflammatory response. This behavior was found to be specific for dPGS and was not found for other polyanions [Weinhart et al., 2011a]. Recent studies identified a complex structure-activity relationship, implying that multivalency, particle size, as well as the structural flexibility all define and can modulate the biological activity of dPGS [Paulus et al., 2014].

The core-multishell nanocarrier system investigated here, consists of a 10 kDa dPG core and two additional shells (Figure 5.2). The first shell is formed by an aliphatic diacid chain with 18 carbon atoms, while the second shell is built up from mono methyl ether poly(ethylene glycol) (mPEG) with 6 repeat units of glycol. CMS nanocarriers have been shown to be good carrier for hydrophobic, poorly water-soluble drugs [Türk et al., 2004, Radowski et al., 2007, Küchler et al., 2009b]. They have been shown to target tumor tissue [Quadir et al., 2008] and have been studied for the delivery of anti-inflammatory drugs and pain killers. Wolf and coworkers were able to show in an in-vitro model that CMS nanocarriers are a promising system for the topical application of opioids for pain reduction in severe skin disorders [Wolf et al., 2009]. CMS nanocarriers promoted wound healing, did not show any toxicity and took up both the opioid morphine and also the anti-inflammatory transcription factor TGF-β1.

In my thesis, the aim was to use time-resolved fluorescence spectroscopy to determine different physicochemical properties of a dendritic polyglycerol sulfate (dPGS) nanoparticle and core-multishell (CMS) nanocarriers, such as the size, molecular dynamics and drug distribution, which are of importance for the biomedical application. I will briefly present the principles of time-correlated single photon counting, describe the experimental setup and also the employed data analysis methods, then the results, first for dPGS and then for CMS, and conclude with a discussion.

5.1 Methods

5.1.1 Time-correlated single photon counting

For time-correlated single photon counting (TCSPC) measurements the sample is excited with a short, periodic light pulse. Single emitted photons are detected. The temporal correlation of an individual excitation pulse with the detected photon allows for the determination of the exact temporal delay between the excitation of the sample and the emission of the photon. The counter in the memory channel corresponding to the measured temporal delay is increased by one. Hence, every detected photon contributes to the generation of the histogram of photons over time (Figure 5.3). To generate sufficient numbers of individual photon recordings to reproduce the original waveform, the process of sample excitation and single photon detection has to be performed a large number of times. Therefore, high laser repetition rates are generally considered favorable to TCSPC experiments.

A further aspect needed to be considered for TCSPC measurements is the so-called single photon counting regime, i.e. photon count rates for which the likelihood of detecting multiple photons per excitation pulse is very low. The probability of detecting multiple photons per excitation pulse needs to be very small, because the detector systems have a non negligible dead-time after each detection event. Hence, only the first of multiple photons will be registered, but not the following photons, resulting in a histogram with an overrepresentation of short photon detection times. To ensure that the likelihood of detecting multiple photons per excitation pulse is very small the ratio of photon counts and excitation pulses needs to be kept sufficiently low, about 1:100 to 1:200 [Alexiev et al., 2003, Lakowicz, 2010]. Hence, for the majority of excitation pulses no photon will be detected (Figure 5.3).

In a conventional TCSPC setup the excitation pulse starts the linear charging of a capacitor. The charging process is terminated upon detection of a photon. The resulting voltage is then read out and converted into a specific time delay. In order to prepare the capacitor for the next signal, the capacitor has to be discharged. During this time no further photons can be detected. This is the rate limiting step in most TCSPC systems. To make use of the fast laser repetition rates of modern lasers, the so-called reverse TCSPC operating mode is often employed. Here, the pulse from the detector triggers the charging of the capacitor and the delayed excitation laser pulse is used as the stop signal. The occurrence of capacitor charging cycles is thus greatly reduced compared to the conventional TCSPC setup, since the number of photons detected is considerably smaller than the number of excitation pulses.

Time-correlated single photon counting setup

All cuvette-based time-resolved fluorescence spectroscopy experiments were performed on a home-built TCSPC setup (Figure 5.4) [Alexiev et al., 2003, Kim et al., 2009a]. The laser source, a titanium:sapphire laser (Ti:Sa-Laser,Tsunami model #3950, Spectra Physics) pumped by a 5 W continuous wave diode laser [DL] (Millenia VS, Spectra Physics), has an intrinsic repetition rate of 82 MHz and can generate output wavelengths between 710 nm and 1000 nm. A pulse picker [PP] reduced the repetition rate to 4 MHz, equal to 1 pulse every 250 ns. This guaranteed that the time between two laser pulses was significantly longer than the fluorescence lifetimes to be recorded (here usually between 0.1 ns to 10 ns) and thus ensured the correct assignment of start and stop pulses.

In order to produce the visible wavelength range required to excite the fluorescent dyes used in the TCSPC studies, a frequency doubler [FD] (model #3980, Spectra Physics) was employed, resulting in wavelengths between 355 nm and 500 nm. The frequency doubler generates the second harmonic by means of a lithium borate crystal. The fundamental was removed by a

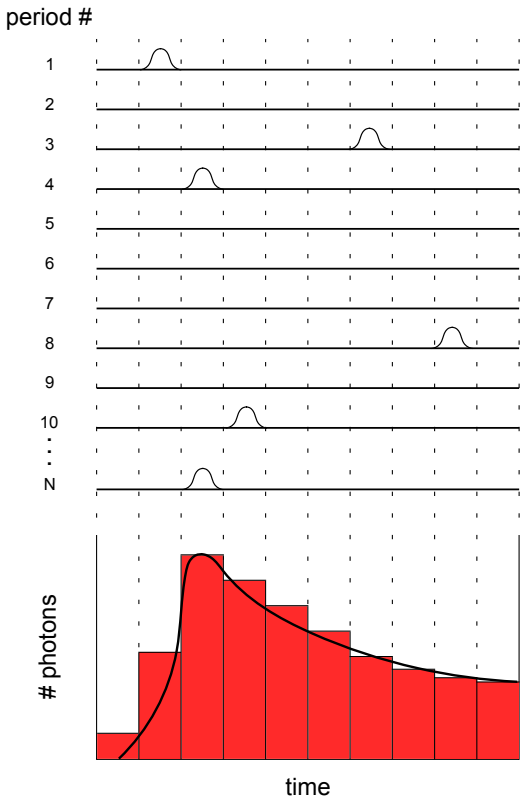

Figure 5.3. Illustration of the measurement principal of TCSPC. For each laser pulse, indicated by the period number, a maximum of one emitted photon per period is detected a certain time after excitation. The counter in the corresponding channel is then increased by one. After many detected photons, the photon histogram represents the fluorescence decay curve. Adapted from [Becker, 2012].

640 nm high-pass filter [HPF].

The frequency doubled Ti:Sa laser output wavelengths were linearly horizontally polarized. To change the polarization of the laser beam to vertical, the beam passed an achromatic Fresnel rhomb [FR]. At a beamsplitter [BS] the laser beam was divided into two separate beams. One was directed into the sample and the other onto a nano-second-photodiode (DET 210, Thorlabs). The latter passed a neutral density filter [ND] and a collimator lens [CL] before it reached the photodiode. The signal of the photodiode was used as the stop signal in this inverse TCSPC setup. It was amplified by a preamplifier [PA], either 1 GHz (Model #9369, EG&G Ortec) or 1.6 GHz (HFAC-26, B&H GmbH)), and then inverted. The inverted signal was directly sent to the TCSPC module (SPC-830, B&H GmbH). In addition, the preamplification of the signal from the photodiode also allowed monitoring the laser output and performance of the laser system with an oscilloscope.

The portion of the laser beam directed into the sample chamber [SC] passed through two neutral density filters [FW], enabling tight control of the excitation intensity and thus also control of the counts of emitted photons per second at the detector. The beam then passed through a Glan-Thompson polarizer [GTP], to ensure that only vertical polarized light passes through, before entering the sample cuvette positioned in a temperature controlled cuvette holder.

The fluorescence emission, detected at a right angle to the excitation, passed through an edge filter [F], removing scattered excitation light, a collimator lens [CL], an iris diaphragm [I] and a polarizer [P] before reaching the detector, a microchannel plate photomultiplier [MCP-PMT] (R3809U, Hamamatsu). The signal from the MCP-PMT was amplified by a preamplifier

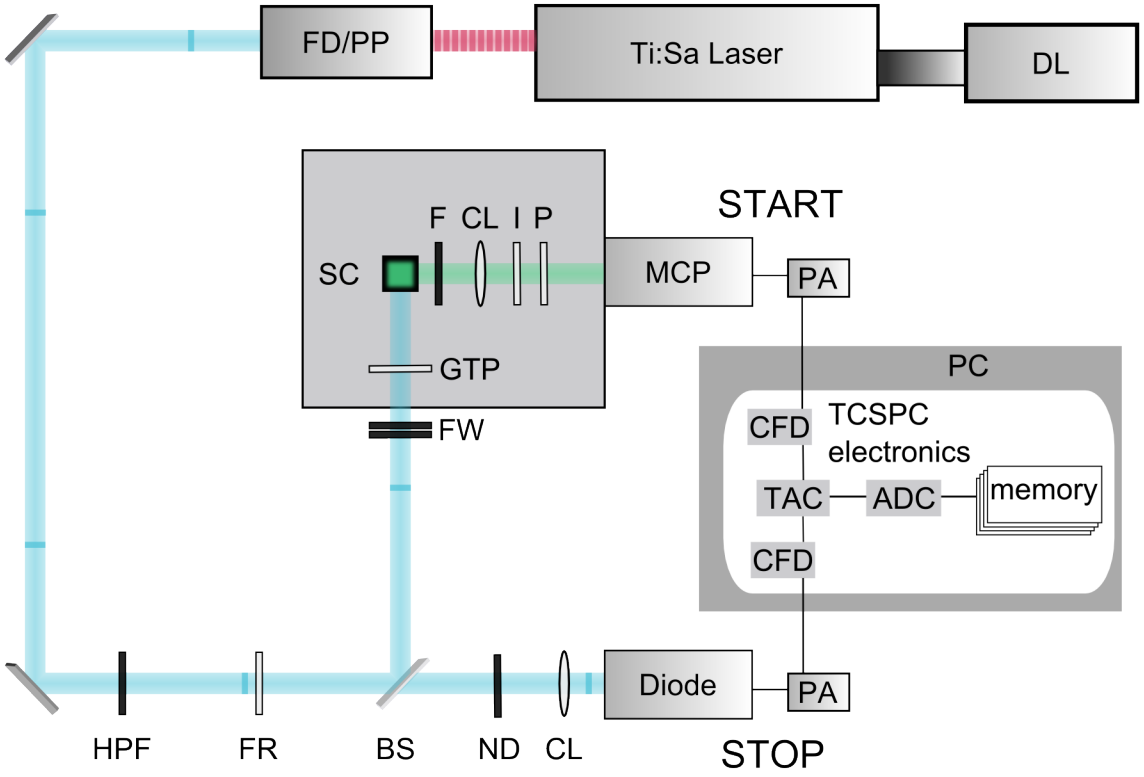

Figure 5.4. Schematic of the TCSPC setup employed. The pulsed laser beam is split into two individual pulses. One triggers a photodiode, while the other excites the sample. An emitted photon hits the detector and the resulting signal is sent to the TCSPC electronics, where, together with the signal from the diode, the arrival time t of the photon is determined and placed into the intensity-time-histograms. Abbreviations: diode laser (DL), frequency doubler (FD), pulse picker (PP), high-pass filter (HP), Fresnel rhomb (FR), beamsplitter (BS), neutral density filter (ND), collimator lens (CL), neutral density filter wheel (FW), Glan-Thompson polarizer (GTP), sample chamber (SC), edge filter (F), iris diaphragm (I), polarizer (P), microchannel plate (MCP), preamplifier (PA), constant fraction discriminator (CFD), time-to-amplitude converter (TAC), analog-to-digital converter (ADC).

[PA] and then fed into the TCSPC module. The TCSPC module combined the main electronic components for signal processing in TCSCP, namely the constant fraction discriminator [CFD], time-to-amplitude converter [TAC], analog-to-digital converter [ADC], and digital memory.

The signal from the photodiode and the MCP-PMT signal each passed through a separate CFD to determine the exact start and stop times. Determining the exact start and stop times, however, is not trivial as laser pulses are not δ-functions but display a temporal width and can vary in intensity. The CFD achieves very precise start and stop times, if the shape of all pulses is identical but the amplitude of the pulses varies, by generating two pulses from both the start and the stop pulse respectively. These are then separately manipulated, one being inverted while the other is delayed in time. Addition of both pulses generates a signal exhibiting a zero-crossing, and allows for a precise determination of a point in time for both the start and the stop pulse. The signal from the CFD was then fed to the TAC and the the ADC converted the signal from the TAC to a time interval Δt and assigned it to a specific channel number.

5.1.2 Data analysis methods

The time-resolved fluorescence data was analyzed with the software package Globals Unlimited V1.2 distributed by the Laboratory of Fluorescence Dynamics at the University of Illinois. The

software package implements the deconvolution of the measured signal S(t) with the instrument response function IRF(T) and subsequent fitting of the deconvoluted fluorescence signal I(t) with model functions based on a sum of exponentials.

Deconvolution

The deconvolution is necessary as the measured signal S(t) is a convolution of the actual fluorescence signal I(t) and the instrument response function IRF(t). The instrument response function is influenced by the laser pulse width and the electronics of the setup and has to be determined experimentally for each data set using a dispersing sample. For the setup used here, the laser pulse width is small, 1-2 ps, compared to the width of the IRF, so that solely the electronics give rise to the shape and width of the IRF. The width of the IRF (full width half maximum (FWHM)), depending on the electronics used and the optical pathway, can be as low as 25 ps. The convoluted signal can be written as:

$$S(t) = \int IRF(t')I(t-t')dt' \; . \tag{5.1}$$

Once the IRF is known from the measurement with the dispersing sample, the deconvoluted signal can be calculated and the fluorescence parameters can be obtained.

Fluorescence lifetime fitting

The fluorescence lifetimes and their respective amplitudes follow from fitting I(t) with the model function

$$I(t) = \sum_i a_i exp(-t/\tau_i) \; , \tag{5.2}$$

where a_i represents the absolute amplitude of the individual lifetimes τ_i. However, for better comparison between different data sets the absolute amplitudes are often replaced by the relative amplitudes α_i and equation 5.1 can be written as

$$I(t) = I_0 \sum_i \alpha_i exp(-t/\tau_i) \; , \tag{5.3}$$

where I_0 is the Intensity at t = 0.

Fluorescence anisotropy fitting

In order to analyze the fluorescence anisotropy, the time resolved anisotropy r(t) is calculated according to:

$$r(t) = \frac{I_\parallel(t) - G \cdot I_\perp(t)}{I_\parallel(t) + G \cdot 2I_\perp(t)} \; , \tag{5.4}$$

where $I_\parallel$ and $I_\perp$ are the deconvoluted fluorescence data from the measured signals $S_\parallel(t)$ and $S_\perp(t)$ and G is the so-called G-factor, a correction factor for polarization dependent differences of the detector sensitivity. The time-dependent anisotropy decay r(t) can be fitted with a sum of exponentials, comparable to those already used in equations 5.2 and 5.3,

$$r(t) = \sum_i b_i exp(-t/\phi_i) \, , \tag{5.5}$$

$$r(t) = r_0 \sum_i \beta_i exp(-t/\phi_i) \tag{5.6}$$

with b_i the absolute amplitudes and β_i the relative amplitudes of the individual rotational correlation time ϕ_i. r_0 is the anisotropy at time t = 0.

Quality of the fit

The fitting routine used by the Globals Unlimited Software package is based on the Levenberg-Marquardt algorithm. The quality of the respective fit is assessed from the residuals and by the value of the reduced χ^2_{red} as determined from

$$\chi^2_{red} = \frac{\chi^2}{N - M - 1} \,, \tag{5.7}$$

where N is the number of data points, M the number of parameters, and χ^2 as given by

$$\chi^2 = \sum_{t=0}^{N-1} (y_i - y(x_i|a_0 \cdots a_{M-1}))^2 \,, \tag{5.8}$$

with the parameters a_i, and y_i and $y(x_i)$ an original data point and the corresponding fit point, respectively.

Exhaustive error analysis

The fitting procedure above yields the fit parameters and an assessment of the quality of the fit. However, it does not give an accuracy for the individual parameters. The accuracy can be determined through an analysis of the confidence intervals. This has to be performed separately for each parameter. The so-called exhaustive error analysis is based upon a sequential analysis of the quality of the fit when varying the parameter under investigation around its optimum value. The parameter under investigation is fixed at a certain value in the vicinity of the optimum and a χ^2_{red} minimization is conducted. Then, the value of the parameter under investigation is slightly shifted and fixed again and a further χ^2_{red} minimization is conducted. Ultimately, the χ^2_{red} can be plotted against the varied parameter and the confidence interval boundaries can then be determined from the intersection with the respective confidence interval level.

To ensure comparability of the confidence interval boundaries between different data sets, the respective χ^2_{red} and number of data points (N) need to be considered in the analysis. The confidence interval boundaries can be obtained from the intersection with the respective confidence interval level, determined from

$$\chi^2_{cl}(p, x) = \chi^2_{min} + \frac{\Delta\chi^2(p, x)}{N} \,, \tag{5.9}$$

where χ^2_{cl} is the χ^2 value for which the parameter under investigation is contained with a given likelihood p. The values used for the likelihood p, coincide with those used for the standard deviation σ of the Gaussian normal distribution, i.e. $p = 68.27\%$ corresponds to 1σ, $p = 95.45\%$ to 2σ and $p = 99.73\%$ corresponds to 3σ. The values for $\Delta\chi^2(p, x)$ can be calculated from the cumultative χ^2 distribution function, and for a degree of freedom of 1 lead to the following values for the different likelihoods: $\Delta\chi^2(\sigma) = 1.00$, $\Delta\chi^2(2\sigma) = 4.00$ and $\Delta\chi^2(3\sigma) = 9.00$ [Kim, 2012].

The exhaustive error analysis was also performed using the software package Globals Unlimited Version 1.2.

Two-state transitions

Temperature dependent data that displayed the characteristics of a two-state transition were fit with a two-state transition model [Eftink, 1994, Winkler et al., 2007, Boreham et al., 2014b,

Boreham et al., 2014a] according to

$$p(T) = \frac{p_{0b} + s_b T + (p_{0a} + s_a T) \cdot exp(\frac{-\Delta H^0 + T\frac{\Delta H^0}{T_c}}{RT})}{1 + exp(\frac{-\Delta H^0 + T\frac{\Delta H^0}{T_c}}{RT})} . \tag{5.10}$$

This equation contains the following six parameters: p_{0b} and p_{0a} the value of the respective fluorescence parameter before and after the transition; the temperature-dependence of the respective parameters before, s_b, and after the transition,s_a; and the apparent enthalpy change, ΔH^0 , and the transition temperature, T_c [Eftink, 1994]. The fits were performed with the software package OriginPro (OriginLab Cooperation).

This equation assumes that only two distinct states exist, one before (B) and one after (A) the transition.

$$B \rightleftharpoons A . \tag{5.11}$$

The equilibrium constant K_{BA} can then be written as

$$K_{BA} = \frac{[A]}{[B]} . \tag{5.12}$$

Using the thermodynamic relation

$$-RTlnK_{BA} = \Delta H - T\Delta S , \tag{5.13}$$

the equilibrium constant can also be written as

$$K_{BA} = exp\left(\frac{-\Delta H + T\Delta S}{RT}\right) . \tag{5.14}$$

Assuming that the value of the parameter under investigation in the transition region is dependent on the relative population (X) of the states before (B) and one after (A) the transition, the relative fractions being directly related to the equilibrium constant through

$$X_B = \frac{1}{1 + K_{BA}} , \tag{5.15}$$

$$X_A = 1 - X_B = 1 - \frac{1}{1 + K_{BA}} = \frac{K_{BA}}{1 + K_{BA}} , \tag{5.16}$$

then the value of the parameter in the transition region is given by

$$p = X_B \cdot p_B + X_A \cdot p_A , \tag{5.17}$$

$$p = \frac{1}{1 + K_{BA}} \cdot p_B + \frac{K_{BA}}{1 + K_{BA}} \cdot p_A . \tag{5.18}$$

Moreover, assuming the temperature dependence of the parameter under investigation is linear, both in the pre- and posttransition state, then the temperature dependence of the parameter can be written as

$$p(T) = \frac{1}{1 + K_B A} \cdot (p_{0b} + s_b T) + \frac{K_B A}{1 + K_B A} \cdot (p_{0a} + s_a T) . \tag{5.19}$$

Inserting equation 5.14 along with the relation for the temperature at the midpoint of the transition $T_c = \frac{\Delta H}{\Delta S}$ this can be rewritten to obtain the equation for the two-state transition model (equation 5.10).

5.2 Results

5.2.1 Physicochemical characterization of a sulfated dendritic polyglycerol

Recent studies identified a complex structure-activity relationship where multivalency, particle size, as well as the structural flexibility all define and can modulate the biological activity of dendritic polyglycerol sulfate (dPGS) [Paulus et al., 2014]. Here, time-resolved fluorescence spectroscopy was applied to characterize the physicochemical properties of dPGS. To this end, a fluorophore label (ICC) was covalently attached to the dPGS surface via a linker. The results presented here have been published [Boreham et al., 2014a].

Environmental sensitivity of dPGS-ICC spectroscopic properties

To investigate the effect of ICC linkage to dPGS the absorption and emission spectra of dPGS-ICC were recorded in H_2O and compared to those obtained for the dye ICC alone (Figure 5.5A). Binding of ICC to dPGS results only in minor changes of the absorption characteristics with only a minimal broadening of the absorption spectrum and an increase in absorption around 520 nm. The emission spectrum is also basically unchanged by the binding of ICC to dPGS. Spectra for dPGS-ICC were also recorded in ethanol to determine if ICC coupled to dPGS is sensitive to a change of the solvent, e.g due to a change in the polarity. In fact, the solvent has an effect on the absorption and emission properties (Figure 5.5B). Both the absorption and emission spectra are red shifted when changing the solvent from H_2O to ethanol and a decrease in absorption around 520 nm was observed.

To further asses the extent of solvent interactions of both ICC and dPGS-ICC, fluorescence excitation-emission scans were measured in five different solvents: water, ethanol, methanol, acetone and DMSO (Figure 5.5C). ICC exhibited solvent-dependent shifts in the characteristic maximum wavelength of absorption, λ_{max}^{abs}, with $\lambda_{max}^{abs} = 550\,nm$ in water, $\lambda_{max}^{abs} = 556\,nm$ in methanol, $\lambda_{max}^{abs} = 556\,nm$ in ethanol, $\lambda_{max}^{abs} = 559\,nm$ in acetone and $\lambda_{max}^{abs} = 560\,nm$ in DMSO, a spread of 10 nm (Figure 5.5C and Table 5.1). The absorption characteristics of dPGS-ICC showed a very similar sensitivity to the solvent, with nearly identical characteristic absorption maxima only exhibiting minimal red shifts of 1 nm to 2 nm. The emission maxima of both ICC and dPGS-ICC also exhibited solvent-dependent shifts comparable in magnitude to the corresponding shifts in the absorption peak, with the most pronounced shift occurring between water and DMSO with 11 nm. These data demonstrate that ICC is a solvent sensitive dye and retains the solvent sensitivity also when bound to dPGS.

The fluorescence lifetime is even more sensitive to the environment than the spectral analysis. The environment can lead to additional components, in this case exponential components, in the fluorescence lifetime decay of the fluorescent dye. To extract the fluorescence decay components from the measurement data, the fluorescence lifetime decay curves were fitted with a single or multiple exponential functions (equation 5.3) and the quality of the fit was then evaluated taking both the residuals and the χ_R^2 into consideration (see 5.1.2). The analysis of lifetime traces for ICC and dPGS-ICC recorded at 20 °C in H_2O and ethanol is shown in Figure 5.6. For ICC in H_2O, two exponential decay components are required. A fit with one decay component results in a good χ_R^2 of 1.3, however the residuals indicate the need for a further decay component (Figure 5.6B). ICC in ethanol clearly requires two exponential decay components, as a fit with one decay component results both in a high χ_R^2 of 10.9 and bad residuals (Figure 5.6B). In the case of dPGS-ICC in H_2O (Figure 5.6C) both the value of the χ_R^2, from 2.7 to 1.0, and the residuals are greatly improved when going from two to three decay components. For dPGS-ICC in $EtOH/H_2O$, a vast improvement was also observed in the χ_R^2 and residuals when going from two to three decay components (Figure 5.6C) was also observed.

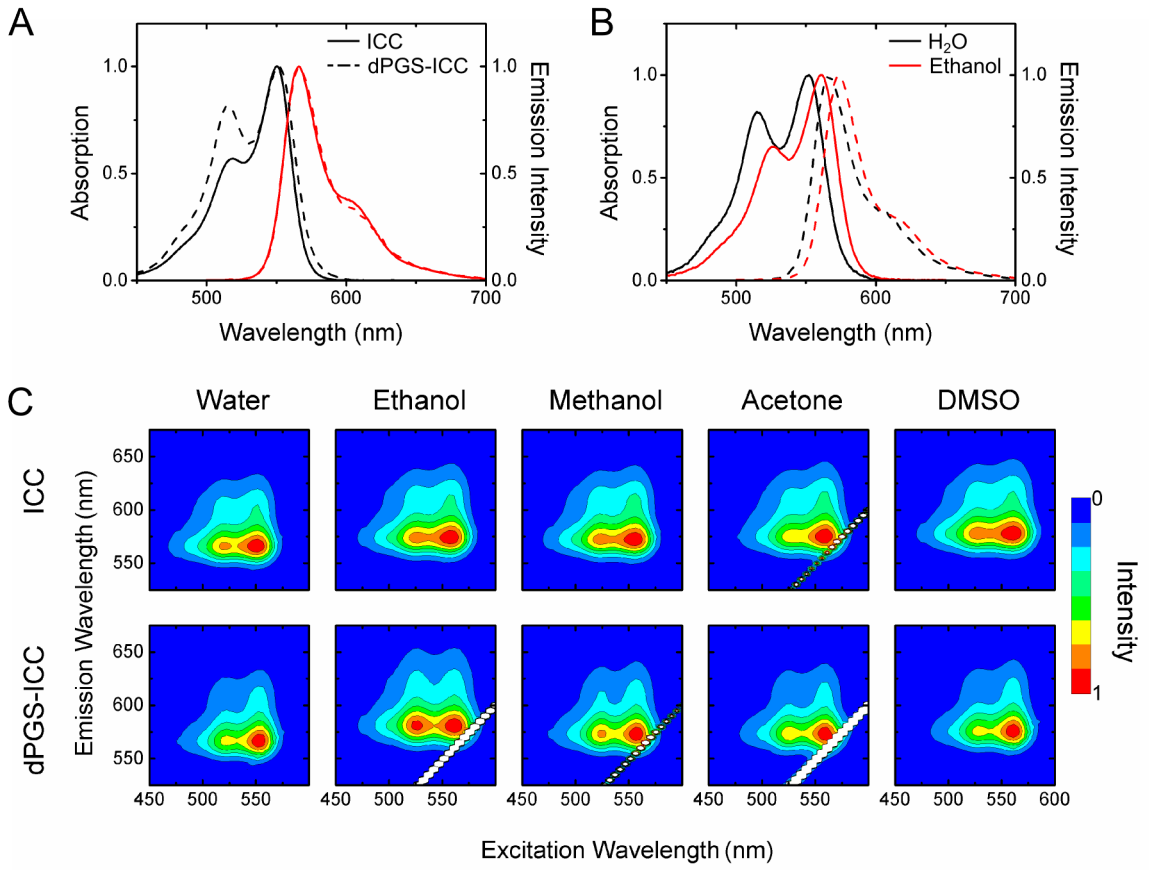

Figure 5.5. Spectroscopic characterization of dPGS-ICC. (A) Comparison of the normalized absorption (black) and normalized emission (red) spectra of ICC (solid) and dPGS-ICC (dash) in H_2O. Emission spectra are shown recorded at an excitation wavelength of 490 nm. (B) Comparison of the normalized absorption (solid) and normalized emission (dash) spectra of dPGS-ICC in H_2O (black) and in ethanol (red). (C) Excitation-emission scans for ICC and dPGS-ICC in various solvents. Emission peak intensities were normalized to 1.

Table 5.1. Wavelength of maximum absorption ($\lambda_{\max}^{\text{abs}}$) and emission ($\lambda_{\max}^{\text{em}}$) for ICC and dPGS-ICC in different solvent environments. The error was ±2 nm for absorption and emission wavelengths.

			ICC		dPGS-ICC	
solvent	property	dielectric constant	λ_{max}^{abs} (nm)	λ_{max}^{em} (nm)	λ_{max}^{abs} (nm)	λ_{max}^{em} (nm)
H_2O	protic	80	550	566	552	566
Methanol	protic	34	556	572	557	573
Ethanol	protic	24	556	574	561	575
Acetone	aprotic	21	559	575	560	574
DMSO	aprotic	44	560	577	563	575

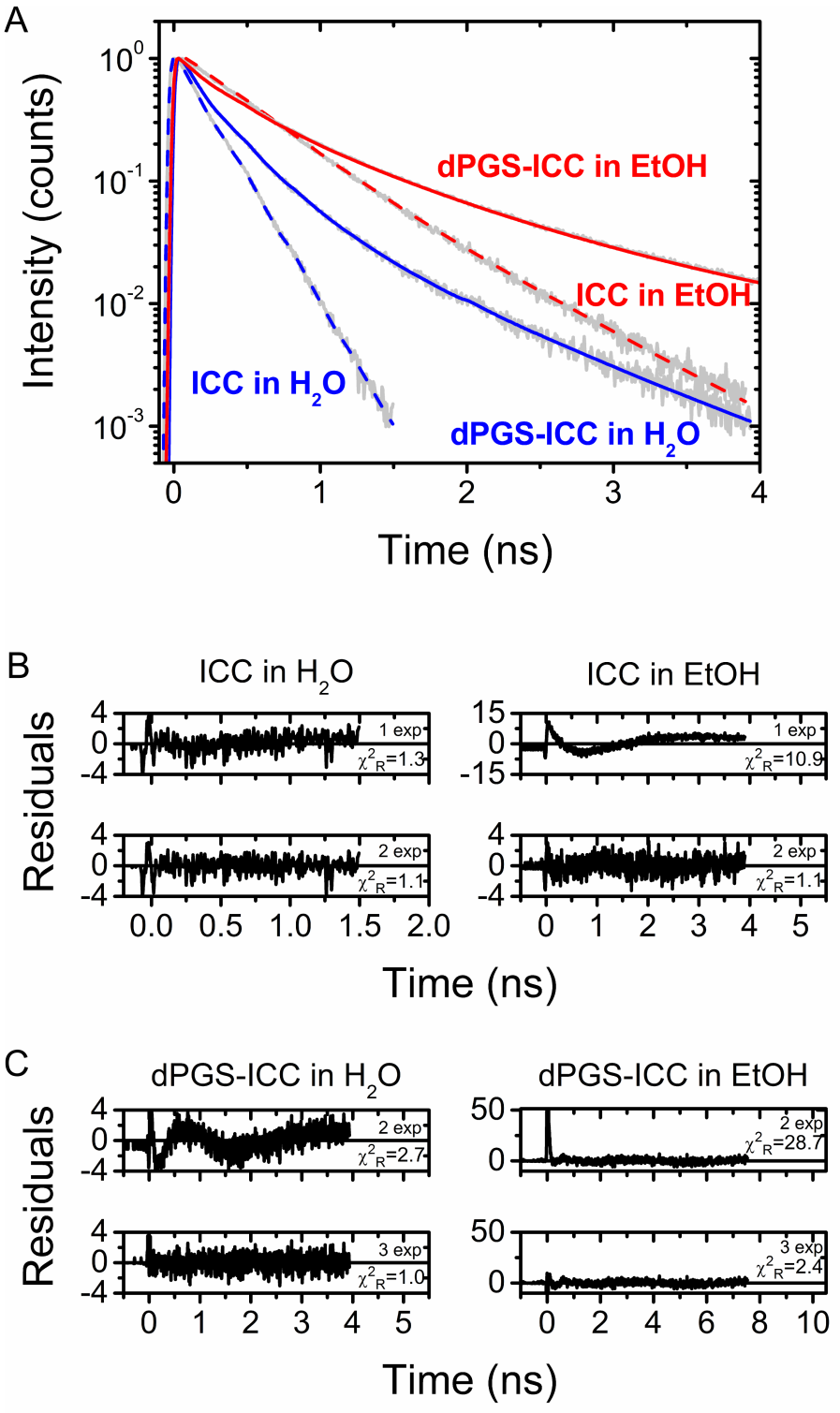

Figure 5.6. Fluorescence lifetime decay curves of ICC and of dPGS-ICC in H2O (blue) and in ethanol (red) at 20 °C. Original data traces are shown in gray, with the respective fit curve overlaid. (B,C) Comparison of the residuals and the χ^2_R for (B) exponential fits with either one or two decay components for ICC in H_2O and in ethanol and (C) for exponential fits with either two or three decay components for dPGS-ICC in H_2O and in ethanol.

It can be seen that the different environments affect the fluorescence lifetime of ICC. A short fluorescence lifetime (τ_1) of 0.18 ns was found for ICC in aqueous solution, with a very small contribution of a 0.3 ns component (τ_2, 2 %). Changing the solvent to ethanol causes a change in the fastest fluorescence lifetime component of ICC from 0.18 ns in water to 0.36 ns. Further, the contribution of the slower decay component (τ_2) is strongly increased (from 2 % to 32 %), while the lifetime is also increased to 0.68 ns. For dPGS-ICC in aqueous solution the local dye environment gives rise to three fluorescence decay components of 0.16 ns, 0.4 ns, and 0.9 ns. The fastest two decay components (τ_1, τ_2) compare to the lifetimes of ICC found in H_2O, though the relative amplitudes are shifted in favor of the second lifetime component. The additional slow decay component (τ_3) of 0.9 ns was absent for ICC in water and is probably caused by the linkage of ICC to the dPGS matrix. The existence of a longer lifetime decay component for ICC has been reported to occur when the rotation around the polymethine linker of ICC is hindered [Chibisov et al., 1995]. When dPGS-ICC resides in ethanol, a less polar environment, the fluorescence decay is also characterized by three fluorescence decay components, though all are slower than for dPGS in water. The relative amplitude of the second lifetime component is increased, while that of the fastest lifetime component is decreased (Table 5.2). A pronounced shift of 1.54 ns is observed for the slowest decay component (τ_3) of dPGS-ICC in ethanol compared to dPGS-ICC in water, hinting at increased interactions of ICC with the dPGS matrix in ethanol.

Table 5.2. Fluorescence lifetime parameters of ICC and dPGS-ICC complex. Fluorescence decay times τ_i, the respective amplitudes α_i as relative values and the reduced χ^2_R are given. Errors were obtained from exhaustive error analysis for 1σ.

sample	τ_1 (ns)	α_1 (%)	τ_2 (ns)	α_2 (%)	τ_3 (ns)	α_3 (%)	χ^2_R
ICC in H_2O	$0.18\ ^{+0.01}_{-0.01}$	$98\ ^{+1}_{-1}$	$0.31\ ^{+0.06}_{-0.04}$	$2\ ^{+4}_{-1}$	–	–	1.1
ICC in ethanol	$0.36\ ^{+0.01}_{-0.01}$	$68\ ^{+1}_{-1}$	$0.68\ ^{+0.01}_{-0.01}$	$32\ ^{+1}_{-1}$	–	–	1.1
dPGS-ICC in H_2O	$0.16\ ^{+0.01}_{-0.01}$	$69\ ^{+3}_{-3}$	$0.36\ ^{+0.03}_{-0.05}$	$26\ ^{+4}_{-5}$	$0.91\ ^{+0.03}_{-0.04}$	$5\ ^{+0.2}_{-0.1}$	1.0
dPGS-ICC in ethanol	$0.25\ ^{+0.01}_{-0.01}$	$54\ ^{+1}_{-1}$	$0.78\ ^{+0.01}_{-0.01}$	$41\ ^{+1}_{-1}$	$2.44\ ^{+0.01}_{-0.01}$	$5\ ^{+1}_{-1}$	2.4

Size of dPGS-ICC as a function of temperature

First, time-resolved fluorescence anisotropy measurements were conducted to further characterize the dPGS-ICC nanocarrier. Using time-resolved fluorescence anisotropy insights have been gained into structural changes and conformational dynamics of biomolecules, e.g. proteins [Alexiev and Farrens, 2014, Alexiev et al., 2003, Kim et al., 2009a, Kim et al., 2012, Kim et al., 2007], but also for other macromolecules such as polymer nanoparticles [Chee et al., 2006, Chee et al., 2011]. Information on the size, via the rotational diffusion of the molecule, as well as segmental dynamics and steric restriction of motions can be obtained. Here, the temperature dependence of the parameters describing the anisotropy decay behavior of ICC and dPGS-ICC was investigated.

The anisotropy decay of ICC was characterized very well by a single rotational correlation time (Figure 5.7A). The rotational correlation time is plotted against the ratio of temperature and viscosity in a Perrin plot (Figure 5.7B). The temperature dependence is linear over the whole temperature range (5 °C–55 °C). According to the Perrin equation ($\phi = \eta V / k_B T$), the slope of a linear fit to the data is equal to the hydrodynamic volume from which the hydrodynamic diameter of the sample can be inferred. Here, the slope was equal to a volume of 4.9 nm^3, which correspond to a hydrodynamic diameter of 2.0 nm (Table 5.3).

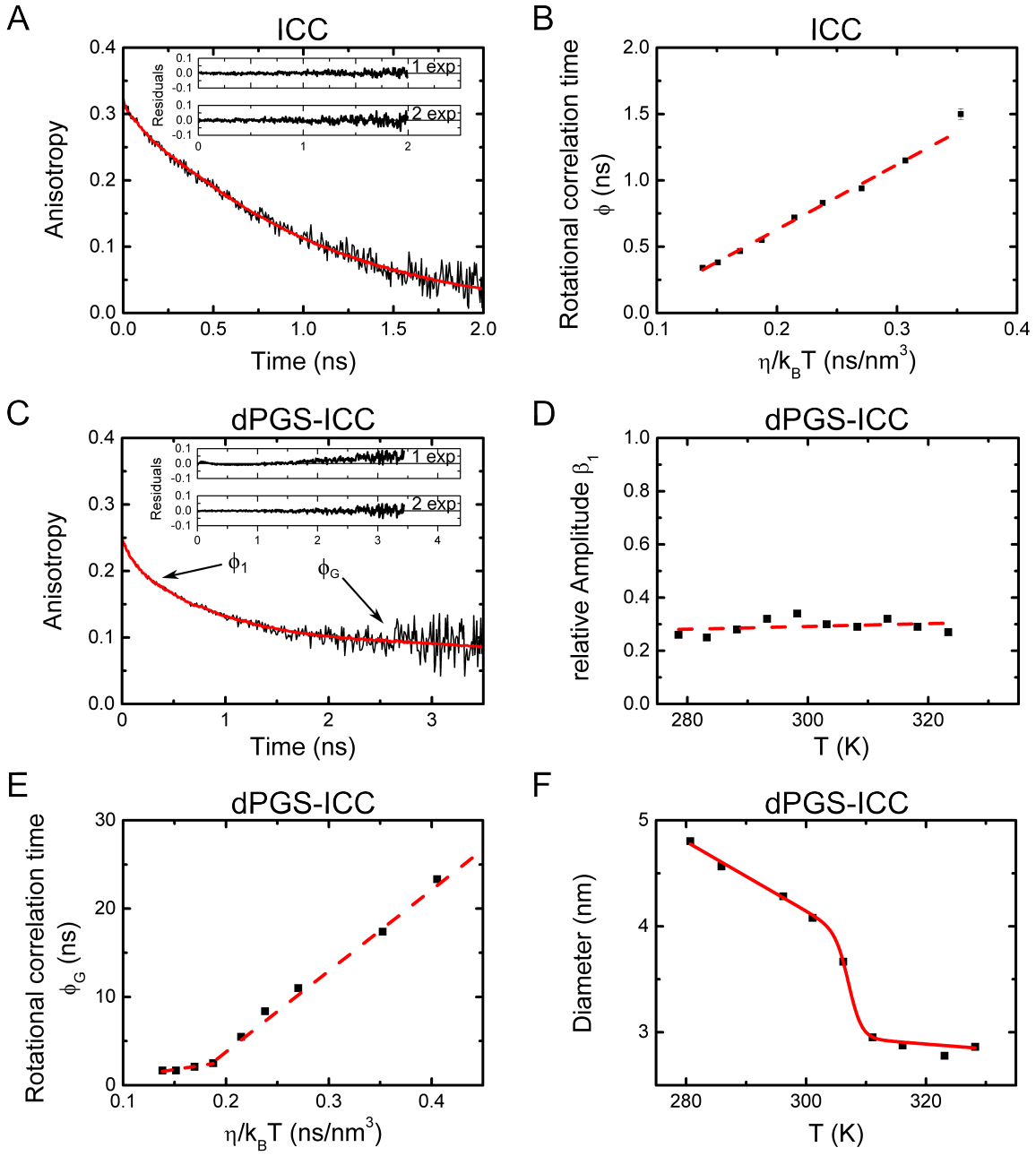

Figure 5.7. Analysis of the anisotropy decay curves for ICC and dPGS-ICC . (A) Anisotropy decay curve of ICC in H2O/ethanol (1:1) at 20 °C. The fit curve is shown in red and the original data in black. The residuals of the fits with one (1 exp; χ^2_R=0.94) and two rotational correlation times (2 exp; χ^2_R=0.94) are shown in the inset. (B) Perrin plot for the rotational correlation time of ICC obtained from anisotropy measurements in the temperature range between 5 °C and 55 °C . The dashed red line indicates the linear behavior of the rotational correlation time. (C) Anisotropy decay curve of dPGS-ICC in H2O/ethanol (1:1) at 20 °C. The fit curve is shown in red and the original data in black. The fast rotational correlation time, ϕ_1, and the slow rotational correlation time, ϕ_G, are indicated. The residuals of fits with one (1 exp; χ^2_R=2.9) or two rotational correlation times (2 exp; χ^2_R=1.4)are shown in the inset. (D) Temperature dependence of the relative amplitude β_1 of the fast rotational correlation time ϕ_1. (E) Perrin plot for ϕ_G of dPGS-ICC in H_2O/ethanol. Temperature regimes with different temperature dependences are evident. The dashed red lines indicate the slope of the data points below and above 30 °C. (F) The diameter for dPGS-ICC nanocarrier calculated from ϕ_G according to $d = \sqrt[3]{6k_BT\phi_G/(\pi\eta)}$ is plotted against the temperature. The solid red line shows the fit with the two state transition model.

For the anisotropy decay curve of dPGS-ICC a fit with a single rotational correlation time was not sufficient to describe the data (Figure 5.7C). The analysis of the χ^2_R and residuals clearly shows that the anisotropy decay is best described using two rotational correlation times. These can be assigned to the rotational motion of the linked ICC dye (fast rotational correlation time, ϕ_1) and the dPGS rotation itself (slow rotational correlation time, ϕ_G). For the anisotropy of dPGS-ICC at 20 °C the two decay components were found to be: $\phi_1 = 0.5$ ns and $\phi_G = 11.0$ ns.

The Perrin plot of ϕ_G for dPGS-ICC did not display a linear dependence of ϕ_G on temperature (Figure 5.7E), but two distinct regions could be identified. A change in the slope occurs at around 33 °C. A much smaller value of the slope was determined for temperatures above 33 °C than for temperatures below 33 °C. Since the slope reflects the volume of dPGS-ICC, it follows that the volume of dPGS-ICC, and hence also the diameter, is reduced above 33 °C. Below 33 °C a hydrodynamic volume of 89.5 nm^3 was derived from the slope, corresponding to a diameter of 5.5 nm for dPGS-ICC (Table 5.3). For temperatures above 33 °C the volume is reduced to 17.9 nm^3, from which the diameter of dPGS-ICC was calculated to be 3.2 nm (Table 5.3).

As the data for the slowest rotational correlation showed a non linear behavior in the Perrin plot, the respective hydrodynamic diameter was also calculated for each temperature from ϕ_G using the relationship $V = k_B T \phi_G / \eta$, directly relating ϕ_G with the volume (V) of the rotator under the assumption of a sphere-like shape of dPGS. The thus obtained diameter values were plotted against the temperature (Figure 5.7F) and a two-state transition is evident. Upon increasing the temperature the initial size of around 4 nm to 5 nm shrinks drastically at a temperature of 33 °C. For temperatures above 33 °C, the size is reduced to roughly 3 nm (Table 5.3). The transition temperature T_c obtained from fitting the data with the two-state transition model was 34.1 °C ± 0.3 °C. The size of dPGS for temperatures below the transition temperature is in accordance with published values [Weinhart et al., 2011b]. To check whether the observed size change of dPGS-ICC has an effect on the conformational space of ICC bound to the surface of dPGS, the temperature dependence of the relative amplitude β_1 was analyzed. No temperature dependency was observed for β_1 (Figure 5.7D), indicating that the shrinkage of dPGS does not affect the conformational space of ICC.

Table 5.3. Hydrodynamic volume (V_H) and diameter (d) of ICC and dPGS-ICC as determined from fluorescence anisotropy measurements by Perrin plots analysis and from the directly calculated diameter.

		Perrin Plot		mean diameter
sample		V_H (nm^3)	d (nm)	d (nm)
ICC		4.9 ± 0.1	2.0 ± 0.1	
dPGS-ICC	below 33 °C	89.5 ± 3.9	5.5 ± 0.1	4.4 ± 0.3
	above 33 °C	17.9 ± 3.4	3.2 ± 0.2	2.9 ± 0.1

5.2.2 Physicochemical characterization of a core-multishell nanocarrier

Drug loading and release properties of nanocarriers are important for their biomedical application and can depend on the environment of the nanocarrier. Here, fluorescence spectroscopy, lifetime and anisotropy measurements were performed to investigate the physiochemical properties of drug loaded CMS nanocarriers and their response to changes in the environment. The CMS nanocarriers were loaded with the fluorescent drug mimetic Nile Red (CMS/NR), which is able to mimic small hydrophobic drug molecules. For comparison, the core of the CMS nanocarriers was also labeled with the dye ICC (CMS-ICC). The results presented here have been published [Boreham et al., 2014b].

Spectroscopic characterization of CMS-ICC and CMS/NR

The spectral properties of the dyes and nanocarrier-dye constructs were characterized by absorption and fluorescence spectroscopy (Figure 5.8). The dye ICC in H_2O has an absorption maximum (λ_{max}^{abs}) at 550 nm and an emission maximum (λ_{max}^{em}) at 566 nm (Figure 5.8A). Covalent linkage of the dye ICC to the dPG core of the CMS nanocarrier shifts the absorption and emission maxima in H_2O to longer wavelengths: to 557 nm for λ_{max}^{abs} and to 574 nm for λ_{max}^{em} (Figure 5.8A).

The dye NR exhibits an absorption maximum at 549 nm and an emission maximum at 628 nm in ethanol (Figure 5.8B). Both the absorption and the fluorescence emission of CMS/NR in ethanol are red shifted compared to NR in ethanol. The CMS/NR absorption peak is at 556 nm and the emission maximum is shifted to 633 nm. The observed spectral shifts upon incorporation of the respective dye, ICC or NR, into the CMS nanocarrier show that the spectral properties of the dye are directly influenced by the incorporation into the CMS nanocarrier.

In order to gain further insights into the surroundings that ICC and NR experience within the CMS architecture, their spectroscopic properties in different solvents were investigated. Fluorescence emission spectra were recorded over a range of excitation wavelengths (excitation-emission scans). The dye ICC shows red shifted absorption and emission spectra when going from polar to more apolar solvents (Figure 5.9), indicating a n-π^* electron transition. When comparing the λ_{max}-values obtained for measurements of free ICC and CMS-ICC in H_2O a red shift was observed. The λ_{max}-values of CMS-ICC are similar to those found for free ICC in ethanol or methanol (Table 5.4 and Figure 5.9). In contrast to ICC, the dye NR shows a

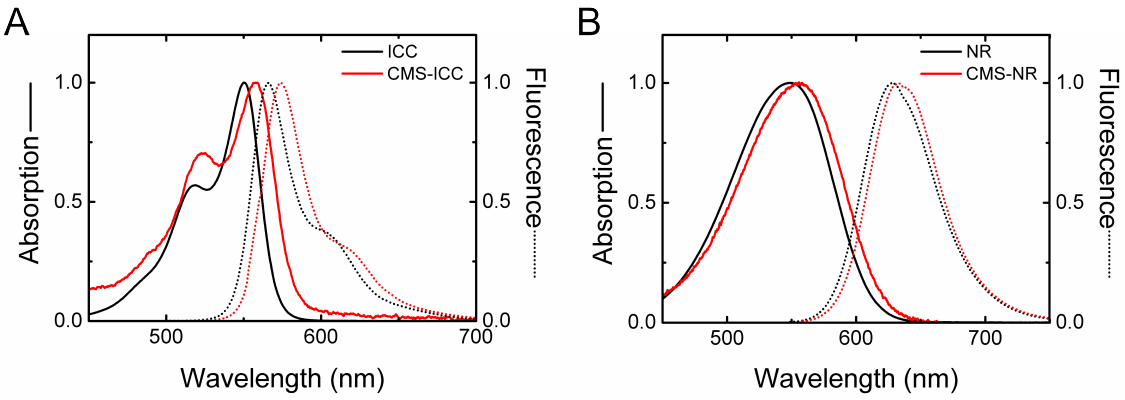

Figure 5.8. Spectral characterization of CMS nanocarrier dye constructs (A) Normalized absorption (solid line) and emission (dotted line) spectra for ICC (black) and CMS-ICC (red) in H_2O. (B) Normalized absorption (solid line) and emission (dotted line) spectra for NR (black) and CMS/NR (red) in ethanol. Conditions as described in 3.2.2.

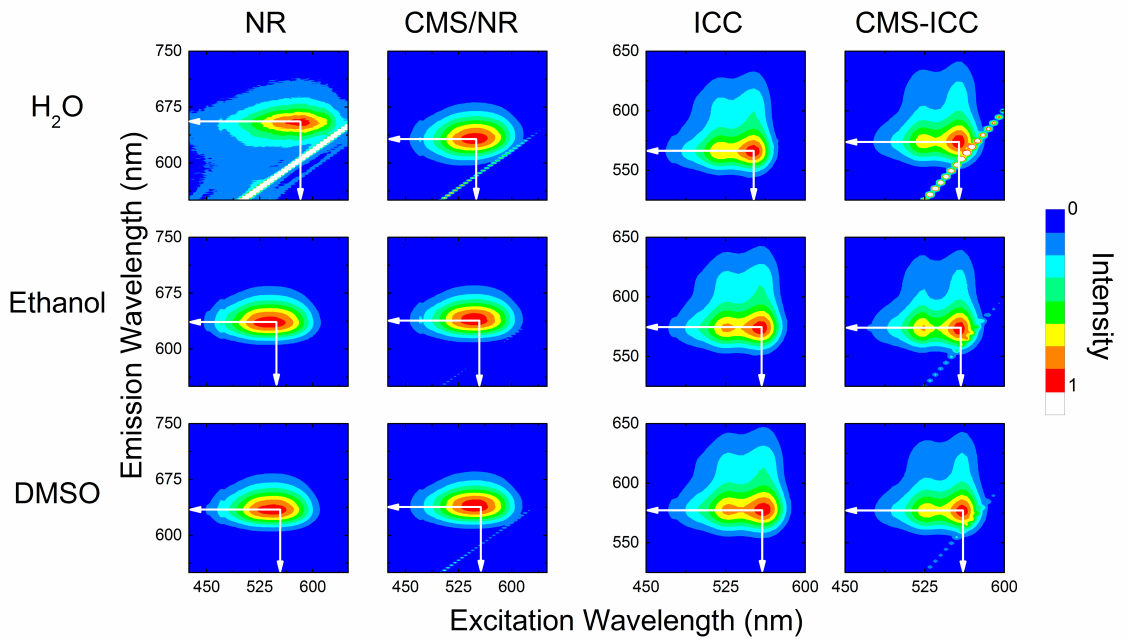

Figure 5.9. Fluorescence excitation-emission scans of NR and ICC as well as CMS/NR and CMS-ICC in different solvents at 20 °C. H_2O (top row); ethanol (middle row); DMSO (bottom row). Conditions as described in 3.2.2. Reprinted with permission from [Boreham et al., 2014b]. Copyright 2014 American Chemical Society.

Table 5.4. Wavelength of maximum absorption (λ_{max}^{abs}) and emission (λ_{max}^{em}) for both dyes and nanocarrier-dye constructs in different solvent environments. The error was ±2 nm for absorption and emission wavelengths. The E_T30 value is given as a measure of the solvents polarity [Reichardt, 1979].

		NR		CMS/NR		ICC		CMS-ICC	
solvent	E_T30 (kcal mol^{-1})	λ_{max}^{abs} (nm)	λ_{max}^{em} (nm)	λ_{max}^{abs} (nm)	λ_{max}^{em} (nm)	λ_{max}^{abs} (nm)	λ_{max}^{em} (nm)	λ_{max}^{abs} (nm)	λ_{max}^{em} (nm)
H_2O	63.1	582	657	557	625	550	566	557	574
Methanol	55.5	552	632	559	638	556	572	557	571
Ethanol	51.9	549	628	556	633	556	574	559	574
Acetone	42.2	534	611	543	626	559	575	561	577
DMSO	45.0	550	627	557	634	560	577	562	577

pronounced blue shift in absorption and emission maxima when going from a polar solvent, e.g. H_2O, to a more apolar solvent (Figure 5.9 and Table 5.4). This indicates that NR undergoes a $\pi - \pi^*$ transition.

Interestingly, when directly comparing the absorption and emission spectra of NR and CMS/NR in aqueous solution a similar blue shift is visible, indicating that NR within the CMS nanocarrier is in a more apolar environment than H_2O. Based on a comparison of the emission maxima measured for CMS/NR in water and NR in the different solvents, this environment is comparable to a solvent such as ethanol in terms of polarity. Also, the strong blue shift observed for CMS/NR in H_2O compared to NR in H_2O indicates that the NR molecules are not in direct contact with the aqueous solvent. When further comparing CMS/NR in H_2O with CMS/NR in more apolar solvents, a red shift of the maximum wavelengths of both the absorption and emission maximum is discernible. Hence, the NR molecules within the CMS nanocarriers are sensitive to changes in the external solvent.

Partitioning of NR in CMS nanocarriers

Next, the higher sensitivity of the fluorescence lifetime was used to investigate the origin of the solvent sensitivity of NR in CMS/NR. While ICC is known to be bound to the dendritic polyglcyerol core of CMS nanocarriers, the location of NR within the hydrophilic and hydrophobic shells is not clearly defined. The NR lifetimes in different solvents were compared to CMS/NR to gain a further understanding of the NR environment within CMS nanocarriers.

Fluorescence lifetime decay curves were measured and analyzed using the fitting procedure (see 5.1.2) with one, two and three exponential components. The quality of the fit was then evaluated taking both the residuals and the χ^2_R into consideration (as described in 5.1.2). Such an analysis of the fluorescence decay curves is shown in Figure 5.10.

NR, but also ICC, clearly displayed different lifetime decays when incorporated into the CMS nanocarrier (Figure 5.10 and Figure 5.11). The fluorescence lifetime decay of NR was found to be solvent dependent (Figure 5.11B), with a lifetime of NR in an ethanol/H_2O mixture of 1.85 ns, while a lifetime of 3.66 ns and 4.12 ns was found in pure ethanol and in DMSO respectivly (Table 5.5). Incorporation of NR into the CMS nanocarrier gave rise to a fluorescence lifetime decay best described with multiple lifetime decay components. In aqueous solution

Table 5.5. Fluorescence lifetime parameters of dyes and dye nanocarrier complexes. Fluorescence decay times τ_i, the respective amplitudes α_i as relative values and the reduced χ^2_R are given. Errors were obtained from exhaustive error analysis for 1σ.

sample	τ_1 (ns)	α_1 (%)	τ_2 (ns)	α_2 (%)	τ_3 (ns)	α_3 (%)	χ^2_R
ICC in H_2O	$0.18\ ^{+0.01}_{-0.01}$	$98\ ^{+1}_{-1}$	$0.31\ ^{+0.06}_{-0.04}$	$2\ ^{+4}_{-1}$	–	–	1.1
ICC in EtOH/H_2O	$0.16\ ^{+0.01}_{-0.02}$	$10\ ^{+1}_{-1}$	$0.50\ ^{+0.01}_{-0.01}$	$90\ ^{+1}_{-1}$	–	–	1.1
CMS-ICC in H_2O	$0.16\ ^{+0.02}_{-0.01}$	$61\ ^{+1}_{-1}$	$0.52\ ^{+0.01}_{-0.02}$	$33\ ^{+1}_{-1}$	$1.40\ ^{+0.01}_{-0.05}$	$6\ ^{+1}_{-1}$	1.1
NR in EtOH/H_2O	–	–	$1.85\ ^{+0.01}_{-0.01}$	100	–	–	1.1
NR in DMSO	–	–	–	–	$4.12\ ^{+0.01}_{-0.01}$	100	1.0
NR in EtOH	–	–	–	–	$3.66\ ^{+0.01}_{-0.01}$	100	1.0
CMS/NR in H_2O	$0.37\ ^{+0.05}_{-0.04}$	$16\ ^{+1}_{-1}$	$1.77\ ^{+0.28}_{-0.22}$	$19\ ^{+1}_{-1}$	$4.38\ ^{+0.09}_{-0.01}$	$65\ ^{+1}_{-2}$	1.0
CMS/NR in EtOH/H_2O	–	–	$1.68\ ^{+0.01}_{-0.02}$	$87\ ^{+1}_{-1}$	$3.51\ ^{+0.06}_{-0.06}$	$13\ ^{+1}_{-1}$	1.0

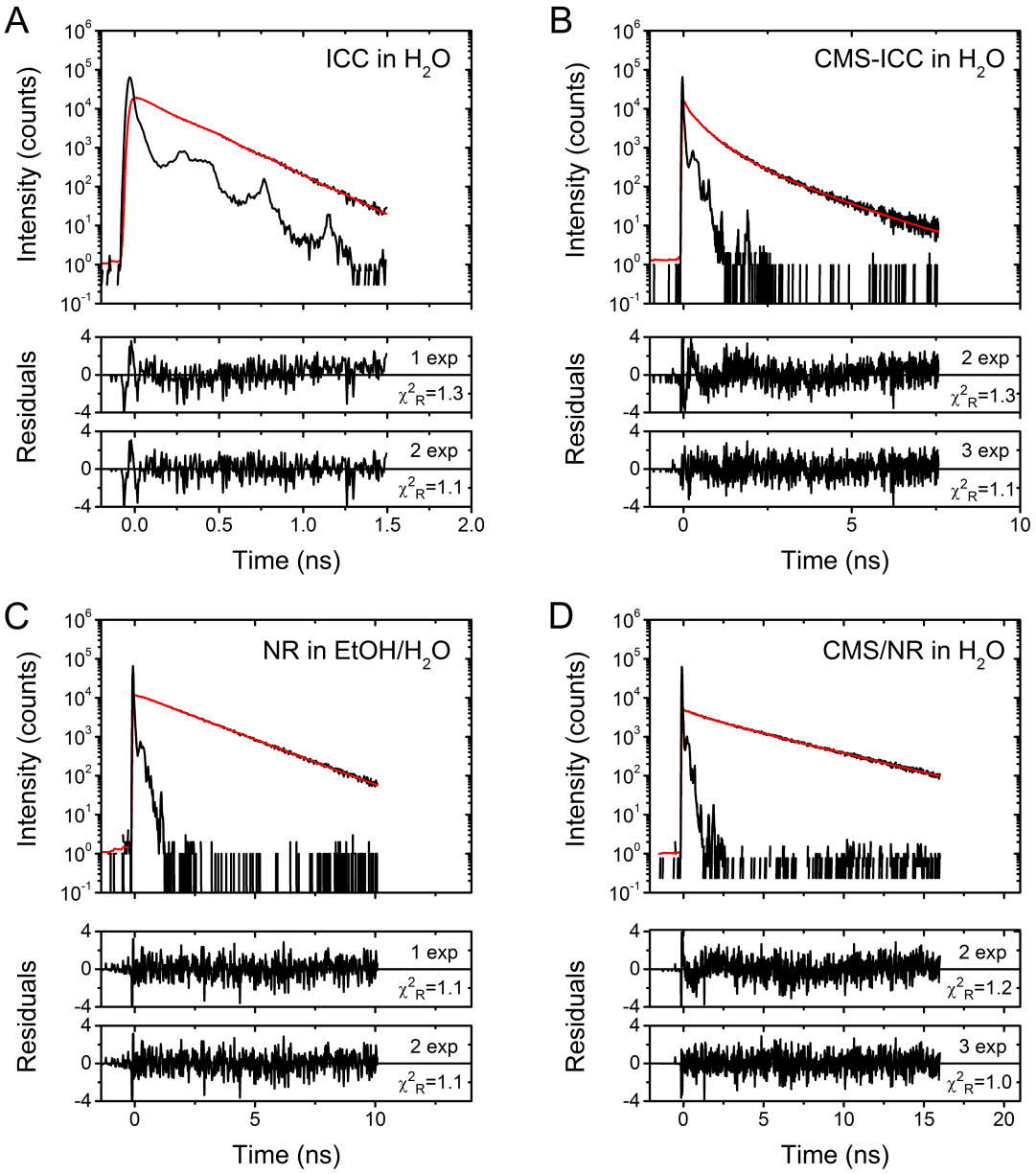

Figure 5.10. Analysis of the lifetimes decay curves of dyes and dye CMS nanocarrier constructs. Original data traces are shown in black, with the respective fit curve overlaid in red. The IRF is also shown. The residuals and the χ^2_R for exponential fits with the indicated number of decay components are shown below the lifetime decay curves (A) Fluorescence lifetime trace of ICC in H_2O and the resulting fit curve for two decay components. (B) Fluorescence lifetime trace of CMS-ICC in H_2O and the resulting fit curve for three decay components. (C) Fluorescence lifetime trace of NR in EtOH/H_2O and the resulting fit curve for one decay component. (D) Fluorescence lifetime trace of CMS-NR in H_2O and the resulting fit curve for three decay components. Conditions as described in 3.2.2.

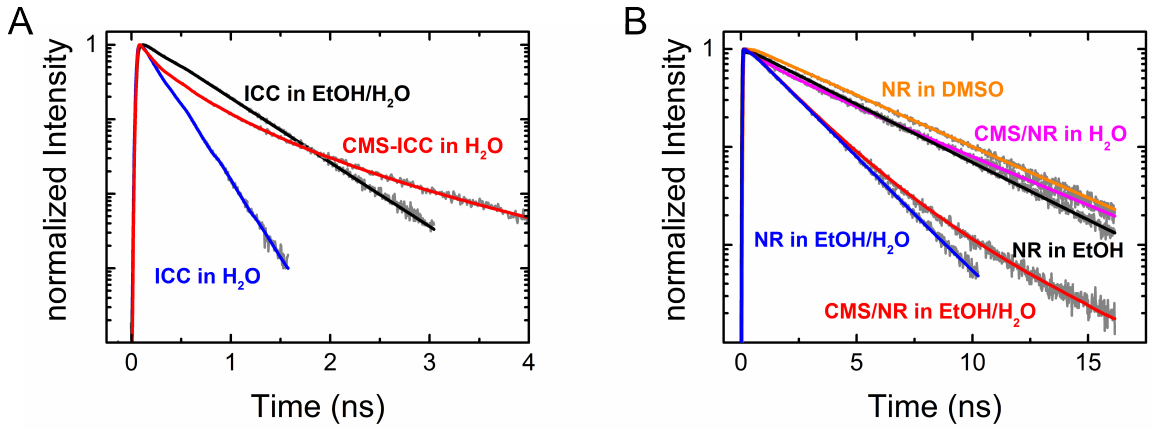

Figure 5.11. Normalized fluorescence lifetime decay curves of dyes and dye CMS nanocarrier complexes in different solvents. Fluorescence decay curves are depicted in dark gray, the colored lines are the respective fit curves.(A) Fluorescence lifetime traces of ICC and CMS-ICC. (B) Fluorescence lifetime traces of NR and CMS/NR in different solvents. Conditions as described in 3.2.2, EtOH/H_2O mixture: 1:1, T=20 °C.

three lifetimes were required to fit the data. These were determined to be 0.37 ns, 1.77 ns and 4.38 ns (Table 5.5). The fast lifetime decay component is absent when CMS/NR is dissolved in an ethanol/H_2O mixture. Here, two lifetimes of 1.68 ns and 3.51 ns were observed. These two lifetimes are similar to the lifetimes seen for NR in an ethanol/H_2O mixture (1.85 ns) and in pure ethanol (3.66 ns). The slow lifetime seen for CMS/NR in aqueous solution is even slower than that observed for NR in DMSO (4.38 ns vs. 4.12 ns), while the intermediate lifetime is similar to NR in an ethanol/H_2O mixture. The fast lifetime component (0.37 ns) was not observed for NR in any solvent studied. The comparison of the lifetimes of NR and CMS/NR in different solvents, suggest that the multiple decay components observed for CMS/NR are a superposition of the lifetimes of NR in different environments. This would mean that NR is distributed within the multishell architecture of the CMS nanocarrier.

A recent study by Fleige et al. [Fleige et al., 2012] compared the spectral position of the NR absorption maximum in pure mPEG/water mixtures and in the CMS/NR nanocarrier and based on the results it was proposed that NR resides in the outer shell of the CMS nanocarrier structure (Figure 5.2). The analysis of the fluorescence lifetimes, described above, indicated a distribution of NR within CMS nanocarriers. To compare the fluorescence lifetimes with different outer shell regions, the fluorescence lifetime decay of NR in mPEG/water mixtures was determined and compared to the lifetimes observed for NR and CMS/NR in different solvents.

The fluorescence lifetime decay of NR is clearly dependent on the water content of the mPEG/water mixture (Figure 5.12A). With increasing water content a faster fluorescence decay was observed. At high water content (50 %,70 %) only one lifetime decay component was found, while at water contents of 20 % and below a second fast lifetime decay component is apparent. The lifetimes were 0.3 ns and 4.1 ns in 100 % mPEG, and with 70 % water content a single lifetime of 1.6 ns was determined. The lifetimes for all mPEG/water mixtures were plotted against the relative mPEG content (Figure 5.12B) and a clear linear dependence is seen for the slower lifetime.

Interestingly, a similar lifetime to the 1.6 ns lifetime of NR at 70 % water content was also observed for NR in ethanol/water and also for CMS/NR in aqueous solution as well as for CMS/NR in ethanol/water. Further, the lifetimes of 0.3 ns and 4.1 ns seen for NR in pure (100 %) mPEG both feature in the fluorescence lifetime decay of CMS/NR in aqueous solution. This suggests that NR is located, on the one hand, in a water devoid region of the CMS nanocarrier,

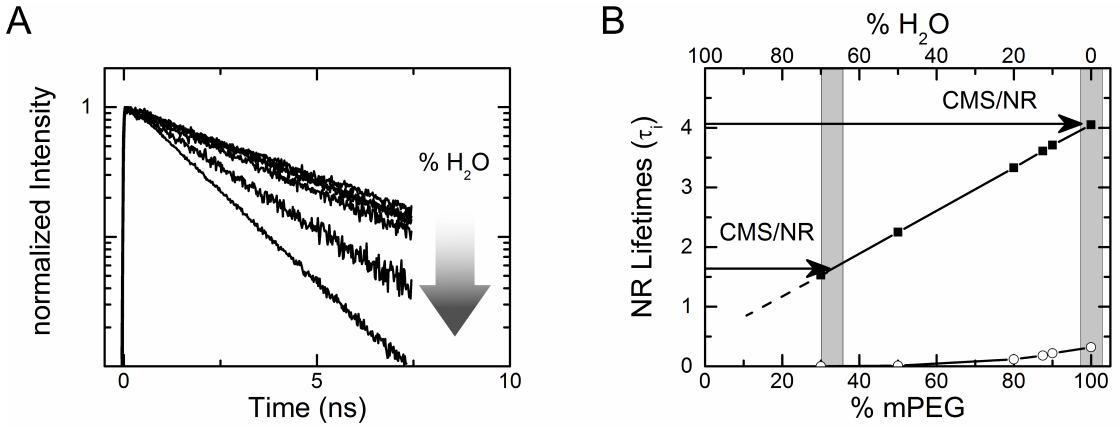

Figure 5.12. Fluorescence lifetime decay analysis of NR dissolved in different mPEG/water mixtures. (A) NR lifetime curves for six different mPEG/water solutions (0 %, 10 %, 12.5 %, 20 %, 50 %, 70 % H_2O). The arrow indicates an increase in water concentration. (B) The fluorescence decay times of NR are plotted as a function of the water content in the mPEG/water solution. Arrows and the gray bars represent the NR fluorescence decay times found in the CMS/NR nanocarrier (∼1.7 ns and ∼4.1 ns). The mean error for the fast lifetime component was ±0.02 ns, and ±0.01 ns for the slow lifetime component, as determined from exhaustive error analysis for 1σ.

and on the other hand in a region comparable to a mPEG/water mixture with a water content of 70 %. The former could well be the region of the mPEG chains furthest away from the nanocarrier surface or even the hydrophobic chain region, while the latter could correspond to a region close to the nanocarrier surface, possibly even the interface with the aqueous solvent.

As the fluorescence lifetime data implicate NR partitioning into different environments within the CMS nanocarrier structure, the amplitude of the respective lifetimes should give insight into the relative distribution of NR within the CMS nanocarrier. The largest amplitude for CMS/NR dissolved in water was associated with the slowest lifetime (4.4 ns), indicating most NR molecules to be in a water devoid region. In contrast, for CMS/NR dissolved in an ethanol/water mixture, the faster lifetime of 1.7 ns has the largest amplitude and most NR molecules should therefore reside in a mPEG region with high water content. This implicates that the partitioning of the NR molecules within the CMS nanocarrier is solvent dependent and that less polar solvents than water induce a shift of NR towards the interface between the CMS nanocarrier and the solvent. These results agree with those obtained from the absorption and emission spectra analysis.

Size of CMS nanocarriers

Time-resolved fluorescence anisotropy measurements can give insight into nanosecond dynamics of the nanocarrier structure and the overall nanocarrier size via rotational dynamics of the dye. Here, the temperature dependence of the rotational dynamics of the dyes was analyzed to detect possible temperature induced changes to the nanocarrier structure that could effect the drug release properties. A characteristic anisotropy decay curve of CMS/NR in aqueous solution at 20 °C is shown in Figure 5.13A. The rotational correlation times were determined to be 0.16 ns, 1.8 ns and 52 ns at 20 °C (Table 5.6). The number of rotational correlation times was not influenced by the temperature.

The size of a particle can be calculated from the slowest rotational correlation time (indicated by ϕ_G in Figure 5.13A) according to $\phi_G = \eta V / k_B T$. The values of the slowest rotational correlation time obtained for temperatures in the range of 5 °C and 55 °C were plotted in a Perrin Plot (Figure 5.13B), i.e. against $\eta / k_B T$. The hydrodynamic volume can then be obtained from the slope of a linear fit to the data, assuming a sphere-like shape of the nanoparticle, and

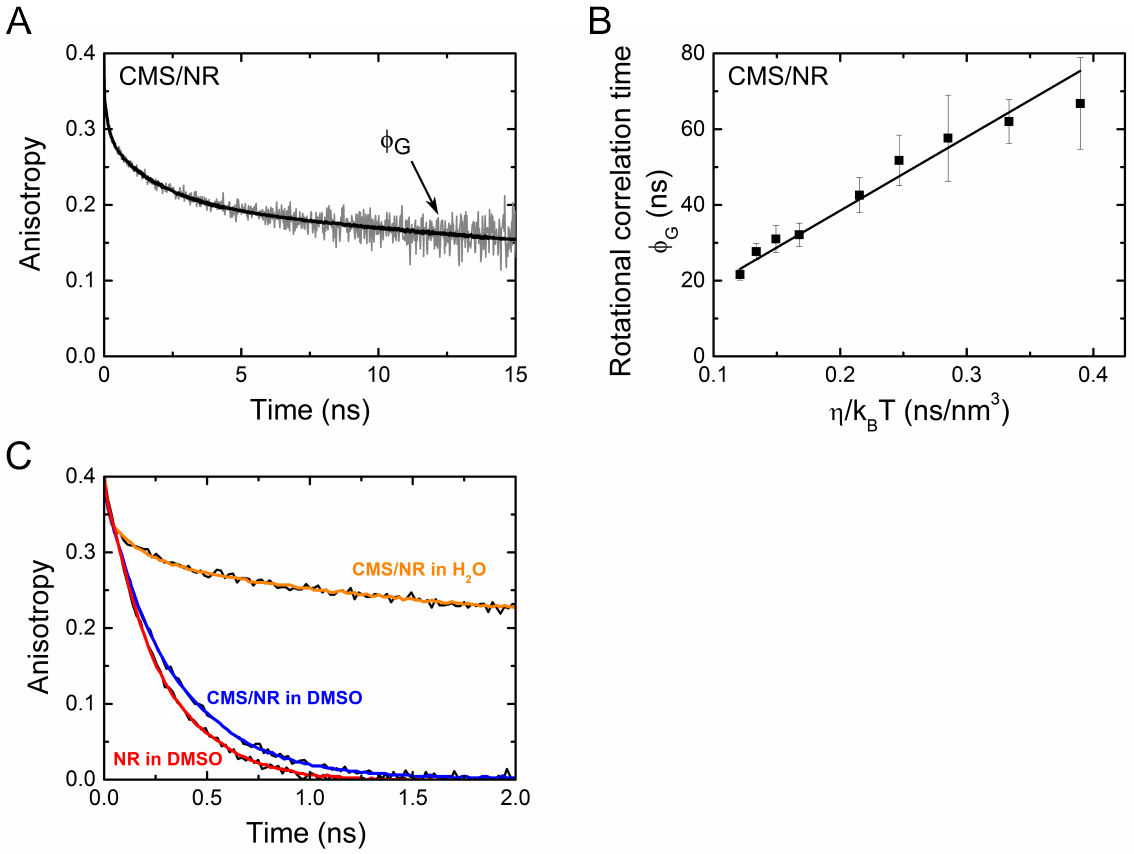

Figure 5.13. Anisotropy decay (r(t)) curves and Perrin plot of CMS/NR . (A) Anisotropy curve for CMS/NR in H_2O at 20 °C. Fit curve is shown on top of raw data. ϕ_G denotes the slowest rotational correlation time. (B) ϕ_G values from anisotropy measurements in the temperature range between 5 °C and 55 °C are plotted against the ratio of viscosity and temperature (Perrin plot) for CMS/NR nanocarrier in H_2O. The volume, and hence the diameter, can be deduced from the slope of the linear fit (black line). Error bars were calculated from exhaustive error analysis for 1σ and the linear fit was performed with instrumental weight of the errors. (C) Anisotropy decay (r(t)) curves of NR in DMSO (red) and CMS/NR nanocarrier in DMSO (blue) as well as in H_2O (orange). Fit curves are color coded. Conditions as described in 3.2.2.

Table 5.6. Fluorescence anisotropy decay parameters for NR (in DMSO) and CMS/NR nanocarrier (in DMSO and H_2O). Errors were obtained from the exhaustive error analysis for 1σ.

sample	ϕ_1 (ns)	β_1 (%)	$\phi_2(ns)$	β_2 (%)	ϕ_3 (ns)	β_3 (%)	χ^2_R
CMS/NR in H_2O	$0.16 \pm^{0.01}_{0.01}$	$16 \pm^{1}_{1}$	$1.8 \pm^{0.3}_{0.2}$	$24 \pm^{1}_{1}$	$52 \pm^{7}_{5}$	$60 \pm^{1}_{2}$	1.1
CMS/NR in DMSO	$0.30 \pm^{0.01}_{0.01}$	100	–	–	–	–	1.0
NR in DMSO	$0.25 \pm^{0.01}_{0.01}$	100	–	–	–	–	1.1

from the volume the hydrodynamic diameter can be calculated. The diameter for CMS/NR in aqueous solution was determined to be 7.2 nm ± 0.5 nm.

As both the spectroscopic properties and the fluorescence lifetime were effected by the environment, the anisotropy decay of CMS/NR in DMSO was also measured for comparison. The anisotropy decay of CMS/NR in DMSO was clearly much faster than for CMS/NR in aqueous solution and much more similar to the anisotropy decay of NR in DMSO (Figure 5.13C). A single rotational correlation time of 0.30 ns was extracted from the fit for CMS/NR, while for NR in DMSO a rotational correlation time of 0.30 ns was obtained (Table 5.6). The temperature dependence of the rotational correlation time of CMS/NR in DMSO was analyzed as for CMS/NR in aqueous solution and a diameter of 1.2 nm ± 0.3 nm was found, clearly smaller than the 7.2 nm ± 0.5 nm observed in aqueous solution.

The very similar rotation correlation times of NR and CMS/NR in DMSO implicate a free rotation of NR when the CMS/NR nanocarrier is dissolved in DMSO. This agrees with the analysis of the fluorescence lifetime decay, where more apolar solvents were shown to lead to a shift of the NR molecules towards the solvent interface. For CMS/NR in DMSO the anisotropy measurement suggest that only minimal interactions with the CMS nanocarrier structure remain.

Temperature dependent conformational transitions in the CMS nanocarrier

The analysis of the fluorescence lifetime showed that the solvent can have an effect on the partitioning of NR within the CMS nanocarrier. The distribution could however also be effected by structural changes within the CMS nanocarrier architecture. The response of the CMS nanocarrier to temperature was investigated and the temperature dependence of fluorescence lifetime and anisotropy parameters indicative of drug distribution and CMS nanocarrier structure were analyzed.

The fluorescence anisotropy decay of CMS/NR was best approximated with a multiexponential decay model with three rotational correlation times. These rotational correlation times can be assigned to different motions. The slowest rotational correlation time represents the rotational diffusion of the whole nanocarrier, as exploited for the size determination. The fastest rotational correlation time represents the rotation of the dye itself, while the intermediate rotational correlation time (ϕ_1) reflects the interaction between the nanocarrier branches and the dye molecules and is a measure of the dynamics and conformational space of the CMS nanocarrier branches. The relative amplitudes give insights into the conformational space of the dye (β_1) and nanocarrier branches (β_2), as well as the overall steric hindrance (β_3).

To analyze the temperature dependence, the relative amplitudes were plotted against the temperature (Figure 5.14A). All three relative amplitudes show a temperature dependent behavior, with an increase of the relative amplitudes β_1 and β_2, indicating an increased mobility, and so the overall steric restriction (β_3) decreased. The observed temperature dependence is characteristic of a two-state transition behavior and the transition temperatures were determined using equation 5.10. The respective transition temperatures T_c were found to be 33 °C ± 1 °C for the relative amplitude β_1, i.e. the motion of the dye, 30 °C ± 1 °C for the dynamics of the nanocarrier branches (β_2) and 31 °C ± 1 °C for the steric restriction by the branches (β_3) (Table 5.7). The overall transition temperature for temperature dependence of all three relative amplitudes was also determined from a global fit, and a value of T_c = 31 °C ± 0.7 °C was obtained (Table 5.7). The increase of the relative amplitudes associated with the freedom of motion above 31 °C indicate that the increase in rotational freedom of NR is accompanied, possibly even slightly preceded as the individual fits might suggest (Table 5.7), by an increase in flexibility of the nanocarrier branches.

The fluorescence lifetime analysis of CMS/NR indicated that the fluorescence lifetime parameters are sensitive to the distribution of NR within the CMS nanocarrier. The relative

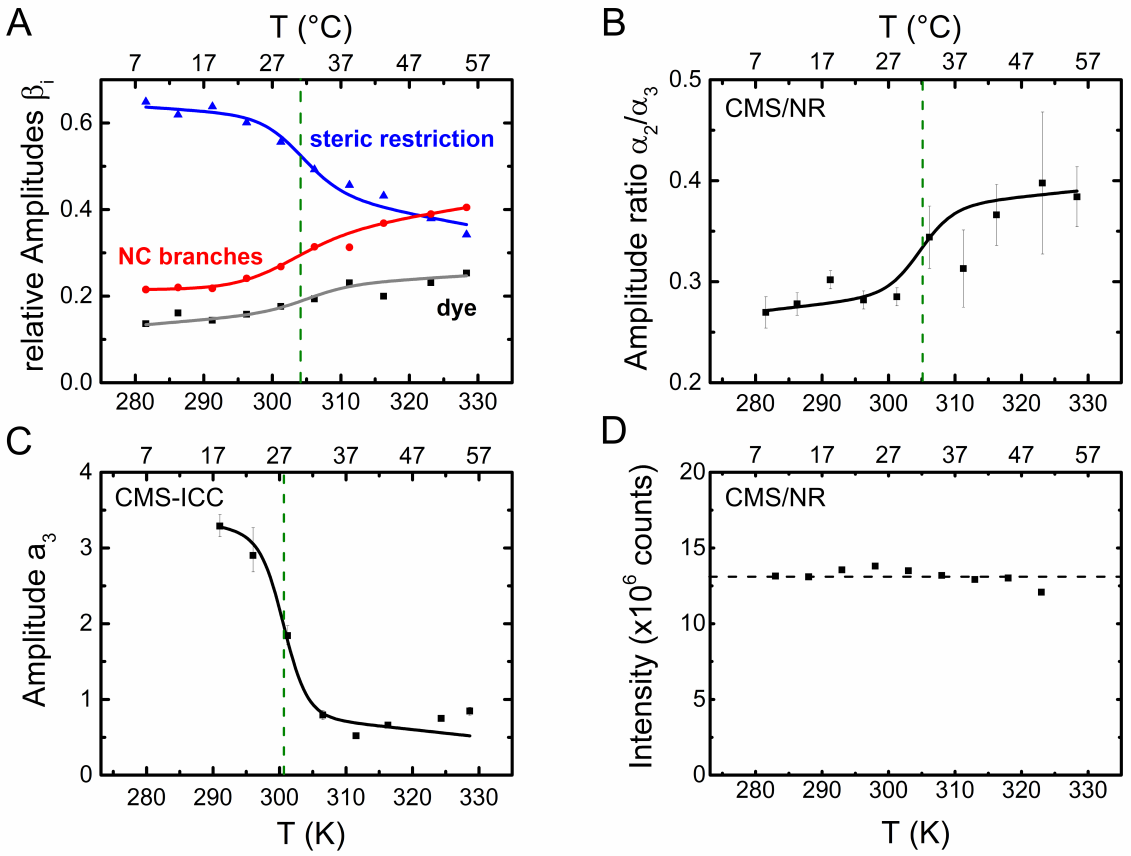

Figure 5.14. Temperature dependence of the anisotropy and lifetime decay parameters of the CMS/NR and CMS-ICC nanocarrier. (A) Temperature dependence for the relative amplitudes of the rotational correlation times of the CMS/NR nanocarrier. The amplitudes are indicative of the conformational space or steric restriction of the dye NR within the CMS nanocarrier architecture and their temperature dependence displays a two-state transition behavior. The respective fit curves according to the two-state transition model (see equation 5.10) are shown (solid line). The error of the relative amplitudes was determined using exhaustive error analysis for 1σ and resulted in following mean errors: dye ± 7 % (max.: 11 %); NC branches ± 4 % (max.: 7 %); steric restriction ± 4 % (max.: 10 %). (B) Temperature dependence of the ratio of the relative amplitudes α_2 and α_3 of the fluorescence decay of CMS/NR. The fit with the two-state transition model (see equation 5.10) is shown (solid line). (C) Temperature dependence of the amplitude a_3 of the fluorescence decay of CMS-ICC. The fit with the two-state transition model (see equation 5.10) is shown (solid line). (D) Integrated intensity of the CMS/NR nanocarrier fluorescence decay curves as a function of temperature. Reprinted with permission from [Boreham et al., 2014b]. Copyright 2014 American Chemical Society.

amplitude α_2 of the intermediate lifetime (τ_2, 1.6 ns) correlated with NR close to the solvent interface, while the relative amplitude α_3 of the slowest lifetime (τ_3, 4.4 ns) could be identified with the lifetime observed in a water devoid region. The temperature dependence of the amplitude ratio of the intermediate and the slow lifetime (α_2/α_3) should therefore be able to reflect on NR redistribution within the CMS nanocarrier.

The temperature dependence of α_2/α_3 revealed an increase of this ratio with increasing temperature (Table 5.5 and Figure 5.14B) and the behavior was again indicative of a two-state transition. The value of the transition temperature T_c was 32 °C ± 2 °C, clearly in the same temperature region as the transition temperatures observed for the amplitudes of the fluorescence anisotropy decay components (Table 5.7). Based on the identification of the different fluorescence lifetime amplitudes, the temperature dependent change of the α_2/α_3 ratio is indicative of a redistribution of NR with more NR molecules close to the solvent interface at higher temperatures.

For the nanoparticle dPGS-ICC a temperature dependent shrinkage was observed. For CMS we did not detect any changes in size. However, as the CMS nanocarrier contains a dPG core with ICC covalently bound, the temperature dependent lifetime behavior of CMS-ICC was investigated. The local environment within the core region of the CMS nanocarrier will determine the ICC fluorescence lifetime decay. CMS-ICC in aqueous solution displayed three lifetime decay components (Figure 5.10 and Table 5.5). The two fast lifetime components of 0.16 ns and 0.52 ns are similar to the predominant lifetime components seen for ICC in aqueous solution (0.18 ns) and in an ethanol/H_2O mixture (0.50 ns) (Table 5.5). This suggests that the dye ICC coupled to the dPG core interacts with polar and less polar environments, most likely the hydrophilic PG core and the adjacent hydrophobic layer. The slowest decay component of 1.40 ns was not observed for the free dye ICC (Table 5.5). Since hindered rotation of the methine linker of ICC is accompanied by longer lifetimes, due to the larger planar π-electron system [Chibisov et al., 1995], the existence of the 1.40 ns relates to the hindrance of the fast rotation of the ICC polymethine linker in CMS-ICC.

CMS-ICC should therefore be sensitive to structural changes in the core region effecting the rotation of the ICC polymethine linker and thus the contribution of slowest lifetime decay component, as indicated by the amplitude a_3. With increasing temperature a decrease of the amplitude a_3 was observed (Table 5.5 and Figure 5.14C), again with the characteristics of a two-state transition, and the transition temperature was determined to be 28 °C ± 2 °C (Table 5.7). This transition temperature is only a few degrees below the transition temperatures observed for the freedom of motion and the NR redistribution (Table 5.7), suggesting that the observed

Table 5.7. Transition temperatures determined from the different lifetime and anisotropy observables.

nanocarrier	observable		parameter	T_c (K)	T_c (°C)
CMS/NR	conformational space	of dye	β_1	305.7 ± 1.1	33 ± 1.1
		of NC branches	β_2	303.0 ± 1.1	30 ± 1.1
		steric restriction by branches	β_3	304.2 ± 1.0	31 ± 1.0
		global fit for	β_1, β_2, β_3	304.1 ± 0.7	31 ± 0.7
	polarity of environment		α_2/α_3	305.2 ± 1.6	32 ± 1.6
CMS-ICC	steric restriction of methine linker		α_3	300.9 ± 1.4	28 ± 1.4

changes could originate in the dPG core. The decrease of the amplitude a_3 with increasing temperature indicates a higher mobility of the ICC dye, with a reduction of the hindrance of the rotation of the ICC polymethine linker, and thus an increased flexibility of the CMS nanocarrier in the dPG core region.

NR retention upon CMS structural changes

The previous results show that temperature can effect NC structure. For biomedical applications it is of great importance if the cargo molecule is released or retained upon temperature induced conformational changes. Premature loss of cargo molecules effects the amount of dye loaded and thus the concentration that can be released at the target location. Here, the fluorescence intensity was used to investigate the drug retention - drug release behavior as a function of temperature. Release of the drug mimetic NR into the aqueous solution must be accompanied by a reduction of the fluorescence intensity, due to the strong fluorescence quenching of NR in aqueous solution. The integral intensity of the fluorescence lifetime decay curves was plotted against the temperature (Figure 5.14D). It can clearly be seen that there are only minor changes in the integral fluorescence intensity with increasing temperature and that these minor changes do not follow a clear trend, but rather fluctuate around a given value. Hence, the temperature induced changes in the CMS nanocarrier do not lead to a release of the drug mimetic NR.

Correlation of CMS nanocarrier aggregation state and NR distribution

The CMS/NR investigated in this study were unimolecular as exemplified by the size of around 7 nm. CMS has however also been reported to form aggregates [Radowski et al., 2007, Fleige et al., 2012]. To investigate the influence of the aggregation state, we determined the fluorescence lifetimes and their relative amplitudes for aggregated CMS/NR. The aggregation was observed via the existence of an end-anisotropy r_∞. The fluorescence lifetimes and the relative amplitudes for the unimolecular and aggregated CMS/NR are shown in Figure 5.15A and Figure 5.15B. The observed lifetimes were very similar, however the relative amplitudes varied. While in unimolecular CMS/NR the largest relative amplitude (78 %) was associated with the slowest lifetime 4 ns (Figure 5.15A), reflecting the NR molecules in a water devoid environment, the amplitude ratio was shifted in aggregated CMS/NR in favor of the 1.6 ns lifetime (Figure 5.15B) indicating almost equal amounts of NR at the solvent water interface and in a water devoid, apolar, environment. Besides solvent and temperature the aggregations state can also influence the NR distribution within the CMS nanocarrier.

It is feasible that a transition from aggregated CMS to unimolecular can be induced by dilution of the CMS nanocarriers. Dilution could for example occur when applied to the blood stream in intravenous injections. As for the temperature induced changes, it is also of great importance that cargo molecule are retained upon dilution, so that they can be released at the desired site. A CMS/NR stock solution was diluted over 4 orders of magnitude and the dye release was investigated via the fluorescence intensity. A linear dependence of the intensity on concentration could be observed in a log-log plot (Figure 5.15C). This indicates that NR is not lost upon dilution and remains within the nanocarrier at least down to concentrations of 10 nM.

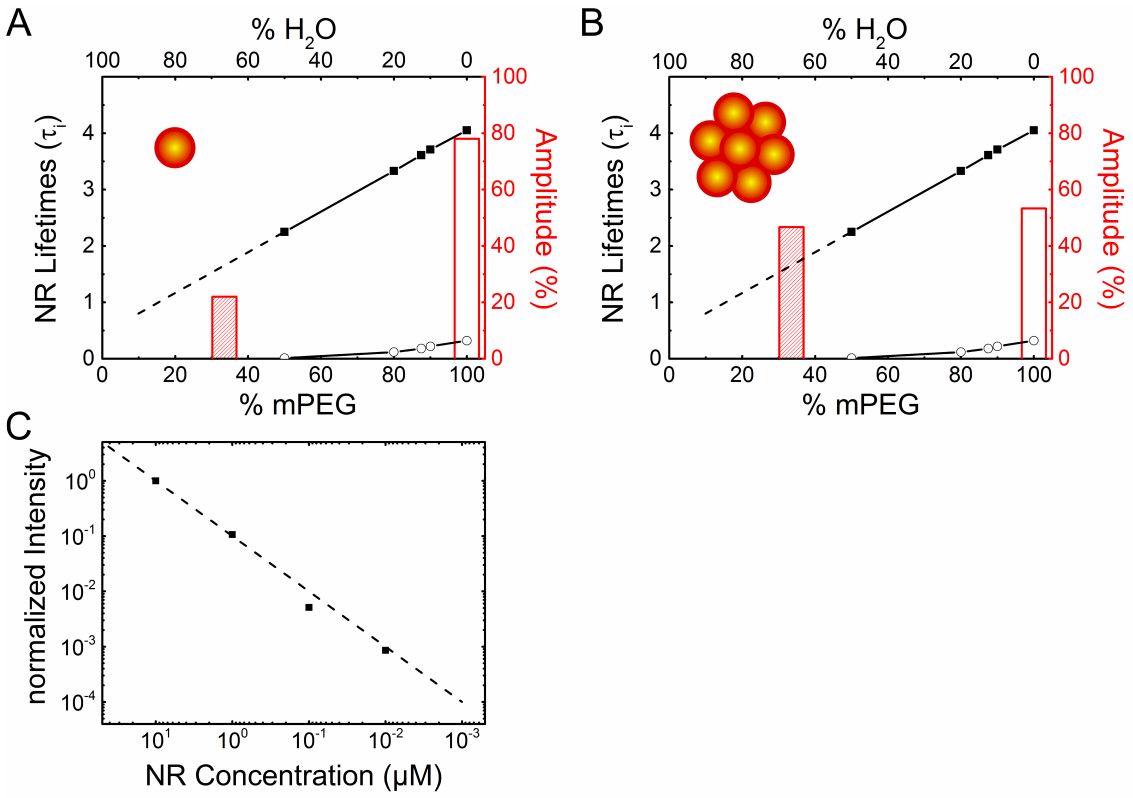

Figure 5.15. CMS nanocarrier aggregation dependent distribution of encapsulated NR within the CMS nanocarrier structure. The amplitude of the two respective NR fluorescence decay times, 1.7 ns (hatched) and 4.1 ns (plain), is depicted in (A) and (B) as a red bar plot within the water content dependence of NR dissolved in mPEG (Figure 5.12). Measurement conditions as in Figure 5.11. (A) 40x diluted CMS/NR from a 5 mg/ml CMS nanocarrier stock solution loaded with NR. Under these conditions CMS/NR appears to be unimolecular. (B) CMS/NR as prepared with larger aggregates (mean diameter ∼100 nm) was observed. The NR concentration was 11 µM. (C) Normalized fluorescence intensity as a function of CMS/NR concentration. The dashed line indicates the linear dependence of NR fluorescence on CMS/NR concentration. Measurement conditions as in Figure 5.9. The error of the peak intensity was ±0.3 %. Reprinted with permission from [Boreham et al., 2014b]. Copyright 2014 American Chemical Society.

5.3 Discussion

In this part of the thesis, time-resolved fluorescence lifetime and anisotropy measurements were used to gain information on physicochemical properties, molecular dynamics and size of nanoparticles and nanocarriers containing dendritic polyglycerol.

Distribution of drug mimetic NR correlates with CMS branch flexibility

The environmental sensitivity of spectroscopic properties and the fluorescence lifetime of NR was combined with information about the segmental dynamics and freedom of motion of the nanocarrier, obtained from fluorescence anisotropy measurements, to gain insight into temperature induced structural changes within the CMS nanocarrier and the effects on the distribution of the hydrophobic drug mimetic NR within the CMS structure. NR is a polarity and hydrogen bond sensitive fluorescent probe [Cser et al., 2002]. Comparison of the fluorescence lifetimes of NR in solvents with different polarity and encapsulated within the CMS nanocarrier allowed for the assignment of the multiple lifetimes observed for CMS/NR to the lifetime of NR in an ethanol/water (1:1) mixture, as well as to the lifetime in the more apolar solvent DMSO.

Since NR is believed to reside in the outer mPEG shell of CMS, as reported in a recent publication [Fleige et al., 2012] using spectroscopic analysis of CMS/NR and NR in mPEG/water mixtures, the fluorescence lifetimes in different mPEG/water mixtures were investigated here. A linear dependence of the NR lifetime on the water content of the mPEG/water mixtures was observed, and at low water contents a fast second lifetime component was detected. The NR lifetimes seen in the mPEG/water mixtures compared well to the lifetimes observed in CMS/NR. The intermediate lifetime component of CMS/NR was similar to NR in a mPEG/water mixture with 70 % water content, while the slow and fast lifetimes of CMS/NR could both be seen in an mPEG/water mixture devoid of water. From these findings it can be concluded that the drug mimetic NR is distributed within two distinct environments of the CMS nanocarrier.

The comparison of NR lifetimes in different solvents and mPEG/water mixtures revealed encapsulated NR to reside in a water devoid, apolar region, and also in a region with a relatively high water content, comparable in polarity to an ethanol/water (1:1) mixture, within the CMS nanocarrier. While the former most likely corresponds to the CMS region at the interface of the mPEG chains with the hydrophobic shell, or even within the hydrophobic shell, the latter is probably close to the interface of the outer mPEG shell with the solvent. Based on the amplitudes of the lifetimes the relative amounts of NR in the different environments could be obtained. For CMS/NR in water at 20 °C only about 20 % of the NR molecules reside close to the solvent interface. Fleige et al. [Fleige et al., 2012] determined the NR environment from a comparison of the absorption maxima of CMS/NR and NR in mPEG/water mixtures. They reported a water content of about 10 %. Here, an absorption maximum for CMS/NR in H_2O of 557 nm was observed, which corresponds to the reported value for 80 % mPEG, i.e. 20 % water. To compare the results from the fluorescence lifetime measurements with the published value, the amplitude weighted mean lifetime was calculated. The mean lifetime of 3.24 ns corresponds to a NR lifetime in around 16 % mPEG/water mixture. Hence, the fluorescence lifetime analysis shows that the water content of the NR environment within CMS/NR determined from absorption maxima is the mean water content of the NR distribution within the CMS nanocarrier.

Next, the influence of environmental changes on the drug distribution in CMS/NR was investigated. Changing the solvent from aqueous solution to ethanol resulted in an increase in the amplitude of the 1.6 ns lifetime. This indicates a shift of NR molecules to the solvent interface, showing that the distribution of the NR molecules is sensitive to the polarity of the solvent. When the temperature was increased, between 5 °C and 55 °C, the amplitudes were seen to shift in favor of the 1.6 ns lifetime. This provides evidence for a temperature induced redistribution

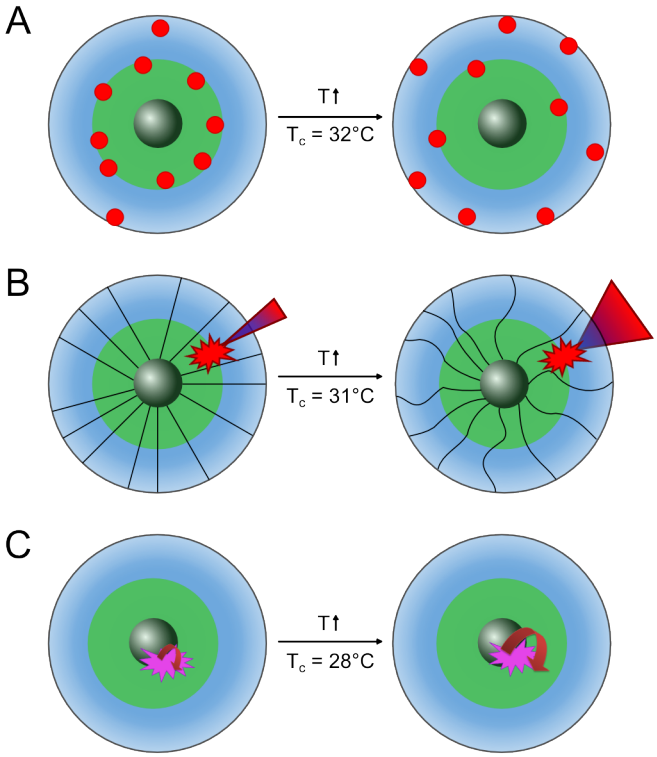

Figure 5.16. Temperature induced transition in CMS nanocarriers as determined from fluorescence lifetime and anisotropy of incorporated dye molecules. (A) The fluorescent drug mimetic NR (red circles) is redistributed within the different shells (blue: hydrophilic; green: hydrophobic; gray: PG core). At temperatures above the transition temperature T_c more drug molecules are close to the solvent interface. (The number of incorporated dye molecules (approximately one per CMS structure) is not drawn to scale but to visualize the distribution.) (B) With increasing temperature the conformational space (indicated by the cone size) of NR increases as well as the flexibility of NC branches. (C) At temperatures below the transition temperature the rotation of the methine linker of the ICC dye coupled to the dPG of the CMS nanocarrier is hindered. With increasing temperature the rotation is increased, indicating more freedom of movement.

of the encapsulated NR molecules (Figure 5.16A). A transition temperature of 32.0 °C ± 1.6 °C was determined from a fit the data according to the two-state transition model. The relative amplitudes of the rotational correlation times of CMS/NR also showed a temperature dependence. Both the relative amplitudes β_1, reflecting the freedom of motion of the dye, and β_2, indicative of the conformational space of the shell branches, increased with temperature. Consequently the overall steric restriction, β_3, was reduced (Figure 5.16B). A global fit of all three transitions with the two-state transition model yielded a transition temperature of 31.0 °C ± 0.7 °C, similar to that observed for the NR drug distribution based on the fluorescence lifetime amplitudes.

While the data for CMS/NR identified a temperature dependent redistribution of the drug mimetic NR toward the solvent interface correlating with changes of branch flexibility in the shell of the CMS nanocarrier, no information on changes in the dPG core of the CMS nanocarrier could be obtained from CMS/NR. CMS-ICC, on the other hand, is sensitive to changes in the dPG core, due to the covalently linked ICC. CMS-ICC exhibited a slow lifetime component indicative of a steric restriction of the ICC polymethine linker rotation. The temperature dependence of the amplitude of this lifetime component was analyzed and with increasing temperature a decrease was observed, indicating a reduction of the steric restriction of the polymethine linker rotation, probably due to an increased flexibility of the CMS nanocarrier core region (Figure 5.16C). The determined transition temperature of 28.0 °C ± 1.4 °C is below the transition temperatures

observed for the shell branch flexibility and NR redistribution, suggesting that the molecular basis for the temperature dependent redistribution might actually originate in the dPG core of the CMS nanocarrier.

Size of CMS and dPGS

Time-resolved fluorescence anisotropy is a powerful tool to determine the size of nanoparticles and to follow changes in size caused by changes in the environment. The slowest rotational correlation time of dyes bound to other molecules describes the tumbling motion of the whole molecule and can be used to determine their size.

For CMS nanocarriers the analysis of the slowest rotational correlation time of encapsulated NR in a Perrin plot revealed a linear behavior with temperature, clearly indicative of a constant size of the CMS nanocarriers over the whole temperature range investigated. From the slope of the Perrin plot a hydrodynamic diameter of 7.2 nm ± 0.5 nm was obtained. The value determined here is in good agreement with reports in the literature [Radowski et al., 2007,Fleige et al., 2012] using dynamic light scattering, where the size of unimeric CMS was estimated to be in the range of 5 nm to 9 nm.

In contrast to CMS, two different slopes were observed in the Perrin plot of the slowest rotational correlation time for dPGS-ICC. Hence, dPGS undergoes a change in size. A closer analysis was conducted by directly plotting the diameter, as calculated from the slowest rotational correlation time, against the temperature. The size dependence followed a two-state transition behavior. The transition temperature T_c was determined to be 34.1 °C ± 0.3 °C. At temperatures above T_c the mean diameter of dPGS was 2.9 nm ± 0.1 nm, while at temperatures below the transition temperature the mean diameter was found to be 4.4 nm ± 0.3 nm. The latter agrees well with the diameter value of 6.5 nm ± 1.5 nm reported by Weinhart et al. [Weinhart et al., 2011b], obtained from DLS measurements at 25 °C.

Molecular mechanism of temperature responsiveness

Both dPGS nanoparticles and CMS nanocarries were shown to be responsive to temperature. The study of thermosensitive polymers is however mainly focused on polymers displaying a so-called low critical phase transition temperature (LCST). The LCST describes the temperature at which the water solubility of the polymer structures is reduced so far that water insoluble aggregates form. These insoluble aggregates are readily detected by turbidity measurements [Mao et al., 2003,Erbil and Saraç, 2002]. The LCST is an intrinsic property of certain polymers, e.g. poly(N-isopropylacrylamide) (PNIPAM). Temperature responsive copolymers can be produced by introducing such polymers into other polymeric structures [Roy et al., 2013].

Dendritic polyglycerols are not known to a have a LCST. None the less the size of dPGS is dependent on the temperature. The main transition in size occurred at physiologically relevant temperatures, i.e. between 30 °C and 40 °C. The dPGS nanoparticle investigated here shrank by nearly 50 %, regarding the diameter, with increasing temperature. The transition temperature was determined to be 34 °C.

It is tempting to speculate that the temperature induced shrinkage is driven by a process similar to the hydrophobic effect. The increasing temperature could allow water molecules previously confined within the dPGS structure to be excluded from dPGS and expelled to the bulk solution. Such a temperature induced dehydration has, for example, been implicated in LCST-type polymer transition [Liu et al., 2014] and also in the swelling behavior observed for polyglycerol gels [Salehpour et al., 2012]. For the polyglycerol-based hydrogels, it was speculated that hydrogen bonds between water molecules and the polymer chains can be broken with increasing temperatures. Water-water interactions, as well as intermolecular interactions of the

polymer chains, become more favorable and the swelling of the hydrogels is thus reduced with increasing temperatures. A similar processes could explain the observed temperature induced shrinkage of dPGS.

A shrinkage of dPGS based on water expulsion could also explain why for CMS nanocarriers no shrinkage was observed, even though CMS nanocarriers contain a dendritic polyglycerol core. CMS nanocarriers have a shell of hydrophobic chains attached to the functional surface groups of the dPG core. The highly hydrophobic environment adjacent to the dPG core of CMS nanocarriers should limit the expulsion of water to the solvent.

However, an increase in flexibility of the CMS nanocarrier core region, as seen from the CMS-ICC lifetime data, was observed. If a weakening of hydrogen bonds is required before water expulsion can trigger dPGS shrinkage, then a thermally induced weakening of hydrogen bonds in the dPG core of the CMS nanocarrier could allow the dPG branches more freedom of motion.

Taking a closer look at the transition temperatures determined for CMS nanocarriers, the T_c observed for the flexibility change of the dPG core was $28\,^{\circ}\mathrm{C} \pm 2\,^{\circ}\mathrm{C}$, while for dPGS the shrinkage was found to have a transition temperature of $34.1\,^{\circ}\mathrm{C} \pm 0.3\,^{\circ}\mathrm{C}$. If the increase in flexibility of the CMS nanocarrier core region is due to the weakening of hydrogen bonds without water expulsion and the dPGS shrinkage is caused by a weakening of hydrogen bonds with water expulsion, then the higher transition temperature of dPGS could well be due to the energy barrier for the water expulsion to the solvent. A similar temperature regime for a weakening of hydrogen bond interactions in polymers was reported for PNIPAM polymers where the LCST was determined to be $32\,^{\circ}\mathrm{C}$ [Chee et al., 2006].

Relevance for biomedical application

The observed shrinkage of dPGS can also impact the biological activity of dPGS. The dPGS nanoparticle has been shown to have anti-inflammatory activity [Dernedde et al., 2010]. It can bind to selectins and thus reduce the leukocyte migration, hence dampening the inflammatory response [Dernedde et al., 2010]. Further, dPGS also inhibited leukocyte chemotaxis by binding to constituents of the immune response mediated by the complement system [Dernedde et al., 2010]. Both dPGS protein interactions were thought to be mediated by the binding of the negatively charged dPGS to positively charged binding motives in the respective protein [Dernedde et al., 2010].

In a recent study comparing the biological activity of differently structured branched polyglycerol sulfates, the L-selectin binding behavior was shown to depend on the multivalency, i.e. the number of sulfate groups, on the dPGS surface [Paulus et al., 2014]. In addition, the particle size and flexibility of the respective branched polyglycerol sulfates also contributed to the complex structure-biological activity relationship [Paulus et al., 2014]. The temperature induced shrinkage observed here can therefore have direct consequences for the biological activity of dPGS, due to the reduction in size, but also due to the concomitant increase in surface charge density. As the reported results on L-selectin binding were obtained from surface plasmon resonance measurements conducted at $25\,^{\circ}\mathrm{C}$ [Dernedde et al., 2010, Paulus et al., 2014], the relative binding effects observed for the different branched polyglycerol sulfates could be affected by physiological temperatures, as at least dendritic polyglycerol sulfate displays a temperature dependence of factors shown to be important for the binding to L-selectin.

For CMS no inherent anti-inflammatory activity has been reported. CMS nanocarriers have been designed as drug carriers, e.g. for analgesics targeting peripheral opioid receptors, anti-inflammatory substances and cancer drugs. Here, the drug distribution was shown to depend on environmental factors. For biomedical applications it is of great importance that the drug is only released at the target site. The drug release was therefore monitored in dependence of temper-

ature and CMS nanocarrier dilution. The fluorescence of the dye NR is considerably quenched in aqueous solution. The NR intensity was analyzed as a function of increasing temperatures, up to 55 °C, and decreasing concentrations, down to 10 nM. In both cases, the results showed no reduction of fluorescence intensity and hence the NR cargo molecule is retained within the CMS nanocarrier. However, the observed increased amount of NR close to the solvent interface at increased temperatures or less polar solvents can be utilized to increase the probability of cargo release at target structures.

Chapter 6

Identifying localization and binding of target molecules against high autofluorescent backgrounds

Application of newly developed fluorescence lifetime imaging microscopy data analysis methods to specific ligand binding as well as skin penetration and biodistribution of nanoparticles and biomolecules

As outlined in chapter 2, nanoparticles and nanocarriers are promising tools for future drug applications, with potential benefits ranging from inherent anti-inflammatory properties to targeted drug delivery in combination with localized and triggered drug release. The multitude of diverse nanoparticles and nanocarriers developed in the recent years and their mainly unknown cytotoxicity mandates a thorough investigation into possible effects on the organism. This includes the transport routes into the organism, the accumulation inside the organism and also their degradation and excretion. These may all vary depending on how they are administered. In addition to synthetic nanoparticles and nanocarriers, alternative transport vehicles based on biomolecules are also under investigation. Biomolecule-based transport should have advantages over synthetic nanoparticles and nanocarriers as they are generally biodegradable and should show reduced cytotoxicity and side effects.

In my thesis, the aim was to investigate the skin penetration behavior and biodistribution of selected nanoparticles and biomolecules in tissue samples. However, the intrinsic autofluorescence of the tissue samples themselves proved highly problematic. High background autofluorescence can also present a problem when wanting to detect specific binding of a fluorescent ligand against a high background fluorescence from unspecifically bound ligands.

Conventional fluorescence microscopy is unable to discriminate between autofluorescence and fluorescence from other sources, or between a ligands fluorescence in the specifically bound or non bound state. FLIM measurements have the advantage that the fluorescence lifetime properties are dependent on the physicochemical environment. However, sample autofluorescence is still a considerable problem, particularly when imaging target probes in tissue samples. The autofluorescence itself is characterized by a complex fluorescence decay, often with multiple components, usually overlapping to a great extent with the fluorescence lifetime of commonly used fluorophores [Rich et al., 2013].

Therefore, new analysis approaches were required to answer the questions at hand, leading to the application of the ratiometric FLIM method (rmFLIM, [Boreham et al., 2011]) and the cluster-based FLIM algorithm developed by R. Brodwolf in the group of Prof. U. Alexiev. In this part of the thesis, I will present the results obtained for the specific detection of ligands, nanoparticles and biomolecules, involved in or with potential application in the treatment of

inflammation and pain, using these newly developed FLIM analysis routines.

Using the rmFLIM analysis, which relies on the specific amplitude ratio of unique fluorescence lifetime curves of fluorescent dyes attached to target molecules, I could successfully discriminate between the specific binding of a fluorescent ligand, naloxone-fluorescein (NLX-Flu), to a receptor, the μ-opioid receptor (MOR), and the high fluorescent background of unspecific binding. Further, a fluorescently labeled nanoparticle, dPGS-ICC, was identified in liver tissue samples. The limits of rmFLIM, in terms of fluorescence lifetime decay components, could also be determined.

In addition, the results are shown for the biodistribution and skin penetration of fluorescently labeled nanoparticles and biomolecules which have been obtained with the cluster-based FLIM routine, which uses similarities in feature space to overcome the poor signal-to-noise ratio inherent to most FLIM measurements without loss in resolution and contrast. First, the results for the skin penetration of the CMS-ICC nanoparticles will be presented, then those for the skin penetration and co-transport of the biomolecules hyaluronic acid and BSA, and finally the results on the biodistribution of silica nanoparticles after injection into mouse skin.

In the following I will briefly outline the principles of fluorescence lifetime imaging microscopy, describe the experimental setup and also the employed data analysis methods. This will be followed by a summary of the experimental procedure, the results for the different samples (as described above) and a discussion.

6.1 Methods

6.1.1 Fluorescence lifetime imaging microscopy

The principles of measuring fluorescence decay curves with a time-correlated single photon counting setup of solution samples in cuvettes (see 5.1.1) can also be applied to measure the fluorescence decay curves in a spatially resolved fashion, i.e. for each image pixel of a microscope image. To this end, the excitation light from a pulsed laser source is coupled into a confocal raster scanning microscope and single emitted photons are registered at the detector (Figure 6.1A).

A confocal raster scanning microscope does not illuminate the whole sample at once, but only a small portion of the sample, the confocal volume, is illuminated at a given time point. A point illumination source, e.g. a laser, is used as excitation light source. To gather information on the whole sample, the confocal volume is moved across the sample, i.e. scanned (Figure 6.1B), and a measurement recorded for each spot. This is usually achieved by a pair of mirrors that can scan the illumination beam across the sample.

The whole image can then be reconstructed from the sequential, individual measurements. The confocality is generated by the introduction of a pinhole into the light path (Figure 6.1C). The pinhole is in a conjugated focal plane to the illumination plane within the sample. The main advantage is the suppression of out-of-focus light by the pinhole, even allowing for the acquisition of 3D-images, by scanning the illumination beam both laterally and in the z-plane.

Fluorescence lifetime imaging microscopy setup

FLIM measurements were performed on a setup combining a conventional microscope with an external confocal laser scanning module (Figure 6.2).

Two different lasers were used to excite the samples, either a pulsed diode laser (BDL-405-SMT, Becker&Hickl GmbH), emitting at 405 nm with a repetition rate of 20 MHz, or a titanium:sapphire laser (Ti:Sa-Laser, Tsunami model # 3950, Spectra Physics) pumped by a 5 W continuous wave diode laser (Millenia VS, Spectra Physics). The repetition rate of the Ti:Sa-Laser was reduced by a pulse picker to 4 MHz, equal to 1 pulse every 250 ns, just as for the cuvette measurements. The Ti:Sa-Laser output frequency was doubled using a frequency doubler [FD], resulting in wavelengths between 355–500 nm. The FLIM setup was also operated in inverse TCSPC mode and therefore the beam from the Ti:Sa-Laser was split by a beamsplitter. One part was directed onto a reference photodiode [RD] (DET 210, Thorlabs), and the resulting signal was fed into the sync entrance of the TCSPC measurement card as the stop signal. For the pulsed diode laser, the sync signal was directly supplied from the diode laser unit and fed into the TCSPC measurement card and no external reference diode was required

The laser light was coupled into the confocal scanning unit (DCS-120, Becker&Hickl GmbH) using kineflex optical fibers [K] (Kineflex 405 and Kineflex 488, QIOPTIQ). Upon entering the scanning unit a neutral density filter wheel [FW] allowed for the reduction of incident laser power. The laser light was directed onto the main dichroic mirror [MD] and then onto a pair of fast galvanometer mirrors [G], enabling the deflection of the laser light onto the sample under different angles in two dimensions, the so-called scanning. The light was reflected off these mirrors into the optical port of a conventional wide-field microscope (Olympus IX-71) and, since the IX-71 is an inverted microscope, passed through the objective to excite the sample. Fluorescence emission was then collected by the same objective lens and guided back onto the galvanometer mirrors. The emitted light was now descanned by the scanning movement of the galvanometer mirrors, i.e. a stationary laser beam was obtained again. The emission light was separated from the excitation light by the main dichroic mirror [MD]. From here it was focused onto a pinhole [P], which was in the emission path and prevented out-of-focus light from

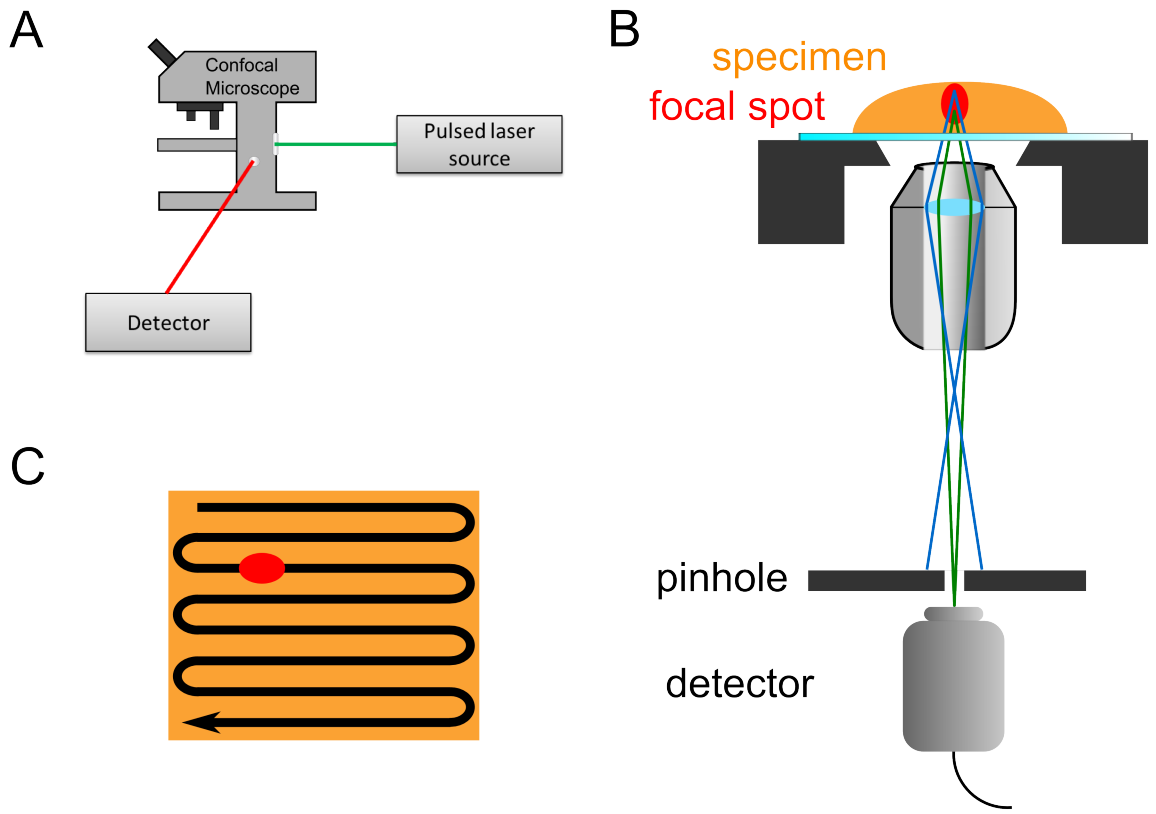

Figure 6.1. Principles of fluorescence microscopy (A) Schematic of a TCSPC-based FLIM setup. The excitation light (green) is directed into the confocal raster scanning microscope and onto the sample. Emitted photons (red) are registered at the detector. (B) Emission light path illustrating the principal of a confocal microscope. Emission light from the conjugate plane with respect to the pinhole (green) is focused onto the pinhole and can therefore reach the detector placed behind the pinhole. Emission light from non-conjugate planes to the pinhole (blue) is not focused onto the pinhole and can therefore not reach the detector. (C) Illustration of the scanning of the sample as used in a confocal scanning microscope. As the confocal spot only accesses a small portion of the sample, the spot is moved across the sample as depicted, and a measurement is recorded for each position.

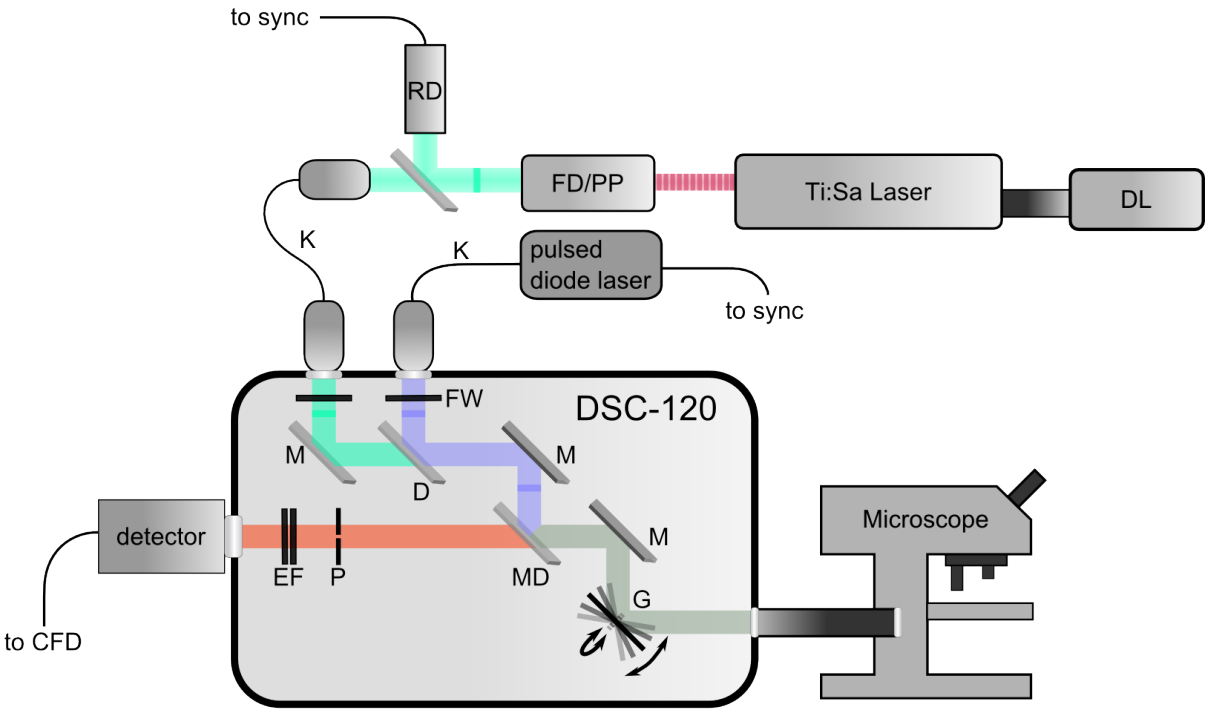

Figure 6.2. Schematic of the FLIM setup employed. A pulsed laser beam, either from a pulsed diode laser or from a Ti:Sa Laser source, can be coupled into the DSC-120 confocal unit via a kineflex fiber and from either laser a reference pulse is sent to the sync input of the measurement card. Once coupled into the DSC-120 the beam is reflected off the main dichroic mirror, deflected of the galvanometer mirrors and coupled into the optical port of an Olympus IX-71 inverted microscope. The emission light also is deflected by the galvanometer mirrors but passes through the dichroic mirror into the emission pathway. The emission light is focused onto a pinhole, thus suppressing out-of-focus light. The spectral detection range can be selected by a pair of emission filters placed into the light path before the detector. The signal from the detector is then sent to the CFD input of the measurement card. Abbreviations: diode laser (DL), frequency doubler (FD), pulse picker (PP), reference diode (RD), kineflex fiber (K), neutral density filter wheel (FW), mirror (M), dichroic mirror (D), main dichroic mirror (MD), galvanometer mirrors (G), pinhole (P), emission filters (EF).

reaching the detector. Two emission filters were used to select the wavelength regime to be recorded before the emission light reaches the detector.

The signal from the detector was then fed into the CFD of the TCSPC measurement card. The TCSPC electronics recorded the time when a photon reaches the detector after a single excitation pulse. In order to achieve the necessary spatially-resolved TCSPC curves, a TCSPC curve had to be measured for each focal volume, i.e. pixel. As photobleaching upon prolonged excitation can be a cause of concern, the scanning of the sample is implemented in most FLIM setups in such a way, that the dwell time per pixel is reduced but the whole sample is scanned a multiple number of times.

6.1.2 FLIM data acquisition and analysis techniques

In this thesis two novel methods for analyzing fluorescence lifetime imaging microscopy (FLIM) data were employed both providing new means to identify fluorescent species against an autofluorescent background.

Ratiometric fluorescence lifetime imaging microscopy

Ratiometric fluorescence lifetime imaging microscopy (rmFLIM [Boreham et al., 2011]) is based on conventional FLIM data analysis, but makes use of special characteristics of the lifetime decay from the molecule of interest not found in the background fluorescence. Conventional FLIM analysis differentiates between fluorescing species purely on the determined lifetimes. The autofluorescent background from organic tissue however can have a complex lifetime decay behavior, with at least one lifetime component very similar to that of the employed dye. Ratiometric FLIM therefore goes one step further and uses the amplitudes ratio of the lifetimes to identify the specific fluorescence lifetime signature of the molecule of interest. The rmFLIM method requires a global fit to the FLIM data set, where the lifetime components of the fluorescence decay curves are predefined and are held constant during the fitting procedure. The respective amplitudes for these fluorescence lifetime are thus determined in each pixel. The rmFLIM data analysis was done using the SPCImage (Version 3.2.3.0, Becker&Hickl) software package.

Cluster-based FLIM analysis

The cluster-based approach was developed by Robert Brodwolf in the group of Prof. Alexiev. Briefly, it aims to overcome the poor signal-to-noise ratio (SNR) complicating quantitative analysis of data obtained from confocal FLIM systems based on TCSPC. At the same time, it increases resolution and contrast, compared to conventional FLIM data analysis. To resolve the unique fluorescence lifetime signature of target molecules, the TCSPC fluorescence decay curves are not fit pixel per pixel. Instead the fluorescence decay curves are grouped according to similarities in feature space (cluster-based method). All pixels with similar lifetime characteristics are grouped in a cluster. The sum of all fluorescence decay curves of all pixels that belong to this cluster is computed, thus generating a specific lifetime curve for each cluster. For the visualization of the different clusters, all pixels belonging to a cluster are color coded in the resulting image.

6.2 Results

6.2.1 Identification of specific ligand binding with rmFLIM

The detection and analysis of protein-ligand interactions in the cellular context is of great importance for basic research and also for pharmacological and clinical applications. Here, in a cooperation with Prof. Stein (Clinic for anesthesiology, Charité Berlin), FLIM measurements using a confocal laser scanning setup (see section 6.1.1) were performed to implement a fast method to evaluate the binding of naloxone-fluorescein to the μ-opioid receptor in overexpressing HEK (human embryonic kidney) cells. Samples were prepared by Dr. Viola Spahn in the group of Prof. Stein. The results presented here are part of a publication by Boreham et al. [Boreham et al., 2011].

NLX-Flu bound to HEK membrane fragments

Naloxone-Fluorescein (NLX-Flu) is a dye labeled variant of the μ-opioid receptor ligand Naloxone (NLX). The absorption of NLX-Flu is characterized by a distinct absorption peak around 492 nm (Figure 6.3A). Experiments were conducted to investigate the binding of NLX-Flu to membrane fragments of HEK293 cells either transfected with the gene for the μ-opioid receptor (+MOR membranes) or to the control sample, not transfected with the gene for the μ-opioid receptor (-MOR membranes). The amount of NLX-Flu in each sample was determined by absorption spectroscopy, using an integrating sphere due to the high scattering caused by the membrane fragments. The results showed identical amounts of NLX-Flu in both samples, despite the absence of μ-opioid receptor in the control sample (Figure 6.3B). Before taking the absorption spectra, the samples had been washed repeatedly to remove any unbound NLX-Flu. The removal of unbound NLX-bound was controlled by monitoring the absorption spectra of the supernatant of the respective washing fractions. Therefore, the NLX-Flu peak in the control sample must stem from unspecific binding of NLX-Flu either to the membrane environment or to other proteins expressed in the HEK293 membrane fragments.

Since specific binding of NLX-Flu to fragments containing the μ-opioid receptor could not be discriminated from unspecific binding solely by absorption spectroscopy, fluorescence lifetime measurements, using a TCSPC cuvette setup as describe in section 5.1.1, were conducted to determine if the fluorescence lifetime decay behavior of NLX-Flu differed between the two sam-

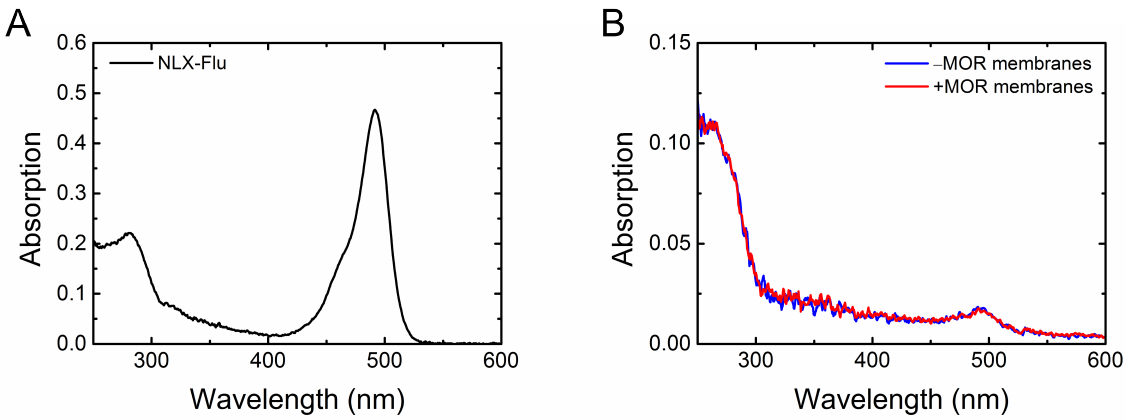

Figure 6.3. Absorption spectra of NLX-Flu. (A) NLX-Flu in 5 mM Tris at pH 9. (B) NLX-Flu with HEK293 membrane fragments from HEK293 cells expressing the μ-opioid receptor (red) and from HEK293 cells not transfected with the μ-opioid receptor (blue)

ples. The lifetime of fluorescein in solution is characterized by a single fluorescence lifetime decay component (Figure 6.4A), with a lifetime of 4 ns. Fluorescein bound to NLX showed a rather similar fluorescence lifetime decay behavior, however an additional decay component of around 0.5 ns was required for a good fit to the data (Figure 6.4B). The fluorescence lifetime decay of NLX-Flu in -MOR membranes and +MOR membranes hardly differed. In both cases, it could be characterized by two decay components (Figure 6.4C,D). A slow component (τ_2) of around 4 ns and a fast component (τ_1) of 0.7 ns. The fast component probably stems from quenching processes, while the slow lifetime component of 4 ns is equivalent to the lifetime observed for fluorescein in solution. Based on these results, discrimination between specific binding of NLX-Flu to the μ-opioid receptor and unspecific binding was not possible.

Identification of specific ligand binding with rmFLIM

The TCSPC cuvette measurements did not reveal any differences between fluorescence lifetimes of NLX-Flu in -MOR membranes and +MOR membranes. FLIM measurements were performed to detect subpopulations of specifically bound NLX-Flu using the additional spatial resolution of the microscopy setup. Binding of NLX-Flu to HEK293 membrane fragments can clearly be seen for both the -MOR membranes and +MOR membranes based purely on the intensity (Figure 6.5A,B). The fluorescence lifetime decay curves were analyzed for differences in the fast lifetime component (τ_1), which would signify NLX-Flu in environments with different quenching. To this end, a fit was performed allowing τ_1 to vary while keeping the 4 ns lifetime component (τ_2) fixed. The false color images, coded according to the value of the fast lifetime (τ_1), show no clear differences between the -MOR membranes and the +MOR membrane samples (Figure 6.5C,D). For both samples the distribution histogram of the fast lifetime component reveals a strong peak around 1 ns (Figure 6.5E).

A further global fit was performed keeping both lifetimes fixed in order to evaluate if any local differences in the amplitude distributions might exist between the samples. The fast component (τ_1) was set to 1 ns and the slow component (τ_2) to 4 ns. The distribution histogram for the ratio of the amplitude of the slow (α_1) and the fast component (α_2) was computed and showed a peak around 3 for NLX-Flu in the -MOR membranes (Figure 6.5H). In contrast, for NLX-Flu in +MOR membranes the corresponding distribution histogram is characterized by an additional peak at an amplitude ratio of 1 (Figure 6.5H).

To differentiate between NLX-Flu bound to the μ-opioid receptor and unspecific binding of NLX-Flu, the FLIM images were color coded according to their amplitude ratio. Values below 1.5 are color coded in red, above 1.5 in blue (Figure 6.5F,G). The threshold value of 1.5 was chosen, as NLX-Flu in the -MOR membranes did not show any values below this range, whereas NLX-Flu in the +MOR membranes showed a pronounced population exhibiting values below 1.5 (Figure 6.5H). Comparing the intensity image with the color coded image highlights that the NLX-Flu specifically bound to the μ-opioid receptor in +MOR membranes is confined to the HEK293 membrane fragment, as is to be expected (Figure 6.5B,G).

To verify that the rmFLIM procedure really identifies specific binding of NLX-Flu to the μ-opioid receptor, a displacement assay was performed. Adding unlabeled ligand in increasing concentration to a sample with a bound labeled ligand will shift the binding equilibrium in favor of the unlabeled ligand. For the rmFLIM data analysis presented here this would mean a reduction in the occurrence of amplitude ratio α_2/α_1 values below 1.5, i.e. red colored pixels in the color coded images, after addition of NLX. The false color coded image for a sample containing NLX-Flu but no NLX (0 μM NLX) is shown in Figure 6.6A. Clearly, the majority of pixels contain specifically bound ligand, signified by the red color. By monitoring this sample upon addition of increasing amounts of NLX, a change in the amplitude ratio of the fast and slow lifetime component could be detected. Upon NLX addition there is a clear reduction in

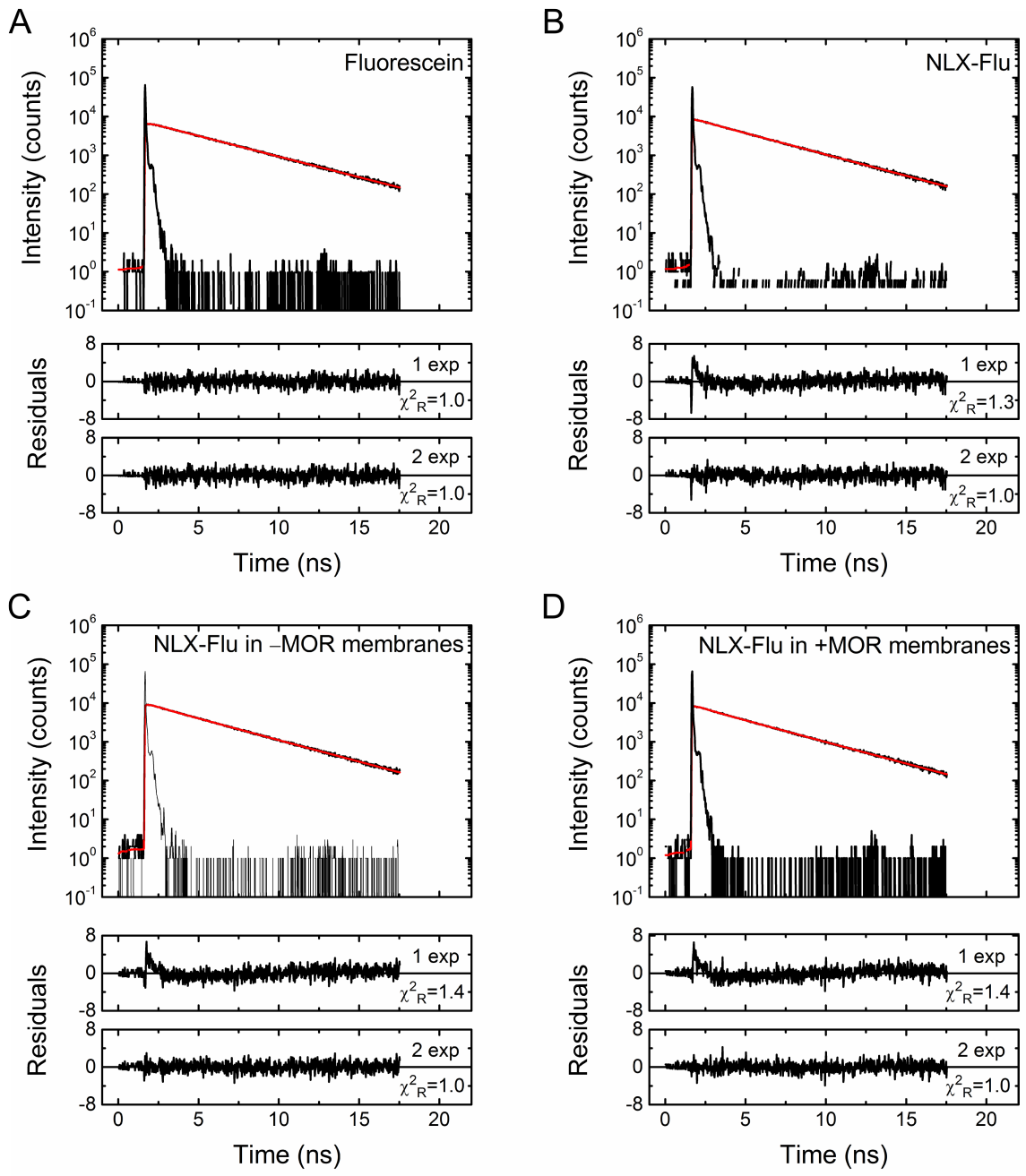

Figure 6.4. Fluorescence lifetime decay curves of NLX-Flu with HEK293 membrane fragments measured by TCSPC cuvette experiments. (A) Fluorescein in 5 mM Tris pH 9. (B) NLX-flu in (C) NLX-Flu with HEK293 membrane fragments not transfected with the μ-opioid receptor (D) NLX-Flu with HEK293 membrane fragments transfected with the μ-opioid receptor. Original data curve, fit curves (red) and the instrument response function is shown for the fit with the best chi square and residuals. The residuals and the reduced χ^2 are given for fits with one and two decay components.

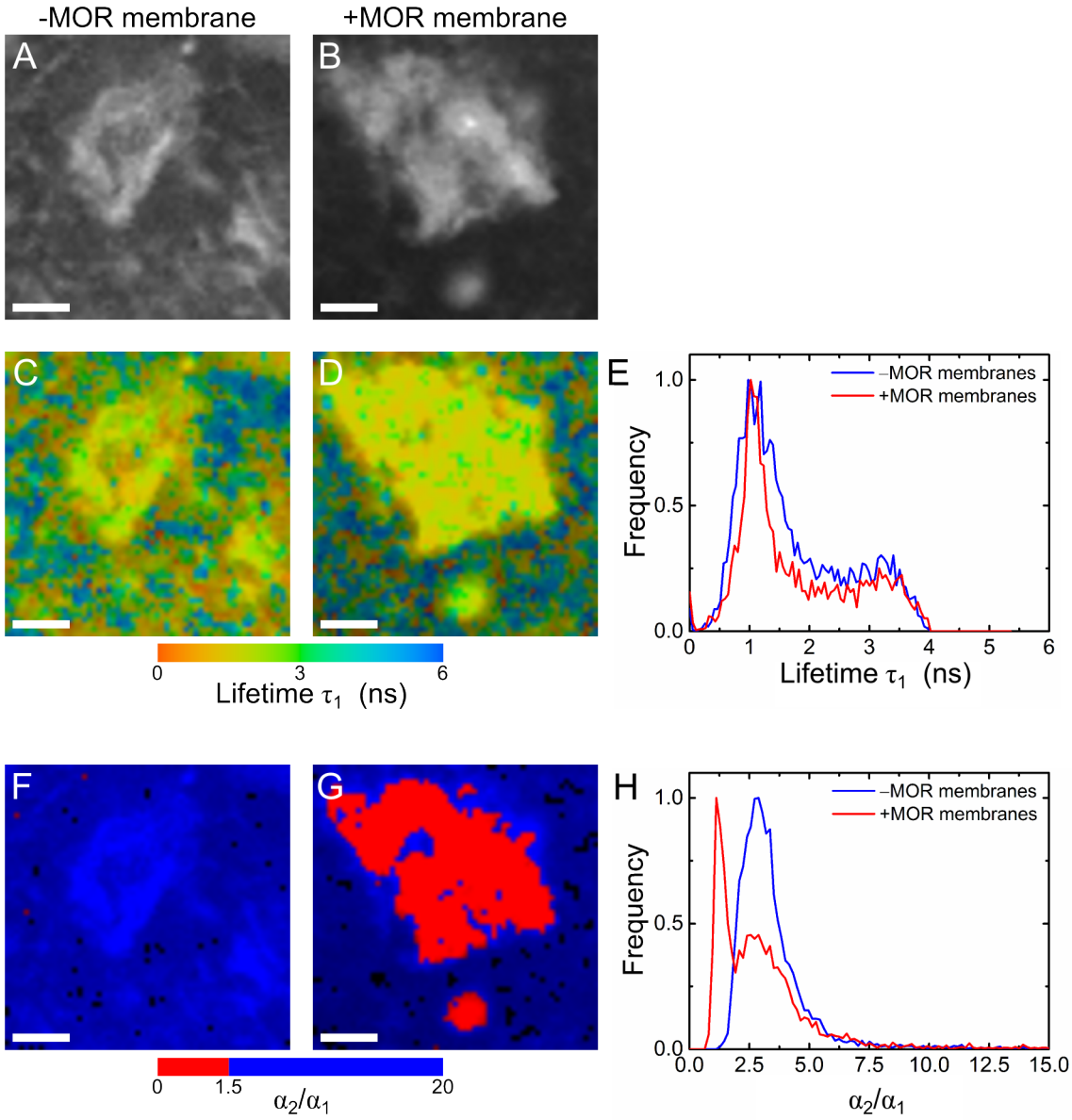

Figure 6.5. Analysis of FLIM data for NLX-Flu binding to μ-opioid receptor. (A,B) FLIM intensity images of NLX-Flu with -MOR membranes and +MOR membranes. (C,D) FLIM data analysis for quenching effects on the fast lifetime component τ_1. The slow component was fixed at 4 ns. (E) Distribution histogram for the relative frequency of the value of the fast lifetime component τ_1 of NLX-Flu in -MOR membrane and +MOR membrane samples. (F,G) False color images coded according to the amplitude ratio α_2/α_1 of NLX-Flu lifetime decay curves as determined from a global fit with the slow lifetime component fixed at 4 ns, and the fast lifetime component fixed at 1 ns. Blue areas correspond to values of α_2/α_1 between 1.5 and 20, red areas to values below 1.5. (H) Distribution histogram of the NLX-Flu amplitude ratio α_2/α_1 in -MOR membrane and +MOR membrane samples. Scale bars: 20 µm

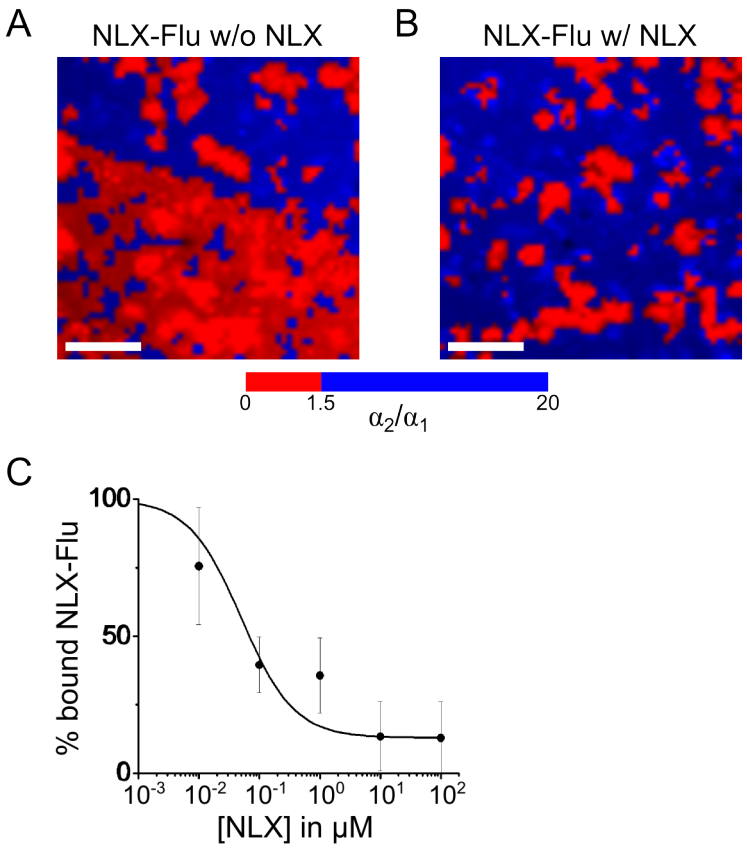

Figure 6.6. Displacement of NLX-Flu bound to the μ-opioid receptor by NLX. (A) rmFLIM image of +MOR membranes without unlabeled NLX but with NLX-Flu (1 µM) specifically bound to the μ-opioid receptor (red). (B) rmFLIM image of the identical sample position as in (A) after addition of 0.1 µM NLX. Scale bars: 25 µm (C) Dose-response curve for displacement of NLX-Flu bound to MOR by nonfluorescent NLX. Data points represent the mean from five independent determinations. The standard deviation is given. The half-maximum concentration for displacement determined from the fit (solid line) is 0.05 µM. (Reprinted with permission from [Boreham et al., 2011]. Copyright 2011 American Chemical Society.)

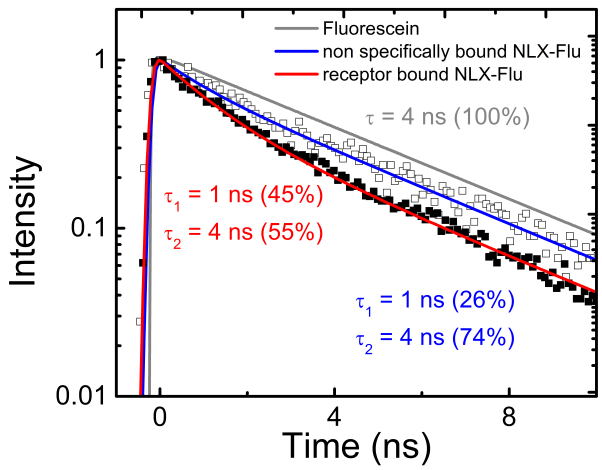

Figure 6.7. Characteristic lifetime decay curve for non specifically bound NLX-Flu and NLX-Flu bound to the μ-opioid receptor as determined by rmFLIM. Solid lines are an exponential fit to the measurement data and shown on top of the original data. The lifetime decay of free fluorescein is also shown. The lifetime decay parameters for a monoexponential fit of the decay of free fluorescein and for biexponential fits to the decay curves of NLX-Flu bound to the μ-opioid receptor and non specifically bound are given.

pixels with an amplitude ratio for specifically bound NLX-Flu, i.e. α_2/α_1 values below 1.5 (see Figure 6.6B for 0.1 µM NLX). This is indicative of a displacement of the specifically bound labeled ligand NLX-Flu by the unlabeled ligand NLX. From the evaluation of the relative amounts of specifically bound ligand for all unlabeled ligand concentrations, from 0.01 µM to 100 µM, a dose-response curve was generated (Figure 6.6C). The half-maximum concentration for displacement was determined to be 50 nM.

After validating the specificity of the binding of NLX-Flu to the µ-opioid receptor, the characteristic lifetime decay curve for NLX-Flu bound to the µ-opioid receptor could be obtained. To this end, the individual fluorescence lifetime decay traces for the red pixels were analyzed and a fluorescence lifetime decay curve characteristic for these pixels was obtained (Figure 6.7). A biexponential fit to the data revealed fluorescence lifetimes of 1 ns, with a relative amplitude of 55 %, and of 4 ns, with a relative amplitude of 45 % (Figure 6.7).

In conclusion, using the rmFLIM approach we could differentiate between NLX-Flu bound to the µ-opioid receptor and unspecifically bound in HEK membranes. The specificity of the identified binding was verified using a displacement assay and finally the rmFLIM approach allowed the extraction of the specific NLX-Flu lifetime curve when bound to the µ-opioid receptor. The rmFLIM approach, based on the specific amplitude ratio of a fluorophore bound to a target structure, is thus a powerful tool to detect a specifically bound fluorescently labeled target molecule against an autofluorescent background, caused here by unspecific binding of NLX-Flu.

6.2.2 Localization of dPGS in rat liver

Successful and safe application of nanoparticles in the field of biomedicine requires sound knowledge about the nanoparticles uptake, biodistribution and also the metabolic clearance. One important component of the total body clearance is the clearance occurring in the liver. The liver is one of the main organs involved in detoxification, where nanoparticles circulating in the blood stream may be filtered out of the blood circulation. Therefore it is important to investigate if administered nanoparticles are present in liver tissue. Here, in cooperation with Prof. Gruber (Institute of Animal Pathology, Freie Universität Berlin), experiments were performed to investigate the metabolic clearance via the liver of dPGS-ICC after injection into the tail of rats. Since we developed the rmFLIM to discriminate specific fluorescence lifetime decays from autofluorescent background, rmFLIM was applied to detect if dPGS-ICC applied to rats can be detected in liver tissue samples. The results presented here are part of a publication by Boreham et al. [Boreham et al., 2011].

Rat liver morphology

Sample preparation and histological imaging was carried by Dr. L. Mundhenk in the work group of Prof. Gruber. A 1 µm thick histological micrograph of a liver section stained with haematoxylin and eosin is shown in Figure 6.8A. A central vein is clearly visible in the center of the image. Further, polygonal hepatocytes (H) containing a centrally located nucleus (N) surrounded by a high amount of eosinophilic cytoplasm can be identified. The hepatocytes (H) are arranged radially in plates around the centrally located central vein (CV). Located between the hepatic plates are the sinusoids (S). An intensity image of the autofluorescence of a comparable unstained section of liver tissue still allows for the assignment of the different characteristic structures (Figure 6.8B).

Conventional FLIM analysis

FLIM measurements were performed on unstained liver sections from rats with injected dPGS-ICC and without injected dPGS-ICC as a control. Rat liver samples show considerable autofluorescence (Figure 6.8B). The autofluorescence decay curve in each pixel was analyzed for both samples. False color FLIM images coded according to the mean lifetime are presented in Figure 6.9A and dPGS-ICC in Figure 6.9B. It can be seen that the mean lifetime in both samples does not differ greatly, with relatively short mean lifetimes prevailing in both samples.

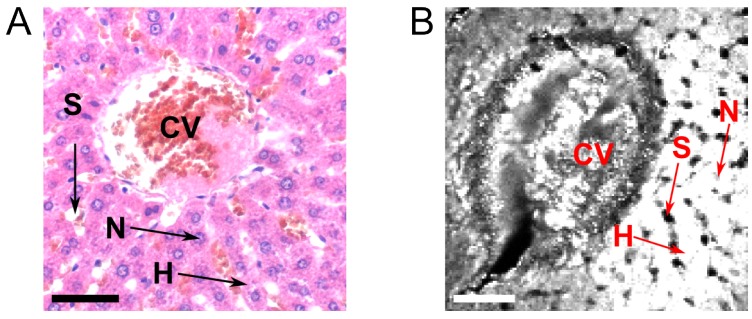

Figure 6.8. Liver images with characteristic structures. A central vein (CV), hepatocyte (H) and hepatocyte nucleus (N) as well as sinusoids (S) are indicated. (A) Histological image of a liver section stained with hematoxylin and eosin. (B) Autofluorescence of liver from the same sample as in part A by confocal raster scanning microscopy. Excitation at 485 nm, emission filter HQ 620/60 nm. Scale bar: 50 µm.

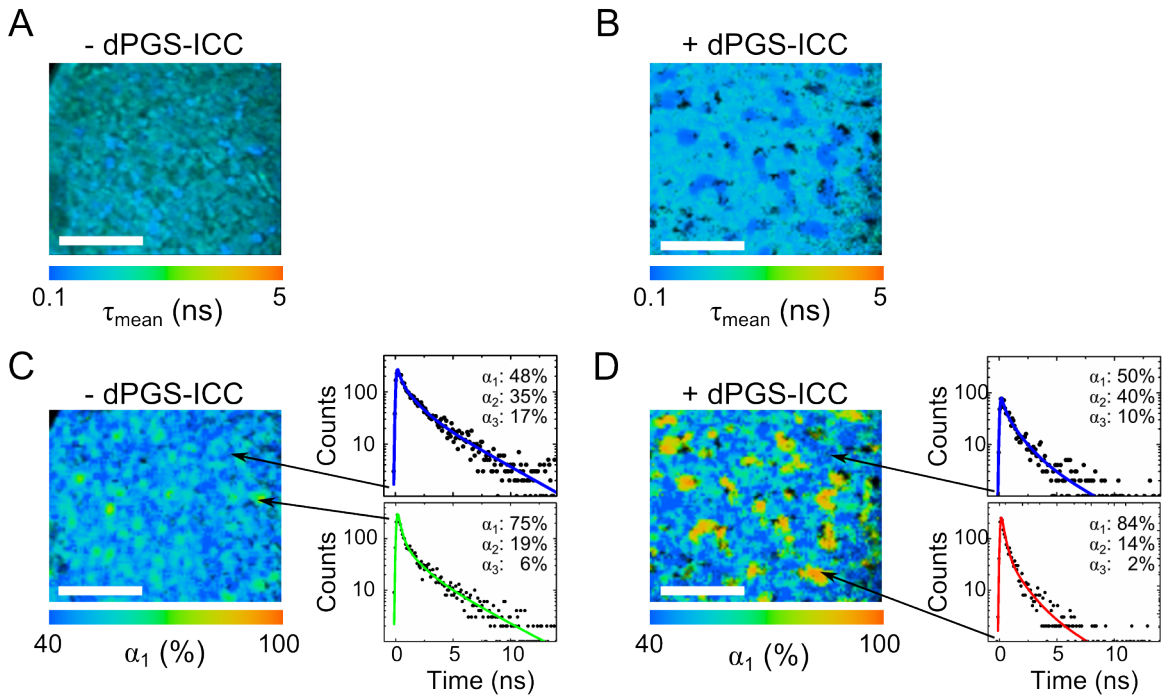

Figure 6.9. Comparison of FLIM images of paraffin embedded rat liver tissue samples with (+ dPGS-ICC) and without dPGS-ICC (− dPGS-ICC). (A, B) False color coding is according to the mean lifetime of a global fit with 3 components. (C, D) Same region as in (A,B). False color coding is based on the amplitude value α_1 of a global lifetime fit with 3 decay components (τ_1=0.27 ns, 1.1 ns, 3.5 ns). Arrows indicate areas with a characteristic distribution of the fluorescence lifetime components, the corresponding lifetime traces are shown. Scale bar: 50 µm.

Since both samples came from different rats, small intrinsic heterogeneities between the samples cannot be ruled out. Analysis of the time-resolved data of the autofluorescence found that a fit with three exponentials resulted in the best approximation of the data. The three lifetime components showed mean values of around 0.27 ns, 1.1 ns and 3.5 ns. The values of 0.27 ns and 1.1 ns contained in the autofluorescence lifetime decay are very similar to those determined by FLIM for dPGS-ICC in solution[1]. No pixels exclusively containing the dPGS-ICC lifetime curve were found. Despite the presence of the 0.27 ns and 1.1 ns components, there was always an additional lifetime component present. A global fit, keeping these three main lifetime components constant, was performed and false color images, coded according to the resulting amplitude of the fastest decay component (α_1), are shown in Figure 6.9C and D, together with representative lifetime traces. More pixels with an increased amount of the fastest decay component (α_1) were observed in the sample with dPGS-ICC. However, it is difficult to unambiguously distinguish dPGS-ICC fluorescence from background autofluorescence based on this conventional FLIM data anaysis.

[1]The fluorescence lifetime decay curves obtained by FLIM could be approximated with two exponentials, while the fluorescence decay curve measured in the cuvette experiments required three lifetime decay components. In the cuvette experiments the two fast components of 0.16 ns and 0.36 ns are relatively close together. These could not be resolved in the FLIM measurements, due to the different time resolutions, 5.34 ps ch^{-1} for the cuvette experiments compared to 90 ps ch^{-1} for the FLIM measurements, added to which the signal to noise ratio in FLIM measurements is usually not as good as in cuvette experiments. The fast lifetime component determined from the FLIM measurements is therefore the mean lifetime of the two fast components observed in the cuvette experiments. The value for the slow lifetime component determined from cuvette and FLIM experiments is comparable.

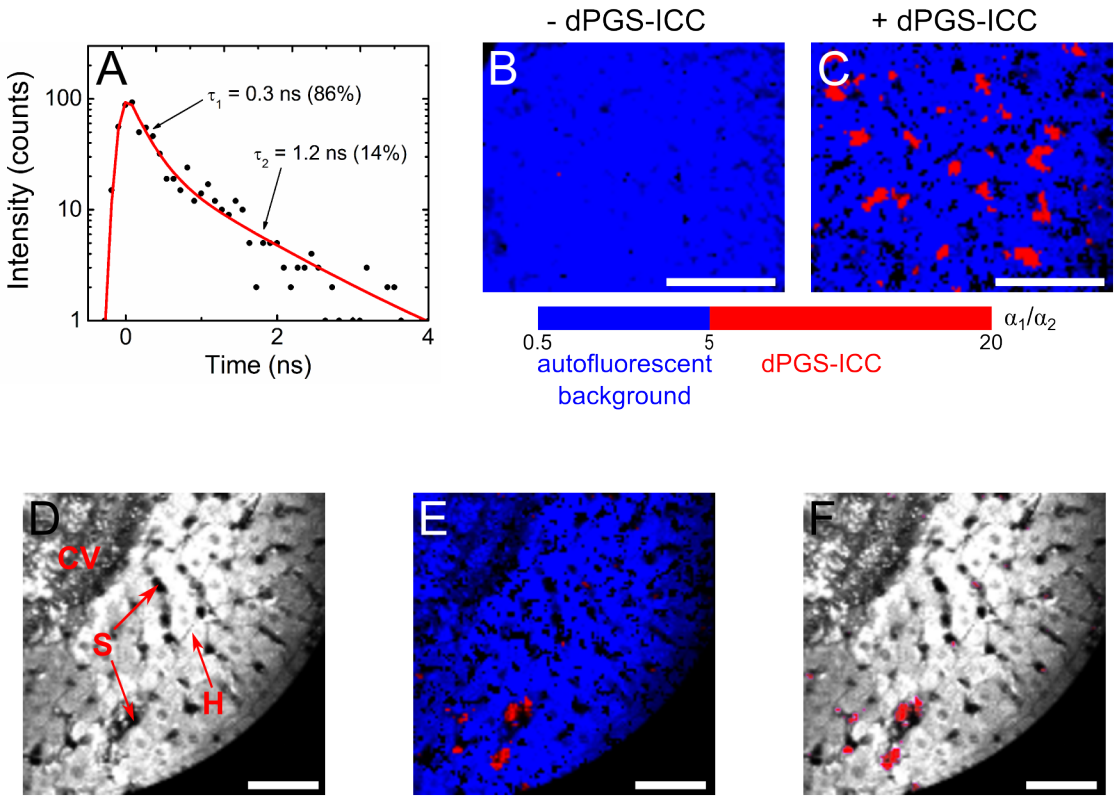

Figure 6.10. rmFLIM plots of liver tissue. (A) Fluorescence lifetime trace of dPGS-ICC. The red line is a biexponential fit to the data. (B,C) Comparison of rmFLIM images of liver sections with and without dPGS-ICC (+dPGS-ICC and -dPGS-ICC). Liver sections are identical to those shown in Figure 6.9. Color coding is based on the amplitude ratio α_1/α_2 of a global lifetime fit with three components ($\tau_1 = 0.27$ ns, $\tau_2 = 1.1$ ns, $\tau_3 = 3.5$ ns). (D) The autofluorescence of a rat liver sections with dPGS-ICC. Central vein (CV), sinusoids (S) and hepatocytes (H) are indicated. (E) False color image of (D) coded according to the fluorescence amplitude ratio α_1/α_2. Color coding as in B and C. (F) Overlay of dPGS−ICC localization (red) and autofluorescence.

dPGS-ICC localization in liver tissue identified with rmFLIM

To apply rmFLIM the amplitude ratio of the unique fluorescence lifetime decay of dPGS-ICC, as determined by FLIM measurements, was used. The short decay component (τ_1) of 0.27 ns had a relative amplitude (α_1) of 86 %, while a relative amplitude of 14 % (α_2) was observed for the longer decay component (τ_2) of 1.1 ns (Fig. 6.10A), i.e. the amplitude ratio α_1/α_2 for dPGS-ICC is around 6. To discriminate the dPGS-ICC fluorescence against the autofluorescent background, the FLIM images were color-coded according to the amplitude ratio of the two shortest lifetime components (α_1/α_2) from the global fit. The α_1/α_2-value of the autofluorescent background ranges from about 0.5 to 4.5 (Fig. 6.10B). A threshold value of 5 was used, which corresponds to 80 % and 16 % relative amplitude of the 0.27 ns and 1.1 ns lifetime species. Amplitude ratio values above 5 are colored in red and indicate the presence of dPGS-ICC, while the amplitude ratio values between 0.5 and 5 are indicative of the autofluorescent background and are colored in blue. The rmFLIM images in Figure 6.10B and C allow for a clear-cut discrimination between autofluorescent background and the localization of dPGS-ICC in the liver tissue. While in the control liver section a predominantly homogeneous blue coloring is visible (Figure 6.10B), the localization of the dPGS-ICC nanocarriers in red shows a patchy pattern (Figure 6.10C).

Figure 6.10D shows a FLIM intensity image of a liver sample from a rat with injected dPGS-ICC. Clearly discernible are the hepatocytes and sinusoids. Part of a central vein is also visible.

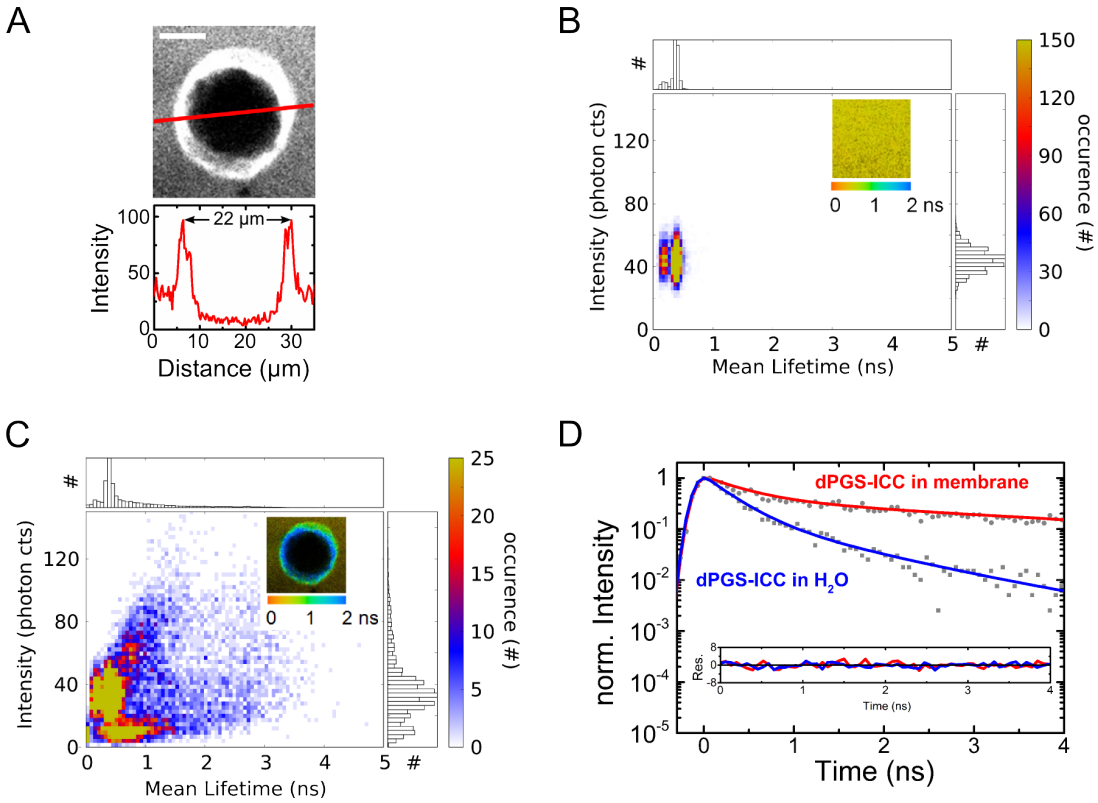

Figure 6.11. Fluorescence lifetime imaging data of dPGS-ICC interacting with GUV. (A) Intensity coded image of dPGS-ICC. The scale bar is 10 µm. Below, the intensity profile through the GUV, as indicated by the red line, is shown. (B) Scatter plot of dPGS-ICC in solution. The intensity is plotted against the mean lifetime and the corresponding histograms are shown. Bin sizes are 50 µm for the mean lifetime and 2.5 photon counts for the intensity. Inset: color coded FLIM image showing dPGS-ICC in solution. (C) Scatter plot of dPGS-ICC interacting with a GUV. Bin sizes are 60 µm for the mean lifetime and 2.5 photon counts for the intensity. Inset: corresponding color coded FLIM image. (D) Fluorescence lifetime curves for dPGS-ICC in H_2O and within the membrane as determined from FLIM measurements. Inset: the respective residues for the fit to the data are shown. GUV preparation and measurement by R. Brodwolf [Brodwolf, 2011].

The corresponding rmFLIM image identified several regions containing dPGS-ICC nanocarriers (Figure 6.10E). The overlay of dPGS-ICC localization (red) and autofluorescence places these regions to the sinusoids. This pattern reflects the location of Kupffer cells, specialized macrophages located in the liver lining the walls of the sinusoids.

Detection of dPGS-ICC in membranes - limit of rmFLIM

There is a possibility that dPGS-ICC might also interact with cell membranes. To test this possibility, we performed an experiment with a model membrane system, giant unilamellar vesicles (GUVs), to study the interaction (diploma work R. Brodwolf, [Boreham et al., 2014a]). Fluorescence lifetime imaging microscopy (FLIM) was used to record the fluorescence decay curves. Based purely on the fluorescence intensity and the corresponding intensity line profile through the DMPC lipid vesicle, it can already be seen from Figure 6.11A that dPGS-ICC interacts with the lipid bilayer of the DMPC-GUVs. Furthermore, since the fluorescence intensity within the GUV is clearly lower than in the exterior solution, dPGS-ICC does not penetrate the membrane. Plots of the intensity against the mean lifetime of each pixel show a distinct population for dPGS-ICC in solution (Figure 6.11B) characterized by a short mean lifetime of around 0.3 to 0.5 ns and intensities ranging from 40 to 70 photon counts. Upon interaction of dPGS-ICC with DMPC-GUV the plot is distinctly different (Figure 6.11C), revealing the

Table 6.1. Fluorescence lifetime parameters of dPGS-ICC determined with FLIM. The table shows the fluorescence decay times τ_i, the respective amplitudes α_i as relative values and the values of the reduced χ^2_R.

environment	τ_1(ns)	α_1 (%)	τ_2(ns)	α_2 (%)	τ_3(ns)	α_3 (%)	χ^2_R
H_2O	0.27	86	1.10	14	–	–	1.1
DMPC-GUV	0.40	66	1.10	6	4.40	29	1.1

appearance of longer ICC lifetime components when interaction of dPGS with lipid membranes occurs (Figure 2B and Table 2). The fluorescence lifetime curves show two distinct fluorescence decay signatures (Figure 6.11D). The fluorescence lifetime of dPGS-ICC in the presence of the lipid membrane model system is characterized by three decay components of 0.40 ns, 1.1 ns, and 4.4 ns (Table 6.1). The individual components are slower than those observed for dPGS-ICC in water using FLIM (Table 6.1), and also slower than those obtained for dPGS-ICC in ethanol from cuvette experiments (Table 6.1).

Using this fluorescence lifetime decay curve, rmFLIM was applied to the dPGS-ICC in rat liver samples, to see if dPGS-ICC is localized to a membrane environment. To this end, rmFLIM images color coded according to the amplitude ratio of the amplitude of the fast lifetime (α_1) and the slowest lifetime (α_3) were computed. However, this resulted in more identifications in the control sample which did not have any dPGS-ICC applied, than in the sample with dPGS-ICC (Figure 6.12). This indicates that the rmFLIM analysis is not applicable when the target molecule displays fluorescence lifetime decay curves with more than two fluorescence decay components.

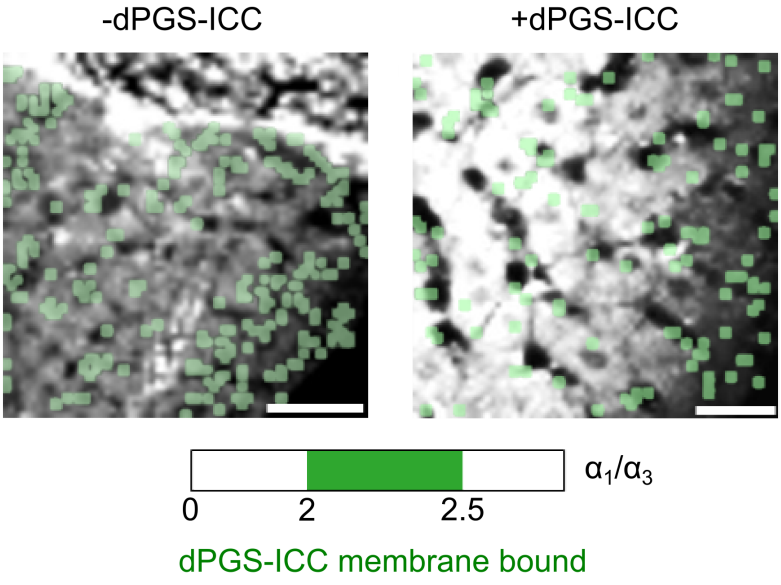

Figure 6.12. Limits of the ratiometric FLIM analysis. rmFLIM images of rat liver sections with (+dPGS-ICC) and without (-dPGS-ICC) dPGS-ICC color coded according to the amplitude ratio α_1/α_3 of dPGS bound to DMPC-GUV membranes. Green areas correspond to an amplitude ratio α_1/α_3 of 2.0 to 2.5. Scale bars: 25 µm

6.2.3 Skin penetration properties of CMS-ICC

Topical application and transdermal drug delivery is thought to be beneficial, e.g. regarding the treatment of localized skin diseases. However, the problem faced by all topically applied systems for transdermal drug delivery is the skin barrier. Currently there is a controversial debate on whether nanosystems can overcome the skin barrier. The required properties for the penetration of the nanosystem, as well as the potential transport pathways, are not understood. As a consequence, a case-by-case study is necessary for each nanosystem under consideration for transdermal application.

In cooperation with Prof. Schäfer-Korting (Institute of Pharmacy, Freie Universität Berlin) and Prof. Haag (Institute of Chemistry and Biochemistry, Freie Universität Berlin) the skin penetration of dendritic core-multishell nanocarriers in normal and damaged skin was investigated. CMS-ICC nanotransporters were applied onto normal and tape-stripped human skin. We then performed FLIM measurements on skin sections to investigate the penetration properties of the CMS-ICC nanocarrier into intact and tape-stripped skin. The data was analyzed with cluster-based FLIM analysis routines, a new method for FLIM data analysis developed by R. Brodwolf in the group of Prof. Alexiev. It is capable to detect specific lifetime signatures, e.g. of target molecules, against high fluorescence backgrounds and overcomes the limitations of rm-FLIM. The results presented here a part of a publication by N. Alnasif, C. Zoschke, E. Fleige, R. Brodwolf, A. Boreham, E. Rühl, K.-M. Eckl, H.-F. Merk, H. C. Hennies, U. Alexiev, R. Haag, S. Küchler and M. Schäfer-Korting [Alnasif et al., 2014]. All skin samples were prepared by N. Alnasif in the group of Prof. Schäfer-Korting.

To compare the penetration properties in normal skin and skin with a barrier deficiency, tape-stripped skin, CMS-ICC was topically applied to both skin types for 24 h. The cluster-based FLIM analysis of the measurement data identified two lifetime clusters for CMS-ICC in normal skin, differing from the autofluorescent background, while in tape-stripped skin only one such cluster was observed (Figure 6.13B,C). In normal skin, one of the two clusters (cyan, Figure 6.13B) is located within the first 50 µm of the skin sample and hardly beyond. Hence, it is limited to the SC and the epidermis. The other cluster (red, Figure 6.13B) is nearly exclusively found at distances larger than 50 µm from the skin surface, i.e. in the dermis. The localization of the sole cluster observed in tape-stripped skin (red, Figure 6.13C) is independent from the distance to the skin surface. This cluster was observed continuously from the skin surface to deeper skin layers, at least 200 µm deep. As the SC is basically completely removed in tape-stripped skin by 30 stripping repetitions this region coincides with the epidermis and dermis. As a control, ICC was also applied to normal skin for 24 h. Cluster-based FLIM analysis of the measurements on the control sample revealed a distinct lifetime cluster for ICC. This cluster is localized to the *stratum corneum* (SC) but not in deeper skin layers (Figure 6.13A). The corresponding lifetime curve clearly differs from that obtained for ICC in solution, with a much slower fluorescence lifetime decay for ICC in the skin (Figure 6.13D,E).

The lifetime decay curves of the different clusters observed in normal and tape-stripped skin, as well as for the ICC control sample, were compared in the different skin layers. In the SC the fluorescence lifetime decay curve for CMS-ICC and ICC clearly differed (Figure 6.13E). The fluorescence lifetime decay for ICC is prolonged compared to CMS-ICC. These differences probably stem from the protection of the ICC within the CMS nanocarrier structure, as there is a double shell which surrounds the ICC bound to the polyglycerol core of CMS nanocarriers. As ICC was not detected in the epidermis of the control sample, only the lifetime decay curves of CMS-ICC could be compared for epidermal and dermal layers. A difference between the lifetime decay curve in normal skin and tape-stripped skin was discernible in the epidermis (Figure 6.13F). In the dermis, however, no such differences between the lifetime decay curve of the respective cluster in normal skin and tape-stripped skin could be identified (Figure 6.13G).

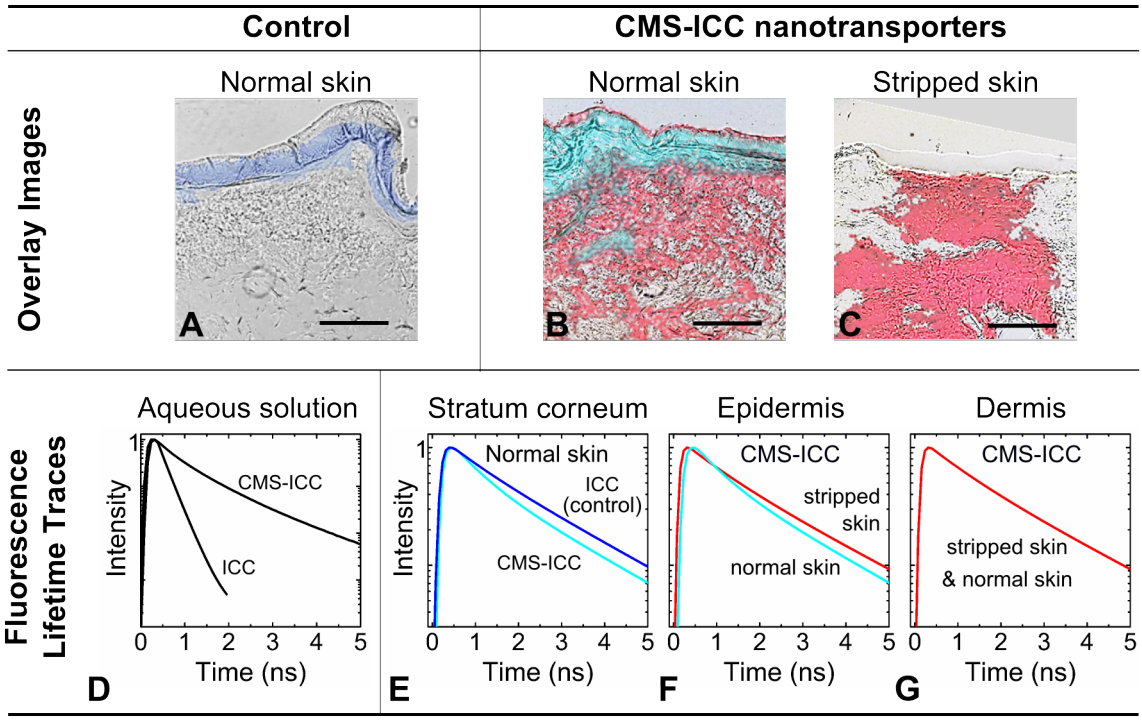

Figure 6.13. Fluorescence lifetime microscopy (FLIM) of CMS-ICC nanotransporters. CMS-ICC nanotransporters were applied onto normal and stripped human skin for 24 h. Representative overlay images (FLIM and bright field) of the same area are shown: (A) As a control, an aqueous ICC solution was applied to normal skin. CMS-ICC nanotransporters were applied to (B) normal skin and (C) stripped skin. The false color coding is based on the unique fluorescence lifetimes of CMS-ICC nanotransporters (cyan, red) or ICC (blue) in the different skin layers. (D) The fluorescence lifetime traces of CMS-ICC nanotransporters and ICC in aqueous solution are shown. (E-G) The fluorescence lifetime traces of CMS-ICC nanotransporters and ICC are shown in the same colors as used in the corresponding overlay images (A-C). All lifetime traces are normalized to 1. Scale bar: 100 µm. (Reprinted from [Alnasif et al., 2014] Copyright 2014, with permission from Elsevier.)

6.2.4 Skin penetration properties of hyaluronic acid and BSA

A biomolecule known to act as an enhancer for topical drug application is hyaluronic acid (HA). Beside its moisturizing capacities it has been used as a transport vehicle for diclofenac [Pirard et al., 2005, Peters and Foster, 1999, Moore and Willoughby, 1995, Brown et al., 1995, Brown and Jones, 2005]. For applications such as intraepidermal vaccinations the delivery of larger molecules, such as proteins, is of interest [Joshi et al., 2014]. In collaboration with Dr. S. Küchler (Institute of Pharmacy, Freie Universität Berlin), M. Witting (Institute for pharmaceutical Technology and Biopharmaceutics, Ludwigs-Maximilians-Universität Munich) and coworkers we were investigating the penetration properties of hyaluronic acid and the model protein bovine serum albumin (BSA) using FLIM.

Bovine serum albumin is a fairly large protein consisting of around 600 amino acids and with a molecular weight of 66 kDa. Fluorescently labeled BSA has been used as a model protein to investigate the penetration of large molecules through skin, e.g. in dependence of the hydration state [Tan et al., 2010] or after skin roller application [Wang et al., 2011], and also as a model protein drug loaded onto nanocarriers [Choi et al., 2012, Poree et al., 2011].

In my work the influence of different HA molecular weights (5 kDa, 100 kDa and 1 MDa) on the penetration of BSA in two skin types, normal skin and, as a model for barrier deficient skin, tape-stripped skin was assessed. For comparison the two components were also investigated separately on both skin types. To allow for visualization of HA and BSA with FLIM both were fluorescently labeled (labeling was performed by M. Witting). HA was labeled with N-methylanthraniloyl (MIA) and BSA with RhodaminB-isothiocyanate (RhB-ITC). In my work, FLIM measurements were performed and, due to the tissue autofluorescence, the cluster FLIM analysis was used to detect the presence of the fluorescently labeled HA and BSA within the skin.

Spectroscopic characterization

First, solutions of fluorescently labeled HA and BSA were characterized regarding their fluorescence properties, providing information on suitable settings for the FLIM experiments. As shown in Figure 6.14A, coupling of MIA to HA, yielding HA-MANT, results in a red shift of the dye absorption with a maximum at 350 nm. However, the broad HA-MANT absorption band allowed for excitation with a 405 nm pulsed diode laser available in the FLIM setup. Absorption and emission properties of HA-MANT samples were independent of the molecular weight (Figure 6.14A) and the emission maximum was at 440 nm.

For RhB-ITC coupled to BSA (BSA-RhB) both the absorption spectrum and emission spectrum were hardly altered compared to RhB (Figure 6.14B), with absorption and emission peak values of 558 nm and 585 nm respectively for BSA-RhB. Since the emission and absorption of the dye labeled conjugates showed an overlap region (Figure 6.14C) they are suited for fluorescence resonance energy transfer (FRET) measurements, which provide information on the distance between the two dyes and hence also between HA and BSA.

Skin type dependent penetration of HA

FLIM measurements were first performed on cryosections of pig skin only treated with HA-MANT to analyze the penetration behavior of HA on its own. With cluster-based FLIM image analysis one lifetime decay cluster belonging to HA-MANT was identified both in normal skin (Figure 6.15A-C) and in tape-stripped skin. In normal skin it was localized to the stratum corneum and epidermis for 5 kDa HA-MANT, albeit rather patchily (Figure 6.15A). For the other two molecular weights the cluster is basically confined to the *stratum corneum* (SC), though with

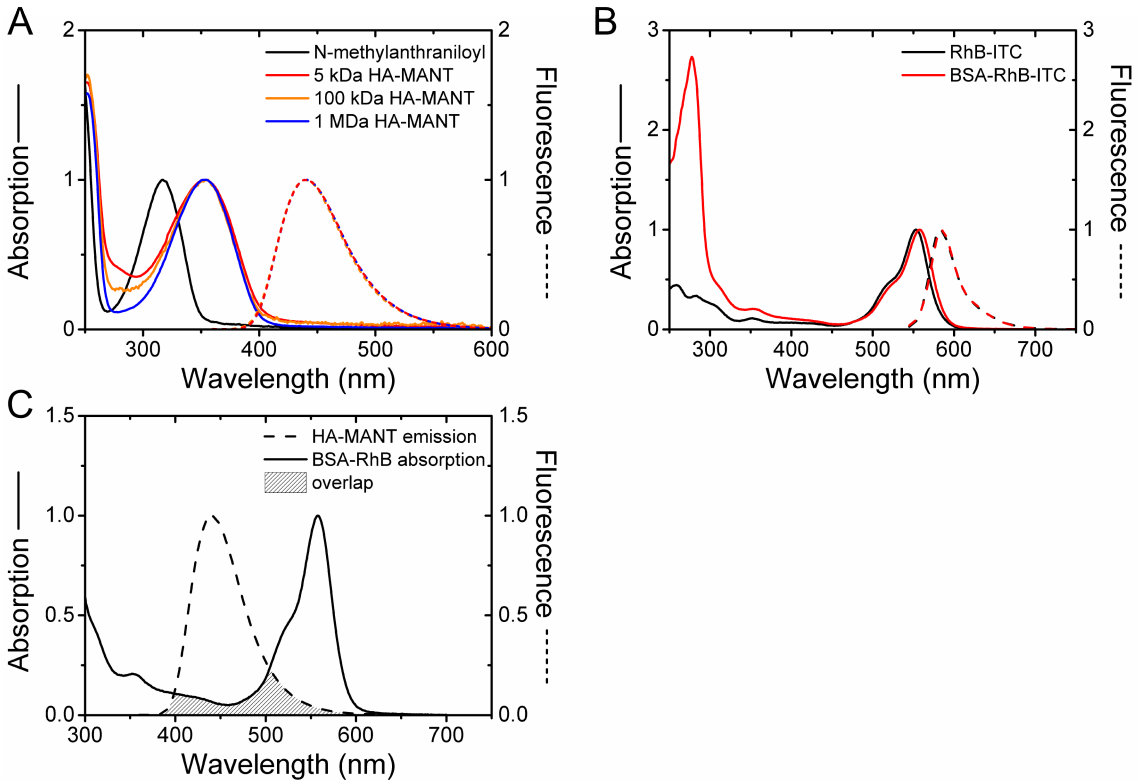

Figure 6.14. Spectral characteristic of HA-MANT and BSA-RhB samples. (A) Absorption spectra, shown as solid line, and emission spectra, depicted as dashed lines, of HA-MANT samples (5 kDa, 100 kDa, 1 MDa). For comparison the absorption spectrum of MIA is also shown. (B) Absorption spectra, shown as solid line, and emission spectra, depicted as dashed lines, for BSA-RhB and RhB. Emission spectra were recorded with 488 nm excitation. (C) Comparison of HA-MANT emission spectra (dashed line, 5 kDa) and BSA-RhB absorption spectra (solid line). The overlap region is highlighted (striped region).

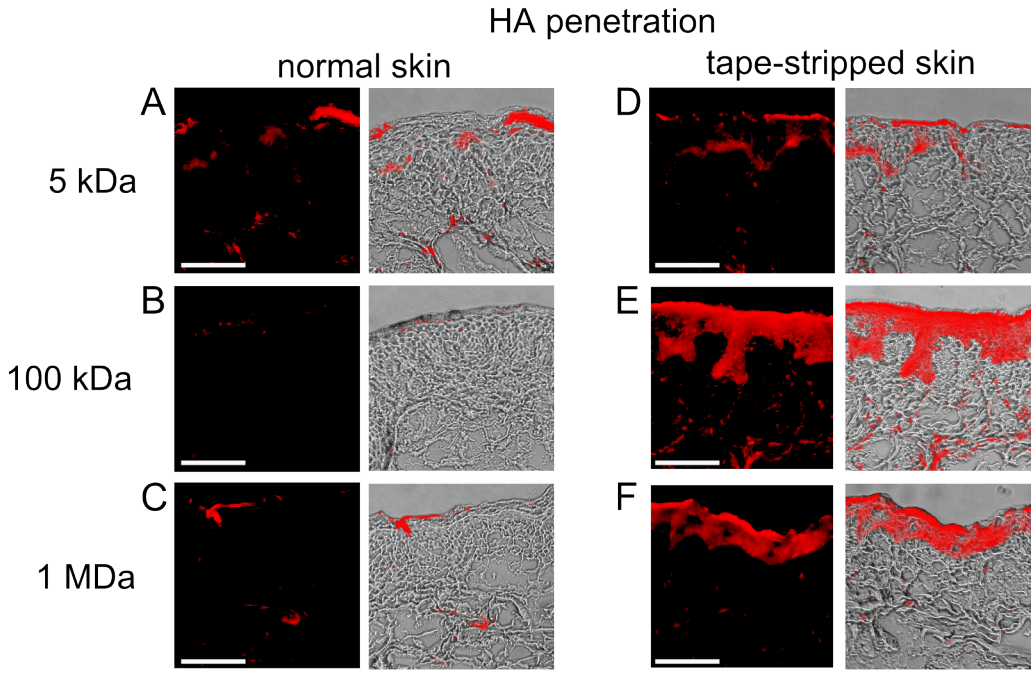

Figure 6.15. Analysis of HA-MANT penetration. For each sample a characteristic area was chosen and false color coded cluster FLIM images of the HA-MANT clusters are shown alongside an overlay of the false color coded image on the corresponding bright field image. Results for 5 kDa, 100 kDa and 1 MDa HA-MANT in (A-C) normal skin and (D-F) tape-stripped skin are shown. Scale bars: 100 µm.

even less patches than observed for 5 kDa HA-MANT (Figure 6.15B,C). In contrast, in tape-stripped skin the cluster belonging to HA-MANT was localized to both the SC and epidermis, independent of the molecular weight of HA.

Skin type dependent penetration enhancement or confinement of BSA by HA

Next, the penetration properties of BSA and the effect of HA on BSA penetration was investigated. The penetration properties of BSA alone were investigated by FLIM measurements on cryosections of pig skin samples treated with BSA-RhB and subsequent cluster-based image analysis. In normal skin, a single lifetime cluster belonging to BSA-RhB could be identified (colored red in Figure 6.16A). This cluster is localized to the SC and epidermis. In tape-stripped skin two distinct lifetime clusters belonging to BSA-RhB could be identified (Figure 6.16B). One is localized to the viable epidermis, colored cyan in Figure 6.16B, and the corresponding lifetime decay deviates strongly from the autofluorescent background as well as from the lifetime decay of the single cluster observed for normal skin (Figure 6.16I). The second cluster is primarily located in the dermis, colored red in Figure 6.16B, and the lifetime decay corresponds to the lifetime decay determined for BSA-RhB in normal skin (Figure 6.16I).

To investigate the effect of HA on BSA penetration, cryosections of intact and tape-stripped pig skin treated with different molecular weight HA-MANT together with BSA-RhB were prepared. The penetration of BSA-RhB was then analyzed. In normal skin, a single lifetime cluster belonging to BSA-RhB could be identified for all three HA molecular weights (colored in red in Figure 6.16C,E,G). However, localization of this BSA-RhB cluster to the epidermis was only observed in the presence of 5 kDa (Figure 6.16C). In the presence of 100 kDa and 1 MDa the occurrence of this cluster was reduced and limited to the SC (Figure 6.16E,G). In

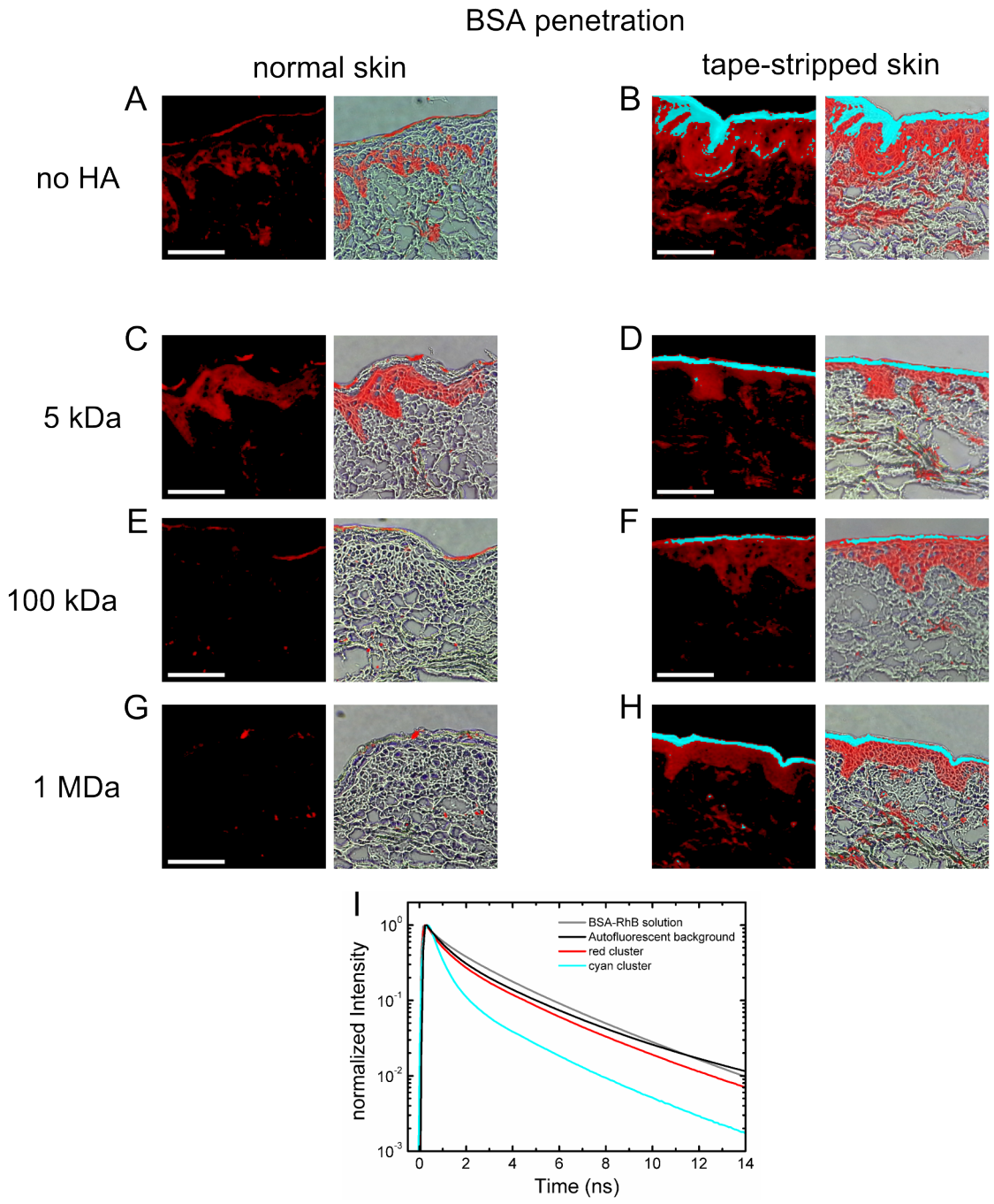

Figure 6.16. Analysis of the penetration of BSA-RhB in normal and tape-stripped skin. For each sample a characteristic area was chosen and false color coded cluster FLIM images of the BSA-RhB clusters are shown alongside an overlay of the false color coded image on the corresponding bright field image. (A,B) Only BSA-RhB, (C,D) BSA-RhB and 5 kDa HA-MANT, (E,F) BSA-RhB and 100 kDa HA-MANT, (G,H) BSA-RhB and 1 MDa HA-MANT. Scale bars: 100 µm. (I) Lifetime curves determined by cluster-based FLIM analysis: autofluorescent background (black), BSA-RhB in solution (gray) and the respective lifetime of the identified cluster (red, cyan).

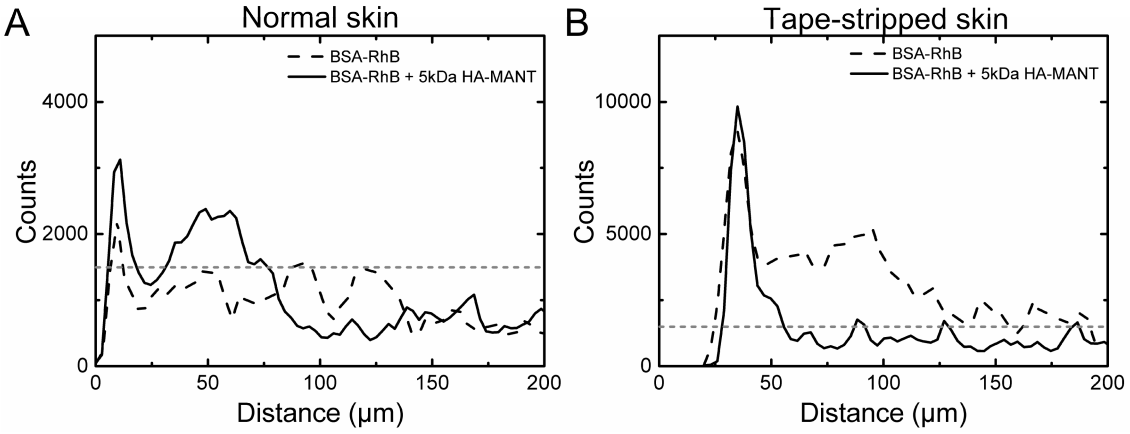

Figure 6.17. Effect of HA on BSA penetration. Averaged intensity line scans for BSA-RhB alone (dashed line) and with 5 kDa HA (solid line) in (A) normal skin and (B) tape-stripped skin. Dashed gray line indicates the background intensity level.

tape-stripped skin, two clusters belonging to BSA were identified for all HA molecular weights (Figure 6.16D,F,H). One, colored in cyan, in the SC and the other, colored in red, in the epidermis, but not in the dermis. The localization of BSA was independent of the molecular weight of HA.

As the fluorescence lifetime is independent of the fluorophore concentration, we used the intensity information to infer the relative amounts of BSA in the respective cluster regions. Averaged intensity line scans for BSA alone and BSA with 5 kDa HA were compared (Figure 6.17). In normal skin the intensity for BSA-RhB with 5 kDa HA is increased in the SC (first 20 nm) and epidermis compared to BSA-RhB alone, where the observed intensities were close to the autofluorescent background (Figure 6.17A). In tape-stripped skin, the intensities observed for BSA-RhB alone were greatly increased compared to the autofluorescent background (Figure 6.17B). The highest increase was found close to the surface of tape-stripped skin, and clearly elevated intensities were found up to 100 nm into the skin. For BSA-RhB in the presence of 5 kDa HA-MANT, high peak values close to the surface were also found, but the intensity dropped to background levels 30 nm into the tape-stripped skin (Figure 6.17B).

Molecular interactions between HA and BSA in skin

The analysis of BSA and HA penetration identified overlapping regions for BSA and HA penetration and the spectroscopic analysis showed that FRET could occur between HA-MANT and BSA-RhB. Hence, the occurrence of FRET emission was investigated on skin samples containing both HA-MANT and BSA-RhB by exciting the samples with 405 nm and detecting the emission between 590 nm and 650 nm, termed FRET channel in the following, specific for BSA-RhB emission. However, the spectroscopic analysis also showed that BSA-RhB exhibits an absorption at 405 nm (Figure 6.14). Therefore fluorescence emission detected in the FRET channel cannot be solely attributed to FRET between HA-MANT and BSA-RhB. It is still possible to determine if the fluorescence signal contains FRET emission, but only if one is able to determine the non FRET emission contribution to the total fluorescence signal. To this end, the emission intensities of BSA-RhB in solution excited at 405 nm and 488 nm were recorded in a fluorescence spectrometer, and the emission intensity was found to be identical (Figure 6.18A). Next, a pig skin sample only treated with BSA-RhB was measured with FLIM. Intensity line scans at identical sample positions showed an intensity difference for excitation at 405 nm compared to 488 nm

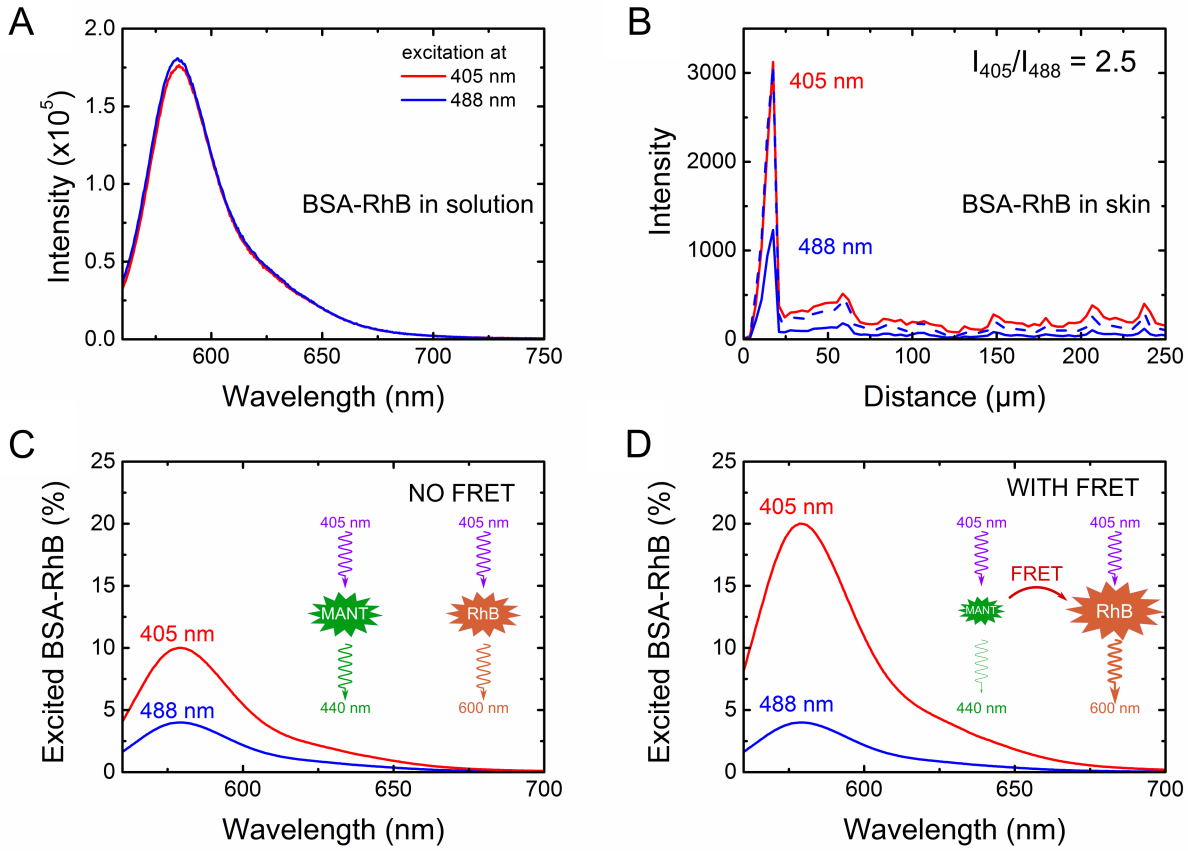

Figure 6.18. Determination of FRET correction factor. (A) Emission spectra of a BSA-RhB in solution excited either at 405 nm or 488 nm. (B) Characteristic intensity line scan of a sample only treated with BSA-RhB and excited either at 405 nm (red curve, pulsed diode laser) or 488 nm (blue curve, Ti:Sa laser). The correction factor of 2.5 was determined from the intensity ratio of the respective peak intensities. The corrected intensity line scan for 488 nm excitation is also shown (dashed blue). Emission filter: HQ620/60. (C,D) Expected emission behavior of samples with both BSA-RhB and HA-MANT in the absence (C) and the presence (D) of FRET. (C) From a total population of BSA-RhB molecules the percentage of excited BSA-RhB differs by a factor of 2.5 between excitation at 488 nm (blue curve) and 405 nm (red curve) when no FRET occurs from MANT to BSA-RhB. Only the BSA-RhB directly excited by 405 nm will contribute to the emission signal above 590 nm. (D) When FRET occurs the same amount of BSA-Rhb is still excited by the 405 nm excitation. Additionally, further BSA-RhB molecules are excited via FRET from HA-MANT, thus increasing the emission signal above 590 nm for 405 nm excitation but not for 488 nm excitation. Hence, the emission intensity ratio I_{ex405}/I_{ex488} will be increased.

(Figure 6.18B). The intensity ratio I_{405}/I_{488} was 2.5. The intensity ratio observed here is due to different laser output powers between the 405 nm pulsed diode laser and the 488 nm excitation from the Ti:Sa laser. In BSA-RhB and HA-MANT samples the FRET contribution can now be determined from a measurement with 488 nm excitation. Assuming no FRET occurs, the ratio of the intensities I_{405}/I_{488} is 2.5 (Figure 6.18C). If FRET occurs, the emission detected for 405 nm excitation should be more than 2.5 times higher than the emission detected for 488 nm excitation, due to additional RhB emission excited by FRET (Figure 6.18D).

The false color coded images from cluster-based FLIM analysis are presented alongside a comparison of line scans measured at 405 nm and 488 nm, allowing for the detection of FRET emission (Figure 6.19). A single lifetime decay curve belonging to BSA-RhB emission was identified in normal skin as well as in tape stripped skin. In normal skin the cluster was localized to the SC and epidermis for 5 kDa HA, mainly to the SC for 100 kDa HA, and nearly absent for 1 MDa HA. In tape-stripped skin the localization was in the SC and epidermis for

5 kDa HA, mainly to epidermis for 100 kDa HA, and in the SC for 1 MDa HA respectively. The intensity line scans of the samples were then evaluated to determine if FRET emission from BSA-RhB contributes to the observed BSA-RhB emission. An intensity ratio I_{405}/I_{488} larger than 2.5 was observed for BSA-RhB in the presence of 5 kDa HA as well as 100 kDa HA in normal skin (Figure 6.19A,B). For all other samples no contribution from FRET emission to the total fluorescence intensity could be detected (Figure 6.19C-F).

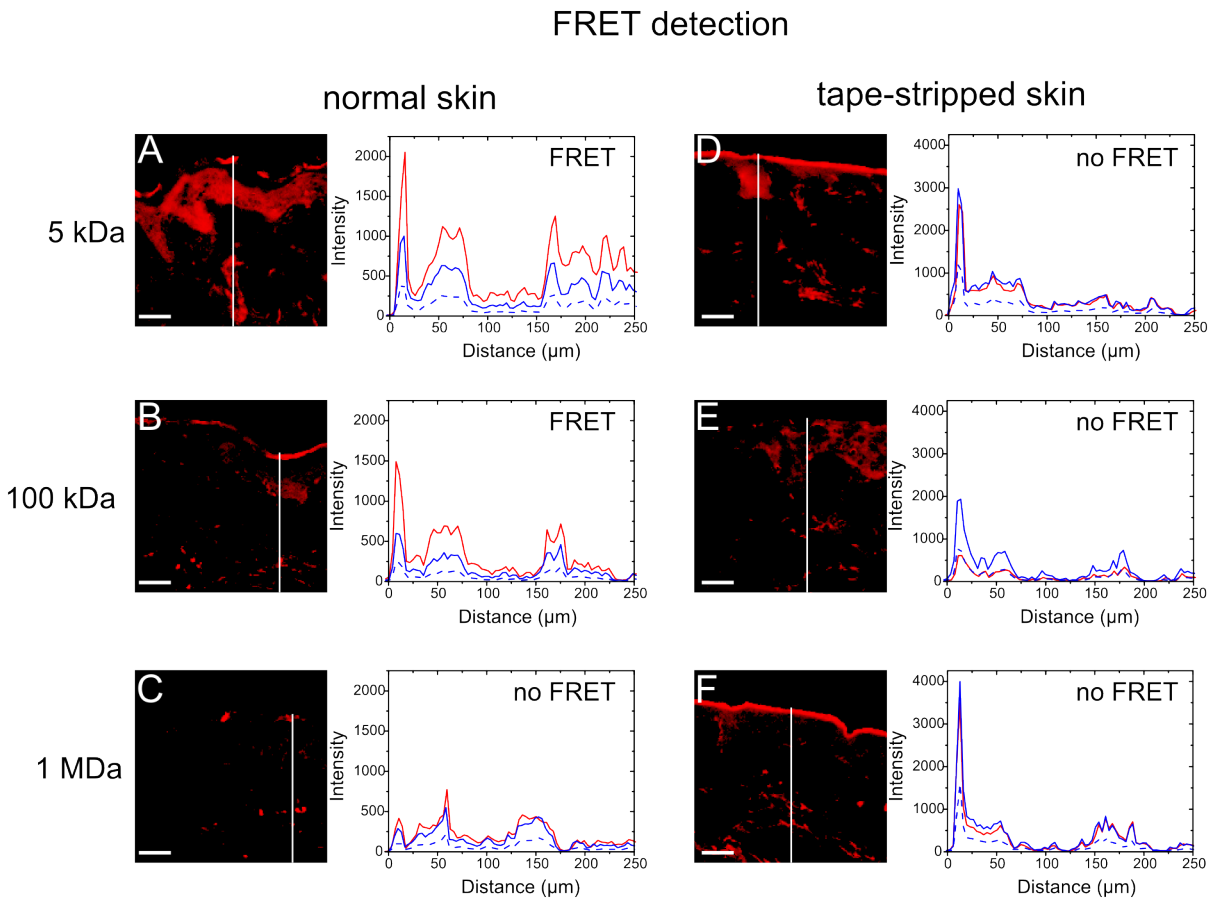

Figure 6.19. Cluster FLIM images for FRET induced BSA-RhB emission and characteristic line scans for excitation at 405 nm (red curve) and 488 nm (dashed blue curve) as well as the corrected curve for 488 nm excitation (blue curve) are shown. Samples containing both BSA-RhB and HA-MANT were excited at 405 nm and emission was detected through a HQ620/60 emission filter specific for BSA-RhB emission. The images obtained from the cluster-based FLIM analysis are shown for the three HA-MANT molecular weights in normal skin (A-C) and tape-stripped skin (D-F). Vertical white lines indicate the position at which the line scan was taken. Scale bars: 50 µm.

6.2.5 Localization of silica nanoparticles in skin

In the previous sections, particle penetration of the skin barrier was analyzed for both synthetic nanocarriers, CMS, and the penetration enhancing effect of biological molecules, hyaluronic acid. One important aspect of particles penetrating the skin barrier and thus entering the organism is the subsequent distribution within the tissue and the whole organism. Here, in cooperation with Prof. Gruber (Department of Veterinary Medicine, Freie Universität Berlin) we used FLIM to investigate the biodistribution of functionalized silica nanoparticles in mouse skin. The results presented here are part of a publication by Ostrowski, D. Nordmeyer, A. Boreham, R. Brodwolf, L. Mundhenk, J. W. Fluhr, J. Lademann, C. Graf, E. Rühl, U. Alexiev and A. D. Gruber [Ostrowski et al., 2014].

Silica particles were injected only into the right flanks of mice with intact skin. Each mouse received an injection with a solution containing 250 µg of AHAPS-functionalized silica nanoparticles once a day over the duration of five days. Tissue samples from the right flank, and also of the contralateral side, the left flank, were prepared and analyzed by FLIM. All samples were prepared by A. Ostrowski in the group of Prof. Gruber. AHAPS functionalized silica nanoparticles were prepared in the group of Prof. Rühl (Department of Chemistry, Freie Universität Berlin).

Figure 6.20 shows intensity images and false color images from FLIM measurements of skin sections from both flanks. Vertical scans, from the stratum corneum right down into the subcutis (Figure 6.20A,B), consist of at least four overlapping measurements, in the case of the right flank five measurements, each with a measurement time of 15 min. Data acquisition was conducted using the SPC software (Becker&Hickl), while data analysis was carried out using an analysis software, based on cluster analysis algorithms, developed in the group. Certain defining structures, such as the ragged barrier that is the stratum corneum, the muscle strands and the contour of the fatty tissue cells can already be clearly identified in the intensity images (Figure 6.20A,B). In the right flank (Figure 6.20B) the muscle strands are well dissected, whereas in the contralateral side (Figure 6.20A) the individual muscle strands are not as pronounced, although the muscular band can still be easily identified. The contralateral side, on the other hand, contains a section through a blood vessel, with a substantial number of blood cells. Using the cluster analysis software, three distinct lifetime regimes could be separated. The main cluster is false color coded in green and could be assigned to the autofluorescent background, whereas the lifetime cluster associated with the erythrocytes is shown in cyan, see (Figure 6.20C). The red coded cluster only occurs in the right flank, the side of injection, and is nearly exclusively localized to the subcutis (Figure 6.20D). This cluster is indicative of the AHAPS functionalized silica particles. The lifetime curves are shown in Figure 6.20E and the parameters associated with the individual lifetime curves are summarized in Table 6.2.

The high particle density suggests that the section imaged here is very close to the initial site of application. The high particle density does not allow for the visualization of individual cells

Table 6.2. Lifetime parameters for the three separated clusters

cluster	τ_1 (ns)	α_1 (%)	τ_2 (ns)	α_2 (%)	τ_3 (ns)	α_3 (%)	τ_4 (ns)	α_4 (%)
autofluorescence	0.39	36	1.23	32	2.64	24	4.97	7
AHAPS-SiNP	0.46	64	0.94	16	2.24	13	2.95	6
erythrocytes	0.25	60	0.64	31	1.69	9	-	-

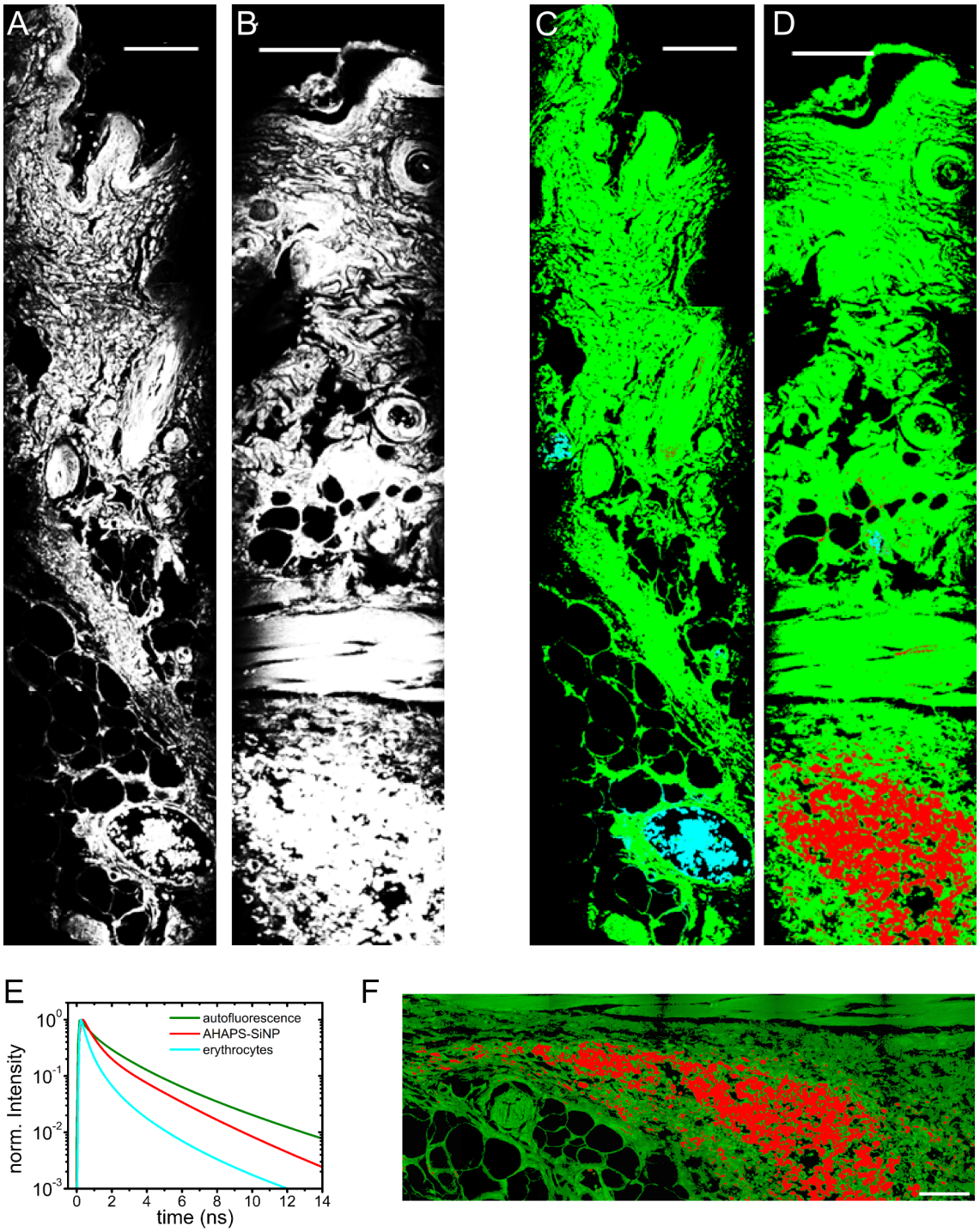

Figure 6.20. FLIM measurements of the injection side and the contralateral side. Intensity images of vertical scans through the contralateral side (A) and the side with injected particles (B) are shown together with the corresponding false color coded cluster FLIM images (C,D). The autofluorescent background is colored in green, the erythrocyte associated cluster in cyan and the cluster identified with the particles in red. The respective lifetime curves are shown (E). (F) is a lateral scan through the subcutis, just below the muscle, of the right flank. High particle density is observed on the right side of the image and markedly lower density on the left. Scale bars: 100 µm

having taken up particles. Therefore lateral scans along the muscle strand were conducted to identify regions with reduced particle density. Figure 6.20F shows such a lateral scan consisting of 6 individual overlapping measurements, spanning nearly 1 mm. It can clearly be seen that the region with the highest particle density is towards the right side of the image, whereas the particle density is drastically reduced toward the left side of the image.

A representative section of a region with low particle density is shown in Figure 6.21A together with a vertical line scan through the section. For comparison, Figure 6.21B shows a corresponding section from the contralateral side, also with a characteristic line scan. The line scans clearly show a dramatic increase in the fluorescence intensity in regions containing the particles. Intensities from autofluorescence reach a maximum of around 500 counts, both in the right flank and in the contralateral side, whereas the regions associated with the AHAPS silica FITC particles exhibit intensities from 1000 up to 5000 counts. In Figure 6.21 the particle clusters were seen to be located inside macrophages. Regions with macrophages, as e.g. indicated by the white box in Figure 6.21A, were measured with an increase in the resolution factor of 5. The resulting false color coded image for the region highlighted in Figure 6.21A is shown in Figure 6.21C. The outline of a macrophage is indicated by the dashed white line. It can clearly be seen that multiple particle clusters are localized within the macrophage, possibly associated with endocytotic compartments such as endosomes. A line scan through the macrophage is also shown, and the intensity peaks associated with the particle clusters are clearly discernible. The reduced peak intensities compared to Figure 6.21A are due to the increased resolution. The intensity of 5 by 5 pixels in Figure 6.21C corresponds to the intensity of one pixel in Figure 6.21A.

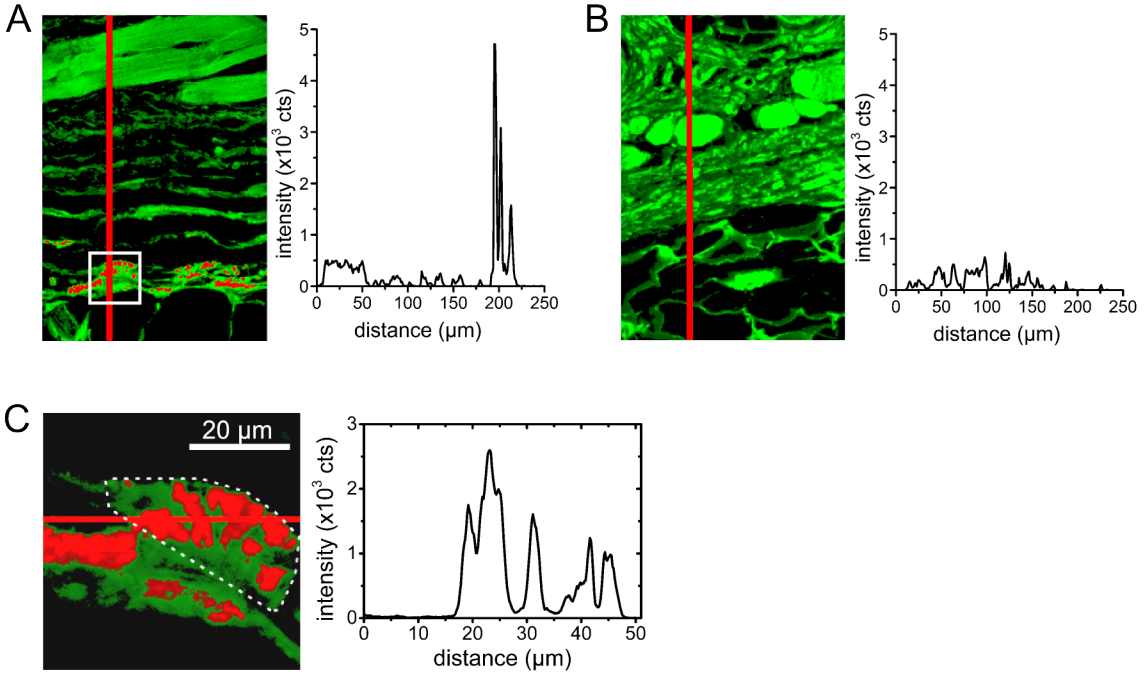

Figure 6.21. Silica clusters in macrophages detected by cluster FLIM analysis. Measurements of a region with low particle density (A) indicate particle clusters within macrophages. Line scans show the intensity profile. (B) Contralateral side does not show any particle clusters and the line scan thus only shows the autofluorescent background. (C) Measurement of the area indicated by the white box in (A) with an increased resolution (factor 5). Dotted white line indicates the macrophage outline and the line scan corresponding to the red line is shown.

Quantitive determination of particle number

The question arose how to approximate the amount of particles taken up by the macrophages. To this end a sample with a defined final concentration of 2.5 µg/µl silica FITC particles was produced. This sample was used as a reference sample, allowing for the correlation of a certain intensity with particle concentration and number. The exact procedure is described below.

For the analysis of the reference sample, an area of 284 x 284 pixels, i.e. 80 650 pixels in total, was selected, corresponding to an area of 50 µm x 50 µm. The integral intensity over all these pixels was calculated to be $1.966 \cdot 10^6$ counts, i.e. 24 counts per pixel. In order to correlate this intensity with the particle amount in micrograms, the volume of the corresponding section is needed. The area size is known to be 50 µm x 50 µm and the height was approximated with the thickness of the paraffin section, i.e. 10 µm. Hence, the volume is estimated as

$$50\,\mu\text{m} \cdot 50\,\mu\text{m} \cdot 10\,\mu\text{m} = 2.5 \cdot 10^{-5}\,\mu\text{l}\,, \tag{6.1}$$

and the mass of the particles in this volume can be calculated using the concentration of $2.5\,\mu\text{g}\,\mu\text{l}^{-1}$ of the solution,

$$m = 2.5\,\frac{\mu\text{g}}{\mu\text{l}} \cdot 2.5 \cdot 10^{-5}\,\mu\text{l} = 62.5\,\text{pg}\,. \tag{6.2}$$

Relating the mass of the particles within the volume of $2.5\,\mu\text{g}\,\mu\text{l}^{-1}$ to the integral intensity results in $1.966 \cdot 10^6$ counts being equal to 62.5 pg, or when normalized to the total amount of pixels, 24 counts equal $7.75 \cdot 10^{-10}$ µg.

In the next step, the total intensity within the particle clusters of the macrophage was obtained. The integral intensity was determined to be 291 358 counts allowing to calculate the total mass of the nanoparticles within the macrophage, using the calibration for the micrograms per counts from the reference sample.

$$291358\ \text{counts} \cdot \frac{7.75 \cdot 10^{-10}\,\mu\text{g}}{24\ \text{counts}} = 9.4\,\text{pg}\,. \tag{6.3}$$

Hence, the macrophage has taken up about 9.4 pg of Silica FITC particles. As the communicated particle content (D. Nordmeyer, Institute of Chemistry and Biochemistry, Freie Universität Berlin) is such, that 1 ml of a $5\,\text{g}\,\text{l}^{-1}$ solution contains $2.8698 \cdot 10^{13}$ particles, the particle number within 9.4 pg can be derived

$$\begin{aligned} c = 5\,\frac{\text{g}}{\text{l}} = 5\,\frac{\text{mg}}{\text{ml}} &= 2.8698 \cdot 10^{13}\ \frac{\text{particles}}{\text{ml}}\,, \\ 5\,\text{mg} &= 2.8698 \cdot 10^{13}\ \text{particles}\,, \\ 9.4\,\text{pg} &= 56\,400\ \text{particles}\,. \end{aligned}$$

Since the particle clusters comprise 3626 pixels, 15.6 particles are contained, on average, in one pixel within the particle clusters inside the macrophage.

As a control, the volume taken up by 56 400 particles was calculated and compared with an estimated volume for a macrophage. The volume of a particle with a diameter of 55 nm is $4.8 \cdot 10^{-20}$ l, and therefore the volume of 56 400 particles, ignoring packing concerns, is 2.7 fl. The volume of a macrophage in a paraffin section is estimated, assuming a length of 20 µm, a width of 15 µm and a height of 10 µm, to be 3 pl. Hence, the volume of the macrophage is over a 1000 times larger, i.e. three magnitudes, than the volume taken up by 56 400 particles, and thus it is completely feasible that a single macrophage can take up around fifty thousand individual AHAPS-silica-FITC-particles.

6.3 Discussion

In this part of the thesis, newly developed FLIM analysis techniques were successfully applied to detect fluorescent target molecules against high background fluorescence. Specific ligand binding, cellular uptake, skin penetration and biodistribution of biomolecules and nanoparticles could be identified using ratiometric FLIM (rmFLIM) and cluster-based FLIM analysis routines.

6.3.1 Ligand binding, cellular interactions and localization in tissue visualized by rmFLIM

Binding of organic fluorophores to a protein changes the local physiochemical environment of the fluorophore. This can lead to effects on the excited state fluorescence. For instance, a specific multi-exponential lifetime signature was observed when a fluorescent dye, fluorescein, was bound to a cysteine residue in the GPCR opsin [Alexiev et al., 2003,Kim et al., 2009b,Kirchberg et al., 2010]. On the basis of this observation a ratiometric FLIM (rmFLIM) approach [Boreham et al., 2011] was applied to detect specific protein-ligand binding against high background fluorescence. Ratiometric mFLIM relies on the detection of distinct amplitude ratios from the specific multiexponential lifetime signature of a protein-ligand complex that is unique compared to the fluorescence lifetime distribution of the background. This is in a sense similar to FRET-FLIM where the shortening of the fluorescence lifetime of the donor due to radiationless energy to the acceptor is used as an indicator for FRET [Kenworthy, 2001].

The fluorescently labeled ligand naloxone (NLX-Flu) specifically bound to its receptor, the μ-opioid receptor, was identified in HEK293 cell membrane fragments despite high background fluorescence using rmFLIM. The fluorescent background stems from non specific binding of NLX-Flu to the membrane fragments or other proteins. The high amount of non specific binding meant that no differences in fluorescence intensity between membrane fragments with and without the μ-opioid receptor were observed. Conventional FLIM analysis was also not sensitive enough to detect specific binding of NLX-Flu to the μ-opioid receptor in membrane fragments. A clear cut differentiation between specific NLX-Flu binding to the μ-opioid receptor and unspecific binding was only possible by rmFLIM analysis, making use of the specific amplitude ratio of the fluorescence lifetime decay of NLX-Flu bound to the μ-opioid receptor.

The specificity of the identified ligand binding was verified by observing the displacement of NLX-Flu from the receptor after addition of increasing concentrations of unlabeled naloxone (NLX). Increasing amounts of NLX led to a decrease in the occurrence of the amplitude ratio of the specifically bound ligand (NLX-Flu), as was expected if NLX-Flu is indeed specifically bound. The NLX concentration required for half-maximum displacement was determined to be 50 nM. A dissociation constant in a comparable range, around 20 nM, for the dissociation of bound NLX-Flu from the μ-opioid receptor is reported in the literature [Madsen et al., 2000]. Hence, the ligand binding identified by rmFLIM was indeed specific ligand binding of NLX-Flu to the μ-opioid receptor in HEK membrane fragments. The observed distribution of the ligand-bound receptor, however, is not homogeneous throughout the cell membrane. This is consistent with the concept of localization of μ-opioid receptors within lipid rafts [Ge et al., 2009].

In essence, ratiometric FLIM was shown to be a fast and sensitive method to evaluate the binding of naloxone-fluorescein to the μ-opioid receptor in overexpressing HEK cells. Further advantages of this method include that no washing or purification steps are required after addition of the ligand, as rmFLIM is able to effectively suppress the background, and that no radioactive substances are required, e.g. as in the radioligand binding assays widely used to study ligand-receptor interactions.

In another experiment rmFLIM was applied to detect fluorescently tagged polyglycerol-based nanocarriers against the autofluorescent background of tissue samples. The localization

of a fluorescently labeled sulfated dendritic polyglycerol nanoparticle (dPGS-ICC) within rat liver tissue could be identified despite the background fluorescence, in this case caused by tissue autofluorescence, using the ratiometric FLIM approach.

The fluorescence lifetime of the dye ICC in solution, as determined by FLIM, is 0.25 ns [Boreham et al., 2011]. When ICC is bound to the surface of dPGS (dPGS-ICC) the fluorescence lifetime decay measured using FLIM was characterized by two lifetime decay components of 0.27 ns and 1.1 ns with relative amplitudes of 86 % and 14 % respectively. The longer lifetime component (1.1 ns) stems from the steric hindrance of the rotation around the ICC methine linker, leading to a larger planar conjugated π-electron system, and longer lifetimes [Chibisov et al., 1995]. The specific amplitude ratio of the unique fluorescence lifetime decay of dPGS-ICC was used to detect dPGS-ICC in rat liver tissue using rmFLIM.

The dPGS-ICC nanoparticle was found to be localized in the liver sinusoids. The observed pattern for dPGS-ICC localization is virtually identical with the distribution of Kupffer cells. Kupffer cells are macrophages, a phagocytotically active cell type of the immune system, that can take up and thus remove substances, both endogenous and exogenous, from the blood stream and degrade them. The localization of dPGS-ICC in Kupffer cells of rat liver was independently shown in further studies using near-IR probes [Licha et al., 2011] as well as autoradiography [Holzhausen et al., 2013] and was not found to exhibit any cytotoxic or detrimental effects on the Kupffer cells [Holzhausen et al., 2013].

Next, we investigated the interaction of dPGS-ICC with lipid membranes. Giant unilamelar vesicles (GUVs) were generated from the phospholipid DMPC as a model membrane system. FLIM intensity images clearly showed that dPGS-ICC accumulates in the DMPC-GUV membrane but does not penetrate into the lumen of DMPC-GUVs. The fluorescence lifetime decay of dPGS-ICC within the membrane was characterized by three fluorescence lifetime decay components. The slowest lifetime, due to the steric restriction of the methine linker, is close to 4 ns, indicating very immobile ICC. A 4 ns component was not observed for dPGS-ICC in water or ethanol and is specific for dPGS-ICC in a membrane environment.

An attempt was made to detect the amplitude ratio of the fast and the slow lifetime components of the unique fluorescence lifetime decay curve of dPGS-ICC in a membrane environment within rat liver tissue. However, the results showed that the rmFLIM analysis is not applicable, probably because the target molecule displayed a fluorescence lifetime decay with more than two fluorescence decay components. Therefore other methods not limited by the number of fluorescence decay components are needed for a more universal detection of fluorescently labeled target molecules against autofluorescent backgrounds. To this end, cluster-based FLIM analysis routines were developed in the group of Prof. Alexiev and were applied to the investigation of skin penetration and cellular uptake of nanoparticles as described in sections 6.2.3, 6.2.4 and 6.2.5 and discussed in the following.

6.3.2 Skin penetration visualized by cluster FLIM

The penetration properties of the CMS-ICC nanocarrier into intact and stripped skin were measured using FLIM and analyzed by cluster-based image routines. In chapter 5 it was shown that the lifetime curves of the free dye ICC and ICC covalently attached to CMS-ICC clearly differ in aqueous solution. The lifetime of CMS-ICC displays a markedly longer fluorescence lifetime decay due to the steric hindrance of the rotation of the methine linker. Analysis of FLIM measurements of ICC applied to intact skin for 24 hours showed that ICC accumulates in the *stratum corneum* (SC) but does not penetrate into deeper skin layers. The corresponding lifetime curve was clearly prolonged compared to ICC free in solution. This indicates that the rotation of the methine linker is drastically reduced by the SC environment.

In contrast to ICC, CMS-ICC could penetrate into the skin beyond the SC. CMS-ICC could

even be identified in the dermis. Interestingly, upon penetration beyond the SC and the epidermis the fluorescence lifetime decay was seen to change. Thus two different unique lifetime decays of CMS-ICC were observed depending on the skin region. In tape-stripped skin, on the other hand, for the whole epidermal and dermal region only one unique lifetime decay could be identified, which compares to that observed in the dermis of normal skin. Taken together, specific reversible conformational changes of CMS-ICC must occur in the SC of intact skin that persist into the epidermal layer but are absent by the time the CMS-ICC nanocarrier reaches the dermis.

The results observed here were obtained on human skin samples treated with $20\,\mu l\,cm^{-1}$ CMS-ICC nanocarrier solution for 24 h under sealed conditions in a Franz Cell chamber. Particularly penetration into normal skin was not necessarily expected, as the intact skin barrier is not easy to overcome. However, Schätzlein and Cevc [Schätzlein and Cevc, 1998] were able to show that ultradeformable vesicles can penetrate mouse skin via hydrophilic penetration pathways. The CMS-ICC nanocarriers applied to the skin surface were also shown to be highly flexible. Atomic force microscopy measurements of CMS-ICC on a surface found values of below 1 nm, as opposed to a size of 7.2 nm for a unimeric CMS nanocarrier determined from time-resolved fluorescence anisotropy measurements (see section 5.2.2 and [Boreham et al., 2014b]), suggesting a highly flexible and squeezable CMS nanocarriers which can stretch out on the surface [Alnasif et al., 2014]. Such a small size would allow for the passage through the pore pathway and thus penetration across the SC, as observed here. In addition, it has been proposed that increased hydration of the skin can lead to a continuous pore pathway [Elias et al., 2002] with pore sizes up to 20 nm. In a confocal microscopy study on fluorescently labeled BSA and porcine skin, Tan and coworkers [Tan et al., 2010] were able to show that even a protein of the size of BSA can penetrate into heavily hydrated porcine skin, using fully wetted gauze, but not into normally hydrated skin. Although the human skin here was probably not hydrated as heavily as that used in the study by Tan et al., an increased hydration of the skin cannot be excluded.

In addition to hydration, other methods for delivering large cargo molecules, e.g. proteins, are being studied. Hyaluronic acid has been shown to be a suitable transport vehicle for the small drug molecule diclofenac [Pirard et al., 2005, Peters and Foster, 1999, Moore and Willoughby, 1995, Brown et al., 1995, Brown and Jones, 2005]. Here, the penetration properties of hyaluronic acid and bovine serum albumin, as a model for a large protein cargo, were studied using FLIM and cluster-based FLIM analysis, and, in particular, the effect of different molecular weight HA on the penetration of BSA into intact and tape-stripped skin was investigated.

The results showed that BSA can hardly penetrate into normal skin after 6 h incubation, while BSA can penetrate even into deeper dermal layers of barrier deficient skin (tape-stripped). HA was also found to penetrate into tape-stripped skin, although not into dermal layers, i.e. it remains within the epidermis. In normal skin, HA penetration was only observed for 5 kDa HA. However, far less HA was detectable here than in tape-stripped skin.

The picture changes when BSA and HA are applied together. Enhancement of BSA penetration into normal skin was seen with 5 kDa HA, while the higher molecular weight HA species studied here did not have any enhancement effects on BSA. In tape-stripped skin all three HA molecular weights confined BSA penetration to the epidermis. To test whether the effect of HA on BSA penetration is accompanied by a close molecular interaction, FRET between HA-MANT and BSA-RhB was investigated. The analysis showed that the confinement of BSA by HA to the epidermis does not require close molecular interactions. In contrast, FRET was observed for the enhancement of BSA penetration by 5 kDa HA into normal skin, indicating close interactions between BSA and HA in the range of 1 nm to 10 nm.

Hence, cluster FLIM revealed that low molecular weight HA can enhance the intraepidermal delivery of a cargo molecule in normal skin, while it can confine the same cargo molecule to the

epidermis in barrier deficient skin. Penetration of HA into the epidermis was already reported in a study investigating the delivery of diclofenac by HA [Brown et al., 1995]. A confinement of HA to the epidermis was also observed. The existence of receptors for HA in the epidermis was postulated to play a role in the confinement of HA to the epidermis [Brown et al., 1995].

6.3.3 Quantification of silica particle uptake by macrophages using cluster FLIM

Investigation were conducted into the localization of silica nanoparticles (SiNP), functionalized at the surface with AHAPS (N-(6-aminohexyl)-aminopropyltrimethoxysilane) and loaded with the fluorescent dye fluorescein, after subcutaneous injection into mouse skin. In the context of a study on the dermal penetration and metabolic clearance of AHAPS-SiNP [Ostrowski et al., 2014] particle localization after subcutaneous injection was investigated using cluster-based FLIM analysis routines. The AHAPS-SiNP fluorescence lifetime decay curve could be clearly differentiated from the lifetime decay curve of the autofluorescence of the skin tissue and erythrocytes. Increasing the spatial resolution of the measurements revealed particle uptake by macrophages. Uptake of SiNP by macrophages has previously been reported for mesoporous silica particles in macrophage cell cultures [Witasp et al., 2009] and interactions of macrophages with polyethyleneimine and (3-Aminopropyl)-triethoxysilane silica particles have also been seen [Kulikova et al., 2010]. Here, the amount of particles taken up by a macrophage could also be determined. An adequate reference sample containing a defined concentration of AHAPS-SiNP was used to determine the amount of particles taken up by a macrophage. The number of particles was calculated to be around 56 000, corresponding to nearly 10 pg of AHAPS-SiNP.

Chapter 7

Summary

In this thesis, time-resolved fluorescence spectroscopy and state-of-the-art fluorescence microscopy was applied, to gain new insights, from the molecular up to the tissue level, into biomolecules and nanoparticles directly involved in or with potential application for the treatment of inflammation and pain. Nanostructured lipid carriers (NLC), dendritic polyglycerol sulfate (dPGS) nanoparticles, core-multishell (CMS) nanocarriers, and silica nanoparticles were investigated as well as ligand interactions of the μ-opioid receptor and effects of hyaluronic acid (HA) on the penetration of biomolecules into the skin. New methodologies of single-molecule and fluorescence lifetime imaging microscopy were employed to visualize nanoparticle structures and nanoparticle distribution in tissue, while the environmental dependence of physicochemical properties of dPGS and CMS were analyzed using time-resolved fluorescence lifetime and anisotropy.

Conflicting results on NLC morphology and the arrangement of the liquid phase were reported in the literature. Here a new method was developed, based on single-molecule microscopy, to visualize the morphology and internal structure of individual NLC particles. From affinity-based labeling experiments, that made use of the affinity of the lipophilic Oxa12 dye to the NLC particles, super-resolution images were produced, showing that the particles have a spherical shape. Two NLC subpopulations with sizes of 115 nm and 173 nm were identified. NLC nanocompartments and there size could be directly visualized from single-molecule measurements of NLC particles containing fluorescent drug mimetics, revealing two populations of nanocompartments with sizes of around 65 nm and 125 nm. A direct comparison of the nanocompartments and NLC particles showed that the fluorescent drug mimetics reside in a liquid core surrounded by a solid shell. In addition, reservoir properties of the NLCs were seen in the drug release profile. This single-molecule fluorescence microscopy method enables systematic investigations of the correlation of the NLC composition with NLC morphology and inner structure and also with drug release properties, which is necessary for a scientific understanding of the principles governing the NLC structure and the design of tailor-made NLCs for in vivo applications, e.g. delivery of anti-inflammatory drugs to inflammatory tissue, without "trial and error" research in the future.

The molecular dynamics and the size of dPGS and CMS nanocarriers as well as the drug distribution within CMS nanocarriers were investigated by means of time-resolved fluorescence lifetime and anisotropy. Interestingly, dPGS showed a temperature dependent shrinkage from 4.4 nm to 2.9 nm, leading to a reduced size at physiological temperatures, while the CMS nanocarriers were shown to have a temperature independent size of 7 nm, indicative of unimeric CMS nanocarriers. Partitioning of a fluorescent drug mimetic into two regions of the CMS nanocarrier with different polarity and water content was revealed by time-resolved fluorescence lifetime measurements. The partitioning was dependent on the environment and temperature. By comparing the data from time-resolved fluorescence lifetime and anisotropy measurements, the temperature dependent partitioning of NR could be correlated to an increase in flexibility of the CMS nanocarrier branches and to changes in flexibility of the dendritic polyglycerol core of CMS nanocarriers. These findings have direct implications for the structure - biological activity relationship of the anti-inflammatory nanoparticle dPGS and for the drug release properties and

successful delivery of anti-inflammatory agents and painkillers by CMS nanocarriers.

Tissue localization and cellular interaction of nanoparticles and biomolecules were investigated with fluoroescence lifetime imaging microscopy (FLIM). Two newly developed FLIM data analysis methods were applied. These were developed for the detection of specific fluorescence lifetime signatures in samples with high fluorescent backgrounds. The following results were obtained. The specific ligand binding of fluorescently labeled naloxone to the μ-opioid receptor could be differentiated from unspecific binding of the ligand in cell membranes. dPGS was shown to localize to specialized macrophages, Kuppfer cells, in the liver of rats. The CMS nanocarrier was observed to penetrate into both normal and barrier deficient skin, while the biomolecule hyaluronic acid (HA) enhances or confines the penetration of a model cargo protein to the viable epidermis, depending on the molecular weight of HA and the skin intactness or damage of the skin barrier. Penetration enhancement of a model cargo protein to the epidermis was seen for 5 kDa HA in normal skin, while all studied molecular weights of HA confined the penetration of the model cargo protein to the epidermis in barrier deficient skin. In mouse skin, the uptake of silica nanoparticles by macrophages was shown and the average number of particles within a macrophage was determined to be 56 000 particles. All of these results highlight the ability of these novel FLIM data analysis techniques to meet the challenges posed by samples with high autofluorescent backgrounds and poor signal-to-noise ratios.

Publications

The following publications resulted from this thesis:

Exploiting Fluorescence Lifetime Plasticity in FLIM: Target Molecule Localization in Cells and Tissues
Boreham A, Kim TY, Spahn V, Stein C, Mundhenk L, Gruber AD, Haag R, Welker P, Licha K, and Alexiev U
ACS Medicinal Chemistry Letters 2011 2 (10), 724-728

Nanodynamics of Dendritic Core-Multishell Nanocarriers
Boreham A, Pfaff M, Fleige E, Haag R, and Alexiev U
Langmuir 2014 30 (6), 1686-1695

Penetration of normal, damaged and diseased skin – An in vitro study on dendritic core-multishell nanotransporters
Alnasif N, Zoschke C, Fleige E, Brodwolf R, Boreham A, Rühl E, Eckl K, Merk H, Hennies HC, Alexiev U, Haag R, Küchler S and Schäfer-Korting M
Journal of Controlled Release, Volume 185, 10 July 2014, Pages 45-50

Skin barrier disruptions in tape stripped and allergic dermatitis models have no effect on dermal penetration and systemic distribution of AHAPS-functionalized silica nanoparticles
Ostrowski A, Nordmeyer D, Boreham A, Brodwolf R, Mundhenk L, Fluhr JW, Lademann J, Graf C, Rühl E, Alexiev U and Gruber AD
Nanomedicine: Nanotechnology, Biology and Medicine, (2014) DOI: 10.1016/j.nano.2014.04.004

Temperature and environment dependent dynamic properties of a dendritic polyglycerol sulfate
Boreham A, Brodwolf R, Pfaff M, Kim TY, Schlieter T, Mundhenk L, Gruber AD, Gröger D, Licha K, Haag R and Alexiev U
Polym. Adv. Technol.(2014). DOI: 10.1002/pat.3355

Under revision

Overview on the Localization of Nanoparticles in Tissue and Cellular Context by Different Imaging Techniques
Ostrowski A, Nordmeyer D, Boreham A, Mundhenk L, Graf C, Rühl E, Alexiev U and Gruber AD
Submitted to: Beilstein Journal of Nanotechnology

Bibliography

[Alexiev and Farrens, 2014] Alexiev, U. and Farrens, D. L. (2014). Fluorescence spectroscopy of rhodopsins: insights and approaches. *Biochim Biophys Acta*, 1837(5):694–709.

[Alexiev et al., 2003] Alexiev, U., Rimke, I., and Pöhlmann, T. (2003). Elucidation of the nature of the conformational changes of the EF-interhelical loop in bacteriorhodopsin and of the helix viii on the cytoplasmic surface of bovine rhodopsin: a time-resolved fluorescence depolarization study. *J Mol Biol*, 328(3):705–719.

[Alnasif et al., 2014] Alnasif, N., Zoschke, C., Fleige, E., Brodwolf, R., Boreham, A., Rühl, E., Eckl, K.-M., Merk, H.-F., Hennies, H. C., Alexiev, U., Haag, R., Küchler, S., and Schäfer-Korting, M. (2014). Penetration of normal, damaged and diseased skin - an in vitro study on dendritic core-multishell nanotransporters. *J Control Release*, 185C:45–50.

[Araújo et al., 2010] Araújo, J., Gonzalez-Mira, E., Egea, M. A., Garcia, M. L., and Souto, E. B. (2010). Optimization and physicochemical characterization of a triamcinolone acetonide-loaded NLC for ocular antiangiogenic applications. *Int J Pharm*, 393(1-2):167–175.

[Baroli, 2010] Baroli, B. (2010). Penetration of nanoparticles and nanomaterials in the skin: fiction or reality? *J Pharm Sci*, 99(1):21–50.

[Baroni et al., 2012] Baroni, A., Buommino, E., De Gregorio, V., Ruocco, E., Ruocco, V., and Wolf, R. (2012). Structure and function of the epidermis related to barrier properties. *Clin Dermatol*, 30(3):257–262.

[Becker, 2012] Becker, W. (2012). *The bh TCSPC Handbook*. 5th edition.

[Biffi et al., 2013] Biffi, S., Dal Monego, S., Dullin, C., Garrovo, C., Bosnjak, B., Licha, K., Welker, P., Epstein, M. M., and Alves, F. (2013). Dendritic polyglycerolsulfate near infrared fluorescent (nirf) dye conjugate for non-invasively monitoring of inflammation in an allergic asthma mouse model. *PLoS One*, 8(2):e57150.

[Bigliardi et al., 2009] Bigliardi, P. L., Tobin, D. J., Gaveriaux-Ruff, C., and Bigliardi-Qi, M. (2009). Opioids and the skin–where do we stand? *Exp Dermatol*, 18(5):424–430.

[Boreham et al., 2014a] Boreham, A., Brodwolf, R., Pfaff, M., Kim, T.-Y., Schlieter, T., Mundhenk, L., Gruber, A. D., Gröger, D., Licha, K., Haag, R., and Alexiev, U. (2014). Temperature and environment dependent dynamic properties of a dendritic polyglycerol sulfate. *Polymers for Advanced Technologies*, accepted.

[Boreham et al., 2011] Boreham, A., Kim, T.-Y., Spahn, V., Stein, C., Mundhenk, L., Gruber, A. D., Haag, R., Welker, P., Licha, K., and Alexiev, U. (2011). Exploiting fluorescence lifetime plasticity in FLIM: Target molecule localization in cells and tissues. *ACS Medicinal Chemistry Letters*, 2(10):724–728.

[Boreham et al., 2014b] Boreham, A., Pfaff, M., Fleige, E., Haag, R., and Alexiev, U. (2014). Nanodynamics of dendritic core-multishell nanocarriers. *Langmuir*, 30:1686–1695.

[Bouwstra et al., 2001] Bouwstra, J., Pilgram, G., Gooris, G., Koerten, H., and Ponec, M. (2001). New aspects of the skin barrier organization. *Skin Pharmacol Appl Skin Physiol*, 14 Suppl 1:52–62.

[Bouwstra et al., 1991] Bouwstra, J. A., Gooris, G. S., van der Spek, J. A., and Bras, W. (1991). Structural investigations of human stratum corneum by small-angle x-ray scattering. *J Invest Dermatol*, 97(6):1005–1012.

[Brandner et al., 2010] Brandner, J. M., Haftek, M., and Niessen, C. M. (2010). Adherens junctions, desmosomes and tight junctions in epidermal barrier function. *The Open Dermatology Journal*, 4:14–20.

[Brodwolf, 2011] Brodwolf, R. (2011). Herstellung und biophysikalische Untersuchung des Modellmembransystems "Giant Unilamellar Vesicles". Diploma thesis.

[Brown and Jones, 2005] Brown, M. B. and Jones, S. A. (2005). Hyaluronic acid: a unique topical vehicle for the localized delivery of drugs to the skin. *J Eur Acad Dermatol Venereol*, 19(3):308–318.

[Brown et al., 1995] Brown, M. B., Marriott, C., and Martin, G. P. (1995). The effect of hyaluronan on the in vitro deposition of diclofenac within the skin. *Int J Tissue React*, 17(4):133–140.

[Bunjes et al., 2001] Bunjes, H., Drechsler, M., Koch, M. H., and Westesen, K. (2001). Incorporation of the model drug ubidecarenone into solid lipid nanoparticles. *Pharm Res*, 18(3):287–293.

[Busch-Dienstfertig and Stein, 2010] Busch-Dienstfertig, M. and Stein, C. (2010). Opioid receptors and opioid peptide-producing leukocytes in inflammatory pain–basic and therapeutic aspects. *Brain Behav Immun*, 24(5):683–694.

[Buzea et al., 2007] Buzea, C., Pacheco, I. I., and Robbie, K. (2007). Nanomaterials and nanoparticles: sources and toxicity. *Biointerphases*, 2(4):MR17–MR71.

[Calderón et al., 2010a] Calderón, M., Quadir, M. A., Sharma, S. K., and Haag, R. (2010). Dendritic polyglycerols for biomedical applications. *Adv Mater*, 22(2):190–218.

[Calderón et al., 2010b] Calderón, M., Quadir, M. A., Strumia, M., and Haag, R. (2010). Functional dendritic polymer architectures as stimuli-responsive nanocarriers. *Biochimie*, 92(9):1242–1251.

[Cevc and Vierl, 2010] Cevc, G. and Vierl, U. (2010). Nanotechnology and the transdermal route: A state of the art review and critical appraisal. *J Control Release*, 141(3):277–299.

[Chee et al., 2006] Chee, C. K., Rimmer, S., Rutkaite, R., Soutar, I., and Swanson, L. (2006). Time-resolved fluorescence anisotropy measurements in the study of poly(n-isopropyl acrylamide)-based systems. *Journal of Photochemistry and Photobiology A: Chemistry*, 180(1 - 2):1 – 8.

[Chee et al., 2011] Chee, C. K., Rimmer, S., Soutar, I., and Swanson, L. (2011). Time-resolved fluorescence anisotropy studies of the interaction of n-isopropyl acrylamide based polymers with sodium dodecyl sulphate. *Soft Matter*, 7:4705–4714.

[Cheng et al., 2012] Cheng, Z., Al Zaki, A., Hui, J. Z., Muzykantov, V. R., and Tsourkas, A. (2012). Multifunctional nanoparticles: cost versus benefit of adding targeting and imaging capabilities. *Science*, 338(6109):903–910.

[Chibisov et al., 1995] Chibisov, A. K., Zakharova, G. V., Goerner, H., Sogulyaev, Y. A., Mushkalo, I. L., and Tolmachev, A. I. (1995). Photorelaxation processes in covalently linked indocarbocyanine and thiacarbocyanine dyes. *The Journal of Physical Chemistry*, 99(3):886–893.

[Choi et al., 2012] Choi, W. I., Lee, J. H., Kim, J.-Y., Kim, J.-C., Kim, Y. H., and Tae, G. (2012). Efficient skin permeation of soluble proteins via flexible and functional nano-carrier. *J Control Release*, 157(2):272–278.

[Cser et al., 2002] Cser, A., Nagy, K., and Biczkó, L. (2002). Fluorescence lifetime of nile red as a probe for the hydrogen bonding strength with its microenvironment. *Chemical Physics Letters*, 360(5-6):473 – 478.

[Damien and Boncheva, 2010] Damien, F. and Boncheva, M. (2010). The extent of orthorhombic lipid phases in the stratum corneum determines the barrier efficiency of human skin in vivo. *J Invest Dermatol*, 130(2):611–614.

[DeAngelis, 2000] DeAngelis, P. L. (2000). Polysaccharide labeling with N-methylisatoic anhydride: generation of ultraviolet chromophores and blue fluorophores. *Anal Biochem*, 284(1):167–169.

[Dernedde et al., 2010] Dernedde, J., Rausch, A., Weinhart, M., Enders, S., Tauber, R., Licha, K., Schirner, M., Zügel, U., von Bonin, A., and Haag, R. (2010). Dendritic polyglycerol sulfates as multivalent inhibitors of inflammation. *Proc Natl Acad Sci U S A*, 107(46):19679–19684.

[Di Meglio et al., 2011] Di Meglio, P., Perera, G. K., and Nestle, F. O. (2011). The multitasking organ: recent insights into skin immune function. *Immunity*, 35(6):857–869.

[Eftink, 1994] Eftink, M. R. (1994). The use of fluorescence methods to monitor unfolding transitions in proteins. *Biophys J*, 66(2 Pt 1):482–501.

[Elias, 1983] Elias, P. M. (1983). Epidermal lipids, barrier function, and desquamation. *J Invest Dermatol*, 80(1 Suppl):44s–49s.

[Elias, 2005] Elias, P. M. (2005). Stratum corneum defensive functions: an integrated view. *J Invest Dermatol*, 125(2):183–200.

[Elias, 2007] Elias, P. M. (2007). The skin barrier as an innate immune element. *Semin Immunopathol*, 29(1):3–14.

[Elias et al., 2002] Elias, P. M., Tsai, J., Menon, G. K., Holleran, W. M., and Feingold, K. R. (2002). The potential of metabolic interventions to enhance transdermal drug delivery. *J Investig Dermatol Symp Proc*, 7(1):79–85.

[Erbil and Saraç, 2002] Erbil, C. and Saraç, A. S. (2002). Description of the turbidity measurements near the phase transition temperature of poly(n-isopropyl acrylamide) copolymers: the effect of ph, concentration, hydrophilic and hydrophobic content on the turbidity. *European Polymer Journal*, 38(7):1305 – 1310.

[Esposito et al., 2008] Esposito, E., Fantin, M., Marti, M., Drechsler, M., Paccamiccio, L., Mariani, P., Sivieri, E., Lain, F., Menegatti, E., Morari, M., and Cortesi, R. (2008). Solid lipid nanoparticles as delivery systems for bromocriptine. *Pharm Res*, 25(7):1521–1530.

[European Science Foundation, 2005] European Science Foundation (2005). *ESF Scientific Forward Look on Nanomedicine*. European Science Foundation, European Science Foundation.

[Feingold and Elias, 2014] Feingold, K. R. and Elias, P. M. (2014). Role of lipids in the formation and maintenance of the cutaneous permeability barrier. *Biochim Biophys Acta*, 1841(3):280–294.

[Filipe et al., 2010] Filipe, V., Hawe, A., and Jiskoot, W. (2010). Critical evaluation of nanoparticle tracking analysis (nta) by nanosight for the measurement of nanoparticles and protein aggregates. *Pharm Res*, 27(5):796–810.

[Fleige et al., 2012] Fleige, E., Quadir, M. A., and Haag, R. (2012). Stimuli-responsive polymeric nanocarriers for the controlled transport of active compounds: concepts and applications. *Adv Drug Deliv Rev*, 64(9):866–884.

[Ge et al., 2009] Ge, X., Qiu, Y., Loh, H. H., and Law, P.-Y. (2009). Grin1 regulates micro-opioid receptor activities by tethering the receptor and g protein in the lipid raft. *J Biol Chem*, 284(52):36521–36534.

[Graf et al., 2012] Graf, C., Gao, Q., Schütz, I., Noufele, C. N., Ruan, W., Posselt, U., Korotianskiy, E., Nordmeyer, D., Rancan, F., Hadam, S., Vogt, A., Lademann, J., Haucke, V., and Rühl, E. (2012). Surface functionalization of silica nanoparticles supports colloidal stability in physiological media and facilitates internalization in cells. *Langmuir*, 28(20):7598–7613.

[Groen et al., 2011] Groen, D., Poole, D. S., Gooris, G. S., and Bouwstra, J. A. (2011). Is an orthorhombic lateral packing and a proper lamellar organization important for the skin barrier function? *Biochim Biophys Acta*, 1808(6):1529–1537.

[Hell, 2007] Hell, S. W. (2007). Far-field optical nanoscopy. *Science*, 316(5828):1153–1158.

[Holzhausen et al., 2013] Holzhausen, C., Gröger, D., Mundhenk, L., Welker, P., Haag, R., and Gruber, A. D. (2013). Tissue and cellular localization of nanoparticles using ^{35}Slabeling and light microscopic autoradiography. *Nanomedicine*, 9(4):465–468.

[Hua and Wu, 2013] Hua, S. and Wu, S. Y. (2013). The use of lipid-based nanocarriers for targeted pain therapies. *Front Pharmacol*, 4:143.

[Imran ul-haq et al., 2012] Imran ul-haq, M., Lai, B. F. L., Chapanian, R., and Kizhakkedathu, J. N. (2012). Influence of architecture of high molecular weight linear and branched polyglycerols on their biocompatibility and biodistribution. *Biomaterials*, 33(35):9135–9147.

[Janssens et al., 2012] Janssens, M., van Smeden, J., Gooris, G. S., Bras, W., Portale, G., Caspers, P. J., Vreeken, R. J., Hankemeier, T., Kezic, S., Wolterbeek, R., Lavrijsen, A. P., and Bouwstra, J. A. (2012). Increase in short-chain ceramides correlates with an altered lipid organization and decreased barrier function in atopic eczema patients. *J Lipid Res*, 53(12):2755–2766.

[Jia et al., 2010] Jia, L., Zhang, D., Li, Z., Duan, C., Wang, Y., Feng, F., Wang, F., Liu, Y., and Zhang, Q. (2010). Nanostructured lipid carriers for parenteral delivery of silybin: Biodistribution and pharmacokinetic studies. *Colloids Surf B Biointerfaces*, 80(2):213–218.

[Jobin Yvon Horiba, 2001] Jobin Yvon Horiba (2001). *FluoroMax®-3 & FluoroMax®-P Operation Manual*. Jobin Yvon Horiba, 2.0 edition.

[Jores et al., 2004] Jores, K., Mehnert, W., Drechsler, M., Bunjes, H., Johann, C., and Mäder, K. (2004). Investigations on the structure of solid lipid nanoparticles (SLN) and oil-loaded solid lipid nanoparticles by photon correlation spectroscopy, field-flow fractionation and transmission electron microscopy. *J Control Release*, 95(2):217–227.

[Joshi et al., 2014] Joshi, M., Butola, B. S., and Saha, K. (2014). Advances in topical drug delivery system: micro to nanofibrous structures. *J Nanosci Nanotechnol*, 14(1):853–867.

[Kainthan and Brooks, 2007] Kainthan, R. K. and Brooks, D. E. (2007). In vivo biological evaluation of high molecular weight hyperbranched polyglycerols. *Biomaterials*, 28(32):4779–4787.

[Kainthan et al., 2007] Kainthan, R. K., Hester, S. R., Levin, E., Devine, D. V., and Brooks, D. E. (2007). In vitro biological evaluation of high molecular weight hyperbranched polyglycerols. *Biomaterials*, 28(31):4581–4590.

[Kainthan et al., 2006] Kainthan, R. K., Janzen, J., Levin, E., Devine, D. V., and Brooks, D. E. (2006). Biocompatibility testing of branched and linear polyglycidol. *Biomacromolecules*, 7(3):703–709.

[Küchler et al., 2009a] Küchler, S., Abdel-Mottaleb, M., Lamprecht, A., Radowski, M. R., Haag, R., and Schäfer-Korting, M. (2009). Influence of nanocarrier type and size on skin delivery of hydrophilic agents. *Int J Pharm*, 377(1-2):169–172.

[Küchler et al., 2009b] Küchler, S., Radowski, M. R., Blaschke, T., Dathe, M., Plendl, J., Haag, R., Schäfer-Korting, M., and Kramer, K. D. (2009). Nanoparticles for skin penetration enhancement - a comparison of a dendritic core-multishell-nanotransporter and solid lipid nanoparticles. *European Journal of Pharmaceutics and Biopharmaceutics*, 71(2):243 – 250.

[Kenworthy, 2001] Kenworthy, A. K. (2001). Imaging protein-protein interactions using fluorescence resonance energy transfer microscopy. *Methods*, 24(3):289–296.

[Khandare et al., 2012] Khandare, J., Calderón, M., Dagia, N. M., and Haag, R. (2012). Multifunctional dendritic polymers in nanomedicine: opportunities and challenges. *Chem Soc Rev*, 41(7):2824–2848.

[Kim, 2012] Kim, T.-Y. (2012). *Zeitaufgelöste fluoreszenzspektroskopische Untersuchungen an der cytoplasmatischen Oberfläche von Rhodopsin*. PhD thesis, Freie Universität Berlin.

[Kim et al., 2009a] Kim, T.-Y., Moeller, M., Winkler, K., Kirchberg, K., and Alexiev, U. (2009). Dissection of environmental changes at the cytoplasmic surface of light-activated bacteriorhodopsin and visual rhodopsin: sequence of spectrally silent steps. *Photochem Photobiol*, 85(2):570–577.

[Kim et al., 2012] Kim, T.-Y., Schlieter, T., Haase, S., and Alexiev, U. (2012). Activation and molecular recognition of the GPCR rhodopsin–insights from time-resolved fluorescence depolarisation and single molecule experiments. *Eur J Cell Biol*, 91(4):300–310.

[Kim et al., 2009b] Kim, T.-Y., Uji-i, H., Möller, M., Muls, B., Hofkens, J., and Alexiev, U. (2009). Monitoring the interaction of a single G-protein key binding site with rhodopsin disk membranes upon light activation. *Biochemistry*, 48(18):3801–3803.

[Kim et al., 2007] Kim, T.-Y., Winkler, K., and Alexiev, U. (2007). Picosecond multidimensional fluorescence spectroscopy: a tool to measure real-time protein dynamics during function. *Photochem Photobiol*, 83(2):378–384.

[Kirchberg et al., 2010] Kirchberg, K., Kim, T.-Y., Haase, S., and Alexiev, U. (2010). Functional interaction structures of the photochromic retinal protein rhodopsin. *Photochem Photobiol Sci*, 9(2):226–233.

[Kneuer et al., 2000] Kneuer, C., Sameti, M., Haltner, E. G., Schiestel, T., Schirra, H., Schmidt, H., and Lehr, C. M. (2000). Silica nanoparticles modified with aminosilanes as carriers for plasmid dna. *Int J Pharm*, 196(2):257–261.

[Kulikova et al., 2010] Kulikova, G. A., Parfenyuk, E. V., Ryabinina, I. V., Antsiferova, Y. S., Sotnikova, N. Y., Posiseeva, L. V., and Eliseeva, M. A. (2010). In vitro studies of interaction of modified silica nanoparticles with different types of immunocompetent cells. *J Biomed Mater Res A*, 95(2):434–439.

[Lademann et al., 2006] Lademann, J., Ilgevicius, A., Zurbau, O., Liess, H. D., Schanzer, S., Weigmann, H. J., Antoniou, C., Pelchrzim, R. V., and Sterry, W. (2006). Penetration studies of topically applied substances: Optical determination of the amount of stratum corneum removed by tape stripping. *J Biomed Opt*, 11(5):054026.

[Lademann et al., 2011] Lademann, J., Richter, H., Schanzer, S., Knorr, F., Meinke, M., Sterry, W., and Patzelt, A. (2011). Penetration and storage of particles in human skin: perspectives and safety aspects. *Eur J Pharm Biopharm*, 77(3):465–468.

[Lakowicz, 2010] Lakowicz, J. R. (2010). *Principles of Fluorescence Spectroscopy*. Springer.

[Lee et al., 2005] Lee, C. C., MacKay, J. A., Fréchet, J. M. J., and Szoka, F. C. (2005). Designing dendrimers for biological applications. *Nat Biotechnol*, 23(12):1517–1526.

[Li and Peck, 2013] Li, S. K. and Peck, K. D. (2013). Passive and iontophoretic transport through the skin polar pathway. *Skin Pharmacol Physiol*, 26(4-6):243–253.

[Licha et al., 2011] Licha, K., Welker, P., Weinhart, M., Wegner, N., Kern, S., Reichert, S., Gemeinhardt, I., Weissbach, C., Ebert, B., Haag, R., and Schirner, M. (2011). Fluorescence imaging with multifunctional polyglycerol sulfates: novel polymeric near-IR probes targeting inflammation. *Bioconjug Chem*, 22(12):2453–2460.

[Liu et al., 2014] Liu, Y., Li, W., Hou, L., and Wu, P. (2014). Thermosensitive hyperbranched polyethylenimine partially substituted with n-isopropylacrylamide monomer: thermodynamics and use in developing a thermosensitive graphene composite. *RSC Adv.*, 4:24263–24271.

[Luan et al., 2014] Luan, J., Zhang, D., Hao, L., Qi, L., Liu, X., Guo, H., Li, C., Guo, Y., Li, T., Zhang, Q., and Zhai, G. (2014). Preparation, characterization and pharmacokinetics of amoitone b-loaded long circulating nanostructured lipid carriers. *Colloids and Surfaces B: Biointerfaces*, 114(0):255 – 260.

[Luo and Saltzman, 2006] Luo, D. and Saltzman, W. M. (2006). Nonviral gene delivery: thinking of silica. *Gene Ther*, 13(7):585–586.

[Madsen et al., 2000] Madsen, B. W., Beglan, C. L., and Spivak, C. E. (2000). Fluorescein-labeled naloxone binding to mu opioid receptors on live chinese hamster ovary cells using confocal fluorescent microscopy. *J Neurosci Methods*, 97(2):123–131.

[Mao et al., 2003] Mao, H., Li, C., Zhang, Y., Bergbreiter, D. E., and Cremer, P. S. (2003). Measuring lcsts by novel temperature gradient methods: evidence for intermolecular interactions in mixed polymer solutions. *J Am Chem Soc*, 125(10):2850–2851.

[Marr and Hildreth, 1980] Marr, D. and Hildreth, E. (1980). Theory of edge detection. *Proc R Soc Lond B Biol Sci*, 207(1167):187–217.

[Mauro, 2006] Mauro, T. (2006). SC pH: Measurement, Origins, and Functions. In Elias, P. and Feingold, K., editors, *Skin Barrier*, chapter 14, pages 223–229. CRC Press.

[Mei et al., 2006] Mei, E., Gao, F., and Hochstrasser, R. M. (2006). Controlled bimolecular collisions allow sub-diffraction limited microscopy of lipid vesicles. *Phys Chem Chem Phys*, 8(17):2077–2082.

[Mitragotri, 2002] Mitragotri, S. (2002). A theoretical analysis of permeation of small hydrophobic solutes across the stratum corneum based on scaled particle theory. *J Pharm Sci*, 91(3):744–752.

[Mitragotri, 2003] Mitragotri, S. (2003). Modeling skin permeability to hydrophilic and hydrophobic solutes based on four permeation pathways. *J Control Release*, 86(1):69–92.

[Müller et al., 2002] Müller, R. H., Radtke, M., and Wissing, S. A. (2002). Nanostructured lipid matrices for improved microencapsulation of drugs. *Int J Pharm*, 242(1-2):121–128.

[Müller et al., 2011] Müller, R. H., Shegokar, R., and Keck, C. M. (2011). 20 years of lipid nanoparticles (SLN & NLC): Present state of development & industrial applications. *Curr Drug Discov Technol*, 8(3):207–227.

[Moore and Willoughby, 1995] Moore, A. R. and Willoughby, D. A. (1995). Hyaluronan as a drug delivery system for diclofenac: a hypothesis for mode of action. *Int J Tissue React*, 17(4):153–156.

[Moreno-Vega et al., 2012] Moreno-Vega, A.-I., Gómez-Quintero, T., Nuñez-Anita, R.-E., Acosta-Torres, L.-S., and Castaño, V. (2012). Polymeric and ceramic nanoparticles in biomedical applications. *Journal of Nanotechnology*, vol. 2012.

[Nanosight Ltd., 2010] Nanosight Ltd. (2010). Nanoparticle Tracking Analysis (NTA) and Dynamic Light Scattering (DLS) - a Comparison. *Application Note*.

[Nino et al., 2010] Nino, M., Calabrò, G., and Santoianni, P. (2010). Topical delivery of active principles: the field of dermatological research. *Dermatol Online J*, 16(1):4.

[Ostrowski et al., 2014] Ostrowski, A., Nordmeyer, D., Boreham, A., Brodwolf, R., Mundhenk, L., Fluhr, J. W., Lademann, J., Graf, C., Rühl, E., Alexiev, U., and Gruber, A. D. (2014). Skin barrier disruptions in tape stripped and allergic dermatitis models have no effect on dermal penetration and systemic distribution of ahaps-functionalized silica nanoparticles. *Nanomedicine*, DOI: 10.1016/j.nano.2014.04.004.

[Papp et al., 2008] Papp, I., Dernedde, J., Enders, S., and Haag, R. (2008). Modular synthesis of multivalent glycoarchitectures and their unique selectin binding behavior. *Chem Commun (Camb)*, (44):5851–5853.

[Patel et al., 2012] Patel, D., Dasgupta, S., Dey, S., Ramani, Y. R., Ray, S., and Mazumder, B. (2012). Nanostructured lipid carriers (NLC)-based gel for the topical delivery of aceclofenac: Preparation, characterization, and in vivo evaluation. *Sci Pharm*, 80(3):749–764.

[Paulus et al., 2014] Paulus, F., Schulze, R., Steinhilber, D., Zieringer, M., Steinke, I., Welker, P., Licha, K., Wedepohl, S., Dernedde, J., and Haag, R. (2014). The effect of polyglycerol sulfate branching on inflammatory processes. *Macromol Biosci*, 14(5):643–654.

[Peck et al., 1994] Peck, K. D., Ghanem, A. H., and Higuchi, W. I. (1994). Hindered diffusion of polar molecules through and effective pore radii estimates of intact and ethanol treated human epidermal membrane. *Pharm Res*, 11(9):1306–1314.

[Peters and Foster, 1999] Peters, D. C. and Foster, R. H. (1999). Diclofenac/hyaluronic acid. *Drugs Aging*, 14(4):313–9; discussion 320–1.

[Petros and DeSimone, 2010] Petros, R. A. and DeSimone, J. M. (2010). Strategies in the design of nanoparticles for therapeutic applications. *Nat Rev Drug Discov*, 9(8):615–627.

[Philippe et al., 2006] Philippe, D., Chakass, D., Thuru, X., Zerbib, P., Tsicopoulos, A., Geboes, K., Bulois, P., Breisse, M., Vorng, H., Gay, J., Colombel, J.-F., Desreumaux, P., and Chamaillard, M. (2006). Mu opioid receptor expression is increased in inflammatory bowel diseases: implications for homeostatic intestinal inflammation. *Gut*, 55(6):815–823.

[Pilgram et al., 1999] Pilgram, G. S., Engelsma-van Pelt, A. M., Bouwstra, J. A., and Koerten, H. K. (1999). Electron diffraction provides new information on human stratum corneum lipid organization studied in relation to depth and temperature. *J Invest Dermatol*, 113(3):403–409.

[Pirard et al., 2005] Pirard, D., Vereecken, P., Mélot, C., and Heenen, M. (2005). Three percent diclofenac in 2.5actinic keratoses: a meta-analysis of the recent studies. *Arch Dermatol Res*, 297(5):185–189.

[Poree et al., 2011] Poree, D. E., Giles, M. D., Lawson, L. B., He, J., and Grayson, S. M. (2011). Synthesis of amphiphilic star block copolymers and their evaluation as transdermal carriers. *Biomacromolecules*, 12(4):898–906.

[Quadir et al., 2008] Quadir, M. A., Radowski, M. R., Kratz, F., Licha, K., Hauff, P., and Haag, R. (2008). Dendritic multishell architectures for drug and dye transport. *Journal of Controlled Release*, 132(3):289 – 294. Proceedings of the Tenth European Symposium on Controlled Drug Delivery.

[Radowski et al., 2007] Radowski, M. R., Shukla, A., von Berlepsch, H., Böttcher, C., Pickaert, G., Rehage, H., and Haag, R. (2007). Supramolecular aggregates of dendritic multishell architectures as universal nanocarriers. *Angew Chem Int Ed Engl*, 46(8):1265–1269.

[Ravi Kumar et al., 2004] Ravi Kumar, M. N. V., Sameti, M., Mohapatra, S. S., Kong, X., Lockey, R. F., Bakowsky, U., Lindenblatt, G., Schmidt, H., and Lehr, C. M. (2004). Cationic silica nanoparticles as gene carriers: synthesis, characterization and transfection efficiency in vitro and in vivo. *J Nanosci Nanotechnol*, 4(7):876–881.

[Reich and Szepietowski, 2012] Reich, A. and Szepietowski, J. C. (2012). Non-analgesic effects of opioids: peripheral opioid receptors as promising targets for future anti-pruritic therapies. *Curr Pharm Des*, 18(37):6021–6024.

[Reichardt, 1979] Reichardt, C. (1979). Empirical parameters of solvent polarity as linear free-energy relationships. *Angewandte Chemie International Edition in English*, 18(2):98–110.

[Rich et al., 2013] Rich, R. M., Stankowska, D. L., Maliwal, B. P., Sørensen, T. J., Laursen, B. W., Krishnamoorthy, R. R., Gryczynski, Z., Borejdo, J., Gryczynski, I., and Fudala, R. (2013). Elimination of autofluorescence background from fluorescence tissue images by use of time-gated detection and the azadioxatriangulenium (adota) fluorophore. *Anal Bioanal Chem*, 405(6):2065–2075.

[Roy et al., 2013] Roy, D., Brooks, W. L. A., and Sumerlin, B. S. (2013). New directions in thermoresponsive polymers. *Chem Soc Rev*, 42(17):7214–7243.

[Ruddy and Hadzija, 1992] Ruddy, S. B. and Hadzija, B. W. (1992). Iontophoretic permeability of polyethylene glycols through hairless rat skin: application of hydrodynamic theory for hindered transport through liquid-filled pores. *Drug Des Discov*, 8(3):207–224.

[Salehpour et al., 2012] Salehpour, S., Zuliani, C. J., and DubÃ©, M. A. (2012). Synthesis of novel stimuli-responsive polyglycerol-based hydrogels. *European Journal of Lipid Science and Technology*, 114(1):92–99.

[Saxton, 1993] Saxton, M. J. (1993). Lateral diffusion in an archipelago. single-particle diffusion. *Biophys J*, 64(6):1766–1780.

[Saxton and Jacobson, 1997] Saxton, M. J. and Jacobson, K. (1997). Single-particle tracking: applications to membrane dynamics. *Annu Rev Biophys Biomol Struct*, 26:373–399.

[Schermelleh et al., 2010] Schermelleh, L., Heintzmann, R., and Leonhardt, H. (2010). A guide to super-resolution fluorescence microscopy. *J Cell Biol*, 190(2):165–175.

[Schäfer-Korting et al., 2007] Schäfer-Korting, M., Mehnert, W., and Korting, H.-C. (2007). Lipid nanoparticles for improved topical application of drugs for skin diseases. *Adv Drug Deliv Rev*, 59(6):427–443.

[Schröter et al., 2009] Schröter, A., Kessner, D., Kiselev, M. A., Hauss, T., Dante, S., and Neubert, R. H. H. (2009). Basic nanostructure of stratum corneum lipid matrices based on ceramides [eos] and [ap]: a neutron diffraction study. *Biophys J*, 97(4):1104–1114.

[Schätzlein and Cevc, 1998] Schätzlein, A. and Cevc, G. (1998). Non-uniform cellular packing of the stratum corneum and permeability barrier function of intact skin: a high-resolution confocal laser scanning microscopy study using highly deformable vesicles (transfersomes). *Br J Dermatol*, 138(4):583–592.

[Selvamuthukumar and Velmurugan, 2012] Selvamuthukumar, S. and Velmurugan, R. (2012). Nanostructured lipid carriers: a potential drug carrier for cancer chemotherapy. *Lipids Health Dis*, 11:159.

[Semrau and Schmidt, 2007] Semrau, S. and Schmidt, T. (2007). Particle image correlation spectroscopy (pics): retrieving nanometer-scale correlations from high-density single-molecule position data. *Biophys J*, 92(2):613–621.

[Sisson et al., 2009] Sisson, A. L., Steinhilber, D., Rossow, T., Welker, P., Licha, K., and Haag, R. (2009). Biocompatible functionalized polyglycerol microgels with cell penetrating properties. *Angew Chem Int Ed Engl*, 48(41):7540–7545.

[Solomon, 1978] Solomon, H. (1978). *Geometric Probability*. Society for Industrial and Applied Mathematics.

[Stein, 2013] Stein, C. (2013). Targeting pain and inflammation by peripherally acting opioids. *Front Pharmacol*, 4:123.

[Swartzendruber et al., 1989] Swartzendruber, D. C., Wertz, P. W., Kitko, D. J., Madison, K. C., and Downing, D. T. (1989). Molecular models of the intercellular lipid lamellae in mammalian stratum corneum. *J Invest Dermatol*, 92(2):251–257.

[Tan et al., 2010] Tan, G., Xu, P., Lawson, L. B., He, J., Freytag, L. C., Clements, J. D., and John, V. T. (2010). Hydration effects on skin microstructure as probed by high-resolution cryo-scanning electron microscopy and mechanistic implications to enhanced transcutaneous delivery of biomacromolecules. *J Pharm Sci*, 99(2):730–740.

[Tezel and Mitragotri, 2003] Tezel, A. and Mitragotri, S. (2003). Interactions of inertial cavitation bubbles with stratum corneum lipid bilayers during low-frequency sonophoresis. *Biophys J*, 85(6):3502–3512.

[Türk et al., 2004] Türk, H., Haag, R., and Alban, S. (2004). Dendritic polyglycerol sulfates as new heparin analogues and potent inhibitors of the complement system. *Bioconjug Chem*, 15(1):162–167.

[Tsai et al., 2012] Tsai, M.-J., Wu, P.-C., Huang, Y.-B., Chang, J.-S., Lin, C.-L., Tsai, Y.-H., and Fang, J.-Y. (2012). Baicalein loaded in tocol nanostructured lipid carriers (tocol NLCs) for enhanced stability and brain targeting. *Int J Pharm*, 423(2):461–470.

[van Smeden et al., 2014] van Smeden, J., Janssens, M., Gooris, G. S., and Bouwstra, J. A. (2014). The important role of stratum corneum lipids for the cutaneous barrier function. *Biochim Biophys Acta*, 1841(3):295–313.

[Wang et al., 2008] Wang, L., Zhao, W., and Tan, W. (2008). Bioconjugated silica nanoparticles: Development and applications. *Nano Research*, 1(2):99–115.

[Wang et al., 2011] Wang, Q., Jaimes-Lizcano, Y. A., Lawson, L. B., John, V. T., and Papadopoulos, K. D. (2011). Improved dermal delivery of FITC-BSA using a combination of passive and active methods. *J Pharm Sci*, 100(11):4804–4814.

[Weinhart et al., 2011a] Weinhart, M., Gröger, D., Enders, S., Dernedde, J., and Haag, R. (2011). Synthesis of dendritic polyglycerol anions and their efficiency toward l-selectin inhibition. *Biomacromolecules*, 12(7):2502–2511.

[Weinhart et al., 2011b] Weinhart, M., Gröger, D., Enders, S., Riese, S. B., Dernedde, J., Kainthan, R. K., Brooks, D. E., and Haag, R. (2011). The role of dimension in multivalent binding events: structure-activity relationship of dendritic polyglycerol sulfate binding to l-selectin in correlation with size and surface charge density. *Macromol Biosci*, 11(8):1088–1098.

[Weissleder et al., 2014] Weissleder, R., Nahrendorf, M., and Pittet, M. J. (2014). Imaging macrophages with nanoparticles. *Nat Mater*, 13(2):125–138.

[Wertz, 2013] Wertz, P. W. (2013). Current understanding of skin biology pertinent to skin penetration: skin biochemistry. *Skin Pharmacol Physiol*, 26(4-6):217–226.

[Winkler et al., 2007] Winkler, K., Winter, A., Rueckert, C., Uchanska-Ziegler, B., and Alexiev, U. (2007). Natural MHC class i polymorphism controls the pathway of peptide dissociation from HLA-B27 complexes. *Biophys J*, 93(8):2743–2755.

[Witasp et al., 2009] Witasp, E., Kupferschmidt, N., Bengtsson, L., Hultenby, K., Smedman, C., Paulie, S., Garcia-Bennett, A. E., and Fadeel, B. (2009). Efficient internalization of mesoporous silica particles of different sizes by primary human macrophages without impairment of macrophage clearance of apoptotic or antibody-opsonized target cells. *Toxicol Appl Pharmacol*, 239(3):306–319.

[Wolf et al., 2009] Wolf, N. B., Küchler, S., Radowski, M. R., Blaschke, T., Kramer, K. D., Weindl, G., Kleuser, B., Haag, R., and Schäfer-Korting, M. (2009). Influences of opioids and nanoparticles on in vitro wound healing models. *Eur J Pharm Biopharm*, 73(1):34–42.

Acknowledgment

First of all I would like to thank Prof. Dr. Ulrike Alexiev for giving me the opportunity to conduct the research for my PhD thesis in her group and to work on the application of diverse fluorescence-based methods to questions raised by the exciting new field of nanomedicine. In addition, I also would like to thank her for all the discussion of ideas and results as well as the experimental procedures and also for all the discussions and suggestions to my thesis.

I would also like to thank Prof. Dr. Karsten Heyne for agreeing to be the second supervisor to my PhD project.

A special thanks goes to all of my collaborators for supplying me with samples and for the discussion of the results. Especially to Prof. Rainer Haag and Dr. Emanuel Fleige from the Chemistry Department of the FUB, Prof. Achim D. Gruber, Dr. Lars Mundhenck and Anja Ostrowski from the Department of Veterinary Medicine of the FUB, Prof. Dr. Monika Schäfer-Korting, Dr. Sarah Küchler, Nesrin Alnasif (from the Pharmacy Department of the FUB) and Madeleine Witting (Institute of Pharmaceutical Technology and Biopharmaceutics, LMU Munich), Prof. Keck (Institute of Applied Logistic and Polymer Sciences, University of Applied Sciences Kaiserslautern) and Daniel Peters (Institute of Pharmacy, FUB), Dr. Kai Licha from mivenion as well as Prof. Christoph Stein and Dr. Viola Stein from the Department of Anesthesiology and Operative Intensive Care Medicine at the Charité.

Further, I would like to acknowledge my Master/Diploma and Bachelor Students Marcus Pfaff, Robert Brodwolf, Alexander Wolf, Robert Streeck, Jannis Althoff, Jens Pikkemaat, Johannes Stellmacher, Alexander Schulz and Marcus Trautmann.

Also all the colleagues, past and present, I had the pleasure of working with in the last couple of years. In particular Dr. Tai-Yang Kim for his constant assistance and patience with the laser setups, Dr. Kristina Kirchberg for always having an open ear and my office colleague Dr. Boris Repen for the good chats and the laughs we shared. Robert Brodwolf, Thomas Schlieter and Dr. Sebastian Haase for developing many of the analysis routines without which I could not have obtained many of my results and also Jens Balke, Pierre Volz, Alexander Wolf for their time spent on proof-reading various passages of this thesis. In addition, I would like to thank them and Constantin Schneider and Alex Griffin for sharing many of my responsibilities in the management of the labs in the final stages of my thesis, helping me to focus on my writing.

Last but not least I would like to thank my friends and my family for all their support and help in the final stages of the thesis and in particular my wife Alexandra for her continued support through all the ups and downs that accompany a PhD thesis and for always believing in me.

Selbstständigkeitserklärung

Hiermit bestätige ich, Alexander Dylan Piers Boreham, dass ich die vorliegende Dissertation mit dem Titel: „From molecules to tissue: Fluorescence spectroscopy and microscopy of nanoparticles and biomolecules involved in inflammation and pain“ selbstständig und ohne unerlaubte Hilfe angefertigt habe. Ich versichere, dass ich ausschließlich die angegebenen Quellen und Hilfen in Anspruch genommen habe.

Berlin, den 31.07.2014